

Evolution of the sub-oceanic mantle lithosphere beneath the SW Pacific region

by

Natasha Barrett

A thesis submitted in partial fulfillment of the requirements for the degree of

Doctor of Philosophy

Department of Earth and Atmospheric Sciences
University of Alberta

© Natasha Barrett, 2021

ABSTRACT

The sub-oceanic mantle lithosphere is a fundamental component of Earth's dynamic evolution, however, much of this region remains inaccessible for the most part. As a result, many outstanding questions remain with regard to its variability beneath ocean basins, plateaux and islands, the possible role of such lithosphere in forming some of the larger scale features observed in the oceans and even in continent formation. This thesis investigates the processes and evolution of the sub-oceanic lithospheric mantle beneath the Southwest (SW) Pacific region via two direct sampling methods: 1) basalt-hosted peridotite xenoliths erupted by volcanic eruptions from Koro Island in eastern Fiji, and 2) tectonically exposed sections of mantle lithosphere as ophiolite peridotites from the Marum ophiolite and Papuan Ultramafic Belt (PUB) in Papua New Guinea (PNG). Both studies are located in the SW Pacific region that formed via complex tectonic interactions between the Pacific and Indo-Australian plate, and collectively, provide information on the melt depletion and subsequent melt enrichment history of the underlying mantle lithosphere of this vast region.

Chapter 2 reports new petrological, geochemical, highly siderophile element (HSE: Os, Ir, Ru, Pt, Pd, and Re), and Os isotope data from a suite of spinel peridotite xenoliths hosted in <3 Ma alkali basalts from Koro Island in eastern Fiji. These xenoliths are dominated by lherzolites, with a smaller population of harzburgites, dunites, and wehrlites. Residual signatures from orthopyroxene, olivine and the whole-rock chemistry correspond to partial melting of ~5% to <25%. Residual clinopyroxene is scarce but displays lower HREE than orthopyroxene when present, a disequilibrium feature providing evidence of former equilibration with garnet and pre-existing thickened lithosphere. The lack of hydrous phases, along with spinel fO_2 values ranging from moderately reduced to slightly oxidised (FMQ -1.1 to 0.74) are distinct from typical fore-arc mantle signatures, however, spinel $Fe^{3+}/\Sigma Fe$ ratios >0.25 and prominent negative Ce anomalies in olivine are associated with more oxidising conditions, suggesting that this pre-existing thickened lithosphere may resemble back-arc mantle lithosphere that has since been overprinted by metasomatism. The dominant metasomatic process recorded in these samples occurs as silicate melt-rock interaction that resulted in the production of wehrlites comprised of metasomatic clinopyroxene and olivines with lower forsterite (<Fo₈₈) contents than typical mantle peridotite, likely formed at the expense of residual orthopyroxene. A separate, but less common/extensive

metasomatic process produced dunite and harzburgite xenoliths characterized by higher spinel chrome number (Cr#) vs. Ti contents. The Koro peridotites therefore record a multi-stage re-enrichment history involving the interaction with melts of varying source composition. Whole-rock platinum group element (PGE) signatures reflect the addition of metasomatic sulfides (<30 µm) that have precipitated along grain boundaries and within crystalized late-stage clinopyroxene melts. The mean $^{187}\text{Os}/^{188}\text{Os}$ ratio for Koro peridotites is 0.1269 ± 0.0027 and overlaps with the most recent peak (~0.1260) observed in OIB-hosted peridotite xenoliths from Samoa, to the east of Fiji. The Koro peridotites, along with other oceanic peridotites, show no relationship with typical melt depletion indices (i.e., Al_2O_3 wt. %, Cr# in spinel and Fo content in olivine), reflecting convecting mantle heterogeneity and mixing due to metasomatism rather than a single partial melt-extraction event. The widespread silicate melt metasomatism and perturbed geothermal gradient beneath Koro support indications from seismology studies that the removal of back-arc lithosphere could have been linked to the ingress of Samoan plume material beneath Fiji as a result of slab rollback of the subducting Pacific Plate.

Chapter 3 focuses on the formation of tectonite peridotites from the PUB and Marum ophiolites of PNG that represent some of the most melt-depleted mantle peridotites on Earth. These peridotites are characterized by olivine Fo contents between Fo_{91.2} to Fo_{94.6} (median = Fo_{92.3}) and spinel Cr# values between 0.71 to 0.95. Whole-rock Al and Ca contents reach very low abundances (0.03–0.35 wt. % Al_2O_3 ; 0.03–0.25 wt. % CaO) and high Cr/Al ratios (1.3–12.7). These melt-depletion indices extend to more extensive levels of melt depletion than median values for cratonic peridotites. The origin of these ultra-depleted mantle residues is re-examined through new major element, trace element, HSE and Os isotope data to better understand the timing and processes involved in the formation of such ultra-depleted mantle compositions. Comparison with residues produced from experimental studies and modelling indicate that the geochemistry of these mantle tectonites reflect ~25 to > 40 % partial melting of fertile mantle peridotite. The most melt-depleted examples of these peridotites are observed in the PUB harzburgite tectonites, and exceed levels of melting predicted from single-stage anhydrous melt experiments. While initial melting could have occurred under anhydrous conditions, the ultra-depleted compositions indicate that a water-fluxed melt environment is essential, at some stage in their evolution, to reach such extensive levels of melt depletion. The presence of such a melting environment in the development of a nascent intra-oceanic arc system in this region is supported by the occurrence of low-Ca boninites overlying the

PUB that are among the most “depleted” melts observed in subduction systems. The Marum dunite tectonites show similarly depleted major element compositions, however, their higher olivine HREE abundances suggest they are of replacive origin and their major element chemistry may not reflect true levels of depletion. The Marum harzburgite tectonite compositions are not as melt depleted as the PUB harzburgite tectonites, and do not necessitate hydrous conditions if produced at low pressures (≤ 2 GPa) and high temperatures ($\sim 1250\text{--}1350$ °C). Associated overlying cumulate peridotite and gabbro sequences and basaltic lavas (from the PUB) indicate formation from magnesian mafic magmas more depleted than MORB and resembling the fore-arc basalts (FAB) found associated with subduction initiation at some oceanic island arcs. This evidence collectively points towards a two-stage melt evolution. The first melt stage most likely occurred during subduction initiation and production of FAB-like lavas, while the second stage, for some peridotites, involved a water-fluxed environment resulting in the production the extremely depleted peridotite residues of the PUB and eruption of the overlying boninite lavas. Unusual whole-rock HSE signatures in the Marum and PUB tectonites are characterized by very low Os, Ir and Pt abundances and do not reflect typical Ir-group (Ir, Os, Ru) PGE to Pt-group (Pd, Pt) PGE depletion patterns observed in large degree melt residues such as cratonic peridotites or the most depleted oceanic peridotites. Such HSE patterns may reflect dissolution of PGE-rich phases by melt-rock interaction, possibly by interaction with an aggressive subduction-related fluid. $^{187}\text{Os}/^{188}\text{Os}$ ratios reflect values within the range of modern convecting mantle, indicating that these very depleted compositions are not linked to ancient melt depletion events as commonly perceived.

PREFACE

This thesis is original work conducted by Natasha Barrett under the direct supervision of Professor Graham Pearson at the University of Alberta. Sample specimens for Chapter 2 were collected by Natasha Barrett, Graham Pearson, and Neil Kumar in 2016, and Holger Sommer in 2012. Specimens for Chapter 3 were made available by Lynton Jaques and Ignacio González-Álvarez. All laboratory work done at the University of Alberta was conducted by Natasha Barret, excepting some ICP-MS whole-rock trace element analyses in Chapter 3 collected by Sarah Woodland. All analyses done at the Australian National University were collected by Lynton Jaques, who also provided some scientific input and feedback for Chapter 3. Modified versions of Chapters 2 and 3 are intended for publication to international journals.

ACKNOWLEDGEMENTS

This PhD thesis was made possible with the help of many over the last 4 years. Firstly, thank you to my advisor, Graham Pearson, for providing your research expertise, and offering many opportunities throughout my PhD to help me build a strong foundation of scientific skills, both in the laboratory and in the field. Thank you to my examining committee Thomas Stachel, Bob Luth, Stephen Johnson, and Marguerite Godard, for contributing your expertise and feedback on this thesis and during the examination. Thank you to Tom Chacko for chairing both my candidacy and PhD defense, but also for supporting all of us EAS graduate students during your time as grad chair.

Field work and sample collection in Fiji was made possible in collaboration with Holger Sommer and Neil Kumar from The University of the South Pacific. I would like to acknowledge the Mineral Resources Department of Fiji for granting permits to collect samples, and each village on Koro Island (Kade, Navaga, Tavua, Nabasovi, Nabuna, Vatulele, Nathamaki, Tuatua, Nasau, Naqaidamu, Sinuvaca, Namacu, Nakodu, and Mudu) for permission to stay on Koro and the invitation to participate in a sevusevu. The specimens for this study were collected from the land of Navaga and Nasau. A special thanks to our local guide, Maciu, who helped us with carrying samples and clearing paths through dense vegetation with a machete. I would also like to thank Satendra Kumar who helped with cutting samples at USP, and Steve Foley and Dorit Jacob for hosting me during my transit in Sydney on route to Fiji.

I'm grateful to Sarah Woodland for training me in the clean lab, teaching me how to operate the mass spectrometers, and being an all-round great person to work with. Thank you to Andrew Locock for helping with the EPMA assistance, Yan Luo for LA-ICP-MS assistance, to Stan Mertzman for running whole-rock major element analyses, Martin Von Dollan for making thin sections, Mark Labbe for helping me fix numerous things on many occasions, and Anetta Banas for organising and coordinating the DERTS program. I'm thankful for additional financial support from the Patricia Anne Cavell Graduate Scholarship in Earth Sciences, Owen Schlosser Memorial Scholarship, and a National Geographic Early Career Grant to do a second field campaign in Fiji. Additional samples were kindly provided by Ignacio Gonzalez-Alvarez, and Lynton Jaques, and

Holger Sommer. Thank you to James Day, Bob Luth, James Scott, and Sasha Wilson for providing some olivines for LA-ICP-MS analyses during this project as well.

To all my EAS peers and everyone who is part of the DERTS/mantle research group, thank you for the great science conversations, friendships and camping trips that have made this experience all the more memorable. Finally, to my family and to my partner Tyler for your incredible support throughout this process.

TABLE OF CONTENTS

ABSTRACT.....	ii
PREFACE	v
ACKNOWLEDGEMENTS.....	vi
TABLE OF CONTENTS.....	viii
LIST OF FIGURES	xi
LIST OF TABLES.....	xii
Chapter 1	1
1.1. BACKGROUND.....	1
1.1.1. Defining oceanic mantle lithosphere	3
1.1.2. Mantle xenoliths.....	3
1.1.3. Ophiolites	4
1.2. PRINCIPAL THEMES	5
1.2.1. Residue vs. cumulate origin.....	5
1.2.2. Melt-rock interaction vs. metasomatism.....	6
1.2.3. HSE budget of the mantle	6
1.3. PROJECT AIMS	7
1.3.1. Aims for Chapter 2: Fijian peridotite xenoliths	7
1.3.2. Aims for Chapter 3: Papuan ophiolite peridotites.....	8
Chapter 2	9
2.1. INTRODUCTION.....	9
2.2. GEOLOGICAL BACKGROUND.....	10
2.2.1. Summary of the geological history of the Fijian Islands	10
2.2.2. Geological context of Koro Island.....	11

2.3. PERIDOTITE DESCRIPTIONS AND PETROGRAPHY	13
2.4. METHODS.....	16
2.4.1. Whole-rock major and trace elements	16
2.4.2. Electron Probe Microanalysis.....	19
2.4.3. Mössbauer spectroscopy	19
2.4.4. Laser ablation inductively coupled plasma mass spectrometry (LA-ICP-MS)	20
2.4.5. Os isotope and HSE: isotope dilution chemistry	21
2.4.6. Os isotope and HSE: mass spectrometry	21
2.5. RESULTS.....	22
2.5.1. Major element chemistry	23
2.5.2. Whole-rock major and trace chemistry.....	24
2.5.3. Trace element mineral chemistry	40
2.5.3.5. Inter-mineral partitioning	48
2.5.4. P-T and log fO ₂ calculations	51
2.5.5. ¹⁸⁷ Os/ ¹⁸⁸ Os and HSE signatures	55
2.6. DISCUSSION	62
2.6.1. Residual origin for Koro peridotite xenoliths	62
2.6.2. Refertilization/metasomatism of the Koro lithosphere	69
2.6.3. Koro xenolith comparisons to normal oceanic mantle lithosphere.....	73
2.6.4. Evidence for a pre-existing thickened lithosphere.....	74
2.6.5. SW Pacific regional tectonic implications	76
2.7. SUMMARY AND CONCLUSION.....	78
Chapter 3.....	80
3.1. INTRODUCTION.....	80
3.2. GEOLOGICAL CONTEXT AND SAMPLES.....	81

3.2.1. Geological context	81
3.2.2. Geology and petrography of the peridotites.....	84
3.3. ANALYTICAL METHODS.....	87
3.4. RESULTS.....	88
3.4.1. Mineral chemistry: major elements	88
3.4.2. Whole-rock major and trace elements	93
3.4.3. Mineral Chemistry: in-situ trace elements	103
3.4.4. Whole-rock HSE and Os isotope signatures.....	107
3.5. DISCUSSION	112
3.5.1. Equilibration conditions.....	112
3.5.2. Extent and environment of melt depletion in the PNG ophiolite peridotites.....	112
3.5.3. Evidence for a multi-stage melting model	118
3.5.4. Reconciling the extreme HSE variability in the PNG mantle with melting and melt-rock reaction processes	122
3.5.5. Origin of the PNG mantle tectonites.....	125
3.6. SUMMARY AND CONCLUSIONS	126
Chapter 4.....	128
4.1. Relationships between mantle melting, HSE and Os isotope systematics.....	128
4.2. Mantle metasomatism / melt-rock interaction	129
4.3. SW Pacific mantle evolution in the context of the Pacific	130
4.4. Recommendations for future work	131
BIBLIOGRAPHY	135
APPENDICES	157
Appendix 1. Chapter 2 supplementary figures	157
Appendix 2. Chapter 3 supplementary figures	159

Appendix 3. Chapter 2 supplementary tables	160
Appendix 4. Chapter 3 supplementary tables	232
Appendix 5. Standards and LOD values.....	244
Appendix 6. Database references.....	286

LIST OF FIGURES

Figure 1.1. Tectonic setting of the SW Pacific region.....	2
Figure 2.1. Tectonic context and regional geology of Koro Island	12
Figure 2.2. Hand sample summary of the main Koro peridotite xenolith lithologies	14
Figure 2.3. Major petrographic features in the Koro peridotites	15
Figure 2.4. BSE images of sulfides in the Koro peridotites.....	18
Figure 2.5. Koro peridotite olivine Fo vs. spinel Cr# (OSMA plot).....	25
Figure 2.6. Koro peridotite whole-rock Al ₂ O ₃ and CaO vs. MgO plots.....	32
Figure 2.7. Koro peridotite whole-rock normalized trace elements	39
Figure 2.8. Koro host basalt total alkalis vs. silica (TAS) diagram and normalized trace element abundances.....	42
Figure 2.9. Box and whisker plots of Al, Ti, Ni, Ca, V, and Co in olivine	43
Figure 2.10. Koro peridotite REE normalized olivine abundances	45
Figure 2.11. [La/Yb] _N vs. Ti/Eu in clinopyroxene (carbonatite vs. silicate metasomatism test)..	48
Figure 2.12. Inter-mineral partitioning for select REE in Koro peridotites	49
Figure 2.13. Koro peridotite REE normalized clinopyroxene and orthopyroxene abundances ...	50
Figure 2.14. Mineral concentration ratios ($D^{opx/cpx}$) for REE in Koro peridotites plotted against experimentally derived and equilibrated natural peridotites.....	52
Figure 2.15. Spinel Fe ³⁺ /ΣFe ratios measured by Mössbauer spectroscopy in Koro peridotites..	56
Figure 2.16. Koro peridotite whole-rock normalized PGE abundances	61
Figure 2.17. Koro peridotite Cr#-TiO ₂ relationships within spinel and between spinel and clinopyroxene.....	64

Figure 2.18. Estimates for degree of melting in Koro peridotites compared to partial melting experiments	65
Figure 2.19. $^{187}\text{Os}/^{188}\text{Os}$ vs. Al_2O_3 wt. % and $^{187}\text{Os}/^{188}\text{Os}$ vs. Os in Koro peridotites.....	68
Figure 2.20. Kernel density estimate plot of $^{187}\text{Os}/^{188}\text{Os}$ ratios in Koro peridotites.....	69
Figure 2.21. Pressure-temperature estimates in Koro peridotites	75
Figure 2.22. Schematic showing Samoan plume and rollback of the Pacific Plate.....	77
Figure 3.1. Schematic geological map of New Guinea with PNG ophiolite localities.....	82
Figure 3.2. Major element plots for olivine, orthopyroxene and spinel in the PNG tectonites	89
Figure 3.3. Variations in spinel Cr# vs. olivine Fo content in the PNG tectonites.....	92
Figure 3.4. Whole-rock major elements abundances in the PNG tectonites	101
Figure 3.5. PNG tectonite whole-rock trace element and REE normalized abundances.....	102
Figure 3.6. PNG tectonite whole-rock Ti vs. Yb and V vs. Yb plots	104
Figure 3.7. REE normalized patterns in olivine from the PNG tectonites.....	106
Figure 3.8. PNG tectonites chondrite normalized PGE abundances	110
Figure 3.9. $^{187}\text{Os}/^{188}\text{Os}$ vs. Os ppm, Al_2O_3 wt. %, and $[\text{Pt}/\text{Pd}]_{\text{N}}$ in the PNG tectonites.....	111
Figure 3.10. Spinel Cr# vs. TiO_2 wt. % in the PNG tectonites.....	117
Figure 3.11. Kernel density estimate plot for $^{187}\text{Os}/^{188}\text{Os}$ in the PNG tectonite peridotites.....	122
Figure 4.1. Geological map of Moala, Matuku and Totoya Islands	134

LIST OF TABLES

Table 2-1. Whole-rock XRF major and trace element abundances in Koro peridotites.....	26
Table 2-2. Whole-rock ICP-MS trace element abundances in Koro peridotites	34
Table 2-3. Whole-rock XRF major and trace element abundances in Koro host basalts	35
Table 2-4. Whole-rock ICP-MS trace element abundances in Koro host basalts.....	41
Table 2-5. Calculated temperatures and pressures in Koro peridotites	53
Table 2-6. Os isotopes and HSE abundances in Koro peridotites	57
Table 3-1. Whole-rock XRF major and trace element abundances in PNG tectonites.....	94
Table 3-2. Whole-rock ICP-MS trace element abundances in PNG tectonites	98
Table 3-3. Os isotopes and HSE abundances in PNG tectonites	108

Chapter 1

Introduction

1.1. BACKGROUND

The Earth's oceanic mantle lithosphere is possibly the most well understood portion of the mantle interior. This is due to a number of geological phenomena (i.e., tectonic processes or deeply sourced volcanic eruptions) that allow for direct sampling of this region, and a general knowledge of mid-ocean ridge evolution with seafloor age (e.g., Stein & Stein, 1992). Despite this, samples of oceanic mantle lithosphere have shown this part of the Earth to be highly heterogeneous in chemical composition and lithology, particularly in more complex geodynamic environments such as beneath subduction zones, oceanic plateaux, or beneath intraplate/plume-related oceanic settings. In various oceanic settings, the mantle lithosphere can be exposed at depths from as shallow as ~6.5 km (e.g., White & Klein, 2014) and extend to depths of ~120 km or more beneath older and thicker oceanic plateaus (e.g., Ishikawa, 2011).

This thesis project will focus on the composition and evolution of the lithospheric mantle beneath the Southwest (SW) Pacific Islands, as sampled by peridotite xenoliths hosted in <3 Ma alkali basalts (Coulson, 1973) from the Fijian Islands, and ophiolitic mantle peridotites from the Papuan Ultramafic Belt (PUB) and Marum ophiolite in Papua New Guinea (PNG) (Fig. 1.1). The SW Pacific Islands (New Guinea, Solomon Islands, Fiji, New Caledonia, Vanuatu, Tonga, Samoa) are part of a geologically complex region on Earth recording multiple episodes of rifting, active spreading, subduction polarity reversals, intraplate-, and subduction-related volcanism. Studying the geology of these islands has contributed vital information regarding the understanding of collisional and subduction processes between the Indo-Australian and Pacific Plate margin, however, the oceanic lithosphere beneath this region, with the exception of the Ontong Java Plateau (e.g., Nixon & Coleman, 1978; Nixon & Boyd, 1979; Ishikawa *et al.*, 2004, 2011; Demouchy *et al.*, 2015), still remains poorly characterized. This plate margin, including the eastern margin of Gondwana recorded in eastern Australia, Western Antarctica, South America, and more

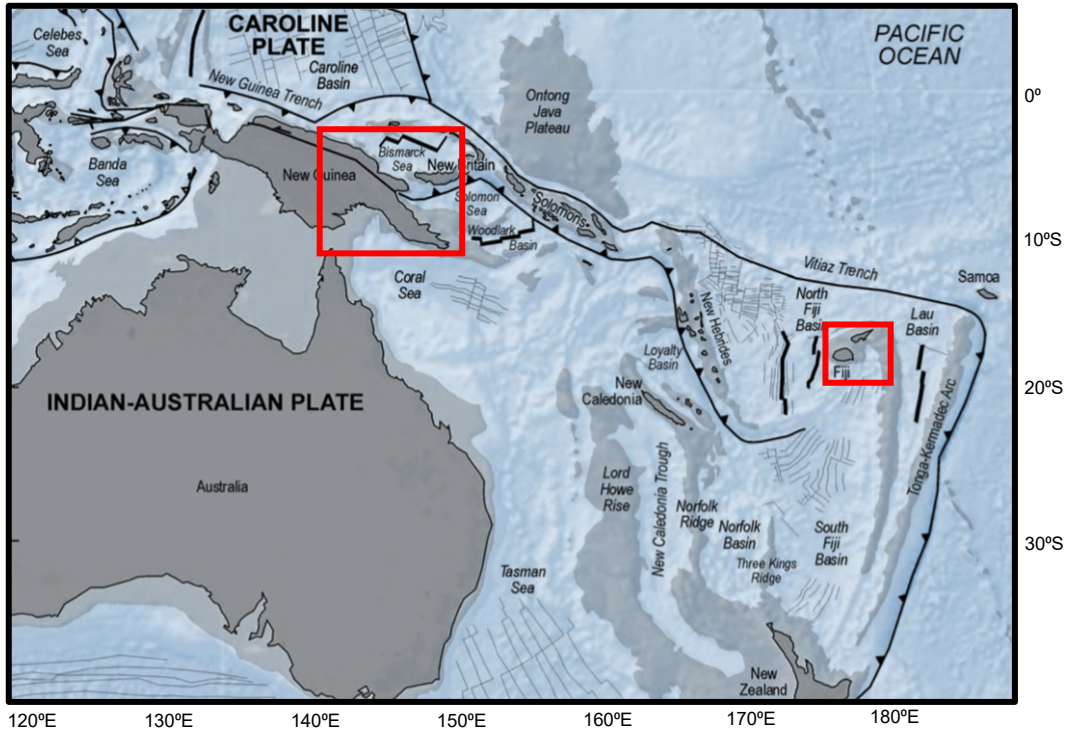


Figure 1.1. Tectonic configuration of the SW Pacific showing the major tectonic features (Hall, 2002) modified after Whatmough *et al.* (2008) superimposed on the Esri Ocean Base map. Red rectangles indicate study areas in Papua New Guinea (left) and Fiji (right).

recently New Zealand, has been demonstrated to be geologically significant for understanding the role of subduction in post-Archean crustal production and continent stabilization (e.g., Liu *et al.*, 2015; Scott *et al.*, 2019). To date, there are no previous studies of the mantle root underpinning the Fijian Islands and very few PNG peridotites have been previously studied (e.g., England & Davies, 1973; Jaques & Chappell, 1980; Kaczmarek *et al.*, 2015). Such samples have the potential to record complex melting, metasomatism, and compositional changes related to post-entrainment and exhumation events (Anderson, 2007), providing a unique opportunity to study the age, depth, and isotopic and geochemical diversity of the lithospheric mantle beneath the SW Pacific Islands. In general, understanding the evolution and geological processes at these depths is essential for quantifying the Earth's thermal budget, crust-mantle differentiation, and subsequent growth of new islands and continents (e.g., Hofmann, 1988).

1.1.1. Defining oceanic mantle lithosphere

Earth's upper boundary for oceanic mantle lithosphere can be defined either by the seismic Mohorovičić Discontinuity (Moho) based on a change in P-wave velocity from $7.1\text{--}7.5\text{ km s}^{-1}$ in the lowermost oceanic crust to 8.1 km s^{-1} in the upper mantle (e.g., Clague & Straley, 1977), or by the petrographic Moho defined by the boundary between gabbros/cumulates and peridotites (e.g., Moores & Vine, 1971; Jackson *et al.*, 1975). This petrographic distinction is not always clear (see section 1.1.2), and several discrepancies exist between the seismically defined Moho and the petrographically defined Moho (Artemieva, 2011). The lower limit for the ocean mantle lithosphere is the lithosphere–asthenosphere boundary (LAB) separating the cold rigid lithosphere from the hotter viscoelastic convecting asthenosphere (Fischer *et al.*, 2010). Beneath oceanic basins this has been estimated at ~ 70 kms depth based on changes in seismic velocity with depth (e.g., Rychert & Shearer, 2009), however, the exact cause of this seismic boundary, as to whether it resembles a thermal boundary or is controlled by mantle melting remains unresolved. Petrologically, the LAB beneath oceanic basins is based on the wet solidus–geotherm intersection (Green *et al.*, 2010; Niu & Green, 2018) due to the influence of water on rheology. In the mantle wedge of subduction zones this has been recently approximated at $950\text{--}1000\text{ }^{\circ}\text{C}$ at 3 GPa (Wang *et al.*, 2020).

1.1.2. Mantle xenoliths

Peridotite xenoliths have long been recognized to often resemble fragments of Earth's mantle with the first realisation that oceanic peridotite xenoliths were genetically distinct rocks from their host basalt from Ross *et al.* (1954), with important earlier contributions from Ernst (1936), Frechen (1948), and Turner & Bartrum (1928). Since then, mantle xenoliths have provided a wealth of information concerning the Earth's interior to complement geophysical data (Nixon, 1980; Pearson *et al.*, 2003). Xenoliths have both advantages and disadvantages to tectonically emplaced peridotites. Their mineralogy and major element chemistry denote pressure-temperature (P-T) conditions within the spinel stability field ($\sim 900\text{--}1400\text{ }^{\circ}\text{C}$ and $\sim 0.7\text{--}3.0\text{ GPa}$; Koga *et al.* 1999; Klemme, 2004), and typically extents of melt removal between 5–20% (Luguet & Reisberg, 2016). Therefore, they have the potential to sample deeper and more fertile depths in the oceanic mantle (e.g., Bodinier & Godard, 2003). However, peridotite xenoliths may also be more susceptible to re-fertilization compared to large tectonic blocks (e.g., Eggler, 1987; Zindler & Jagoutz, 1988;

McKenzie, 1989) and recent studies have shown large compositional variations in mantle xenoliths that sample the lithosphere beneath oceanic islands, reflecting complex melting processes, re-enrichment, and metasomatism in the sub-oceanic lithosphere (e.g., Simon *et al.*, 2008).

Peridotite xenoliths from oceanic settings have been mostly sampled within intraplate hotspot volcanoes such as Hawaii (e.g., Ross *et al.*, 1954), Samoan and Cook-Austral Islands (e.g., Hauri & Hart, 1993; Snortum *et al.*, 2019; Jackson *et al.*, 2016), Tahiti (e.g., Tracy, 1980; Simon *et al.*, 2008), Canary Islands (e.g., Neumann, 1991, 1995), Dragon Seamount (southern Tore-Madeira rise) (e.g., Merle *et al.*, 2012), and Noronha Island, Brazil (Kogarko *et al.*, 2001). Other oceanic xenoliths include those found in oceanic plateau settings such as the Solomon Islands–Ontong Java Plateau (e.g., Ishikawa *et al.*, 2004, 2007, 2011) and Kerguelen Plateau (e.g., Grégoire *et al.*, 2000), as well as in subduction settings such as the Bismarck archipelago (Franz & Wirth, 2000; McInnes *et al.*, 2001; Franz, 2002; Soustelle *et al.*, 2013; Tollar *et al.*, 2015, 2017), Tonga (Birner *et al.*, 2017), SW Japan (e.g., Abe *et al.*, 1998; Senda *et al.*, 2007), Vanuatu (Barsdell & Smith, 1989), and the Philippines (Maury *et al.*, 1992). Unlike previously studied oceanic xenoliths from well-known geotectonic environments, the xenoliths in the eastern Fijian Islands have the potential to sample either arc-like or intra-plate lithosphere due to the complex tectonic configuration of Fiji. Part of this study will use the Fijian mantle xenoliths to try to constrain better the larger-scale geodynamic processes that have been responsible for the current setting of the Fiji archipelago.

1.1.3. Ophiolites

Ophiolites resemble large sections of oceanic crust and mantle lithosphere (Penrose participants, 1972) and from the viewpoint of documenting mantle processes they have some advantages over mantle xenoliths due to the capability of being able to observe field relationships. However, ophiolites tend to expose shallower mantle depths compared to xenolith suites, as they need to be tectonically emplaced and are often more susceptible to low temperature alteration. Ophiolite genesis is not straightforward, and various models for their formation have undergone considerable changes as summarized in Dilek (2003). Only shortly after the ophiolite definition was established by the Penrose field conference participants in 1972, Miyashiro (1973) made a connection between ophiolite genesis and subduction based on geochemical evidence for an island arc affinity in the Troodos ophiolite in Cyprus. Following the supra-subduction zone (SSZ) ophiolite concept introduced by Pearce *et al.* (1984), the study by Miyashiro (1973) was re-evaluated and discussed

in more detail by Pearce & Robinson (2010), who suggested the formation of these bodies during subduction initiation or above a slab edge rather than in an island arc. Nonetheless, the preliminary subduction relationship suggested by Miyashiro (1973) was a significant turning point for the possibility of ophiolite genesis in a subduction setting, although it is important to note that not all ophiolites are considered to be SSZ-type ophiolites, e.g., the Masirah Island ophiolite in Oman that is thought to have formed above a mid-ocean ridge setting based on its MORB-like lava compositions (Rollinson, 2017). The SSZ ophiolite concept is important for this study because such settings are often associated with highly depleted peridotites—the focus of Chapter 3. These depleted peridotites are characterized by high temperature structural fabrics in the harzburgites and dunites or “metamorphic tectonites”, first defined after field mapping by Moores & Vine (1971).

1.2. PRINCIPAL THEMES

Outlined in this section are a number of continuing themes and current knowledge gaps that will be covered in this thesis.

1.2.1. *Residue vs. cumulate origin*

Peridotite cumulates (including orthocumulates, mesocumulates, and adcumulates; Wager *et al.*, 1960) that originate as igneous rocks via fractional crystallization (Irvine, 1982), often have the same mineralogy as residual peridotites (i.e., mantle residues after melt extraction), and very subtle chemical distinctions. Yet distinguishing their origin has profound implications for the geodynamic interpretation of such rocks. The petrological distinction between crust and mantle in the oceanic lithosphere is often not clear, and can be gradational between crust and regions of upwelling mantle, referred to as the mantle transition zone (MTZ) (Boudier & Nicolas, 1995). As a result, cumulate peridotites are considered to be part of the lowermost crust, whereas, residual peridotites tend to be considered fragments of mantle lithosphere. In order to best evaluate partial melting processes in the mantle and better understanding the geodynamic environment, it is important to identify peridotites of non-mantle origin, such as magmatic cumulates (e.g., Sen & Jones, 1990), versus peridotites that represent mantle residues after partial melting (e.g., Simon *et al.*, 2008). Partial melting of the Earth’s mantle is a geological phenomenon in itself, and understanding the causes and consequences of melting is essential for reconciling basalt petrogenesis and the growth of volcanic islands. Partial melting can occur through adiabatic

decompression, typical of mantle beneath mid ocean ridge centres, addition of heat, such as the influx of plume material, or addition of volatiles such as water from a dehydrating slab and lowering the peridotite solidus. The peridotite tectonites from the PNG ophiolite, in particular, are some of the most melt-depleted peridotites recognized on Earth (Jaques & Chappell, 1980; Boyd, 1989), and therefore, are ideal specimens for studying partial melting in the mantle lithosphere.

1.2.2. *Melt-rock interaction vs. metasomatism*

Metasomatism is the broad term used to describe prevalent metamorphic fluid interaction that can result in either chemical or mineralogical changes to the rock (Zharikov *et al.*, 2007). Melt-rock interaction is a subset of metasomatism, and in this thesis, specifically refers to the interaction between peridotite (rock) and either silicate, hydrous, and/or carbonatitic melts (e.g., Bodinier *et al.*, 2004). It is important to recognize metasomatic processes as they can overprint signatures for partial melting.

1.2.3. *HSE budget of the mantle*

Highly siderophile elements (HSE: Os, Ir, Ru, Pt, Pd, Re) and the ^{187}Re - ^{187}Os system are important for investigating the extent and timing of melt depletion in the mantle (Walker *et al.*, 1988, Shirey & Walker, 1998). HSEs play a pivotal role in understanding solid Earth evolution in general, however, the HSE budget in the mantle remains under-constrained. While these elements are a large focus of this thesis, there are a number of caveats when applied to mantle peridotites, specifically post-Archean oceanic mantle lithosphere, that should be addressed. HSE abundances and the Os isotope composition of the Earth's mantle is understood to be set by the addition of chondritic material during late accretion (Chou, 1978; Morgan, 1986). As a consequence, calculated Re-Os depletion ages will depend on the choice of primitive mantle evolution curve, whether that is based on ordinary(O)-chondrite, carbonaceous(C)-chondrite, or (enstatite)E-chondrite, or primitive upper mantle (PUM) estimates (e.g., Meisel *et al.*, 2001; Becker *et al.*, 2006) as well as the degree of heterogeneity in these potential parental materials. A combination of ancient melt-depletion processes leaving mantle residues of varying states of depletion within the convecting upper mantle combined with the re-mixing of mantle with subducting oceanic crust means that calculated model ages from oceanic mantle rarely reflect a single melt extraction age or a geologically meaningful Re-Os isochron, and have model age uncertainties as large as the calculated age, for Phanerozoic melting events (e.g., Pearson *et al.*, 2007). HSEs are resistant to

low temperature alteration and serpentinization, however, there is evidence for the addition of radiogenic Os during subduction recycling and silicate metasomatism (e.g., Brandon *et al.*, 1996). HSEs are chalcophile and bond with sulfur to form sulfides whereas Re is more lithophile due to multiple valence states. The precipitation of residual and metasomatic sulfides, and element mobility needs to be taken into account when assessing HSE and Os isotope data. The HSE systematics of highly depleted peridotites has mainly been a focus of studies of cratonic peridotites (e.g., Pearson *et al.*, 2004; Aulbach *et al.*, 2016). In this thesis, HSE systematics are examined in a suite of peridotites from what are perhaps Earth's most melt-depleted mantle derived rocks—the mantle suite of the PUB, to examine similarities and differences in HSE behaviour in SSZ melt residues at very high degrees of melt depletion.

1.3. PROJECT AIMS

The Pacific Ocean is the largest ocean basin on Earth spanning over 150 million square kilometres (e.g., NOAA), yet little is known about the underlying mantle lithosphere beneath this vast area as most of the sub-oceanic mantle is inaccessible for geological sampling. This thesis will aim to address this knowledge gap and the above principal themes using two suites of peridotites from Fiji and PNG that represent two different geodynamic settings in the SW Pacific region. Based on the known regional geology of each of these localities, a number of aims have been devised for each respective study.

1.3.1. *Aims for Chapter 2: Fijian peridotite xenoliths*

Chapter 2 will focus on addressing the nature of the lithospheric mantle beneath the complex tectonic region of Fiji and test if there is a link between lithospheric structure and processes recorded in the petrography and geochemistry. To do this, the Koro peridotites from eastern Fiji will be compared to other regions of accreted lithospheric mantle in the SW Pacific such as the young continent of Zealandia, where Liu *et al.* 2015 found evidence for highly depleted peridotites that recorded diverse depletion ages beneath New Zealand that raise the possibility that New Zealand is underpinned by a complex lithospheric keel constructed by oceanic arc collision. This study will use Os isotope measurements to determine if any ancient melt residues were trapped as lithosphere beneath eastern Fiji. The surrounding geological context of Fiji includes back-arc basin rifting (Lau Basin), active subduction (Tonga trench), several remnant arcs (e.g., Lau-Colville Ridge), and is in close proximity to Samoa that is underlain by a large mantle plume. This will

offer an opportunity to study potential interplays between ridge melting, subduction and plume activity in the Fiji region of the SW Pacific.

1.3.2. Aims for Chapter 3: Papuan ophiolite peridotites

Chapter 3 will aim to understand processes that are responsible for producing what are possibly the most incompatible element depleted peridotites recorded on Earth. This study will determine the range of melting, the geological environment that formed the Papuan ophiolite peridotites and how this may or may not be reflected in the HSE systematics of these mantle rocks. Similar to the Fiji peridotite study, Os isotope systematics will be used to determine the age of melting events that created the Marum PUB ophiolites, what similarities exist with other sections of accreted mantle lithosphere in the SW Pacific, if there is any record of ancient residues incorporated into the lithosphere in this region, and if these ages have any relationship with large extents of melt depletion.

Chapter 2

Lithospheric thinning and modification beneath eastern Fiji by influence of the Samoan mantle plume documented in peridotite xenoliths from Koro Island

2.1. INTRODUCTION

Geological sampling of the Earth's upper mantle through peridotite xenoliths is essential for quantifying the Earth's thermal budget, crust-mantle differentiation, and subsequent growth of islands and continents (e.g., Boyd, 1973; Rudnick & Nyblade, 1998; Hofmann, 1988; Pearson, 2007; Liu *et al.*, 2015; Scott *et al.*, 2019). Such peridotites have the potential to record complex melting, metasomatism, and compositional changes related to their spatial and temporal evolution, providing a unique opportunity to study the geochemical diversity, redox state, and isotopic composition of the lithospheric mantle. There have been several Os isotope and/or highly siderophile element (HSE: Os, Ir, Ru, Pt, Pd and Re) studies on sub-oceanic mantle xenoliths (Schaefer *et al.*, 2002; Bizimis *et al.*, 2007; Simon *et al.*, 2008; Ishikawa *et al.*, 2011; Jackson *et al.*, 2016; Snortum *et al.*, 2019), arc-related peridotite xenoliths (Brandon *et al.*, 1996; McInnes *et al.*, 1999; Liu *et al.*, 2015; Scott *et al.*, 2019), and abyssal peridotites (Snow & Reisberg, 1995; Lassiter *et al.*, 2014; Standish *et al.*, 2002; Day *et al.*, 2017) that have provided an in-depth picture of the Os isotope and HSE systematics in various non-cratonic settings. Many of these non-cratonic peridotite xenoliths record highly refractory geochemical signatures combined with sub-chondritic Os isotope compositions that provide important information linking mantle processes with lithospheric evolution.

Although a number of recent studies have documented the nature and evolution of parts of the mantle that underpin the SW Pacific region (e.g., Marchesi *et al.*, 2009; Ishikawa *et al.*, 2011; Scott *et al.*, 2019; Snortum *et al.*, 2019), the origin, nature and age of mantle lithosphere beneath the tectonically complex Fijian archipelago remains an uncharacterized portion of this major oceanic lithosphere domain. Presented here is a petrological and geochemical investigation of the

lithospheric mantle root underpinning Fiji, making this study an important new addition to understanding the geological evolution of the sub-oceanic mantle beneath the SW Pacific region. With these aims, this study will focus on 42 peridotites selected from a suite of 582 xenoliths collected from <3 Ma alkali basalts from Koro Island, Fiji.

2.2. GEOLOGICAL BACKGROUND

2.2.1. *Summary of the geological history of the Fijian Islands*

The Fijian Islands formed, in a broad sense, as a product of the tectonic interactions between the Pacific and Indo-Australian Plate margins (Chase, 1971). The main island of Fiji and the Lau-Colville Ridge is a remnant arc (known as the Vitiaz Trench Lineament), and was once part of a continuous active arc comprised of Fiji, Vanuatu and Tonga (Gill & McDougall, 1973; Gill, 1970; Gill, 1976; Coleman & Packham, 1976; Begg & Gray, 2002 and references therein), and also the continent of Zealandia (Segev *et al.*, 2012). The subduction of the Pacific Plate beneath the Indo-Australian Plate caused the emplacement of a number of intrusions and the generation of arc volcanics (McDougall, 1963). The oldest record of this arc (Yavuna arc) is preserved in late Eocene to early Miocene volcanics on the main island of Fiji (Gill, 1987; Rodda, 1994). The break-up of the Vitiaz arc caused the development of a major transform fault to the north of Fiji around 12 Ma, referred to as the Fiji Fracture Zone (FFZ), which forms the boundary between the Australian and Pacific Plates (Auzende *et al.*, 1988a). Between 10–3 Ma a ~135° counter-clockwise rotation of the Fiji Platform occurred (Taylor *et al.*, 2000) and opened up the North Fiji Basin attaching Viti Levu to the Pacific Plate (Auzende *et al.*, 1988b). The opening of the North Fiji Basin was caused by the clockwise rotation of the Vanuatu–New Hebrides arc that resulted from the buckling of a ribbon continent spanning from the Northland Peninsula in New Zealand through to New Caledonia and the d’Entrecasteaux ridge (NNNCd’E) (Johnston, 2004). During this time, trondhjemite and gabbroic plutonism (~10 Ma), a transition from calc-alkaline to tholeiitic volcanism (10–6 Ma), and low-K rhyolite volcanism (~7 Ma) were all taking place (Gill, 1987; Rodda, 1994). Between 6–3 Ma, there was also active spreading of the Lau Basin (Parson *et al.*, 1990; Taylor *et al.*, 2000; Gill & Whelan, 1989). At around 5.5 Ma a ~70° counter-clockwise rotation event (part of the ~135° counter-clockwise rotation), was responsible for the present-day boundary of the Fiji Platform (Whelan *et al.*, 1985). This is also the same time that

shoshonitic volcanism was reported to have ended (Morrison, 1980; Leslie *et al.*, 2009). When the main counter-clockwise rotation event ceased, there was also a rapid switch from arc to OIB volcanism between 3.3–2.8 Ma, which, with the exception of andesitic volcanism in Kandavu Island that continued from 3.0–0.7 Ma that is related to the subduction in the south of Fiji (Gill, 1976; Whelan, 1985; Gill & Whelan, 1989). By ~3 Ma, the current Fijian Islands were bordered by three sea-floor spreading centres (Fig. 2.1): 1) the Lau inter-arc basin between the Taupo-Kermadec-Tonga (TKT) frontal arc and remnant Lau-Colville Ridge, 2) the Northern Fiji Basin, the spreading centre for the Hunter-Vanuatu trench-arc, and 3) South Fiji Basin, between the TKT arc and the continental crust from New Zealand to New Caledonia representing the margin of Gondwanaland to the south (Mortimer *et al.*, 2007; Davey, 1982).

2.2.2. Geological context of Koro Island

Koro Island lies to east of the main island of Viti Levu, at the boundary between the Lau Ridge and the Fiji Platform (Fig. 2.1). There have been several detailed studies on the Koro Island host-lavas and other Fijian ocean island basalts (FOIBs) (Coulson, 1973; Whelan *et al.*, 1985; Gill, 1976; Hindle & Colley, 1981; Gill, 1984; Gill & Whelan, 1989; Cole *et al.*, 1990), including more recent multi-isotope studies (Pearce *et al.*, 2007; Price *et al.*, 2017). Gill & Whelan (1989) divided FOIB into Type I and Type II basalts, building on the classifications by Woodhall (1985). Type I FOIB are characterized by olivine phenocrysts with Cr-spinel inclusions, and sometimes contain microphenocrysts of plagioclase. No augite phenocrysts are present in Type I FOIB. Type I whole-rock chemistry is typically >9 wt. % MgO, 45–47 wt. % SiO₂, with high concentrations of high field strength elements (HFSEs) and large-ion lithophile elements (LILEs). Type II FOIB are typically older in age and contain plagioclase (An_{60–70}) as the dominant phenocrysts, followed by olivine (Fo_{65–70}), and sporadic <0.5 mm augite phenocrysts. Their chemistry is characterized by higher SiO₂ wt. % compared to Type I, MgO <6 wt.%, and they have lower HFSE and LILE, particularly K, P, Zr, and Y to Nb. Type II volcanics are also characterized by DUPAL (Dupré & Allégre, 1983)-like isotopic traits (Hart, 1984).

Koro Island formed as a large shield volcano (Gill & Whelan, 1989), followed by NNE trending fissure type eruptions, consisting of sub-aerial aa lava flows forming several vents along centre of the island, and most recently, localised alkali basalt volcanism—the host for the xenoliths studied here. Surface volcanism on Koro has been dated between 2.6 to 1.0 Ma by K-Ar

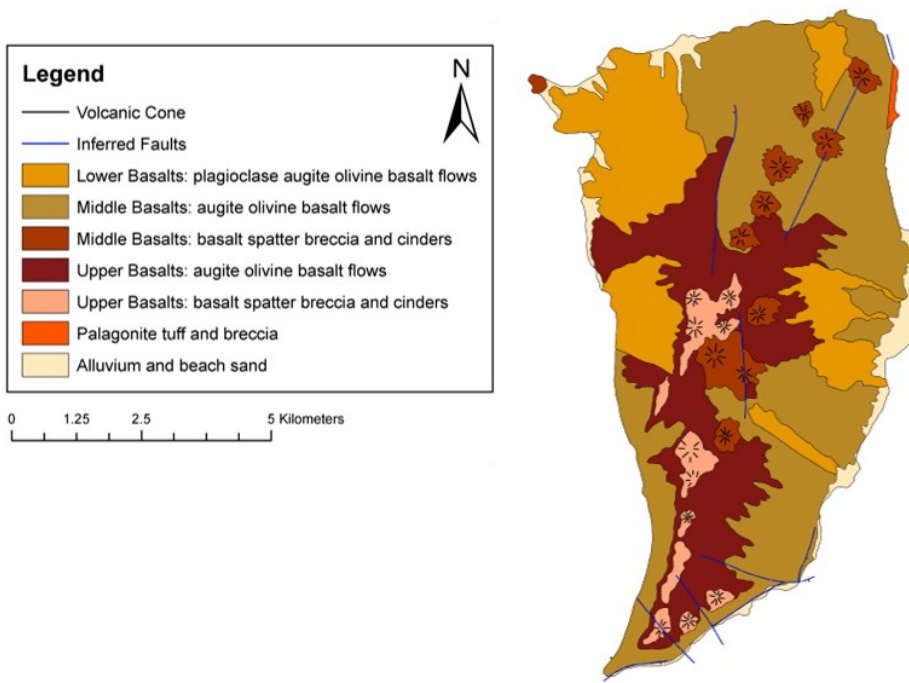
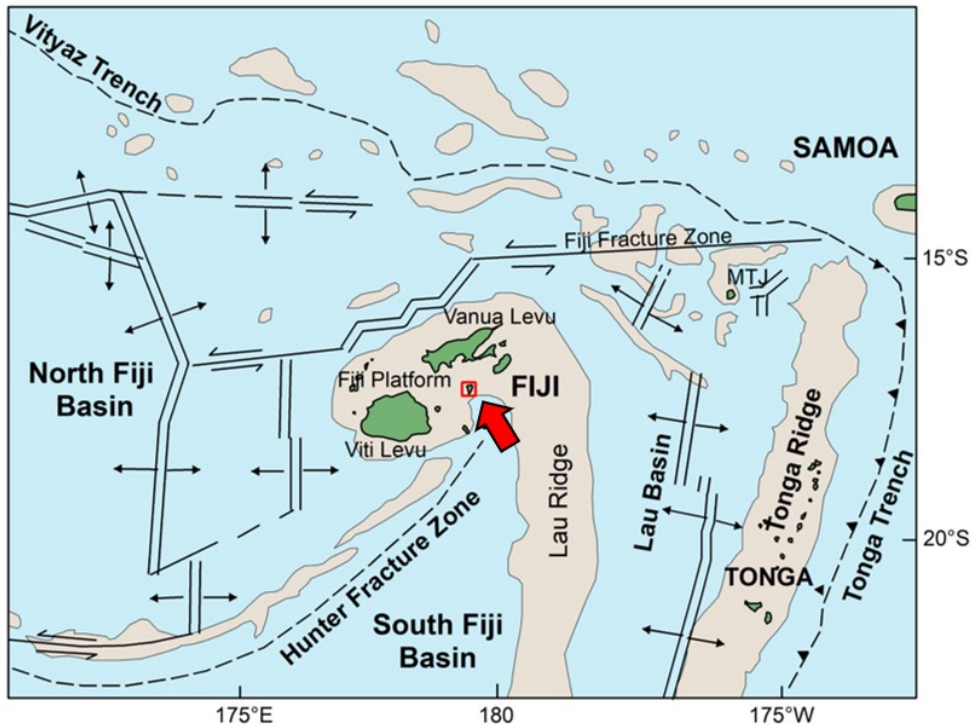


Figure 2.1. Tectonic context for Fiji, Tonga and Samoa digitized after Hathway (1993) and Auzende *et al.* (1995). Koro Island is outlined within the red box (see arrow). Geological units of Koro Island digitized after Coulson (1976).

geochronology (Coulson, 1973; Gill, 1976), suggesting evolved lava compositions from Type II to Type I FOIBs (Woodhall, 1985; Gill & Whelan, 1989). Additionally, bathymetric data from Smith & Sandwell (1997) raise the possibility that Koro is part of the remnant Lau-Colville Ridge arc system that has since rotated with the Fiji Plateau. As Fiji was once part of an active volcanic arc that later experienced separation from what is now the Tonga-Kermadec Ridge, it is possible that peridotite xenoliths sampled from the lithosphere beneath Koro Island may represent either mantle residues or cumulates sourced from either a sub-oceanic, sub-arc or a back-arc lithosphere. These possibilities for the origin of Koro peridotites are examined below.

2.3. PERIDOTITE DESCRIPTIONS AND PETROGRAPHY

Peridotite xenoliths in this study were collected from Koro Island, ~140 km east of the main island of Fiji (Fig. 2.1), and sampled mostly as float, encased in host volcanic rock, or within a single alkali-basalt dyke ($17^{\circ} 23' 26''$ S, $179^{\circ} 23' 24''$ E). Koro xenoliths range from <2 cm to 10 cm in size, and are dominated by spinel lherzolites, with wehrlite, harzburgite, and dunite xenoliths making up less than 12 % of the sample population (Figs. 2.2a–f). The peridotites are predominantly ultra-fresh, with a few showing weak alteration and iddingsitized olivine. The peridotites have widely variable grain sizes, but are typically coarse-grained (~2 mm) with protogranular textures, with some complex intergrowths between spinel, orthopyroxene, clinopyroxene. As there is only one occurrence of augite in these peridotites the term “clinopyroxene” will refer specifically to diopside throughout this paper unless stated otherwise. Koro peridotites show similar petrographic features to oceanic island peridotite xenoliths (e.g., Neumann, 1991) including subgrains in olivine and orthopyroxene, and olivine neoblasts. Some Koro lherzolites show localized regions of clinopyroxene banding also observable in hand specimen. Reaction rims in clinopyroxene are also common, possibly associated with the recrystallization of clinopyroxene (Fig. 2.3a). Orthopyroxene exsolution lamellae are also observed in clinopyroxene and vice-versa in orthopyroxene (Fig. 2.3b). In several wehrlite xenoliths, olivine grains appear to have a “cumulus-like” morphology (i.e., chadacrysts) surrounded by a matrix of clinopyroxene resembling a late infiltrating melt (Fig. 2.3c). Within these olivine grains, trace amounts of orthopyroxene can be seen in backscattered electron (BSE)

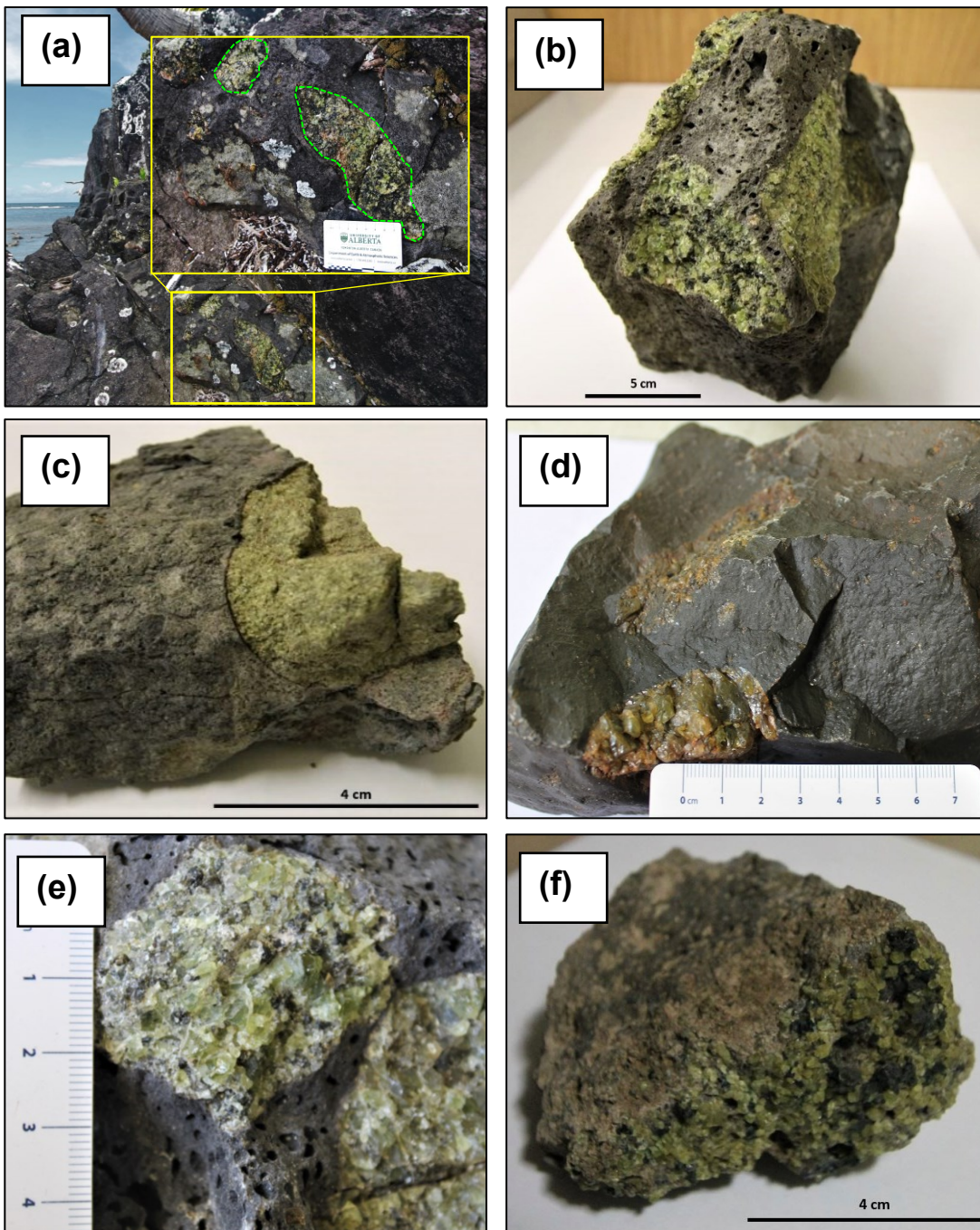


Figure 2.2. Hand sample summary of major peridotite xenolith lithologies from Koro. (a) Lherzolites-in-situ, (b) Iherzolite (sample K015A-2), (c) fine-grained dunite (sample K008), (d) coarse-grained dunite (sample FJ024), (e) harzburgite (samples FJ186), (f) wehrlite (sample K014-1).

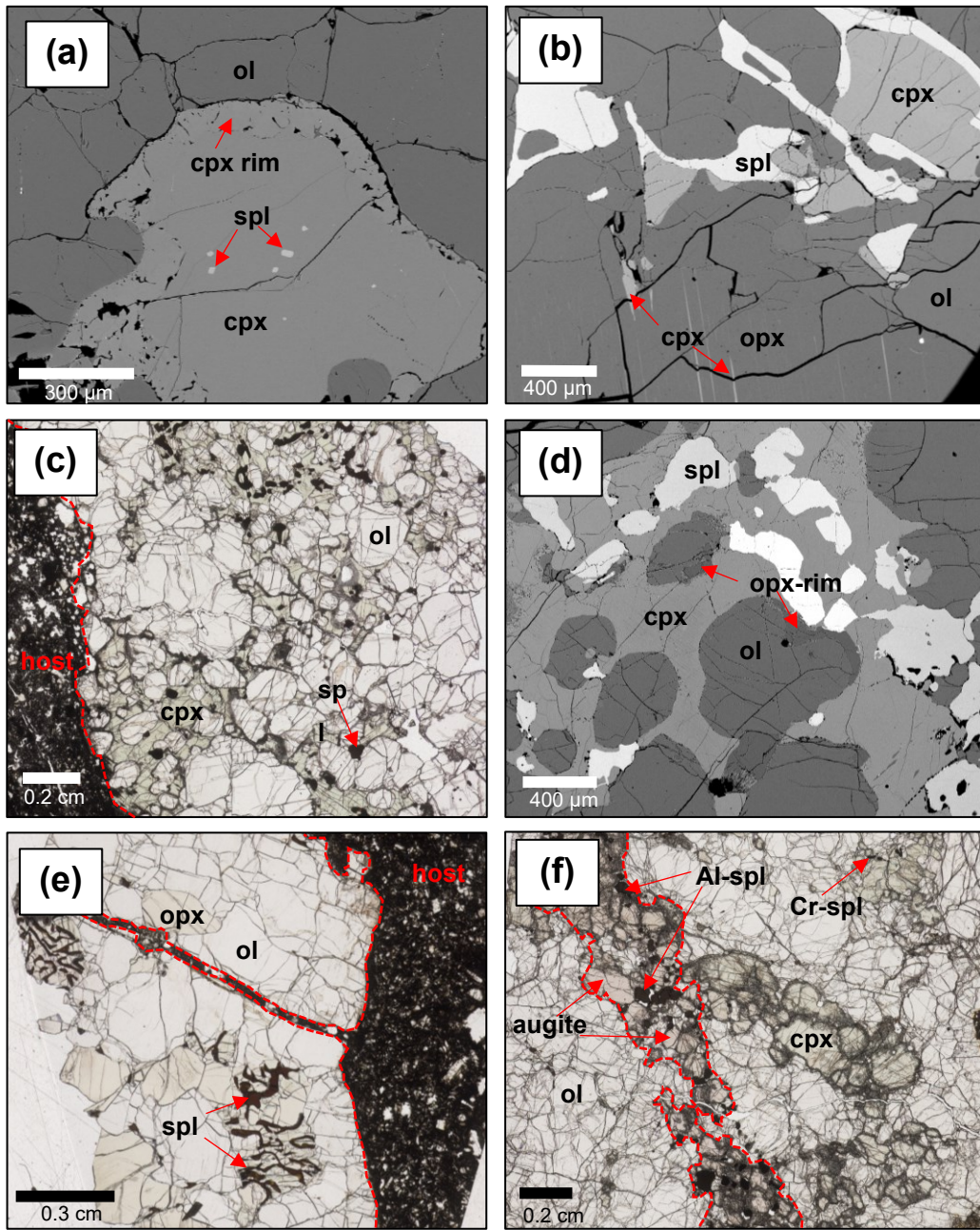


Figure 2.3. Summary of major petrographic features in the Koro peridotites. (a) BSE image of spinel inclusions in clinopyroxene, with clinopyroxene containing a visible rim (sample FJ167-2). (b) BSE image of lherzolite FJ185-1 showing clinopyroxene exsolution in orthopyroxene and spinel symplectite textures. (c) PPL image of olivine within a clinopyroxene matrix (wehrlite K047-1). (d) Backscattered electron (BSE) image of wehrlite K047-1 showing orthopyroxene replacement by olivine. (e) PPL image of spinel symplectite replacement textures (lherzolite K015A-2). (f) PPL image of augite vein containing Al-spinel cross-cutting wehrlite K048A-1. Red dashed line denotes boundary between host basalt and peridotite. All spinel is chromian spinel (Cr-spl) except where noted in (f).

imaging along the outer edges (Fig. 2.3d), possibly representing remnant orthopyroxene that has since been consumed.

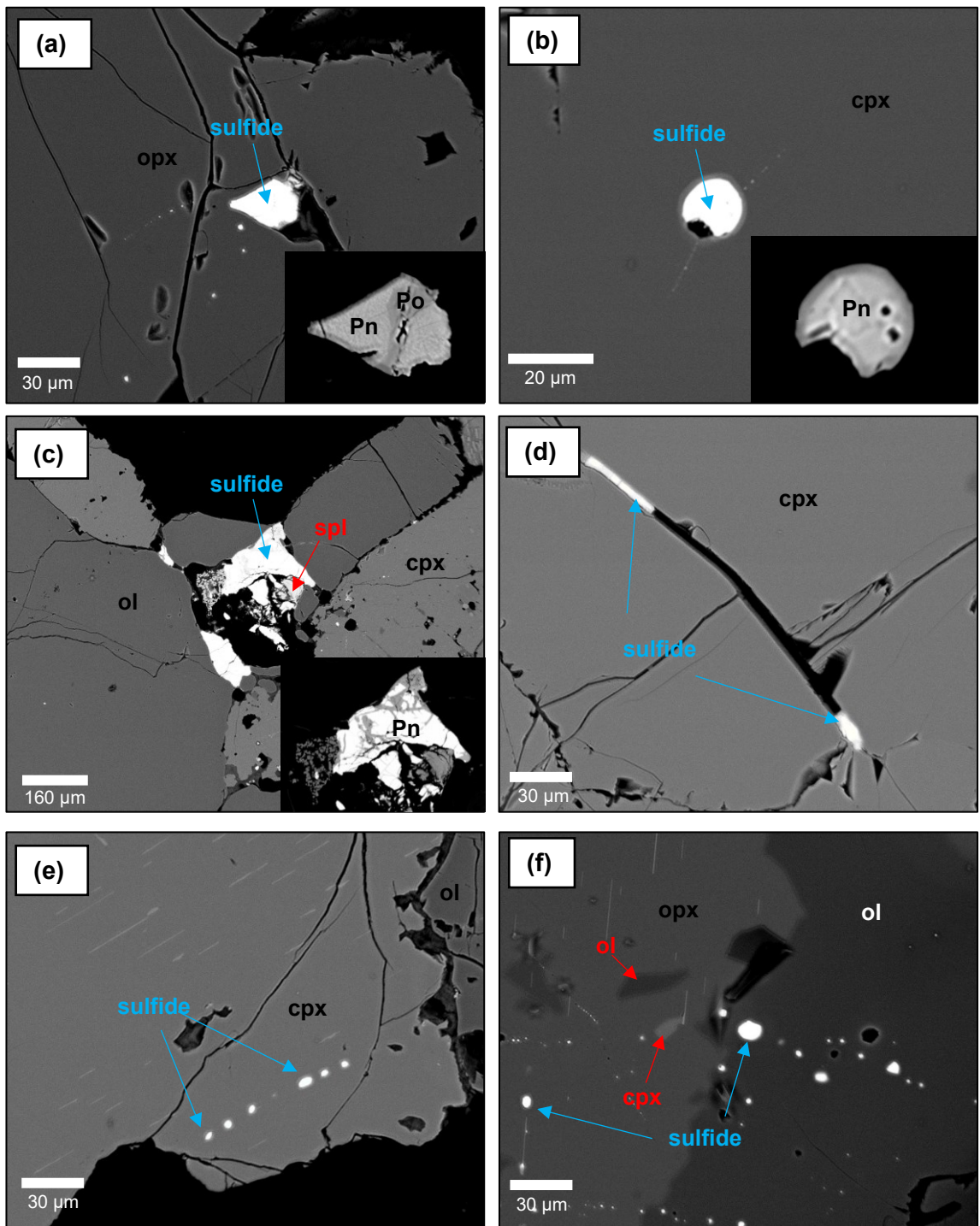
Spinel is present as three different growth textures, 1) spinel symplectites of spl + cpx and spl + opx, also referred to as vermicular intergrowths (Fig. 2.3e), 2) as spinel clusters (Figs 2.3c, 2.3d, and 2.3f), or 3) as sub-idiomorphic growths. Symplectite textures occur in the majority of Koro lherzolites and commonly display a thin outer rim of magnetite. Wehrlites, however, typically have spinel clusters found within interstitial clinopyroxene. Regardless of the spinel growth texture, spinel and clinopyroxene are typically spatially associated, with the former often found along clinopyroxene exsolution within orthopyroxene. While no “seams” of spinel clusters, typical of cumulus spinel were observed in either the Koro wehrlites or other peridotites, some spinel clusters show slight linear arrays of grains (e.g., wehrlite K048A-1) that could indicate a similar process, or the coalescence of intercumulus spinel (e.g., Hunter, 1987). The only occurrence of Cr-poor spinel occurring as clusters is within an Al-rich augite vein from sample K048A-1 (Fig. 2.3f). Trace amounts of plagioclase were observed in only three peridotite thin sections (K048A-1, K011-1, and FJ194).

BSE imaging of fourteen xenoliths to search for sulfides revealed base-metal sulfides (BMS) in the range from 8–20 µm in diameter, dominated by pentlandite and pyrrhotite. When these phases are observed together in a grain, pentlandite forms the outer rim (Figs. 2.4a & 2.4b). Most sulfides occur along fractures and grain boundaries (Figs. 2.4c & 2.4d), as trails across one or more mineral grain (Figs. 2.4e & 2.4f), or in association with spinel (Figs. 2.4h & 2.4g). The observed spinel textural associations are not considered to be primary, but rather secondary metasomatic sulfides following the criteria of Luguet & Pearson (2019). A rounded sulfide (<15 µm) in sample FJ188-2 (Fig. 2.4b) shows similarities to residual rounded sulfides, however, it occurs within interstitial clinopyroxene, suggesting a metasomatic origin.

2.4. METHODS

2.4.1. Whole-rock major and trace elements

Sample preparation was performed using rock preparation facilities at The University of the South Pacific and the University of Alberta (UofA). To minimise metal contamination, saw-cut rock surfaces



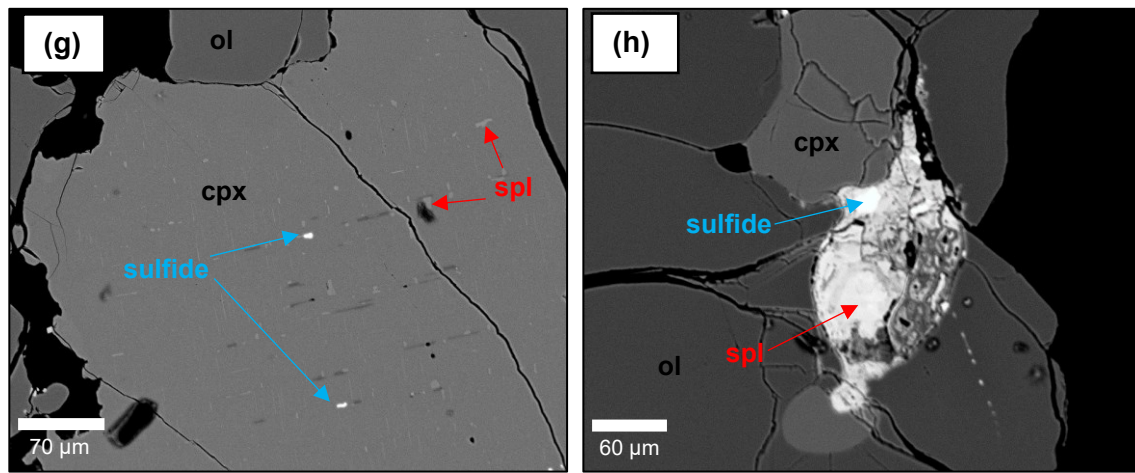


Figure 2.4. BSE images of select Koro peridotites showing sulfide morphology and relationship between sulfides and associated phases. Po = pyrrhotite and Pn = pentlandite. Peridotite sample numbers: (a) K050A-2, (b) FJ188-2, (c) K049-1, (d) FJ167-2, (e) FJ205, (f) FJ167-2 (g) K050A-2, and (h) FJ185-1.

were abraded with corundum paper and ultrasonicated for 15 minutes in deionized water. Samples were crushed using an agate mortar and pestle and milled into a fine powder using an agate puck and ring mill. Blanks were assessed by grinding high purity quartz which produced negligible concentrations (<1 picogram) of all HSEs. 10 to 16 grams of peridotite xenolith powders were weighed and analysed at the X-ray Laboratory at Franklin and Marshal College, USA for major elements and selected minor and trace elements. These concentrations were measured by x-ray fluorescence (XRF) in lithium tetraborate ($\text{Li}_2\text{B}_4\text{O}_7$) fused disks using methods described in Mertzman (2015). Where sample material was limited (i.e., <12 g), powder pellets were used to measure minor elements, and thus Ni data are consequently less accurate due to low intensities relative to Ti and Cr. Peridotite reference powder MUH-1 (IAG, 2015) was included as an internal standard for peridotites and basalt reference powder BHVO-2 (Wilson, 1998) as an internal standard for host basalts. Long-term measurement repeatability is reported in Waterton *et al.* (2020).

Whole-rock trace elements were measured in low resolution mode using a ThermoScientific Element XR ICP-MS at the UofA's Arctic Resources Geochemistry Laboratory. Samples were prepared by weighing ~0.1 g of powder and dissolving the sample in 1 ml of concentrated (conc.) HNO_3 and 4 ml of conc. HF. The solution was refluxed for 24 hours at 150 °C and dried down. An additional 1 ml conc. HNO_3 was added for refluxing a second time. This

step was repeated, and an additional 2.5 ml of conc. HNO₃ was added and refluxed overnight. Samples underwent a total 5000x dilution in 3% HNO₃. Standard powders MUH-1 and OKUM (Peters & Pettke, 2017), and BCR-2 and BHVO-2 (Raczek *et al.*, 2001) were included during analysis to monitor repeatability.

2.4.2. *Electron Probe Microanalysis*

In-situ major element analysis was completed on olivine, clinopyroxene, orthopyroxene, spinel and sulfide phases using the JEOL8900R and CAMECA SX100 electron microprobe analyzer (EPMA) at the UofA Electron Microprobe Laboratory. 50 µm polished thin sections and grain mounts were coated with a 25 nm of carbon prior to analysis. Analytical conditions consisted of an accelerating voltage of 20 kV, beam current of 20 nA, and count times of 30 secs on-peak. A fully-focused beam size (<1 µm) was used for most analyses and beam spot size of 2 µm used to analyze calibration materials and selected minor phases (e.g., plagioclase). For selected olivine grains, a high precision method was employed for measuring low Al concentrations in olivine with intended applications for Al-in-olivine thermometry (e.g., Wan *et al.*, 2008; Coogan *et al.*, 2014; Bussweiler *et al.*, 2017). The high precision measurements come from two WDS source beams with an increased beam current of 100 nA with an increased on-peak analysis time for Al, Cr and Ca at 240 seconds, 120 seconds for Co and 40 secs for Mn and Ni. An accelerating voltage of 20 kV and beam spot size of 2 µm were also used for the high precision method. Off-peak times for all analyses were the same as the respective on-peak times. Analysis time was ~4 minutes per analyses for the routine method and ~5 minutes for the high precision method. Secondary standards Fo_{90.5} San Carlos olivine and EPS1-ilmenite-1 were analysed throughout the analytical session to monitor spectrometer drift, accuracy and precision. The average limit of detection of Al content in olivine using the high precision method was 0.0009 wt. % compared to the general method of 0.008 wt. % using the Single Point Detection Limit calculation (Scott & Love, 1983). The full list of standard reference materials and analyser crystals are provided in Appendix 5.

2.4.3. *Mössbauer spectroscopy*

Fe³⁺/ΣFe values were measured via Mössbauer spectroscopy on five handpicked spinel separates (6–12 mg) at the Goethe-Universität, Germany following the methods outlined in Uenver-Thiele

et al. (2014) and Woodland *et al.* (2006). Prior to analysis, grains were refluxed in concentrated HF overnight and treated with HCl for 6 hours to ensure the removal silicates and magnetite. $\Delta \log fO_2$ (FMQ) values were calculated using ol-opx-spl equilibrium in the program: “Gt & Sp oxybarometry” available from Miller *et al.* (2016 and references therein). Input temperatures were calculated using the cpx–opx solvus thermometer of Taylor (1998), with an input pressure of 1.5 GPa.

2.4.4. *Laser ablation inductively coupled plasma mass spectrometry (LA-ICP-MS)*

Minor and trace elements in olivine, orthopyroxene, clinopyroxene, and spinel have been analysed in thin sections from twenty-one Koro peridotites and 147 picked olivine grains using a ThermoScientific Element XR with attached 193 nm laser system at the UofA Arctic Resources Geochemistry Laboratory. Instrument tuning was performed on NIST612 (Jochum *et al.*, 2011). A minimum signal intensity of $\sim 160\,000$ cps and maximum of $\sim 250\,000$ cps on ^{175}Lu was achieved and ThO^+/Th^+ production rates were maintained below 3 %. The laser system was operated at 10–13 Hz and a laser fluence (measured at the ablation site) $\sim 3.6\text{ J/cm}^2$. San Carlos olivine SC-GB was used as a primary standard for most olivine trace elements using the same standard and method described in Bussweiler *et al.* (2019). For rare earth elements (REE) in olivine, silicate glass NIST612 (Jochum *et al.*, 2011) was used as the calibration standard, with SC-GB used as the secondary standard due to typically low REE concentrations in SC-GB. Clinopyroxene, orthopyroxene and spinel were calibrated using NIST612, with NIST614 and NIST616 (Jochum *et al.*, 2011) used as secondary standards for the pyroxenes, and USGS basaltic glass GSD-1G (Jochum *et al.*, 2011) as a secondary standard for spinel. Internal standardization was done using predetermined EPMA values of Cr and Al for spinel, Ca for clinopyroxene, Mg for orthopyroxene, and Si for olivine. For olivine analyses, a background time of 180 seconds and ablation time of 60 seconds, and for pyroxene and spinel analyses, a background time of 90 seconds and an ablation time of 45 seconds was used. Spot sizes varied from 50–130 μm in diameter depending on grain size. REEs were analysed in separate sessions to minimize instrumental interferences associated with settling times on the magnet analyser when elements with a large mass range are analysed (e.g., Latkoczy & Günther, 2002). In all sessions the Ba signal was monitored to test if grains were ablated past the silicate glass. Data reduction was carried out using Iolite software version 6.37 (Paton *et al.*, 2011). All LA-ICP-MS analyses reported in this study are above Iolite software detection limits (Appendix 5).

2.4.5. Os isotope and HSE: isotope dilution chemistry

Chemical separation techniques for Os and other HSE—Pt, Ir, Ru, Pd and Re were carried out via isotope dilution methods at the UofA Arctic Resources Geochemistry Laboratory following Pearson & Woodland (2000). Approximately 1 g of whole-rock powder is spiked with a mixed platinum group element (PGE)-¹⁹⁰Os spike and digested in inverse aqua regia (~2 ml HCl and ~5 ml sparged HNO₃) in an Anton Paar high-pressure ashing (HPA-S) for 16 hours at 290°C (Reisberg & Meisel, 2002). Prior to sample analysis, a cleaning run was completed with ~10 ml of concentrated HNO₃ for 3 hours at 260°C. Blanks were spiked with a tailored low abundance spike and the OKUM standard (IAG, 2015) with a spike appropriate for komatiite/picrite Os abundances, while peridotite reference material GP-13 (Pearson *et al.*, 2004) and the Koro peridotites were spiked with the UofA Peridotite-3 (P3) spike. Osmium was extracted by solvent extraction into CHCl₃, back extracted into HBr (Cohen & Waters, 1996), and purified via micro-distillation with a mixed Cr₂O₇²⁻ and H₂SO₄⁻ solution into 15 µl of concentrated HBr (Birck *et al.*, 1997). Pt, Ir, Ru, Pd and Re were purified from the aqua regia portion via anion exchange column chemistry using an AG1x8, 100 to 200 mesh resin. Pd, Pt-Ir and Re-Ru were collected as separate cuts in 12 N HCl, 16 N HNO₃ and 6 N HNO₃, respectively. Samples were refluxed in a 0.5 ml 23 N HF and 2 ml of 12 N HNO₃ solution to ensure elements Hf and Zr pass through the resin more efficiently, and further cleaned in 5 ml 6 N HCl, and 5 ml 1 N HCl prior to column chemistry.

2.4.6. Os isotope and HSE: mass spectrometry

All mass spectrometry measurements were conducted in the Arctic Resources Geochemistry Laboratory at the UofA. Os was measured as OsO₃⁻ on a Thermo Fisher Triton Thermal Ionisation Mass Spectrometer operated in negative mode (N-TIMS; Creaser *et al.*, 1991), using a single secondary electron multiplier detector (SEM) operated in ion pulse-counting mode (IC1, B, C). High purity O₂ gas is introduced via a leak valve into the ion source chamber and adjusted manually to maintain a HV pressure of ~1.0 x 10⁻⁷ mbar. Durham Romil Osmium Standards (DrOsS; Luguet *et al.*, 2008) of 5 ng and 0.5 ng, along with peridotite reference materials GP-13 (Pearson *et al.*, 2004) and OKUM (IAG, 2015) were also analysed via N-TIMS. DrOsS results show agreement with accepted reference values ¹⁸⁶Os/¹⁸⁸Os = 0.1199293 ± 58 and ¹⁸⁷Os/¹⁸⁸Os = 0.160924 ± 4 (2 SD; n=8; Luguet *et al.*, 2008) and with the long-term performance of the Arctic Resources Geochemistry Laboratory (Liu & Pearson, 2014). SEM blank measurements included

50 cycles with the blank adjusted after every 10 cycles, with a 2 second integration time per sequence and idle time of 1 second between sequences, for a total analysis time of \sim 2 min. For sample loading, strips of Pt wire were cut into \sim 1.25 cm lengths and welded onto filament holders. Prior to sample loading, the filaments were degassed in air at 2.1 Amps for 10 minutes and left overnight to reduce Os contributions from the filament. Osmium from the peridotite samples and reference materials were taken up with 2 μ l of HBr and loaded onto the Pt filaments and dried down using a current of 0.6 Amps. Once dried, 1 μ l of Ba(OH)₂ activator was placed to cover the HBr and dried down again at the same conditions. Corrections were made to the raw isotope ratios for ¹⁷O and ¹⁸O oxide interferences, spike contributions (Eugster *et al.*, 1969), exponential fractionation, and mass fractionation using a normalizing ratio of ¹⁹²Os/¹⁸⁸OsO₃ = 3.0827 (Luck & Allegre, 1983).

PGEs and Re were measured in solution mode using a Nu AttoM High Resolution Mass Spectrometer. Instrument tuning and low-resolution mass calibration done in HNO₃ solution with known ¹¹⁵In concentration, along with elements ⁷Li, ²⁴Mg, ⁴⁵Sc, ⁵⁹Co, ⁸⁹Y, ¹³³Cs, ¹⁵⁹Tb, ¹⁶⁹Tm, ²⁰⁸Pb, and ²³⁸U. Pt-Ir and Re-Ru column cuts were diluted in 1.5 ml 0.8 N HNO₃ and Pd cuts diluted in 1.5 ml 0.5 N HCl prior to measurement. Peridotite samples and a mixed 1 ppb PGE and Re standard were scanned for masses ⁸⁵Rb, ⁸⁸Sr, ⁸⁹Y, ⁹⁰Zr, ⁹⁵Mo, ⁹⁹Ru, ¹⁰⁰Ru, ¹⁰¹Ru, ¹⁰⁵Pd, ¹⁰⁶Pd, ¹⁰⁸Pd, ¹¹¹Cd, ¹⁶⁹Tm, ¹⁷²Yb, ¹⁷⁵Lu, ¹⁷⁸Hf, ¹⁸⁵Re, ¹⁸⁷Re, ¹⁸⁹Os, ¹⁹¹Ir, ¹⁹³Ir, ¹⁹⁴Pt, and ¹⁹⁵Pt. Reference materials OKUM and GP-13 were used to test accuracy and reproducibility, and 0.8 N HNO₃ and 0.5 N HCl acid blanks were used to measure background mass interferences. Oxide production rates were monitored throughout the analytical session by measuring RbO, SrO, YO, ZrO, MoO, TmO, YbO, LuO, HfO. 120 second wash-out and 60 second analysis time were used for each sample, with a longer background times of 180 seconds after each oxide standard. An isotope correlation graph for Ru isotopes was plotted to test isotope interferences from the instrument, with a normalization applied using the raw isotope ratios ⁹⁹Ru/¹⁰¹Ru vs. ¹⁰⁰Ru/¹⁰¹Ru for all samples. Samples that did not follow this trend are excluded from the results as outliers. Procedural blanks during the analysis of these samples (n=9) are as follows: Os = 0.0041 \pm 0.0003 ng/g, Ir = 0.0016 \pm 0.0002 ng/g, Ru = 0.0316 \pm 0.0411 ng/g, Pd = 0.0140 \pm 0.0119 ng/g, Pt = 0.0474 \pm 0.0100 ng/g, and Re = 0.0084 \pm 0.0014 ng/g. All final data were corrected for appropriate blanks.

2.5. RESULTS

2.5.1. Major element chemistry

Major element compositions in olivine were also measured in picked grains from 147 Koro peridotite xenoliths to gain a general sense of the distribution in olivine compositions within the entire sample population (Appendix 3). Major element compositions for olivine, orthopyroxene, clinopyroxene and spinel were also measured on selected Koro xenoliths ($n=30$; Appendix 3), filtered on the basis of their olivine compositions (from olivine grain analyses) and textures to represent the lithological diversity of the entire sample suite.

2.5.1.1. Olivine

Forsterite ($Fo = 100 \times Mg/(Mg+Fe)$ molar) contents in olivine from both thin section and picked grains range from $Fo_{84.1-91.2}$, with a mean value of $Fo_{89.5}$ excluding rim analyses. Based on these olivine analyses, the majority of Koro peridotites correspond to the Frey & Prinz (1978) classification as Group I xenoliths (i.e., Fo_{86-91}). While Fo contents in olivine do not fall within the Frey & Prinz (1978) Group II range (i.e., Fo_{62-78}), 5% of the olivines from Koro peridotites fall below Fo_{86} and show similar petrographic and geochemical features to Group II. The Fo contents in olivine from Koro peridotites range between $Fo_{84.1-91.0}$ in lherzolites, $Fo_{89.3-90.4}$ in harzburgites, $Fo_{85.7-91.2}$ in dunites, and $Fo_{85.1-88}$ in wehrellites. Ni contents in olivine from these wehrellites (0.24–0.33 wt. % NiO) are also lower than harzburgites (0.34–0.39 wt.% NiO), and most lherzolites (0.27–0.42 wt. % NiO) and dunites (0.27 – 0.40 wt.% NiO).

2.5.1.2. Pyroxenes

Major element variations in orthopyroxene between peridotites is particularly evident in Al_2O_3 and FeO_{tot} . For orthopyroxene in harzburgites, Al_2O_3 and FeO_{tot} show a much more restricted range ($Al_2O_3 = 1.7-3.6$ wt. %; $FeO_{tot} = 6.1-6.5$ wt.%) compared to lherzolites ($Al_2O_3 = 2.7-6.0$ wt. %; $FeO_{tot} = 6.1-8.8$ wt. %). Orthopyroxene occurs as trace amounts in wehrellites and dunites, where it shows higher concentrations of Al_2O_3 and FeO_{tot} compared to both harzburgites and lherzolites ($Al_2O_3 = 4.1-5.3$ wt. %, $FeO_{tot} = 6.5-9.1$ wt. %). Clinopyroxene in wehrellites also shows higher concentrations of Al_2O_3 (4.98–6.27 wt. %) and FeO_{tot} (3.35–4.59 wt.%) compared to dunites and harzburgites ($Al_2O_3 = 1.29-3.33$ wt. %; $FeO_{tot} = 1.92-3.09$ wt. %). The Al_2O_3 content of clinopyroxenes in dunites and harzburgites have a similar range ($Al_2O_3 = 2.14-3.66$ wt. %) and are easily distinguishable from clinopyroxene in wehrellites ($Al_2O_3 = 4.98-6.14$ wt. %). Al_2O_3 in clinopyroxene from lherzolites show larger variations (2.50–5.26 wt. %) and span the

compositional range for clinopyroxene in both dunites, harzburgites and wehrlites. This is supported by the disequilibria textures most common in lherzolites with Fo contents in olivine below Fo₈₉.

2.5.1.3. *Spinel*

Koro peridotites investigated in this study all contain Cr-rich spinel (referred herein as spinel) with the exception of the Al-, Ti-rich spinel in the augite vein from wehrlite K048A-1. Large variations in chrome number ($\text{Cr\#} = \text{Cr}/(\text{Cr} + \text{Al})$ molar) exist in spinel found within the harzburgite–dunite suite ($\text{Cr\#} = 24.9\text{--}50.7$ and $21.2\text{--}55.7$, respectively), while Cr\# in spinel from lherzolites is more restricted ($\text{Cr\#} = 15.2\text{--}36.3$). The lowest Cr\# spinels (excluding the Al-, Ti-rich spinel) are found in the spinel clusters from the wehrlites ($\text{Cr\#} = 13.1\text{--}33.7$). Similar spinel grain clusters are also observed in high Cr\# dunites and harzburgites, suggesting spinel Cr\# is not always linked to spinel morphology. Co-existing spinel Cr\# and olivine Fo contents follow a typical melt-depletion trend (olivine spinel mantle array–OSMA: Arai, 1994) in most lherzolite and harzburgite peridotites (Fig. 2.5). The wehrlites and some lherzolites, in contrast, do not follow this OSMA trend, and extend toward lower Fo contents with spinel Cr\# restricted to <0.40 .

2.5.2. *Whole-rock major and trace chemistry*

2.5.2.1. *Peridotite chemistry*

Whole-rock major element compositions in the Koro peridotites (Table 2.1) are typical of non-cratonic spinel peridotite xenoliths (e.g., Pearson *et al.*, 2003). Whole-rock Al_2O_3 and CaO vs. MgO in Koro peridotites (Figs. 2.6a & 2.6b) are largely controlled by their olivine modal abundance, where the lowest CaO and Al_2O_3 contents and highest MgO contents are documented in the Koro dunites. Koro peridotites show a similar compositional range to previously documented OIB-hosted peridotite xenoliths and abyssal peridotites, and follow a partial melting trend from primitive mantle (PM) compositions towards lower Al_2O_3 and CaO and higher MgO contents. OIB-hosted peridotite xenoliths from Simon *et al.* (2008) show a greater range in whole-rock Al_2O_3 extending to more fertile compositions, whereas Al_2O_3 in the Koro peridotites are <3.5 wt %. Ni and Co contents do not show significant variations across different lithologies; however, these elements still correlate well with whole-rock Al_2O_3 , suggesting that Co and Ni-rich bearing phases (i.e., sulfides) are volumetrically insignificant and have little effect on compositional trends defined by these minor elements. Whole-rock Cr contents range from 513–3111 ppm in dunites

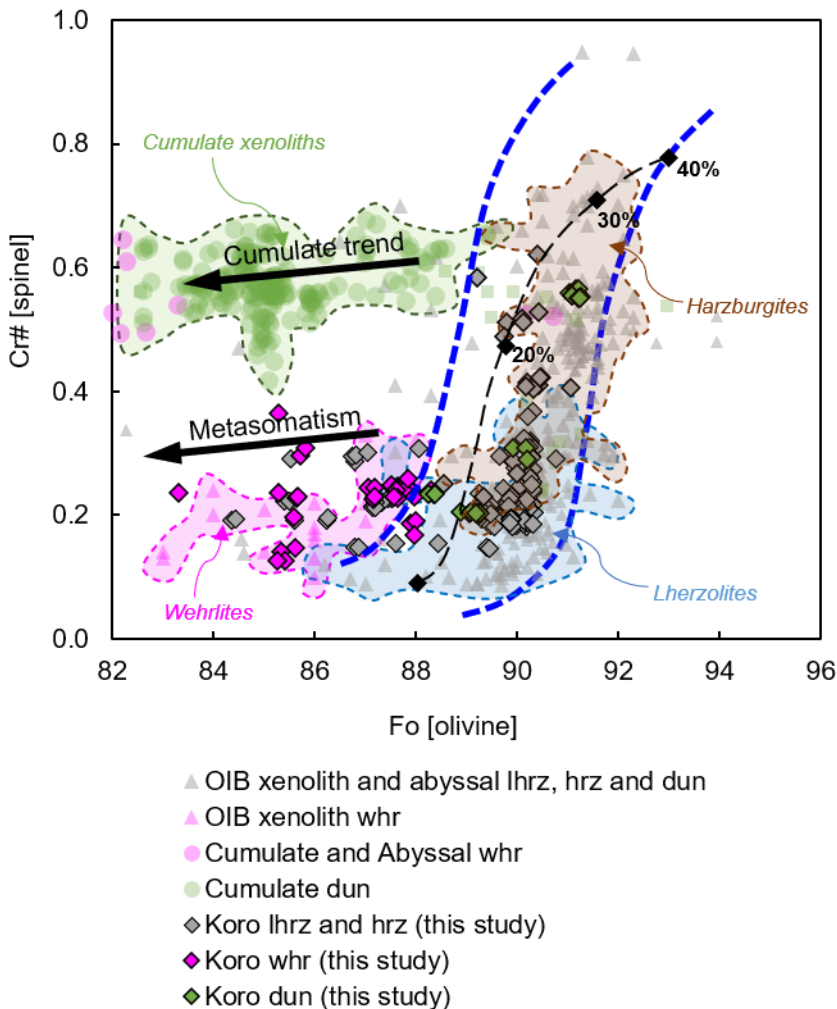


Figure 2.5. Olivine Fo vs. spinel Cr# values in the Koro peridotites (black outlined diamonds) plotted on the olivine-spinel mantle array (OSMA; Arai, 1994) shown by the dark blue dashed lines and partial melt estimates following the 1–2 GPa trend from Arai (1994). Ocean island basalt (OIB)-hosted lherzolite and harzburgite xenoliths from Simon *et al.* (2008) and OIB-hosted wehrlite xenoliths from Patkó *et al.* (2019). Abyssal peridotites from Warren (2016) noting that all abyssal dunites and wehrlites only occur as “veined peridotites” (see Warren, 2016). Cumulate dunite xenoliths are from Peters *et al.* (2016) and cumulate wehrlite xenoliths from both Sen & Presnall (1986) and Peters *et al.* (2016). Shaded fields represent OIB and abyssal peridotite data for lherzolites (blue), harzburgites (brown), wehrlites (pink), and cumulates (green).

Table 2 1: Whole-rock major and trace element abundance data for Koro peridotites

Sample:	K008	FJ024	K048A-2	FJ063	FJ186	K011-1	K015A-2	K015A-3	K041-2	K042-2	K048A-3	K049-1	K050A-1
Rock type:	Dun	Dun	Hz	Hz	Hz	Lhz	Lhz	Lhz	Lhz	Lhz	Lhz	Lhz	Lhz
<i>XRF (wt.%)</i>													
SiO ₂	40.95	40.69	44.04	43.73	43.26	44.68	44.37	44.35	45.22	45.28	44.13	44.50	44.22
TiO ₂	0.06	0.01	0.02	0.03	0.02	0.04	0.03	0.02	0.04	0.03	0.04	0.03	0.02
Al ₂ O ₃	0.73	0.17	1.66	0.89	0.94	1.61	1.74	1.62	2.15	2.16	1.35	1.76	1.46
FeO*	8.80	9.83	8.67	8.94	8.73	8.71	8.88	8.63	8.47	8.31	8.73	8.64	8.64
MnO	0.15	0.13	0.14	0.15	0.14	0.14	0.14	0.14	0.14	0.13	0.13	0.14	0.13
MgO	48.35	48.94	43.59	45.65	46.15	43.14	43.59	44.16	42.60	42.08	44.52	42.67	43.42
CaO	0.81	0.20	1.80	0.55	0.70	1.54	1.20	1.02	1.33	1.96	1.07	2.18	2.04
Na ₂ O	0.08	0.02	0.07	0.04	0.05	0.09	0.04	0.05	0.04	0.05	0.03	0.07	0.06
K ₂ O	0.02	—	—	0.02	—	0.04	—	—	—	—	—	—	—
P ₂ O ₅	0.04	—	—	—	—	0.01	—	—	—	0.01	—	—	—
SUM	100.00	100.00	100.00	100.00	100.00	100.00	100.00	100.00	100.00	100.00	100.00	100.00	100.00
LOI	-0.30	-0.18	-0.28	-0.20	-0.25	-0.10	-0.36	-0.27	-0.20	—	-0.31	-0.05	-0.16
<i>XRF (ppm)</i>													
Rb	—	—	<0.5	—	<0.5	—	<0.5	<0.5	<0.5	<0.5	—	<0.5	<0.5
Sr	32	18	1	15	1	14	2	1	6	1	16	1	1
Y	—	—	<0.5	—	<0.5	—	<0.5	<0.5	<0.5	2	—	<0.5	<0.5
Zr	9	3	2	10	2	4	3	2	2	<1	6	<2	<2
V	12	8	45	16	35	40	47	52	55	53	37	56	48
Ni	2246	2540	2179	1952	2286	2078	2067	2126	1958	2083	2366	2014	2119
Cr	3111	513	2518	2036	2822	2613	2468	2818	2269	2882	2579	2392	2106
Nb	—	—	<0.5	—	<0.5	—	<0.5	<0.5	<0.5	<0.5	—	<0.5	<0.5
Ga	—	—	1.5	—	0.6	—	0.9	1.5	2.1	2.9	—	1	0.8
Cu	—	—	9	—	7	—	15	<2	5	3	—	5	18
Zn	—	—	53	—	52	—	53	54	54	45	—	58	50
Co	144	138	115	91	124	105	117	119	117	106	125	113	116
Ba	—	—	3	—	<3	—	<3	4	<3	<3	—	<3	<3
La	—	—	<2	—	<2	—	<2	<2	<2	<2	—	<2	<2

Ce	-	-	<2	-	<2	-	<2	<2	<2	<1	-	<2	<2
U	-	-	<0.5	-	<0.5	-	<0.5	<0.5	<0.5	<0.5	-	<0.5	<0.5
Th	-	-	<0.5	-	<0.5	-	<0.5	<0.5	<0.5	<0.5	-	<0.5	<0.5
Sc	-	-	5	-	3	-	5	4	7	4	-	7	6
Pb	-	-	<2	-	<2	-	<2	<2	<2	<1	-	<2	<2

Table 2.1: Continued

Sample:	K050A-2	K050A-5	K051	K052-1	K067-1	K102	K205	FJ167-2	FJ167-3	FJ184-2	FJ185-1	FJ187-1
Rock type:	Lhrz	Lhrz	Lhrz	Lhrz	Lhrz	Lhrz	Lhrz	Lhrz	Lhrz	Lhrz	Lhrz	Lhrz
<i>XRF (wt.%)</i>												
SiO ₂	44.12	43.81	44.20	44.77	44.59	44.76	44.89	45.20	44.59	44.44	45.21	45.46
TiO ₂	0.04	0.05	0.04	0.07	0.04	0.05	0.03	0.05	0.06	0.04	0.04	0.05
Al ₂ O ₃	1.44	1.39	1.82	2.48	1.99	2.39	2.02	2.55	2.15	2.00	2.53	2.41
FeO*	9.48	8.68	8.73	8.43	8.48	8.92	8.55	8.42	9.24	8.54	8.23	8.26
MnO	0.15	0.15	0.13	0.14	0.14	0.15	0.13	0.13	0.14	0.13	0.13	0.13
MgO	43.54	44.25	42.77	42.03	42.50	41.44	42.34	41.18	42.53	43.01	41.92	41.50
CaO	1.17	1.59	2.25	1.98	2.16	1.96	1.97	2.40	1.19	1.78	1.86	2.13
Na ₂ O	0.05	0.08	0.05	0.09	0.07	0.20	0.07	0.07	0.07	0.05	0.07	0.05
K ₂ O	—	—	—	—	0.02	0.12	0.01	—	—	—	—	—
P ₂ O ₅	—	—	—	0.01	0.01	0.02	—	—	0.01	—	0.01	—
SUM	100.00	100.00	100.00	100.00	100.00	100.00	100.00	100.00	100.00	100.00	100.00	100.00
LOI	-0.48	-0.29	-0.07	0.29	0.10	0.51	0.06	-0.21	-0.44	-0.04	-0.23	-0.18
<i>XRF (ppm)</i>												
Rb	<0.5	—	—	—	<0.5	1.9	—	<0.5	<0.5	<0.5	<0.5	<0.5
Sr	3	4	6	8	2	20	4	3	7	15	2	3
Y	<0.5	—	—	—	0.7	<0.5	—	2.8	<0.5	2.4	—	1.7
Zr	2	11	12	11	2	<2	10	3	<2	3	<1	3
V	43	40	52	66	55	49	53	58	52	49	66	60
Ni	2050	2414	2088	1995	2061	2028	2003	1874	1967	2092	1861	1893
Cr	2423	3367	2316	3535	3131	3038	2294	3084	2523	2307	3544	2946
Nb	<0.5	—	—	—	<0.5	<0.5	—	<0.5	<0.5	<0.5	<0.5	<0.5
Ga	1.6	—	—	—	2	1.9	—	1.5	2.1	1.3	3.3	2.1
Cu	8	—	—	—	39	51	—	3	<2	2	5	6
Zn	63	—	—	—	57	59	—	55	57	52	50	54
Co	122	114	107	97	116	116	108	112	117	113	105	109
Ba	<3	—	—	—	9	9	—	9	<3	<3	<3	<3
La	<2	—	—	—	<2	<2	—	<2	<2	<2	<2	<2
Ce	<2	—	—	—	<2	<2	—	<2	<2	<2	<1	<2
U	<0.5	—	—	—	<0.5	<0.5	—	<0.5	<0.5	<0.5	<0.5	<0.5

Th	<0.5	—	—	—	<0.5	<0.5	—	<0.5	<0.5	<0.5	,0.5	<0.5
Sc	4	—	—	—	6	6	—	7	5	5	<1	7
Pb	<2	—	—	—	<2	<2	—	<2	<2	<2	<1	<2

Table 2.1: Continued

Sample:	FJ187-2	FJ188-1	FJ188-2	FJ190A-1	FJ190A-2	FJ205	K014-1	K046	K048A-1	FJ194	K049-2
Rock type:	Lhrz	Lhrz	Lhrz	Lhrz	Lhrz	Lhrz	Whr	Whr	Whr	Whr	OI Gabbro
<i>XRF (wt.%)</i>											
SiO ₂	45.12	44.82	45.27	44.88	44.71	44.25	41.28	39.91	44.49	41.70	44.70
TiO ₂	0.13	0.06	0.08	0.07	0.14	0.03	0.17	0.06	0.02	0.22	0.97
Al ₂ O ₃	2.48	2.12	2.65	2.41	3.53	2.00	1.84	0.90	1.53	2.03	10.23
FeO*	9.98	9.28	8.56	9.08	8.73	8.38	11.96	11.27	8.48	11.49	7.66
MnO	0.17	0.15	0.01	0.14	0.14	0.13	0.18	0.16	0.13	0.18	0.12
MgO	40.45	42.26	40.66	41.43	39.61	42.01	40.37	47.03	43.17	39.24	18.47
CaO	1.52	1.22	2.57	1.88	2.92	3.13	3.92	0.58	2.11	4.91	16.93
Na ₂ O	0.11	0.08	0.15	0.10	0.19	0.05	0.20	0.07	0.07	0.19	0.62
K ₂ O	–	–	0.04	–	0.01	–	0.02	–	–	–	0.01
P ₂ O ₅	0.01	0.01	0.02	0.01	0.01	–	0.04	0.01	–	0.03	0.03
SUM	100.00	100.00	100.00	100.00	100.00	100.00	100.00	100.00	100.00	100.00	100.00
LOI	-0.51	-0.34	-0.01	-0.39	-0.36	-0.09	-0.15	-0.53	-0.26	-0.17	-0.05
<i>XRF (ppm)</i>											
Rb	<0.5	<0.5	<0.5	–	–	<0.5	<0.5	<0.5	–	<0.5	<0.5
Sr	12	6	3	10	35	1	25	2	3	27	62
Y	5.5	5.4	1	–	–	3	6	<0.5	–	7.9	25.2
Zr	<2	<2	<1	4	20	4	<2	2	7	<2	25
V	61	56	67	67	74	62	54	28	49	66	300
Ni	1675	1915	2028	2178	2405	2012	1323	2309	2040	1269	485
Cr	2290	2432	3561	2636	2725	2925	1418	1958	2066	1666	1392
Nb	<0.5	<0.5	<0.5	–	–	<0.5	<0.5	<0.5	–	<0.5	<0.5
Ga	2.4	2.4	2.5	–	–	1.6	1.3	1.3	–	2.4	13.9
Cu	5	<2	6	–	–	15	4	10	–	6	33
Zn	72	62	51	–	–	52	82	73	–	81	76
Co	121	118	106	104	94	108	149	140	96	147	53
Ba	11	<3	<3	–	–	<3	6	<3	–	15	8
La	<2	<2	<2	–	–	<2	<2	<2	–	<2	7
Ce	<2	<2	<1	–	–	<2	<2	<2	–	<2	14
U	<0.5	<0.5	<0.5	–	–	<0.5	<0.5	<0.5	–	<0.5	<0.5

Th	<0.5	<0.5	<0.5	—	—	<0.5	<0.5	<0.5	—	<0.5	<0.5
Sc	8	5	2	—	—	7	12	1	—	13	53
Pb	<2	<2	<1	—	—	<2	<2	<2	—	<2	<2

Major elements (wt. %) are measured by XRF and values anhydrous normalized to 100. Trace elements (ppm) are measured on pressed powder pellets. FeO* = Total Fe_2O_3 and FeO. LOI = Loss on ignition.

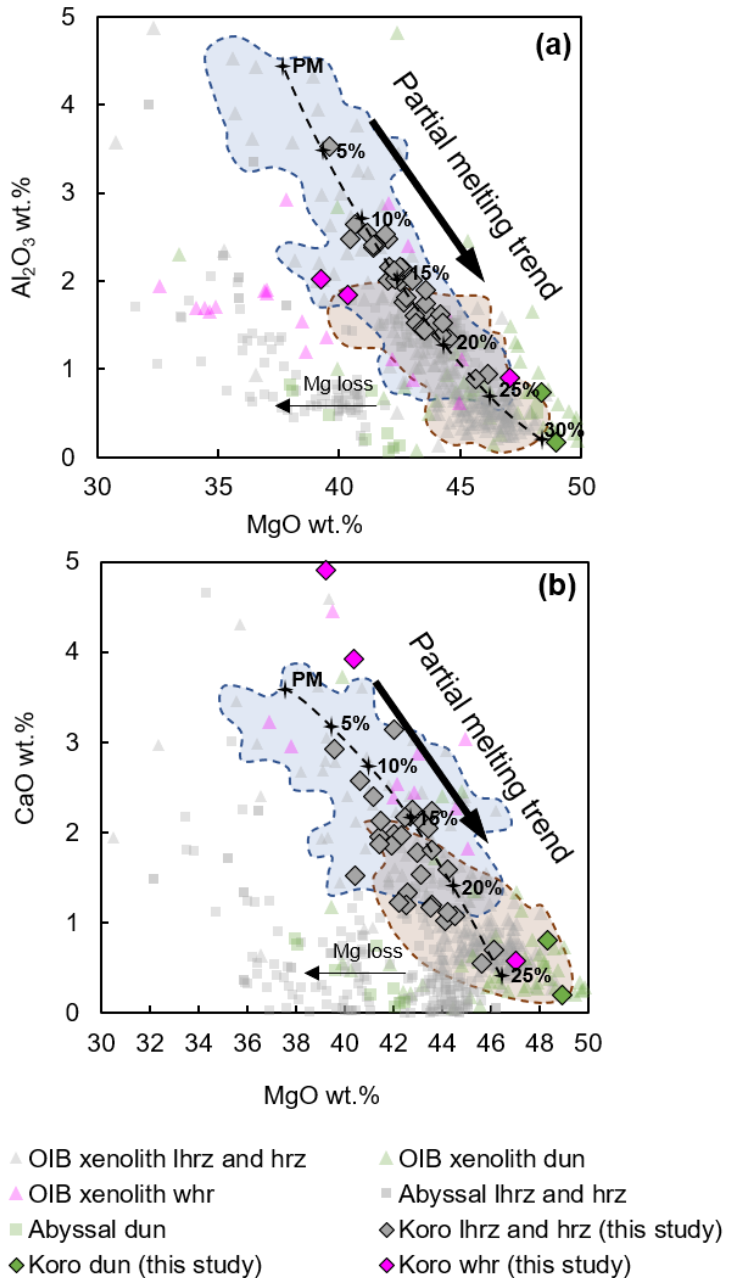


Figure 2.6. (a) and (b) Whole-rock Al_2O_3 wt. % and CaO wt. % vs. whole-rock MgO wt. % in Koro peridotites. Global OIB xenoliths from Simon *et al.* (2008) and abyssal peridotites from the GeoReM database (<http://georem.mpch-mainz.gwdg.de>). Shaded fields represent OIB and abyssal peridotite data for Iherzolites (blue) and harzburgites (brown) excluding outliers from Mg-loss. Partial melting trends and primitive mantle (PM) composition from Niu (1997).

and harzburgites, 2106–3561 ppm in lherzolites and 1418–2066 in wehrlites, and appear to be controlled by spinel modal abundance.

Whole-rock trace elements measured in the Koro peridotites are presented in Table 2.2 and PM normalized abundances plotted in Figs. 2.7a & 2.7b. Compared to average trace element compositions in intraplate OIB-hosted peridotites from the Cook-Austral Islands (Snortum *et al.*, 2019), the Koro peridotites have lower abundances of most measured trace elements. A depletion trend from elements Th through to Cs is also observed in the Koro peridotites, whereas the Cook-Austral peridotites show an enrichment trend from Th to Cs. In comparison to the trace element average from Tonga fore-arc peridotites (Birner *et al.*, 2017), the Koro peridotites have higher trace elements abundances except for Cs, U, and Sr. Diagnostic “arc” signatures such as strong Nb/Ta fractionation due to negative Nb anomalies shown in the Tonga peridotites (Fig. 2.7a) are not evident in the Koro peridotites. However, a number of Koro peridotites display positive Sr anomalies that are observed in the Tonga peridotites but absent in the Cook-Austral peridotites. Most Koro peridotites are also characterized by positive middle rare earth element (MREE: Sm, Eu, Gd, Tb) to heavy rare earth element (HREE: Dy, Ho, Er, Yb, Lu) slopes that are similar to HREE patterns in the Tonga peridotites. Koro peridotites that do not display this pattern are most common in wehrlites and display flat or negative MREE to HREE slopes that are more comparable to the Cook-Austral peridotites. Late-stage light rare earth element (LREE: La, Ce, Pr, Nd) enrichments are evident in all Koro peridotites, and are particularly noticeable when overlaid by modelled REE partial melt estimates in Fig. 2.7b. In order to make reliable estimates for the degree of partial melting, peridotites that do not show a positive MREE to HREE slope (i.e., “residual” trend) or that show LREE enrichments are excluded. Based on these HREE abundances, partial melt estimates for the Koro peridotites generally range between 20–25% with the lowest HREE recorded in a harzburgite. The only sample that exceeds 25% partial melting is the cpx-free dunite that displays lower REE abundances and an overall “U-shaped” pattern. The cpx-bearing dunite on the other hand, displays a REE pattern similar to several lherzolites and wehrlites.

2.5.2.2. Host-basalt chemistry

Koro peridotite host basalts were sampled as either float samples with their enclosed xenoliths, or from one large vesicular basalt dyke. Major and minor element compositions of the host basalt MgO contents range from 8.2–13.8 wt.%, SiO₂ ranging between 43.8–46.0 wt.%, and total alkalis

Table 2.2: Whole-rock trace element abundances via solution ICP-MS for Koro peridotite xenoliths

	Sample: K011-1 K015A-2 K041-2 K042-2 FJ167-2 FJ167-3 FJ188-1 FJ063								K008	FJ024	K014-1	K046	K048A-1
Rock type:	Lhrz	Lhrz	Lhrz	Lhrz	Lhrz	Lhrz	Hzr	Dun	Dun	Whr	Whr	Whr	Whr
<i>ICP-MS (ppm)</i>													
Rb	1.098	0.048	0.043	0.027	0.018	0.097	0.046	0.752	0.696	0.072	0.363	0.131	0.112
Sr	9.559	2.936	9.614	—	3.598	9.066	7.742	4.421	15.749	1.889	38.331	3.215	2.296
Y	0.634	0.647	0.791	0.913	1.282	0.991	1.136	0.251	0.823	0.061	2.995	0.585	0.738
Nb	0.313	0.160	0.292	0.056	0.124	0.394	0.303	0.146	0.810	0.030	1.603	0.287	0.492
Mo	0.554	0.508	0.456	0.456	0.428	0.417	0.468	0.485	0.606	0.644	0.365	0.512	0.545
Cs	0.007	0.001	0.001	0.001	0.001	0.002	0.001	0.006	0.007	0.002	0.002	0.004	0.003
Ba	4.674	0.460	2.122	—	—	2.784	1.153	3.895	12.135	—	16.667	1.326	0.826
La	0.271	0.165	0.426	0.032	0.139	0.477	0.443	0.051	0.697	0.032	2.097	0.227	0.503
Ce	0.574	0.294	0.569	0.060	0.314	1.177	1.212	0.128	1.418	0.046	4.389	0.505	0.836
Pr	0.071	0.025	0.077	0.008	0.039	0.146	0.168	0.016	0.165	0.006	0.519	0.080	0.063
Nd	0.283	0.084	0.279	0.034	0.164	0.638	0.760	0.075	0.695	0.027	2.209	0.379	0.172
Sm	0.062	0.023	0.054	0.019	0.055	0.139	0.173	0.027	0.155	0.005	0.526	0.102	0.029
Eu	0.025	0.009	0.019	0.010	0.024	0.048	0.058	0.009	0.051	0.001	0.184	0.033	0.009
Gd	0.062	0.038	0.065	0.051	0.099	0.150	0.164	0.024	0.158	0.001	0.576	0.103	0.044
Tb	0.014	0.011	0.015	0.016	0.025	0.026	0.030	0.006	0.025	0.001	0.099	0.018	0.012
Dy	0.097	0.094	0.119	0.139	0.202	0.175	0.197	0.042	0.152	0.008	0.621	0.120	0.103
Ho	0.025	0.025	0.031	0.037	0.051	0.040	0.043	0.010	0.033	0.002	0.121	0.022	0.028
Er	0.085	0.093	0.104	0.123	0.173	0.127	0.147	0.034	0.089	0.009	0.352	0.071	0.102
Yb	0.109	0.121	0.139	0.155	0.188	0.161	0.180	0.051	0.097	0.018	0.312	0.073	0.135
Lu	0.020	0.022	0.026	0.027	0.034	0.028	0.031	0.009	0.016	0.005	0.049	0.013	0.024
Hf	0.030	—	0.032	—	—	0.090	0.096	—	0.072	—	0.406	0.036	0.055
Ta	0.016	0.007	0.015	0.002	0.004	0.027	0.021	0.004	0.043	0.002	0.131	0.015	0.035
Pb	—	—	—	—	—	—	—	—	—	0.105	—	—	—
Th	0.027	0.036	0.044	0.003	0.011	0.048	0.038	0.007	0.081	0.006	0.264	0.028	0.450
U	0.015	0.051	0.019	0.004	0.046	0.015	0.021	0.004	0.047	0.037	0.141	0.023	0.147

Table 2.3: Whole-rock major and trace element abundance data for Koro host basalts

Sample:	B-K008	[†] B-K041-2	B-K045	B-K046	B-K047-1	B-K047-2	B-FJ024	B-K159
Rock type:	AB	AB	AB	AB	AB	AB	AB	AB
<i>XRF (wt. %)</i>								
SiO ₂	46.0	43.8	45.4	45.3	45.7	45.4	45.6	44.9
TiO ₂	2.2	2.5	2.1	2.3	2.3	2.3	2.0	2.2
Al ₂ O ₃	16.0	14.9	13.6	14.3	14.5	14.3	13.8	13.7
FeO*	10.7	10.7	10.4	10.8	10.5	10.5	10.8	10.8
MnO	0.2	0.2	0.2	0.2	0.2	0.2	0.2	0.2
MgO	8.2	13.8	12.5	11.5	11.1	11.4	13.2	13.1
CaO	11.1	10.7	11.9	11.5	11.2	11.4	10.2	10.9
Na ₂ O	4.1	2.3	2.9	3.3	3.8	3.6	2.9	2.6
K ₂ O	0.7	0.6	0.5	0.4	0.4	0.4	0.9	0.9
P ₂ O ₅	0.8	0.5	0.4	0.5	0.5	0.5	0.5	0.5
SUM	100.0	100.0	100.0	100.0	100.0	100.0	100.0	100.0
LOI	1.31	1.92	0.35	0.53	0.52	1.50	1.33	1.46
<i>XRF (ppm)</i>								
Rb	22.1	–	10.9	20.1	6.9	7.1	7.8	19.4
Sr	888	602	500	567	598	627	254	592
Y	31.5	–	28.9	29.1	30	32.1	15.6	32.7
Zr	186	193	163	191	196	196	90	170
V	284	262	275	281	280	287	109	248
Ni	165	–	303	265	236	250	195	335
Cr	293	549	559	530	475	481	353	685
Nb	39.4	–	33.8	41.4	46.4	43.4	17.5	38.4
Ga	15.8	–	14.3	15.3	15.4	15.6	7.8	14.8
Cu	107	–	83	84	83	95	44	78
Zn	78	–	79	80	79	81	39	82
Co	47	–	60	60	56	57	29	59
Ba	427	–	277	347	365	345	140	338
La	22	–	15	15	17	16	15	13
Ce	37	–	26	31	31	29	22	30
U	<0.5	–	<0.5	<0.5	0.5	1	<0.5	<0.5

Th	<0.5	—	0.8	0.8	1.3	0.8	5.6	0.5
Sc	29	—	32	29	31	31	6	29
Pb	1	—	<1	<1	<1	1	<1	<1

Table 2.3: Continued

Sample:	B-FJ063	B-FJ167-2 / B-FJ167-3	B-K049-1	B-FJ186-1	B-FJ188-1/B-FJ188-2
Rock type:	AB	AB	AB	AB	AB
<i>XRF (wt.%)</i>					
SiO ₂	45.8	44.9	45.2	45.1	44.7
TiO ₂	2.2	2.4	2.4	2.5	2.5
Al ₂ O ₃	16.1	14.5	14.5	14.5	14.8
FeO*	10.9	10.2	10.3	10.4	10.6
MnO	0.2	0.2	0.2	0.2	0.2
MgO	8.4	13.0	12.1	11.8	12.2
CaO	11.1	10.7	10.7	10.5	10.7
Na ₂ O	3.5	2.8	3.1	3.2	2.9
K ₂ O	1.0	0.8	1.1	1.3	1.0
P ₂ O ₅	0.7	0.5	0.5	0.5	0.5
SUM	100.0	100.0	100.0	100.0	100.0
LOI	1.88	1.07	0.38	0.46	0.48
<i>XRF (ppm)</i>					
Rb	20.2	12.0	21.7	24.8	16.8
Sr	1331	606	591	592	633
Y	31.2	34.9	31.8	32.5	33.6
Zr	192	182	187	196	189
V	301	260	262	261	270
Ni	169	315	279	273	281
Cr	378	583	552	521	534
Nb	37.9	39.5	41.4	44.6	43.5
Ga	14.4	14.4	14.8	15.2	14.7
Cu	87	65	64	72	71
Zn	79	75	71	85	73
Co	49	61	55	57	58
Ba	395	355	330	370	373
La	15	13	13	14	13
Ce	32	27	25	29	24
U	<0.5	0.5	<0.5	1	<0.5

Th	<0.5	1.2	1.2	1	2
Sc	32	28	29	27	28
Pb	<1	<1	<1	<1	<1

Major elements (wt.%) are measured by XRF and values anhydrous normalized to 100. Trace elements (ppm) are measured on pressed powder pellets. FeO* = Total Fe₂O₃ and FeO. B- = host alkali basalt (AB) for each respective peridotite xenolith.

[†]= analyses on limited sample material (<3 g). LOI = Loss on ignition.

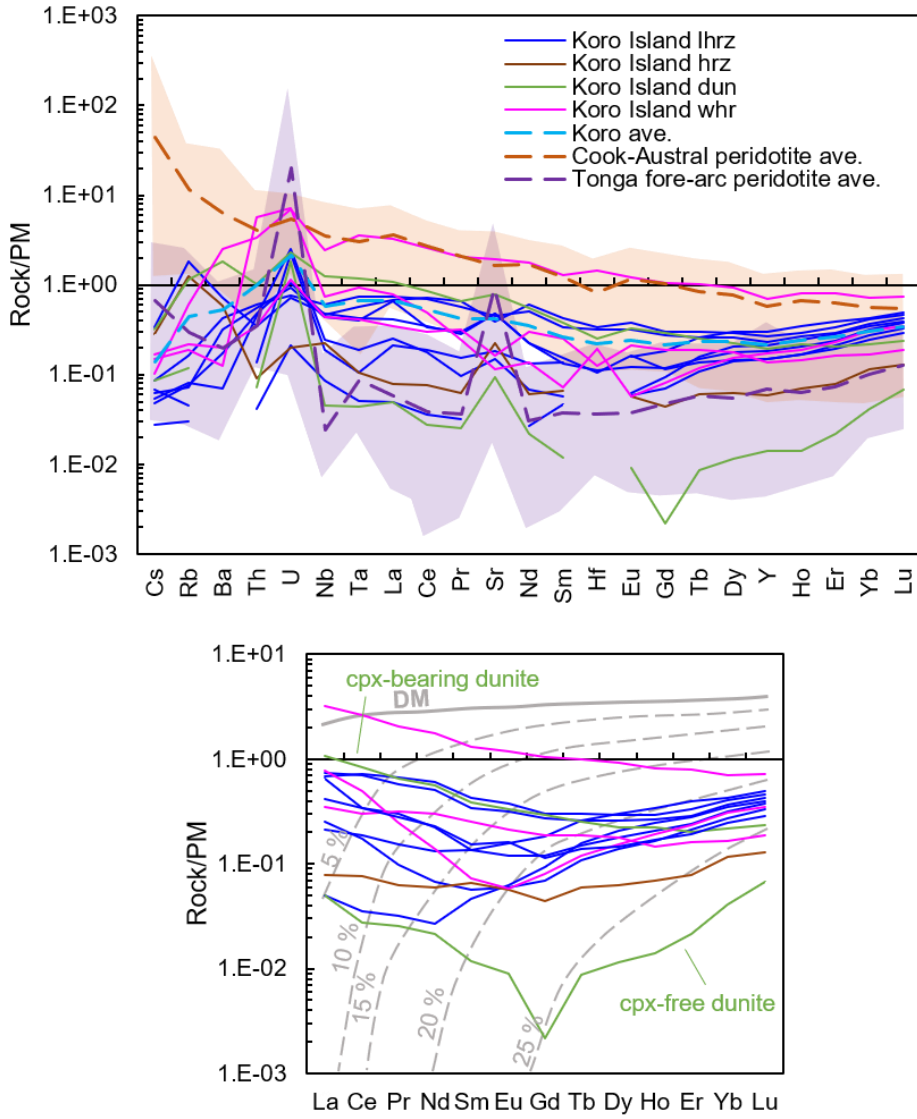


Figure 2.7. (a) Whole-rock trace elements in Koro peridotite xenoliths and Koro host basalts normalized to primitive mantle (McDonough & Sun, 1995). Shaded field in orange represents OIB-hosted peridotite xenoliths from Cook-Austral Islands from Snortum *et al.* (2019) and purple shaded field represents fore-arc peridotites from Birner *et al.* (2017). (b) Whole-rock REE in Koro peridotites plotted against anhydrous partial melt-estimates from 0–25 % in the spinel stability field following Hellebrand *et al.* (2002) using partition coefficients from Ionov *et al.* (2002). Depleted mantle (DM) starting compositions are from Salters & Stracke (2004).

$(\text{Na}_2\text{O}_3 + \text{K}_2\text{O})$ between 2.9–4.8 wt.%, classifying in the total alkali vs. silica (TAS; $\text{Na}_2\text{O} + \text{K}_2\text{O}$ vs. SiO_2) system at the boundary between alkali and tholeiitic basalt (Fig. 2.8a; Table 2.3). Sample B-K041-2 is slightly more picritic due to the lower total alkalis. The Koro host basalts are notably lower in SiO_2 compared to Fijian shoshonite series arc basalts whose SiO_2 ranges from 46.9–56.6 wt. % (Gill & Whelan, 1989; Rogers & Setterfield, 1994; Leslie *et al.*, 2009). TiO_2 contents in the Koro host basalts range between 2.2–2.5 wt.%, and are notably higher than the Fijian shoshonite series basalts (0.50–1.36 wt. %).

Whole-rock trace elements abundances in the Koro host basalts (Fig. 2.8b; Table 2.4) are consistent with the OIB trace element abundances from Sun & McDonough (1989). Some exceptions include positive Sr anomalies in two Koro host basalts that are similar to Sr signatures observed in the Fijian arc basalts, however, the Koro host lavas are distinct from Fijian arc basalts. Fijian arc basalts display typical arc signatures such as Nb/Ta fractionation, along with negative Nb, Ta, Th and Hf anomalies. The Koro host basalts are also distinct from back-arc basin basalt (BABB) and mid ocean ridge basalt (MORB) compositions from Gale *et al.* (2013) that have lower incompatible trace element abundances.

2.5.3. Trace element mineral chemistry

2.5.3.1. Olivine

Trace elements measured in olivine grains picked from 165 peridotite xenoliths, fifteen peridotite xenoliths in thin section, and two olivine phenocrysts from the host basalt of xenolith FJ024 are provided in Appendix 3. Following an initial assessment using major element mineral chemistry and disequilibria textures, lherzolites and harzburgites with olivine Fo contents $\geq \text{Fo}_{89.5}$ are classified as likely mantle residues. This benchmark is derived from recognizing that wehrellites are metasomatic products that have Fo contents in olivine up to $\sim \text{Fo}_{88}$ (i.e., exceeding the Fo_{87} mantle criteria in Frey & Prinz, 1978). $\text{Fo}_{89.5}$ is further assessed as an appropriate discriminant for a mantle origin by measuring Al, Ti, Ca, and Ni in olivine and comparing the results with a combination of accepted values for mantle olivine: $\text{Al} < 130$ ppm, $\text{Ca} \leq 715$ ppm; $\text{Ti} < 70$ ppm, $\text{Ni} \geq 2350$ ppm (Foley *et al.*, 2013; Bussweiler *et al.*, 2017 and references therein). Koro lherzolites and harzburgites with olivine contents $> \text{Fo}_{89.5}$ and meet this trace element criteria are henceforth referred to as “mantle”. Box and whisker plots were used to compare the distribution of elements Al, Ti, Ca, Ni, V and Co

Table 2.4: Whole-rock trace element abundances via solution ICP-MS for Koro host basalts

Sample:	B-K049	B-K041-2	B-K008	B-FJ063	B-K047	B-FJ167
Rock type:	AB	AB	AB	AB	AB	AB
<i>ICP-MS (ppm)</i>						
Rb	24.6	11.9	24.1	23.4	10.3	14.7
Sr	647.3	651.2	1011.8	1728.5	624.0	621.5
Y	27.6	27.2	30.5	30.2	25.6	24.5
Nb	42.2	43.7	42.5	41.8	46.5	38.0
Mo	1.9	1.9	1.8	1.3	2.3	1.7
Cs	0.2	0.1	0.4	0.4	0.4	0.1
Ba	421.9	357.9	499.3	480.1	421.2	375.2
La	33.1	30.5	36.7	37.2	32.1	28.2
Ce	69.1	63.7	75.7	74.8	64.9	59.1
Pr	7.9	7.1	8.6	8.2	7.4	6.7
Nd	33.9	30.5	34.9	34.7	30.8	28.8
Sm	7.0	6.4	7.1	7.0	6.4	6.1
Eu	2.3	2.1	2.2	2.2	2.0	1.9
Gd	7.4	6.4	6.7	6.9	6.3	5.9
Tb	1.1	0.9	1.0	1.0	0.9	0.9
Dy	5.9	5.4	5.6	5.5	5.1	5.0
Ho	1.2	1.0	1.1	1.1	1.0	1.0
Er	3.2	2.8	2.8	2.9	2.7	2.6
Yb	2.9	2.3	2.7	2.6	2.2	2.2
Lu	0.4	0.4	0.4	0.4	0.3	0.3
Hf	5.7	4.6	4.1	4.0	4.7	4.4
Ta	3.0	2.4	2.2	2.2	2.5	2.2
Pb	2.6	1.9	3.2	3.0	2.0	1.9
Th	4.2	3.4	3.4	3.4	3.7	3.2
U	1.2	0.8	1.0	1.1	1.0	0.8

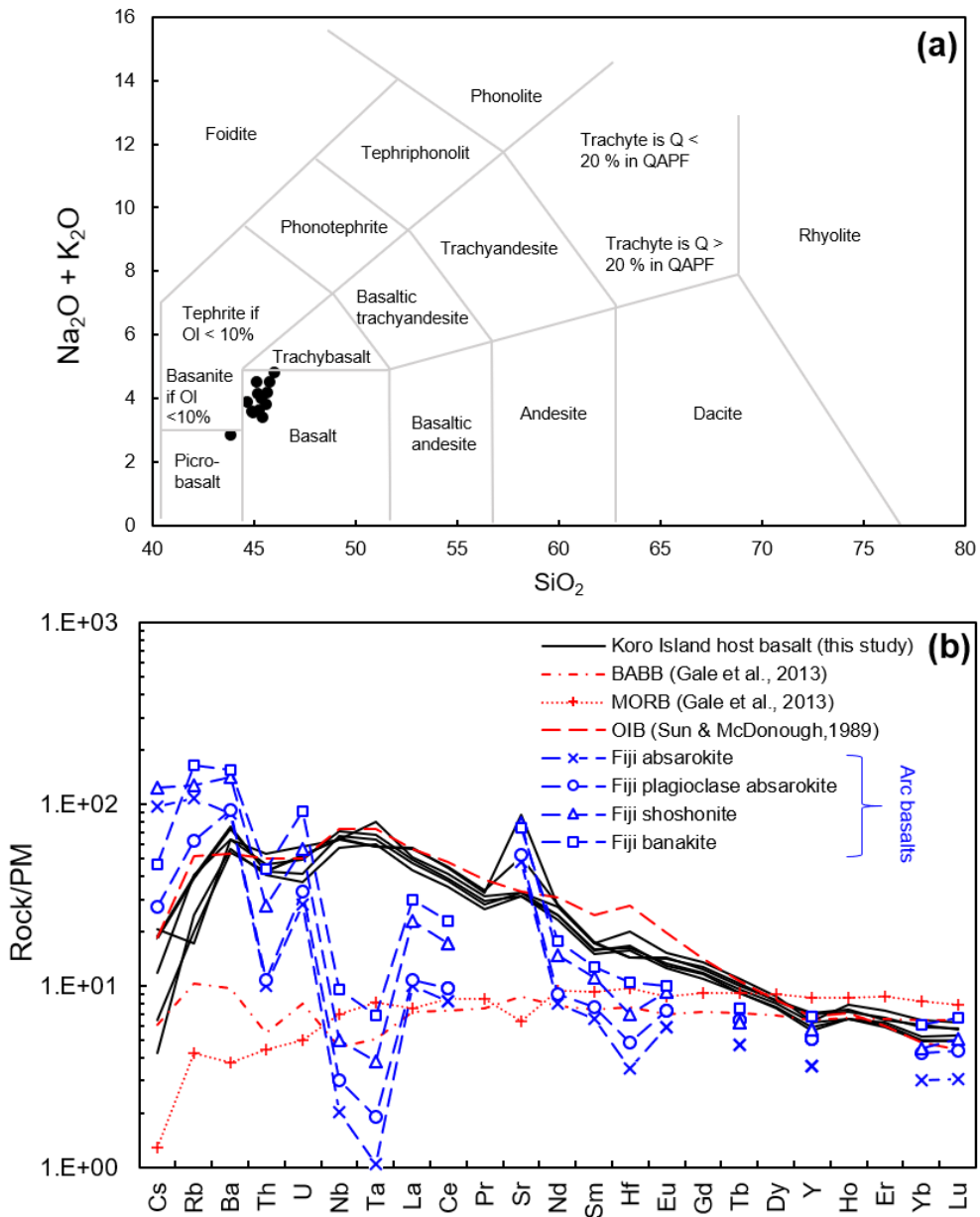


Figure 2.8. (a) Koro host basalt major element classification bases on total alkalis vs. silica (TAS) diagram after Le Bas *et al.* (1986). (b) Koro host basalt trace elements normalized to PM (McDonough & Sun, 1995) plotted against back-arc basin basalt (BABB) and mid ocean ridge basalt (MORB) values from Gale *et al.* (2013), and OIB values from Sun & McDonough (1989).

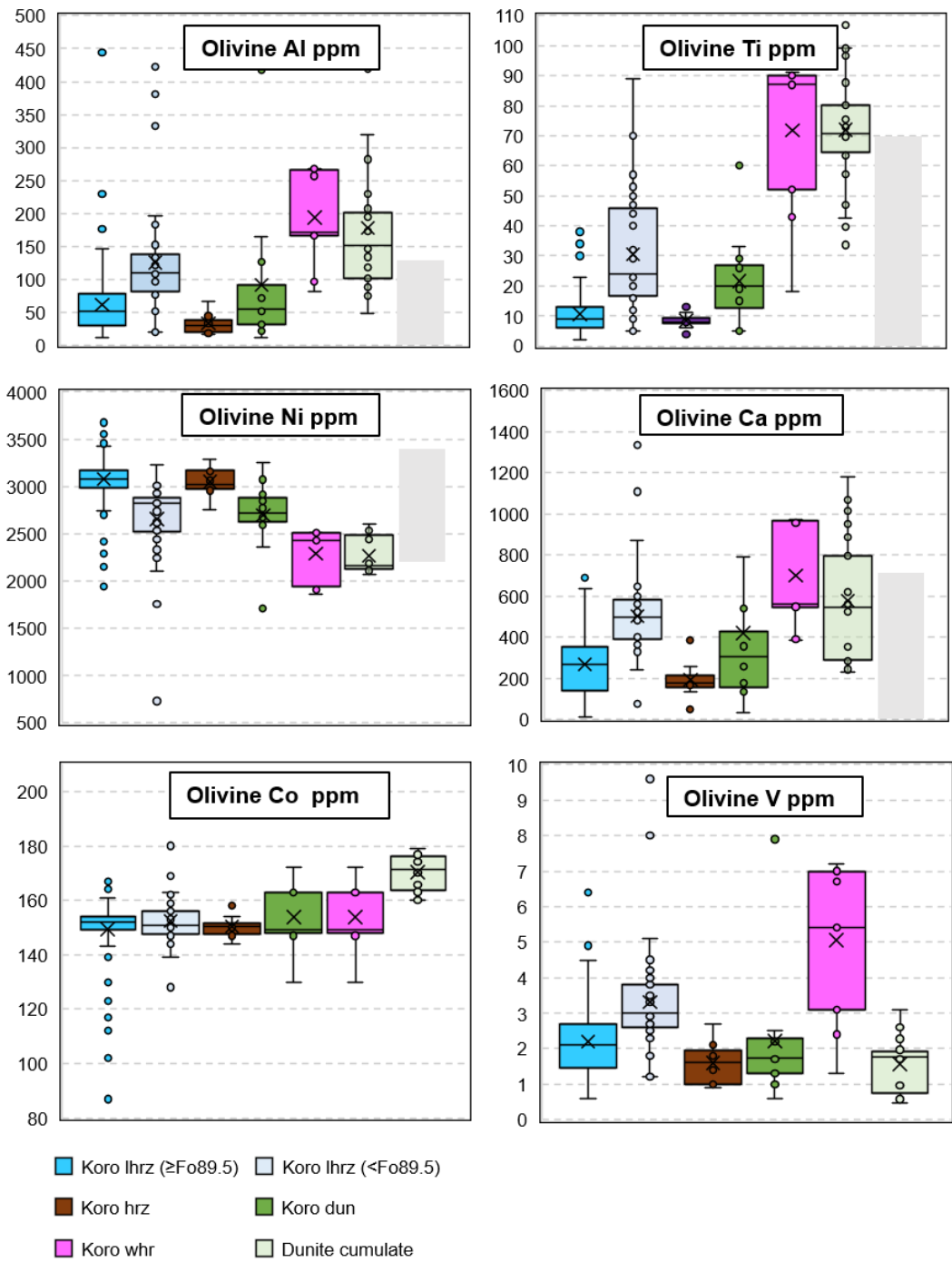


Figure 2.9. Box and whisker plots showing the variation in elements Al, Ti, Ni, Ca, V, and Co in olivine between Koro peridotite xenoliths of different lithologies. Dunite cumulate xenoliths from Peters *et al.* (2006) are plotted for comparison. Shaded grey field denotes mantle range based on Foley *et al.* (2013) and Bussweiler *et al.* (2017) as discussed in text. X denotes median values.

in olivine amongst different lithologies within the Koro suite (Fig. 2.9). Several olivine grains from previously recognized dunite cumulates from Reunion Island (Peters *et al.*, 2016) were also measured for comparison. Olivine in a small number of Koro lherzolites, including those with olivine contents $>\text{Fo}_{89.5}$ contain Al, Ti, Ca and Ni concentrations that lie outside the parameters for residual mantle olivine, but do not appear to show any obvious petrographic differences to other Koro lherzolites. Most Koro wehrlite olivines fall outside the mantle olivine trace element criteria, in agreement with their major elements. Wehrelite olivines show large elemental variations and are distinct from Koro lherzolites, dunites and harzburgites with the exception of Co. Vanadium concentrations in olivine from wehrellites are notably higher than olivines from Koro lherzolites, harzburgites and dunites, along with cumulate dunites from the Reunion. Within the wehrelite group, low Al, Ca, Ni, Ti, Sc, and V contents are observed in samples that show strong petrographic evidence for olivine and clinopyroxene disequilibria (e.g., melt infiltrating textures; Fig. 2.3c), whereas wehrellites with higher concentrations of these elements tend to show greater textural equilibration between adjacent cpx-olivine grains. Olivine trace elements in the Koro dunites fall within the accepted mantle range, and notably, are distinct from the Reunion cumulates in all first-row transition elements except for V. Two olivine grains from the host basalt of FJ024 (sample B-FJ024) were measured and compared with the dunitic xenolith within FJ024 to further test if xenoliths are of volcanic olivine origin. The Fo content of olivine from the host basalt ($\text{Fo}_{89.1}$) is only slightly lower to olivine Fo content in xenolith FJ024 ($\text{Fo}_{90.2}$), whereas Al and Ca contents in the host basalt olivine are considerably higher (296 ± 11 ppm and 1100 ± 3 ppm, respectively), falling outside the mantle olivine range.

Grouping of the REE systematics of olivine from Koro peridotites is based on their lithologies and whether they have “mantle-like” olivine (i.e., $\geq\text{Fo}_{89.5}$) and Al, Ca, Ti and Ni in olivine contents discussed above (Figs. 2.10a–e). The chondrite-normalized REE patterns are plotted against fractional melting models for peridotite expressed as REE in olivine, showing a melt-depletion estimates $<20\%$, however, the modelled starting depleted mantle (DM) values slightly underestimate the starting REE abundances, shown by the Koro peridotites plotting above 0% melting. Apart from a few anomalous samples, olivine in the Koro peridotites are characterized by HREE to LREE depletions. Most of these olivines are also characterized by a negative Ce anomaly that is most prominent in the lherzolites with olivine $\geq\text{Fo}_{89.5}$ and harzburgites, and less prominent in olivine from wehrellites and dunites, however, this could also reflect the

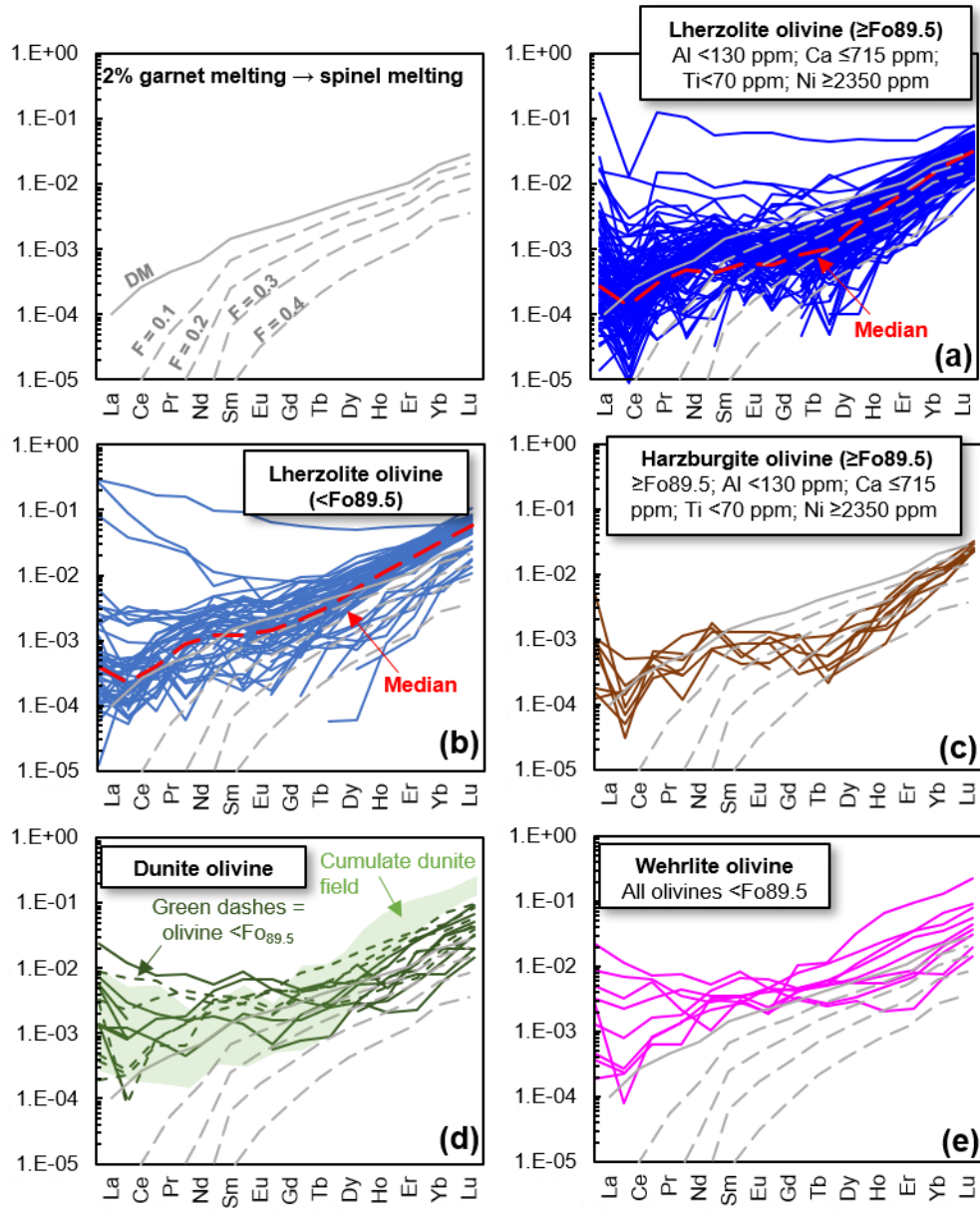


Figure 2.10. Rare Earth elements (REE) in Koro olivines normalized to PM (McDonough & Sun, 1995). Grey dashed lines represent 0–15% melting of olivine in the spinel stability field assuming 2% melting in the garnet stability field following the Hellebrand *et al.* (2002) method using starting DM compositions are from Salters & Stracke (2004) and REE in olivine (forsterite) partition coefficients from Burnham & O'Neill (2020). (a) and (b) show REE in olivine from Iherzolites with olivine $\geq\text{Fo}_{89.5}$ (with Al <130 ppm; Ca \leq 715 ppm; Ti <70 ppm; Ni \geq 2350 ppm) and olivine $<\text{Fo}_{89.5}$, respectively. (c) (d) and (e) show olivine REE in harzburgites, wehrellites and dunites, respectively. REE in olivine measurements on cumulate dunites from Peters *et al.* (2016) are shown in (d) to compare with the Koro dunites. Red dashed lines in (a) and (b) denote median values for Iherzolite olivines.

limited number of wehrlites and dunites analysed. Olivines in harzburgites show a similar general REE pattern to the median REE in both lherzolites with olivine \geq Fo_{89.5} and <Fo_{89.5} characterized by HREE to MREE depletions, flat MREEs, and negative Ce anomalies forming an overall “seat-shaped” REE pattern (Figs. 2.10a–c). The only subtle difference may be the slightly flatter MREEs in harzburgite olivines compared to olivine in lherzolites, and generally less REE scatter in harzburgite olivines compared to lherzolites, however, this could also reflect fewer analysed samples. Olivines from the Koro dunites have lower HREE abundances compared to cumulate xenoliths from Reunion Island (Fig. 2.10d). These characteristics of the Koro dunite olivines are consistent with their first-row transition metals characteristics from Fig. 2.9, showing that the Koro dunites are distinct from dunite cumulates in terms of their Al, Ti, Ni, Ca, and Co in olivine contents.

2.5.3.2. *Orthopyroxene*

Trace elements in orthopyroxene were measured in eighteen peridotite xenoliths (Appendix 3). First-row transition metals (Sc, V, Co, Ni, Cu, Zn) in orthopyroxene do show systematic variations between dunites, harzburgites, and lherzolites that are either above or below the olivine Fo_{89.5} criteria. The systematics of the measured HFSE—Ti, Nb, Zr, and REE in orthopyroxene from the Koro peridotites are also not coherent between lithologies. While orthopyroxene with Ti <200 ppm is only found in lherzolites with olivine \geq Fo_{89.5} and harzburgites, some orthopyroxenes from these rocks have Ti contents exceeding 1000 ppm (e.g., harzburgite FJ063: 830–1167 ppm Ti). These large Ti variations in orthopyroxene are consistent with Ti addition through metasomatism, even in the most depleted peridotites (e.g., 0.2–1434 ppm; Scott *et al.*, 2016). The exception is wehrlites with Ti contents in orthopyroxene exceeding these maximum values (945–2900 ppm). The Koro wehrlites also have the highest total REE in orthopyroxene whereas the lowest values are recorded in harzburgites and lherzolites with olivine \geq Fo_{89.5}. Orthopyroxene in almost all Koro peridotites is characterized by LREE to HREE depletions (see *section 2.5.3.5.* below).

2.5.3.3. *Clinopyroxene*

Trace elements in clinopyroxene measured in twenty-one peridotite (Appendix 3). Similar to orthopyroxene, the measured HFSE—Ti, Zr, Nb in clinopyroxene tend to reflect variable amounts of metasomatism rather than melt depletion. These values are summarized as: Ti = 63–7541 ppm; Zr = 0.2–179 ppm; Nb = 0.02–0.73 ppm in lherzolites, Ti = 687–1167 ppm; Zr = 10.8–15 ppm; Nb = 0.07–0.21 ppm in dunites, Ti = 503–883 ppm; Zr = 2.2–9.3 ppm; Nb = 0.03–0.07 ppm in

harzburgites, and $\text{Ti} = 3393\text{--}8135 \text{ ppm}$; $\text{Zr} = 34.6\text{--}18.0 \text{ ppm}$; $\text{Nb} = 1.46\text{--}7.50 \text{ ppm}$ in wehrlites. The Koro harzburgites and wehrlites appear to be distinct from the carbonatite derived clinopyroxene from the Samoan and Austral Island xenoliths (cpx2 ; Hauri *et al.*, 1993) that record higher clinopyroxene values of $\text{Ti} = 10950 \text{ ppm}$, $\text{Zr} = 50.7$, $\text{Nb} = 0.10 \text{ ppm}$ in harzburgites, and lower clinopyroxene values of $\text{Ti} = 185 \text{ ppm}$, $\text{Zr} = 13.4$, and $\text{Nb} = 1.30 \text{ ppm}$ in wehrlites. Total REE abundances in clinopyroxene are indistinguishable across different lithologies due to widely variable LREE and HREE fractionation. MREE_N to HREE_N depletions (i.e., $[\text{Dy/Yb}]_N > 1$) are only observed in lherzolites (both above and below olivine $\text{Fo}_{89.5}$) and in wehrlites. These include peridotites that show evidence for infiltrating clinopyroxene textures, that also tend to have higher concentrations of Zr, Ti, Ga, Y, V, and total HREE_N in clinopyroxene. Lherzolites FJ167-2 and FJ167-3 are notable outliers in the Koro peridotite suite because elements that are sensitive to both melting and metasomatism (Ni, Mn, Co, V, Sc, Ti, and total HREE_N) in clinopyroxene are significantly lower in there lherzolites compared to other Koro peridotites. Relationships between La_N/Yb_N versus Ti/Eu in clinopyroxene (Fig. 2.11) reflect predominantly silicate melt metasomatism with some minor overlap with peridotites that reflect carbonatite melt metasomatism. The origin of clinopyroxene in these samples will be discussed in terms of their inter-mineral partitioning below.

2.5.3.4. *Spinel*

Spinel trace elements were measured in fourteen peridotite xenoliths (Appendix 3). These measured trace elements show large amounts of variability, and in most cases, do not distinguish peridotites of different lithology. Some exceptions include Ti contents in wehrlites that range between 5539–4500 ppm, whereas other peridotites are significantly lower and range between 278–2574 ppm. Ni and Ga concentrations are lower in spinels from harzburgites, that range between 1397–1597 ppm in Ni and 45–52 ppm in Ga. In contrast, spinels from lherzolites, dunites and wehrilte range between 2070–3821 ppm in Ni and 55–114 ppm in Ga.

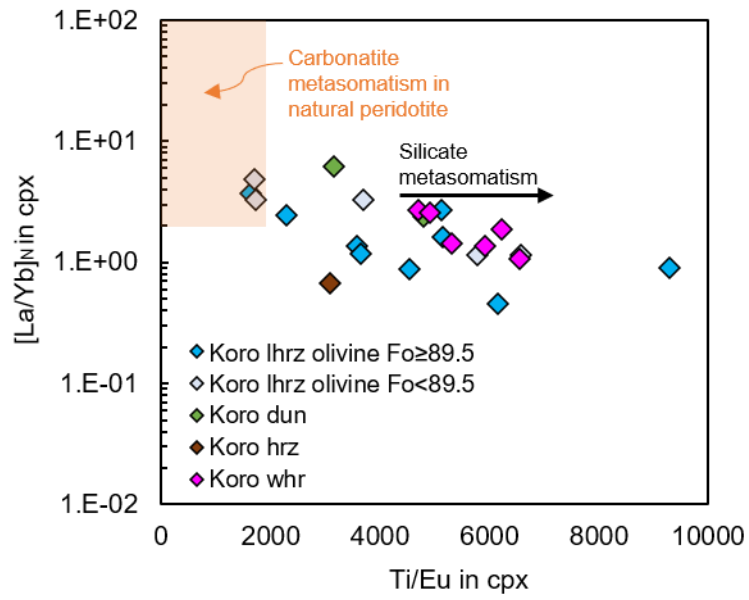


Figure 2.11. Clinopyroxene $[La/Yb]_N$ vs. Ti/Eu relationships in the Koro peridotites as a test for carbonatite vs. silicate metasomatism. Shaded orange field roughly represents clinopyroxene values in carbonatite metasomatized natural peridotites from Yaxley *et al.* (1998), Coltorti *et al.* (1999) and Neumann *et al.* (2002).

2.5.3.5. Inter-mineral partitioning

HREE partitioning as shown by $[Dy/Ce]_N$ amongst orthopyroxene, clinopyroxene, and olivine displays a positive correlation with each other and with olivine Fo (e.g., Figs. 2.12a, 2.12c & 2.12d). The relationship with HREE in orthopyroxene and spinel Cr# is more complex, with two distinct trends toward harzburgite and wehrlite in opposite directions reflecting the two distinct olivine Fo vs. spinel Cr# trends (Fig. 2.5). Total REE partitioning as shown by $[Ce/Yb]_N$ between orthopyroxene, clinopyroxene and olivine (Figs. 2.12e & 2.12f) shows no clear relationship to each other, likely indicating that LREEs are being disturbed more than HREE by metasomatism. To assess the controls on REE behaviour between mineral phases, primitive mantle (PM)-normalized REE of orthopyroxene-clinopyroxene pairs were plotted and grouped based on their similar patterns (Figs. 2.13a–e), and plotted against calculated residues from fractional melting, for their respective phase. These plots show that LREE are independent of melt depletion. At least four different orthopyroxene-clinopyroxene REE inter-mineral combinations are

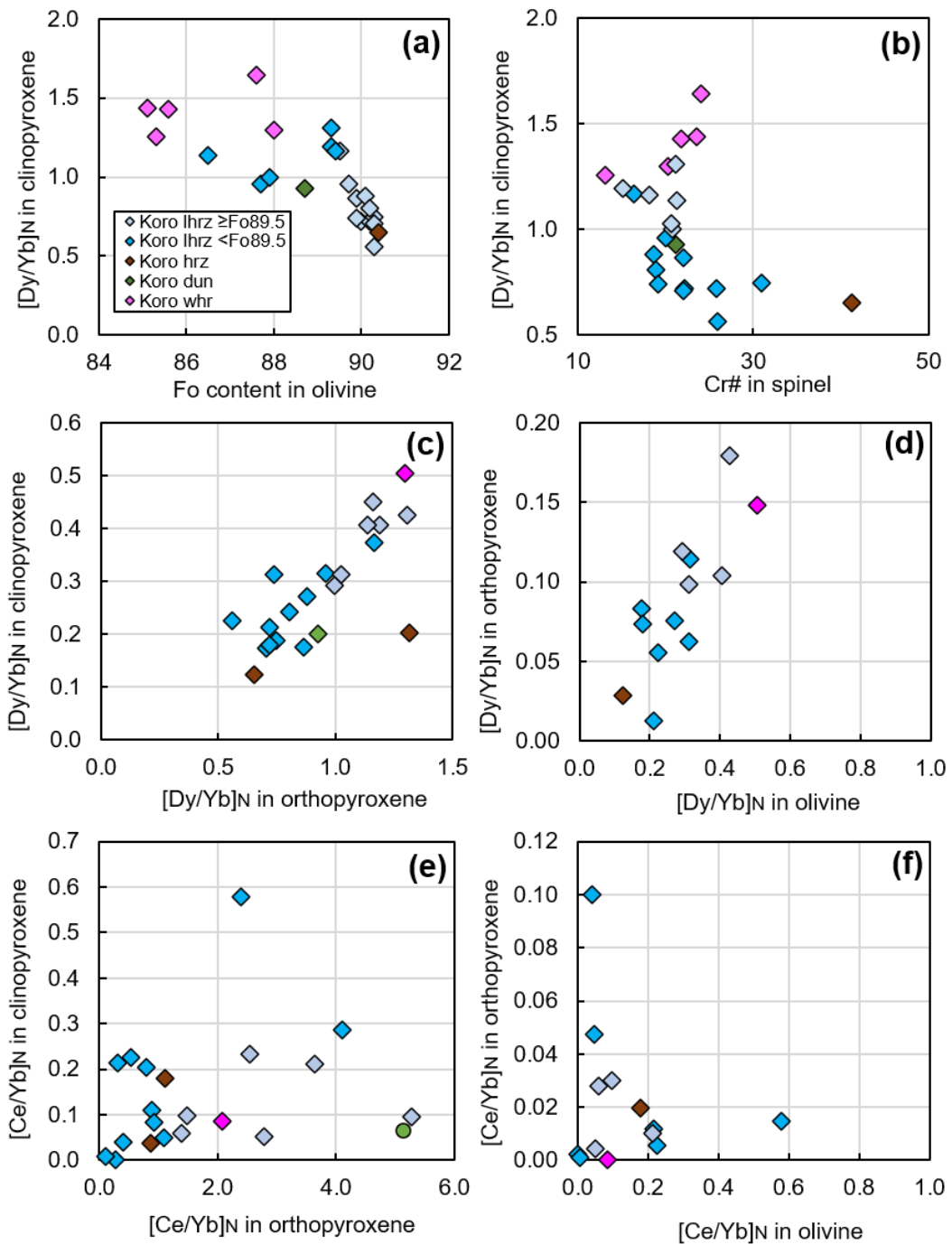


Figure 2.12. (a) and (b) Relationship between major element melt-depletion proxies (olivine Fo content and spinel Cr#) vs. HREE fractionation in clinopyroxene. (c) to (f) HREE inter-mineral partitioning between clinopyroxene, orthopyroxene, and olivine in the Koro peridotites.

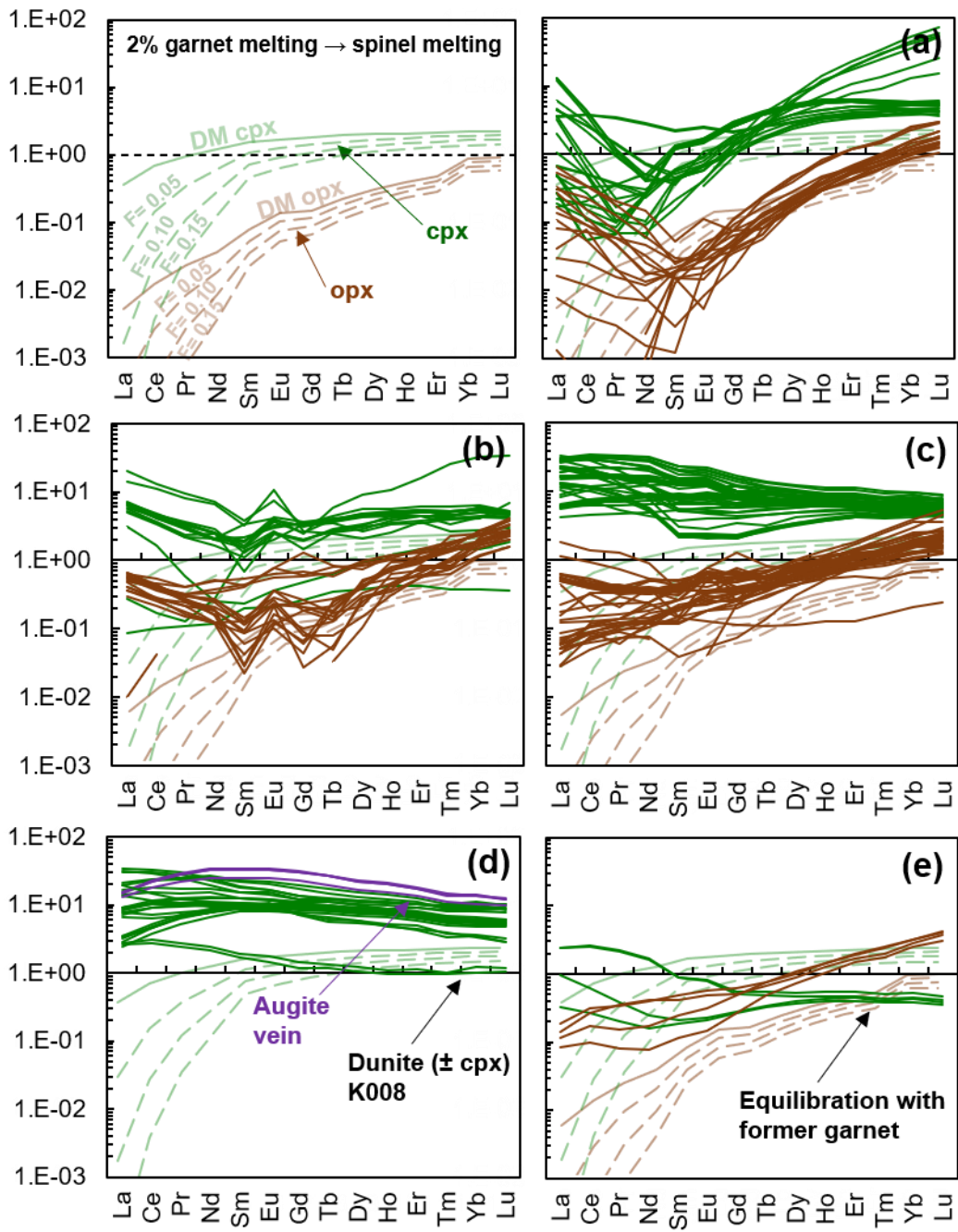


Figure 2.13. Clinopyroxene (cpx) and orthopyroxene (opx) REE abundances normalized to PM (McDonough & Sun, 1995). Dashed lines represent 5 % increments between 0–15% melting of opx and cpx in the spinel stability field, assuming 2% melting in the garnet stability field (after Hellebrand, 2002). Starting DM compositions are from Salters & Strake (2004). (a) to (c) represent coexisting cpx-opx pairs from multiple Koro peridotites that have been grouped based on similar REE patterns. Cpx REE abundances in wehrlite xenoliths are shown (d) along with augite cpx REE abundances. Residual clinopyroxene REE characterized by low HREE abundances due to equilibration with garnet in shown in (d).

identified from the Koro peridotites in Figs. 2.13a–d, reflecting different degrees of melt depletion in combination with one or more metasomatic processes. Some peridotites show curved HREE depletion patterns in both clinopyroxene and orthopyroxene in combination with sharp LREE enrichments (Fig. 2.13a). The LREE_N enrichment in these samples resemble late-stage LREE addition that has affected both clinopyroxene and orthopyroxene in a similar manner. Clinopyroxene and orthopyroxene in some peridotites are also characterized by a positive Eu anomaly and LREE enrichment (Fig. 2.13b), however, none of the three peridotites that show trace amounts of plagioclase show this positive Eu anomaly. Some orthopyroxene and clinopyroxene pairs show diverging HREE to LREE trends (Fig. 2.13c) indicating dis-equilibration between these phases—this is also indicated by comparing opx/cpx concentration ratios in the Koro peridotites (Fig. 2.14) to partition co-efficients ($D^{opx/cpx}$) from experiments and other equilibrated mantle peridotites (Liang *et al.*, 2013; Garrido *et al.*, 2000). Lherzolites FJ167-2 and FJ167-3 are unique within the Koro suite as clinopyroxene in these samples show conspicuously low HREE with little HREE to MREE fractionation (Fig. 2.13e). This is evident in their opx/cpx concentration ratios in Fig. 2.14 that are distinct from other lherzolite pyroxene pairs, along with wehrlites, harzburgites, and dunites.

2.5.4. *P-T and log fO₂ calculations*

2.5.4.1. *Geothermometry*

Equilibration temperatures for the Koro peridotites were calculated using a number of conventional geothermometers (Table 2.5). Where necessary, temperatures were calculated using an assumed pressure of 1.5 GPa (within the spinel stability field of ~0.7–3.0 GPa; Koga *et al.*, 1999; Klemme, 2004). Two-pyroxene thermometers of Brey & Köhler (1990) (T_{BKN}) and Taylor (1998) T_{Ta98} (an updated version of T_{BKN}) yield temperatures ranging between 676–1185 °C and 614–1160 °C, respectively. The REE-in-two-pyroxene thermometer (T_{REE}) (Liang *et al.*, 2013) and aluminium exchange between olivine and Cr-spinel thermometer ($T_{Al\text{-}ol\text{-}spl}}$) (Wan *et al.*, 2008) yield higher temperatures (789–1175 °C and 860–1659 °C, respectively) compared to T_{BKN} and T_{Ta98} . T_{REE} has the additional advantage of testing chemical equilibration between orthopyroxene and clinopyroxene phases using the linear regression assessment described in Liang *et al.* (2013).

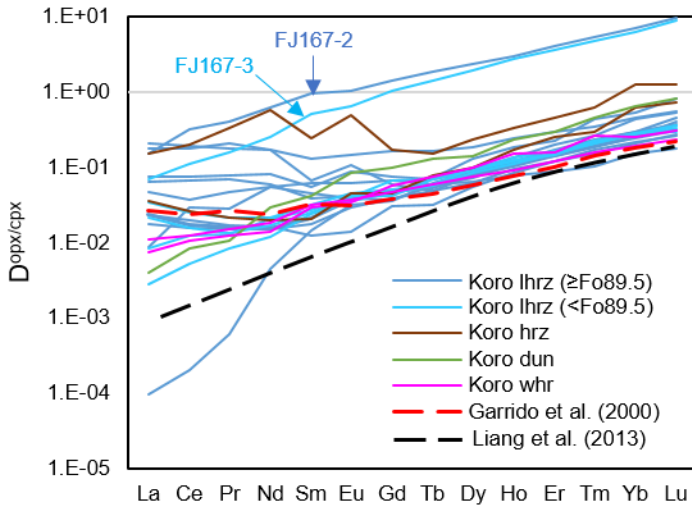


Figure 2.14. Mineral concentration ratios for REE between opx and cpx ($D^{opx/cpx}$) in the Koro peridotites plotted against $D^{opx/cpx}$ values in experimentally derived and equilibrated natural peridotites from Liang *et al.* (2013) and Garrido *et al.* (2000), respectively. Koro peridotites FJ167-2 and FJ167-3 show noticeably higher $D^{opx/cpx}$ values and correspond to lherzolites in Fig. 2.13e above.

Using this procedure, REE that fall off the regression line (mostly LREE) were identified and these data points omitted to re-calculate T_{REE} values accordingly. Using this method again, REE between orthopyroxene and clinopyroxene in peridotites K050A-2, K050A-1, FJ167-2 and FJ167-3 were identified as not being in chemical equilibrium, and therefore their calculated T_{REE} values are omitted from Table 2.5.

2.5.4.2. Geobarometry

Pressures in spinel facies peridotites were calculated following the method described in D'Souza *et al.* (2020). D'Souza *et al.* (2020) suggest that the Ca-exchange geobarometer between olivine and clinopyroxene (P_{KB}) (Köhler & Brey, 1990) can be reliable for estimating pressures for spinel facies lherzolites when used in combination with the $T_{Al\text{-}ol\text{-}spl}$ thermometer. Calculated pressures for spinel lherzolites range between <0.1 to 0.9 GPa, excluding pressures that were calculated using $T_{Al\text{-}ol\text{-}spl}$ input temperatures below the 950–1250 °C calibration range by D'Souza *et al.* (2020). These lower-than-expected pressures for spinel peridotites that fall within the plagioclase stability field are probably due to large Ca variations in olivine that can range up to 94 ppm within

Table 2.5: Calculated temperatures and pressures for Koro peridotite xenoliths

Sample	T _[BKN] (°C)	T _[Ta98] (°C)	T _[REE] (°C)	±1s	T _[Al-ol-spl] (°C)	P _[KB] (GPa)	Fe ³⁺ /ΣFe spl	logfO2	FMQ
<i>Lherzolites ≥Fo_{89.5}</i>									
*K011-1	889	895	1046	16	821	—	—	—	—
*K015A-2	940	940	1192	36	904	—	—	—	—
*K041-2	963	1041	860	28	942	—	0.291 ± 0.004	-9.2	0.25
K042-2	953	947	1110	26	979	—	—	—	—
K047-2	1106	1077	1157	16	1070	—	—	—	—
*K049-1	815	813	1113	24	891	—	0.249 ± 0.005	-13.3	-0.17
K050A-1	812	799	—	—	954	0.91	—	—	—
*K067-1	995	989	1152	19	870	-	—	—	—
FJ167-2	968	952	—	—	1038	0.16	0.263 ± 0.006	-10.7	0.05
*FJ181	1066	1054	1659	22	862	—	—	—	—
FJ188-1	1185	1160	1217	24	989	0.03	—	—	—
FJ185-1	949	941	1224	38	963	—	0.276 ± 0.006	-10.3	0.58
*FJ205	632	614	1272	56	793	—	—	—	—
<i>Lherzolites <Fo_{89.5}</i>									
K045	1108	1092	1264	7	1121	0.44	—	—	—
*K050A-2	878	966	—	—	900	—	—	—	—
FJ167-3	954	916	—	—	1022	0.07	0.301 ± 0.006	-11.0	0.30
FJ185-2	999	970	1251	19	1067	0.75	—	—	—
FJ188-2	1043	1013	1217	24	1009	—	—	—	—
FJ190A-1	1028	1006	1177	8	1002	0.53	—	—	—
<i>Harzburgites</i>									
K048A-2	860	865	—	—	844	—	—	—	—
FJ063	676	650	1170	5	904	—	—	—	—
FJ186	733	740	1564	7	815	—	—	—	—
<i>Dunites</i>									
K008	—	—	—	—	880	—	—	—	—
K159	833	810	1342	29	929	—	—	—	—
FJ024	—	—	—	—	789	—	—	—	—
<i>Wehrlites</i>									

K014-1	1012	1003	—	—	983	—	—	—	—
K046	—	—	—	—	1175	—	—	—	—
K047-1	1074	1018	—	—	1094	—	—	—	—
FJ194	1003	964	—	—	1001	—	—	—	—

$T_{[BKN]}$ = two-pyroxene thermometer from Brey & Köhler (1990); $T_{[Ta98]}$ = two-pyroxene thermometer from Taylor (1998); $T_{[REE]}$ = two-pyroxene thermometer from Liang *et al.* (2013); $T_{[Al-in-ol-spl]}$ = Al between olivine and spinel thermometer from Wan *et al.* (2008). $P_{[KB]}$ = Ca-in-olivine / Ca-in-clinopyroxene barometer from Köhler & Brey (1990) using temperatures from $T_{[Al-in-ol-spl]}$. Preset pressure of 1.5 GPa is used for fO_2 and FMQ calculations. Peridotites that fall outside the 950–1250 °C calibration range for $P_{[KB]}$ D'Souza *et al.* (2020) are omitted.

the same sample, and have a significant affect on the calculated pressures. The Ca-exchange reaction between olivine and clinopyroxene is temperature sensitive (e.g., McDonough & Rudnick, 1998), and Ca in olivine can be easily reset during various metasomatic processes (e.g., xenolith emplacement). In order to use this geobarometer with more confidence and account for metasomatic processes, Ca concentrations in multiple olivine grains were measured within each xenolith to identify anomalously high olivine Ca concentrations, to exclude them from the P_{KB} calculations. Additionally, pressures were only calculated for lherzolites as the P_{KB} geobarometer was developed for clinopyroxene-saturated systems with olivine contents $\sim\text{Fo}_{90}$, however, observed disequilibrium textures between olivine and clinopyroxene also present similar challenges for lherzolites. Some lherzolites with lower calculated pressures also contain traces of plagioclase (e.g., sample K049-1) and hence may reflect relatively accurate estimates.

2.5.4.3. Oxygen fugacity

Calculated $\Delta\log f\text{O}_2$ measured in five Koro lherzolites (Table 2.5) range between -0.17 to +0.58 log units relative to the FMQ buffer (O'Neill, 1987). Koro lherzolites were also compared to averages from arc peridotite xenoliths (Bénard *et al.*, 2018) that give $f\text{O}_2$ values ranging from +0.04 to +1.68 log units relative to FMQ, reflecting the more oxidised mantle conditions of most arc settings. $\Delta\log f\text{O}_2$ values calculated in the Koro peridotites are less oxidised than typical forearc peridotites, however, they show some overlap with the least oxidized forearc peridotites. Measured spinel $\text{Fe}^{3+}/\Sigma\text{Fe}$ vs. Cr# contents in the Koro peridotites are distinct from typical oceanic mantle recorded in abyssal peridotites (Fig. 2.15) due to the unusually high Fe^{3+} contents in Koro spinels, but the Koro peridotite field does overlap with subduction-related xenoliths in general and are distinct from abyssal peridotite spinels.

2.5.5. $^{187}\text{Os}/^{188}\text{Os}$ and HSE signatures

Twenty-six peridotite xenoliths were analysed for their Os isotope ratios and HSE abundances (Table 2.6). $^{187}\text{Os}/^{188}\text{Os}$ ratios are between 0.1201 to 0.1326, spanning the range of Os isotope ratios observed in peridotites from typical oceanic mantle (e.g., Becker & Dale, 2016) and extending to slightly more radiogenic Os isotope compositions observed in fore-arc peridotites (e.g., Brandon *et al.*, 1996; McInnes *et al.*, 1999). HSE concentrations range between Os = 0.015–13.4 ppb, Ir = 0.076–3.27 ppb, Ru = 0.063–10.4 ppb, Pt = 0.982–5.31 ppb, Pd = 1.02–41.9 ppb,

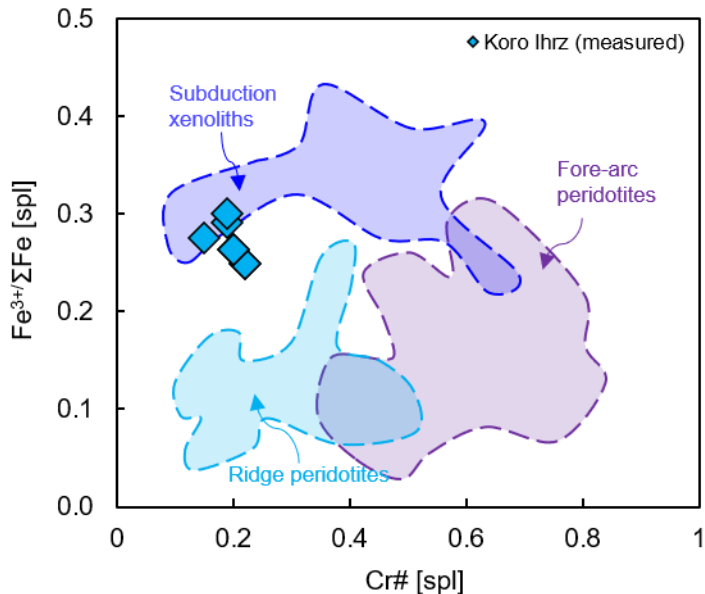


Figure 2.15. Spinel $\text{Fe}^{3+}/\Sigma\text{Fe}$ ratios measured by Mössbauer spectroscopy (see Appendix 1 for Mössbauer spectra) for select Koro Iherzolites (K041-2, K049-1, FJ167-2, FJ167-3, and FJ185-1). Fields for subduction peridotites, fore-arc peridotites and ridge peridotites are from Birner *et al.* (2017 and references there-in).

and Re 0.004–0.21 ppb. Some of these Os concentrations are considerably lower than those expected for bulk peridotites (e.g., Pearson *et al.*, 2004). Chondrite-normalized HSE patterns for the Koro peridotites (Figs. 2.16a–c) do not show typical trends associated with melt depletion (i.e., P-PGE group depletion relative to I-PGE group) (Crocket, 1979; Barnes *et al.*, 1986; Pearson *et al.*, 2004; Aulbach *et al.*, 2014). Excluding the outliers highlighted in Fig. 2.16a, the Koro peridotites show little PGE inter-element fractionation other than a slight Pt depletion and minor Pd enrichment. This pattern is consistent across both Iherzolites, harzburgites and wehrellites, indicating that PGE fractionation is not controlled by lithology or apparent level of major element depletion. Koro peridotites have a similar overall PGE pattern to both abyssal and OIB peridotites (Fig. 2.16b) with a slightly more pronounced Pt depletion, possibly related to the presence of the minor pentlandite which typically has a strong negative Pt anomaly (e.g., Luguet & Pearson, 2019).

Table 2.6: Os isotopes and HSE abundances in Koro peridotite xenoliths

Sample	Rock type	Fo[ol]	Cr# [spl]	Al ₂ O ₃ wt. %	¹⁸⁷ Os/ ¹⁸⁸ Os	Abs. 2σ	Os (ppb)	Abs. 2σ	¹⁸⁷ Re/ ¹⁸⁸ Os	Abs. 2σ	T _{RD} (Ma)
<i>Lherzolites ≥Fo_{89.5}</i>											
K011-1	Lhrz (± pl)	90.2	31.0	1.6	0.1251	0.0006	13.44	0.12	0.0099	0.0015	447
K041-2	Lhrz	89.8	19.1	2.1	0.1201	0.0008	3.43	0.04	0.0461	0.0052	1153
K042-2	Lhrz	90.1	18.7	2.2	0.1261	0.0002	1.84	0.02	0.1775	0.0071	–
K048A-2	Lhrz	90.2	24.9	1.7	0.1261	0.0006	1.77	0.02	0.1736	0.0043	–
K049-1	Lhrz	90.1	22.0	1.8	0.1273	0.0003	0.27	0.01	2.7439	0.1144	–
K050A-1	Lhrz	90.4	24.5	1.4	0.1306	0.0004	1.67	0.01	0.3588	0.0129	–
K067-1	Lhrz	90.1	25.9	2.0	0.1276	0.0002	2.04	0.02	0.0656	0.0016	–
FJ167-2	Lhrz	89.7	19.7	2.6	0.1265	0.0002	1.80	0.02	0.1774	0.0044	–
FJ181	Lhrz	90.1	26.0	1.5	0.1230	0.0002	3.63	0.03	0.1588	0.0119	743
FJ185-1	Lhrz	90.2	19.0	2.5	0.1259	0.0006	2.73	0.03	0.2674	0.0076	338
FJ188-1	Lhrz	89.5	16.4	2.1	0.1273	0.0003	1.96	0.02	0.0738	0.0018	–
FJ205	Lhrz	90.2	21.9	2.0	0.1274	0.0002	1.49	0.01	0.5830	0.0167	–
<i>Lherzolites <Fo_{89.5}</i>											
K015A-2	Lhrz	88.0	22.1	1.7	0.1245	0.0006	1.98	0.02	–	–	539
K047-2	Lhrz	87.9	18.2	1.9	–	–	–	–	–	–	–
K050A-2	Lhrz	89.0	28.3	1.4	0.1266	0.0004	3.22	0.03	0.11	0.0092	–
FJ167-3	Lhrz	89.4	20.9	2.2	0.1275	0.0002	1.67	0.01	0.0981	0.0024	–
FJ188-2	Lhrz	89.3	21.3	2.6	0.1275	0.0004	1.66	0.01	0.2581	0.0065	–
FJ190A-1	Lhrz	88.7	20.8	2.4	0.1292	0.0081	0.02	0.01	7.1616	2.8777	–
<i>Harzburgites</i>											
FJ063	Hrz (± cpx)	90.0	50.7	0.9	0.1214	0.0006	0.68	0.01	0.0260	0.0011	979
FJ186	Hrz (± cpx)	90.3	45.8	0.9	0.1268	0.0003	1.68	0.01	0.2221	0.0089	–
<i>Dunites</i>											
K008	Dun (± cpx)	91.2	55.7	0.7	0.1326	0.0002	0.32	0.01	0.1334	0.0261	–
FJ024	Dun (± cpx)	90.0	30.2	0.2	0.1285	0.0002	6.42	0.05	0.0461	0.0012	–
<i>Wehrlites</i>											
K014-1	Whr	85.7	21.9	1.8	0.1290	0.0004	2.38	0.02	0.4161	0.0118	–
K046	Whr	87.6	24.1	0.9	0.1307	0.0005	2.26	0.02	0.0362	0.0037	–

K048A-1	Whr (\pm aug pl)	85.1	23.5	1.5	0.1274	0.0004	1.99	0.02	0.1876	0.0156	–
FJ194	Whr (\pm pl)	85.7	13.1	2.0	0.1276	0.0005	1.91	0.02	0.1393	0.0034	–

Table 2.6: Continued

Sample:	Ir (ppb)	Abs. 2 σ	Ru (ppb)	Abs. 2 σ	Pt (ppb)	Abs. 2 σ	Pd (ppb)	Abs. 2 σ	Re (ppb)	Abs. 2 σ	(Pt/Pd) _N	(Pt/Ir) _N	(Os/Ir) _N
<i>Lherzolites $\geq F_{O_{89.5}}$</i>													
K011-1	2.04	0.09	4.77	0.15	5.40	0.22	4.27	0.15	0.03	0.00	0.74	0.97	5.92
K041-2	2.40	0.09	5.48	0.16	4.37	0.15	2.02	0.05	0.03	0.00	0.43	0.39	1.28
K042-2	—	—	—	—	—	—	—	—	—	—	—	—	—
K048A-2	2.46	0.12	4.43	0.10	5.19	0.16	2.14	0.06	0.06	0.00	0.38	0.40	0.65
K049-1	0.50	0.01	0.50	0.01	3.72	0.10	2.06	0.06	0.15	0.00	1.69	3.40	0.48
K050A-1	1.49	0.04	3.86	0.09	3.88	0.11	2.04	0.06	0.12	0.00	0.49	0.63	1.01
K067-1	2.59	0.17	5.47	0.13	6.48	0.25	3.30	0.10	0.03	0.00	0.48	0.59	0.71
FJ167-2	2.29	0.07	4.31	0.10	4.32	0.13	1.64	0.04	0.07	0.00	0.35	0.33	0.71
FJ181	2.83	0.14	5.52	0.17	6.13	0.26	2.33	0.07	0.12	0.01	0.35	0.38	1.15
FJ185-1	2.62	0.08	4.25	0.11	5.14	0.17	1.75	0.05	0.15	0.00	0.32	0.31	0.93
FJ188-1	2.19	0.06	4.41	0.11	5.98	0.20	2.04	0.06	0.03	0.00	0.32	0.43	0.80
FJ205	2.12	0.06	4.37	0.11	5.94	0.20	2.48	0.07	0.18	0.00	0.39	0.54	0.63
<i>Lherzolites $< F_{O_{89.5}}$</i>													
K015A-2	1.66	0.07	4.01	0.13	4.88	0.18	1.47	0.04	<LOD	—	0.28	0.41	1.07
K047-2	1.05	0.04	2.36	0.05	1.49	0.05	1.36	0.04	<LOD	—	1.03	0.66	0.00
K050A-2	—	—	—	—	—	—	—	—	—	—	—	—	—
FJ167-3	1.73	0.05	3.90	0.09	4.32	0.13	2.23	0.07	0.03	0.00	0.48	0.59	0.87
FJ188-2	1.81	0.05	3.79	0.09	3.61	0.10	1.72	0.05	0.09	0.00	0.44	0.44	0.82
FJ190A-1	0.08	0.02	0.06	0.00	2.18	0.06	5.31	0.13	0.02	0.00	2.28	32.01	0.18
<i>Harzburgites</i>													
FJ063	1.44	0.04	0.66	0.03	3.32	0.09	0.98	0.02	0.00	0.00	0.28	0.31	0.42
FJ186	3.27	0.08	4.16	0.10	9.38	0.28	2.16	0.06	0.08	0.00	0.21	0.30	0.46
<i>Dunites</i>													
K008	0.27	0.01	0.72	0.02	1.36	0.03	1.02	0.03	0.01	0.00	1.25	2.30	1.06
FJ024	2.33	0.07	10.42	0.40	8.35	0.34	2.45	0.07	0.06	0.00	0.27	0.48	2.47
<i>Wehrlites</i>													
K014-1	2.17	0.07	5.57	0.13	6.67	0.24	4.21	0.14	0.21	0.01	0.59	0.89	0.99
K046	2.42	0.07	5.11	0.12	4.04	0.12	2.17	0.06	0.02	0.00	0.50	0.41	0.84
K048A-1	1.66	0.07	3.67	0.12	3.93	0.14	1.62	0.04	0.08	0.01	0.38	0.45	1.07
FJ194	1.88	0.06	3.72	0.08	4.90	0.15	1.06	0.03	0.06	0.00	0.20	0.26	0.91

T_{RD} ages calculated using O-chondrite values from Walker *et al.* (2002). T_{RD} ages corresponding to $^{187}\text{Os}/^{188}\text{Os}$ ratios above O-chondrite (i.e., negative ages) are omitted.

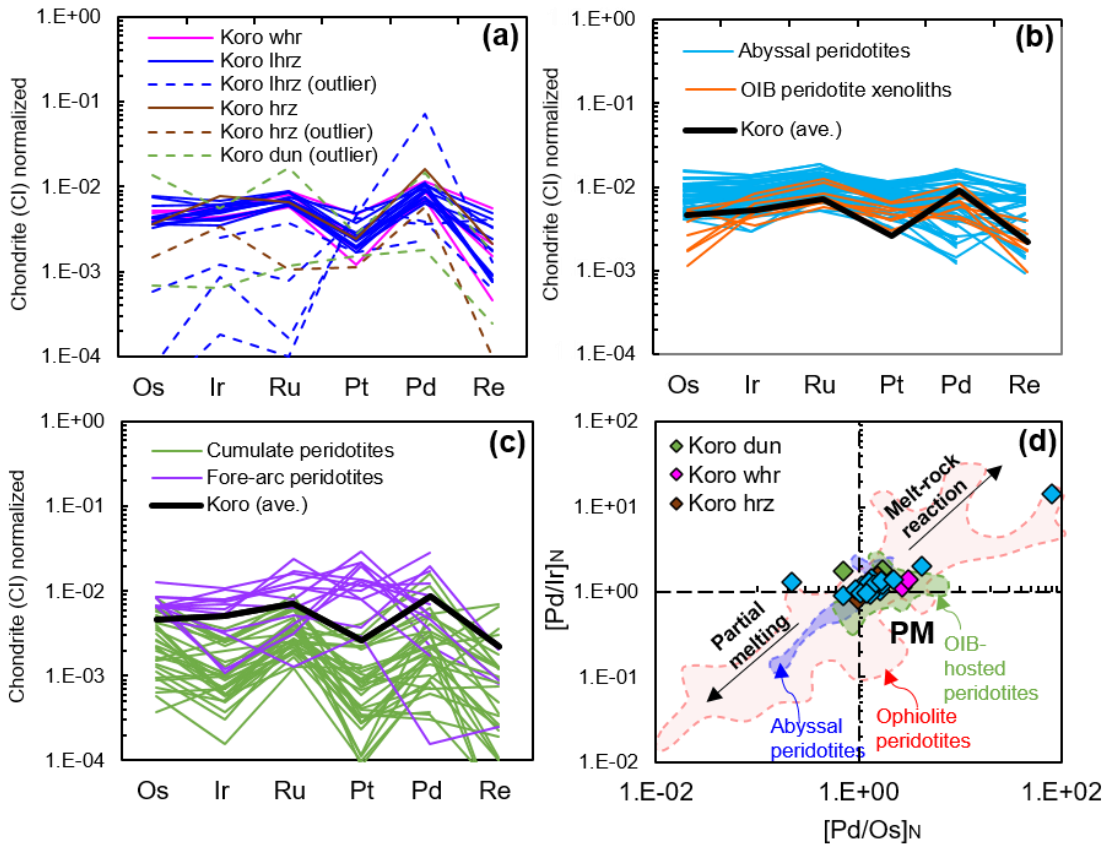


Figure 2.16. (a) Chondrite normalized PGE abundances in Koro peridotites. Outliers denoted by dashed lines resemble samples K042-2, FJ190A-1, K049-1, FJ063, K008, K047-1, and FJ024 that do not follow the uniform PGE pattern observed in the Koro peridotites. (b) Koro average PGE abundances (excluding outliers) plotted against abyssal peridotites (Luguet *et al.*, 2003; Liu *et al.*, 2009; Day *et al.*, 2017) and OIB-hosted peridotite xenoliths (Snortum *et al.*, 2019). (c) Koro average (again excluding outliers) plotted against cumulate peridotite xenoliths (Peters *et al.*, 2016) and fore-arc peridotite xenoliths (McInnes *et al.*, 1999; Widom *et al.*, 2003; Kepezhinskas *et al.*, 2002). (d) Shows $[Pd/Ir]_N$ vs. $[Pd/Os]_N$ relationships with partial melt and melt-rock reaction vectors from Lian *et al.* (2018).

Cumulate and fore-arc peridotites (Fig. 2.16c) on the other hand show significantly greater inter-element PGE fractionation compared to the Koro peridotites. Cumulate peridotites are typically characterized by $[Os/Ir]_N$ fractionation displayed as a negative Ir anomaly and a strong negative Pt anomaly. Fore-arc peridotites often have a positive Pt anomaly (Fig. 2.16c), but their PGE patterns are very variable. $[Pd/Ir]_N$ vs. $[Pd/Os]_N$ ratios excluding the “outlier” samples vary from PM-like compositions to predominantly higher Pd/Ir ratios, in the “metasomatism” field, (Fig. 2.16d), i.e., they lack the low Pd/Ir indicative of melt depletion that characterises some ophiolite and abyssal peridotites. Koro Os/Ir ratios scatter both above and below the PM value. Overall, the Koro Pd-It-Os fractionations are most similar to the systematics observed in mantle peridotites found in other OIB.

2.6. DISCUSSION

2.6.1. *Residual origin for Koro peridotite xenoliths*

Peridotite xenoliths of both mantle and non-mantle origin have been recorded in OIB-hosted lavas from various oceanic settings globally (e.g., Clague, 1988; Sen *et al.*, 1993). It is therefore necessary to identify the proportion of Koro peridotites that represent either: 1) fragments of mantle (i.e., peridotite residues after melting), 2) cumulates that formed via crystal accumulation in the lowermost oceanic crust, or 3) glomerocrysts that crystallized directly from the host basalt (i.e., volcanic olivine). In the previous sections it was established that the Koro peridotite suite is made up of both Group I Cr-diopside xenoliths and Group II Al-augite xenoliths, using the classification of Wilshire & Shervais (1973) and Frey & Prinz (1978). Wilshire & Shervais (1973), here after WS73, interpreted Group II peridotites as cumulate in origin based on their compositions and textures. The lack of intercumulus spinel observed in dunite cumulates (e.g., O'Driscoll *et al.*, 2010) and the presence of spinel symplectite textures observed in most lherzolites, interpreted as garnet breakdown products (e.g., Green & Burnley, 1988), are not typical of WS73 classified cumulates. Furthermore, olivines observed in some wehrlites, including the chadacryst-like olivines that would typically be associated with a cumulate origin, contain relict orthopyroxene (Figs. 2.3c & 2.3d), and are found in association with olivines containing subgrains, a feature that is characteristic of residual upper mantle tectonites (see Chapter 3). First-row transition metals (FRTE: Al, Ti, Ni, Ca, V, and Co) in olivine from the Koro peridotites (Fig. 2.9) were also

considered to determine if the Koro peridotites are mantle-derived, however, show considerable overlap with both the estimated range from mantle olivines and classified dunite cumulates (e.g., Peters *et al.*, 2016), making it difficult to determine if xenoliths are mantle-derived on this basis. Despite this, the median FRTE values in olivine from the Koro lherzolites, dunites and harzburgites fall within the mantle olivine range, however, the Al, Ti and Ca contents in olivine from wehrlites that are slightly higher than mantle olivine, probably reflect metasomatic enrichments. Based on petrographic evidence and geochemical differences (e.g., olivine Fo vs. spinel Cr#; Fig. 2.5) to cumulate peridotites from other locations (classified using the WS73 criteria), the Koro peridotites in this study, excepting wehrlite K048A-1, are characteristic of variably metasomatized peridotite mantle residues.

2.6.1.1. Extent of melt-depletion based on geochemical modelling

Estimating the amount of melt depletion experienced by the Koro peridotites is challenging due to varying amounts of metasomatism super-imposed on these mantle residues. Major elements in peridotite can be compared to various melting experiments to estimate the degree of melt depletion. However, this may be misleading due to melt-rock interaction that can also influence these geochemical signatures (e.g., Kelemen *et al.*, 1992; 1995). This is illustrated by spinel Cr#-TiO₂ relationships (Fig. 2.17a) that show that Koro harzburgites and dunites that have the most apparent melt depletion in terms of their whole-rock major elements, have been overprinted by magma interaction resulting in elevated Cr# and Ti in spinel contents. This magma interaction process is distinct from the wehrlite producing metasomatism shown by the Ti chemistry in both spinel and clinopyroxene (Fig. 2.17b) that will be discussed below. Extent of melting using olivine Fo content and spinel Cr#, and excluding dunites and harzburgites, as estimated using the 1–2 GPa trend from Arai (1994) in Fig. 2.5, yielding melt fraction estimates between ~5% to <25% that are comparable to partial melt estimates from whole-rock Al and Ca abundances (Fig. 2.6). These estimates are also similar, or slightly higher than estimates based on partial melting experiments at 1.5–2.6 GPa (Walter, 1998) and 3–5 GPa (Baker & Stolper, 1994) ranging between <4% and 21%, and melt fraction estimates based on HREE in clinopyroxene (Hellebrand *et al.*, 2001) that range between ~4.5 % to ~18% (Figs. 2.18a & 2.18b). The average spinel Cr# (0.23) and olivine Fo contents (Fo_{89.8}) in the Koro lherzolites correlate to low-degrees of partial melting of around 9 % and 4 % respectively based on these melt experiments.

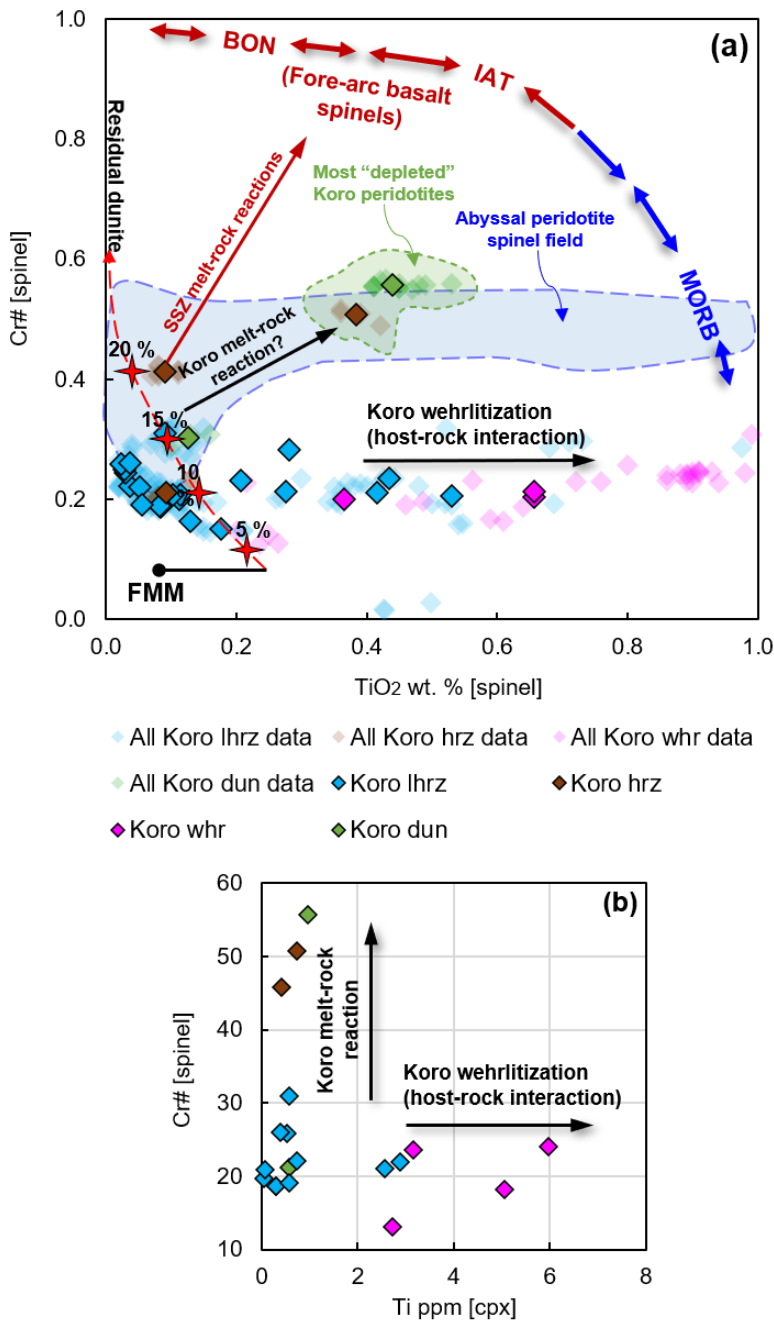


Figure 2.17. (a) Spinel Cr# vs. spinel TiO_2 wt. % relationships in the Koro peridotites to assess partial melting vs. melt-rock reaction. Boninite (BON), island arc tholeiite (IAT) and mid ocean ridge basalt (MORB) regions represent the tectonic setting of the reacting melts based on volcanic spinel compositions adapted from Pearce *et al.* (2000). Fertile MORB mantle (FMM) and the modelled anhydrous partial melting trend (red) from Johnson *et al.* (1990). Dashed blue line represents outlined field for abyssal peridotites from Dick & Bullen (1984). (b) Shows a similar behaviour in the Koro peridotites when spinel Cr# is plotted against Ti in clinopyroxene (cpx).

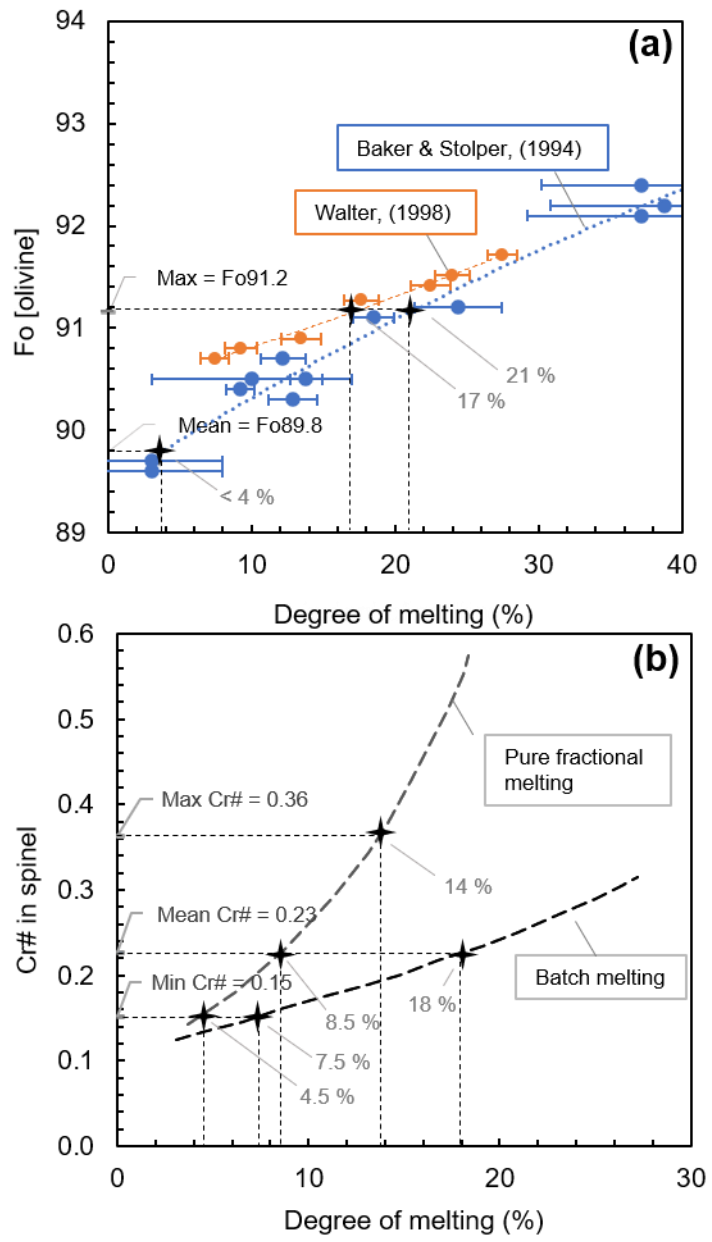


Figure 2.18. Estimates for degree of melting based on olivine Fo content and spinel Cr# in the Koro peridotites based on where these values intersect “best-fit” lines from anhydrous partial melting experiments from (a) Walter (1998) calibrated between 1.5–2.6 GPa, Baker & Stolper (1994) calibrated between 3–5 GPa, and (b) Hellebrand *et al.* (2001) for pure fractional melting and batch melting calibrated from HREE in cpx for spinel Cr# values between 0.10 and 0.60. $Fo_{91.2}$ = maximum olivine Fo value in the Koro peridotites (dunite K008) and $Fo_{89.8}$ = average olivine Fo value in Koro Iherzolites. Cr# 0.15 and Cr# 0.36 represent minimum and maximum spinel Cr# values in Koro Iherzolites respectively.

Extents of melting modelled from whole-rock, olivine and orthopyroxene HREE abundances (Figs. 2.7, 2.10, & 2.13), yield similar melt-estimates to their major elements. LREE in olivine and orthopyroxene, along with REE in clinopyroxenes were not considered for melt estimates as most reflect metasomatic overprinting and originated either wholly or partially from a metasomatic melt. HREE in orthopyroxene (Fig. 2.13) plot above the starting DM compositions from Salters & Strake (2004), possibly due to slightly underestimated starting DM values if it is assumed that metasomatism has little effect on HREE. Melt fraction estimates using HREE in olivine, particularly Er, Yb, Lu, from Fig. 2.10 are probably more reliable than orthopyroxene, and generally range between ~5% to <25%, with most peridotites <10 %. These estimates are consistent with the Koro peridotites being sourced from relatively shallow oceanic mantle depths, subjected to relatively small amounts of adiabatic upwelling, prior to their incorporation in the oceanic lithosphere beneath Koro. Some HREE in Koro olivines gave higher concentrations than depleted mantle compositions, particularly in dunites and wehrellites (Figs. 2.10d & 2.10e), consistent with the metasomatic origin of the wehrellites and providing a strong indication that the dunites are not melting residues.

2.6.1.2. Timing of melt-depletion and PGE–Os isotope systematics

PGE (Os, Ir, Ru, Pt, Pd) and Os isotopes systematics can provide a robust means of determining the timing of melt depletion in mantle-derived peridotites due to the highly siderophile nature of PGE and compatible behaviour of Os relative to Re during partial melting (e.g., Pearson *et al.*, 2003). The Koro peridotite PGEs, excluding outlier-samples with highly irregular PGE patterns, display a negative Pt anomaly, Pd enrichment, and flat I-PGE (Os, Ir, Ru) to P-PGE (Pt, Pd) patterns similar to those of oceanic mantle peridotites that contain secondary pentlandite and pyrrhotite phases formed through melt refertilization by sulfur(S)-saturated melts (e.g., Luguet *et al.*, 2001; Luguet *et al.*, 2003), assuming that base metal sulfides (BMS), when present, are the dominant controls on whole-rock PGE in peridotites (e.g., Alard *et al.*, 2000; Luguet *et al.*, 2001; Luguet & Lorand, 2016; Luguet & Pearson, 2019). PGE patterns in the Koro peridotites, therefore, do not reflect the partial melting process. The negative Pt anomalies may be explained by the presence of pentlandite and pyrrhotite that form by means of low temperature re-equilibration of mono-sulfide solid solution (MSS), as neither sulfide phases withhold Pt in their crystal structure (e.g., Ballhaus & Sylvester, 2000). As long as a complimentary Pt-bearing phase is not precipitated (e.g., Wainwright *et al.*, 2016; Lorand & Luguet, 2016) or has been effectively removed (e.g.,

Hughes *et al.*, 2016), the Pt anomaly should be inherited by the whole-rock peridotite signature. While negative Pt anomalies are slightly more pronounced in the Koro peridotites compared to abyssal peridotites, broad similarities in their chondrite-normalized PGE patterns suggest similar sulfide behaviour to the normal oceanic mantle lithosphere. What is not observed in the abyssal PGE patterns (e.g., Luguet *et al.*, 2003; Liu *et al.*, 2009; Day *et al.*, 2017; Fig. 2.16b) are the highly variable PGE abundances that are observed in several Koro peridotites (see Fig. 2.16a). Unlike the very consistent PGE patterns observed in abyssal peridotites, fore-arc peridotites show significant PGE disturbance and large variations in Ir, Ru, and Pd similar to some of the Koro peridotites. This could provide some evidence that the Koro peridotites have undergone some PGE fractionation/loss via interaction with oxidised subduction-related melts. Os and Ir abundances in fore-arc peridotites (Fig. 2.16c) are higher than the unusually low abundances observed in the Koro peridotites, which are more similar to some subduction-related ophiolite peridotites (see Chapter 3). In the Koro suite, the low Os and Ir abundances and highly irregular PGE patterns include dunite K008 and harzburgite FJ063 that have amongst the most disturbed spinel Cr#-Ti systematics (Fig. 2.17), however, not all peridotites that record PGE disturbances show elevated Ti in spinel abundances, suggesting that interaction with multiple metasomatic melts, some that are sulfide saturated, and some that are sulfide under-saturated, may cause sulfide dissolution and removal / fractionation of I-PGEs. The four wehrlites measured for PGEs in this study do not show any clear PGE disturbances as observed in the “outlier” peridotites from Fig. 2.16a. These wehrlite PGE patterns are indistinguishable from the general patterns shown by most lherzolites, suggesting there is no correlation between PGE removal and wehrlite formation.

Koro peridotites do not show any relationship between $^{187}\text{Os}/^{188}\text{Os}$ and melt depletion indices, such as whole-rock Al_2O_3 , or PGE concentrations (Fig. 2.19). This shows that there is no single melting event that can be related to the Os isotope variability of these peridotites. Instead, these observations provide evidence that PGE fractionation and $^{187}\text{Os}/^{188}\text{Os}$ is controlled by the presence of metasomatic sulfides that formed relatively recently, perhaps during host melt infiltration (giving little time for radiogenic Os to develop), or influenced by recent sulfide loss during dissolution by oxidizing metasomatic melts, which would also decouple PGE signatures from Os isotope ratios. Koro peridotites have a tightly clustered mean $^{187}\text{Os}/^{188}\text{Os}$ ratio of 0.1269 ± 0.0027 , with most of their ratios being very close to “chondritic” ratios (Meisel *et al.*, 2001; Becker *et al.*, 2006), and overlap with the peak in modern oceanic mantle ratios shown by abyssal

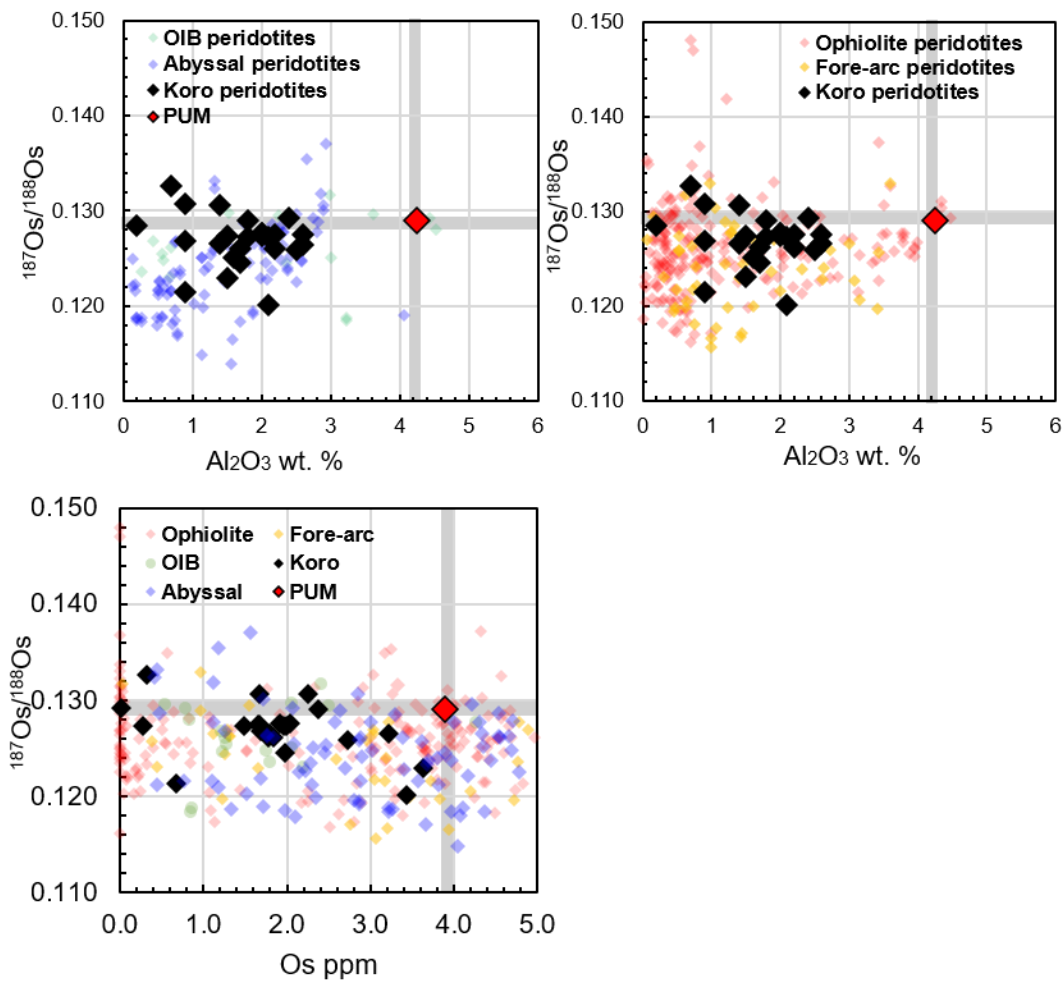


Figure 2.19. (a) and (b) Whole-rock $^{187}\text{Os}/^{188}\text{Os}$ vs. Al_2O_3 wt. % relationships in Koro peridotites plotted against peridotites from OIB-hosted peridotites and abyssal peridotites in (a), and ophiolite and fore-arc peridotites in (b) (see references in Appendix 6). (c) Shows whole-rock $^{187}\text{Os}/^{188}\text{Os}$ vs. Os relationships plotted against OIB-hosted, abyssal, ophiolite, and fore-arc peridotites.

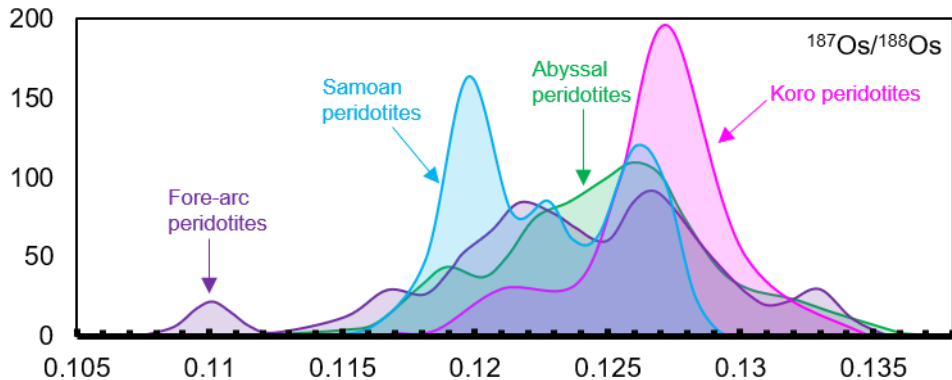


Figure 2.20. Gaussian kernel density estimates for $^{187}\text{Os}/^{188}\text{Os}$ ratios in Koro peridotites (pink) plotted against OIB-hosted Samoan peridotite xenoliths from Jackson *et al.* (2016) (light blue), abyssal peridotites (green), and fore-arc peridotites (purple). References for abyssal and fore-arc peridotites data in Appendix 6.

peridotites, and the most recent peak from fore-arc peridotites and Samoan peridotite xenoliths (Jackson *et al.*, 2016) (Fig. 2.20). The lower $^{187}\text{Os}/^{188}\text{Os}$ ratios from the Koro suite (Table 2.5), resemble, at a lower proportion, the unradiogenic Os isotope signature observed in global modern oceanic mantle (Pearson *et al.*, 2007), that equates to a melt-depletion age of ~1 to 1.3 Ga. The Koro suite does not record any sign of the very unradiogenic values (i.e., $^{187}\text{Os}/^{188}\text{Os} < 0.12$) that have been observed in abyssal peridotites (e.g., Standish *et al.*, 2002; Harvey *et al.*, 2006; Liu *et al.*, 2009), and occasionally in OIB-hosted and fore-arc peridotites (e.g., Parkinson & Pearce 1998; Schaefer *et al.*, 2002). The presence of the “Mesoproterozoic component” identified by Pearson *et al.* (2007) is not related to the formation of the lithospheric block beneath eastern Fiji but is a ubiquitous component, dispersed in Earth’s convecting mantle, that is part of the spectrum of isotopic heterogeneity retained by this reservoir due to past major melt extraction events. The Os isotopic variability in the Koro peridotites thus reflects a combination of signatures inherited from the convecting mantle plus signatures imposed by metasomatic sulfide saturated melts that may have modified the original compositions, to more chondritic values, and therefore it is not possible to define a single melt-depletion event for the lithospheric mantle.

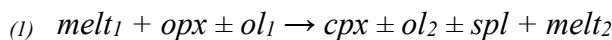
2.6.2. Refertilization/metasomatism of the Koro lithosphere

2.6.2.1. Formation of wehrlites

The Koro wehrlites and some lherzolites reflect extensive metasomatism that causes notable deviation from the mantle depletion trend (i.e., OSMA; Arai, 1994), easily distinguished from the

cumulate trends evident in mineral chemistry, e.g., via significantly lower spinel Cr# contents (Figs. 2.5 & 2.17a). The Koro wehrlites in this study consist of two types: 1) lower crustal or MOHO transition zone (MTZ) wehrlites, and 2) mantle wehrlites that occur within the mantle portion of the lithosphere (e.g., Arai & Takemoto, 2007). An example of a MTZ wehrlite is sample K048A-1 that contains trace amounts of plagioclase and an Al- Ti-rich augite vein (containing Al-spinel) that likely represents a precipitated late-stage melt that cross-cut the diopside-bearing wehrlite, indicating that this sample was in close proximity to the gabbroic lower crustal portion of the MTZ. Incompatible element enrichments in clinopyroxene along with the trace amounts of plagioclase observed in wehrlites have also been ascribed in other peridotite suites to melt-rock interaction in the MTZ (e.g., Whattam *et al.*, 2011). This could be the case for other Koro wehrlites and some Koro lherzolites that record trace amounts of plagioclase (e.g., samples FJ194 and K011-1), however, without any indication that these peridotites interacted with the lower crust (such as the augite vein), the presence of plagioclase could also be explained via metasomatic introduction of plagioclase at deeper mantle depths (e.g., Rampone *et al.*, 1998). All wehrlites are confined to olivine Fo contents <Fo₈₈ and show textural evidence for clinopyroxene infiltration accompanied by high Zr, Ti, Ga, Y, V, HREE in clinopyroxene and trace amounts of relict orthopyroxene consistent with a process of orthopyroxene dissolution. Similar clinopyroxene textures have also been observed in peridotite xenoliths that experienced extensive silicate melt infiltration (e.g., Zinngrebe & Foley, 1995; Glaser *et al.*, 1999).

Within the Koro wehrlites, clinopyroxene trace element systematics, e.g., [La/Yb]_N vs. Ti/Eu (Fig. 2.11) indicate that the metasomatic melt responsible for wehrlitization was predominantly a small-degree silicate melt rather than the carbonatite melts invoked at other oceanic islands (including the SW Pacific) or continental lithosphere (e.g., Hauri *et al.*, 1993; Rudnick, 1993; Yaxley *et al.*, 1998), though a small number of Koro wehrlites indicate more carbonatitic affinities. Most-likely the melts could have been in the “silico-carbonatite” compositional spectrum. The predominant metasomatic melt must have been saturated in olivine and clinopyroxene, and present at high enough melt/rock ratio to replace most orthopyroxene in the residual peridotite protolith via a reaction such as that suggested by Neumann *et al.* (1995):



to describe metasomatism resulting in the formation of wehrlites in peridotite xenoliths from the Canary Islands. In the Koro wehrlite suite, the metasomatic process linked to wehrlite formation

resulted in the growth of secondary olivine and orthopyroxene dissolution by melt-rock interaction similar that proposed by Neumann *et al.* (1995) who invoked reaction between a residual peridotite wall-rock and a pyroxene-undersaturated melt (e.g., Quick, 1981; Kelemen, 1990). Remnant, partially reacted orthopyroxene in the Koro wehrlites and similar clinopyroxene REE patterns in both lherzolites and wehrlites in Figs. 2.13a & 2.13e suggest this reaction has not gone to completion beneath Koro. A similar process has been described for wehrlite xenoliths sampled from the northern Pannonian Basin (Patkó *et al.*, 2019). These wehrlites were interpreted to have formed via asthenosphere derived silicate metasomatism and subsequent orthopyroxene dissolution related to their host basalt volcanism. Host magma interaction would also explain why abyssal peridotites, that are not transported via basalts to the surface, do not follow the wehrlitization trend observed in the Koro peridotites and other OIB-hosted peridotites (Figs. 2.5 & 2.17a). Lastly, the metasomatic melt-rock reaction process described above provides evidence for a wehrlite origin that differs from a typical cumulate origin in the MTZ. It is therefore inferred that the Koro wehrlites, excepting the augite-bearing wehrlite (K048A-1), are mantle derived xenoliths that have been severely modified by silicate metasomatism.

2.6.2.2. Additional metasomatic processes

While it is established that Koro wehrlites and some lherzolites that follow a “wehrlitization” trend described above formed via host-rock interaction, resulting in Ti partitioning from clinopyroxene into Cr-spinel, the Koro dunites and harzburgites with more depleted spinel Cr# chemistry (Fig. 2.17a), show evidence for interaction with melts that are distinct from melts that produced the wehrlites. This is shown by Cr#-Ti relationships (Figs. 2.17a & 2.17b), where the Koro wehrlites with high spinel Cr# do not co-exist with high Ti in spinel or Ti in clinopyroxene, signifying two separate processes, or a buffering effect on the Cr/Al ratio where Cr is sequestered into Cr-diopside that crystallizes elsewhere in the peridotite. This indicates that wehrlitization is not the only metasomatic processes to affect these xenoliths, and the Koro peridotites resemble fragments of modified mantle residues that have undergone at least two separate processes of melt-rock interaction.

Clinopyroxene and orthopyroxene REE patterns from Fig. 2.13 can be used to gain a better insight into what these processes could be. At least four distinct REE patterns in clinopyroxene are recognized in these samples in Fig. 2.13: 1) clinopyroxene characterized by a HREE to MREE depletion with a sharp LREE enrichment “kick” from Sm to La (Fig. 2.13a), 2) clinopyroxene

containing LREE enrichments and marked positive Eu anomalies that are similarly observed in orthopyroxene (Fig. 2.13b), 3) patterns with a systematic increase in HREE to LREE abundances that are in disequilibrium with residual orthopyroxene (e.g., Figs. 2.13c & 2.13d), and 4) clinopyroxene containing low HREE normalized abundances—indicative of garnet equilibration, with slight LREE enrichment (Fig. 2.13d). These complex REE patterns in clinopyroxene in the Koro peridotites potentially record a multi-stage melt and/or metasomatic history in the Koro lithosphere, beyond the intensive modal metasomatism that created the wehrellites. Peridotites that have undergone wehrlitization (both wehrellites and lherzolites) are easy to recognize as they show REE enrichments in clinopyroxene, leaving orthopyroxene seemingly unaffected (Figs. 2.13c & 2.13d). Some of the REE patterns reflect metasomatic processes affecting both clinopyroxene and orthopyroxene (e.g., Figs. 2.13a & 2.13b), and could resemble a separate metasomatic event, or the same process of wehrlitization / silicate metasomatism, but at lower melt-rock ratios, possibly occurring further away from the percolating melts, and therefore, preserving some of the original HREE melt-depletion signatures in both orthopyroxene and clinopyroxene.

Another possible metasomatic style may be indicated by the peridotites that show a marked positive Eu anomaly and subtle LREE enrichments (Fig. 2.13b). This could be from the interaction with hydrothermal fluids that are also marked by a positive Eu anomaly and LREE enrichment such as Lau back-arc basin fluids (Douville *et al.*, 1999). However, a positive Eu anomaly could also be from melting under more oxidizing conditions (e.g., Pirnia *et al.*, 2018), and/or LREE enrichments from inefficient melt extraction during partial melting (e.g., Godard *et al.*, 2008). The steep LREE enrichments combined with contrasting steep HREE depletion trends in some peridotites (e.g., Fig. 2.13a) are unlikely to reflect trapped melts, however, it cannot be ruled out for Koro peridotites with more subtle LREE enrichments (e.g., Fig. 2.13b). Since there does not appear to be a relationship between peridotites with elevated spinel Cr#-Ti (i.e., Cr# > 0.4 and TiO₂ > 0.3 wt. %; Fig. 2.17a) and peridotites that exhibit these pyroxene LREE enrichments and/or positive Eu anomalies (Figs. 2.13a & 2.13b), it is probable that these peridotites with elevated spinel Cr#-Ti (i.e., dunite K008 and harzburgite FJ063) record a separate metasomatic event via interaction with more “arc-like” melts, whereas the remaining peridotites, including those with large cpx-opx REE variations, resemble different degrees of silicate metasomatism, with the highest melt/rock ratios resulting in complete re-equilibration of clinopyroxene to produce wehrellites.

2.6.3. Koro xenolith comparisons to normal oceanic mantle lithosphere

If the Koro peridotites with recognized silicate-melt metasomatism are excluded (i.e., samples that plot along the wehrlite trend), the remaining peridotites show characteristics observed in abyssal peridotites that resemble normal oceanic mantle lithosphere. Similarities to abyssal peridotites include: 1) mineral and whole-rock major element chemistry (e.g., Figs. 2.5 & 2.6), 2) low to moderately high degrees of partial melting (~5% to <25 %), consistent with mostly shallow melt conditions, and 3) calculated fO_2 values ($\Delta \log \text{FMQ}$ -0.17 to +0.58) that are consistent with previously reported abyssal peridotites (e.g., $0.9 \pm 0.7 \log \text{FMQ}$; Bryndzia & Wood, 1990). Despite these characteristics, it is important to recognize that many of these geochemical signatures observed in abyssal peridotite overlap with signatures observed in back-arc peridotites, and would not be reflected in close to zero $\log \text{FMQ}$ values if these values represent interaction with the most recent melts to equilibrate with the peridotites (e.g., Luth & Stachel, 2014), which in this case, would be the FOIBs, not back-arc melts. On this basis, it cannot be firmly concluded that the Koro peridotite xenoliths represent normal oceanic mantle lithosphere, akin to that sampled as abyssal peridotites, on the basis of the above criteria.

Some mineral-chemical evidence for the origin of the Koro lithosphere is ambiguous, for instance, the spinel Cr#-Ti vector drawn in Fig. 2.17a towards the most “depleted” Koro peridotites via melt interaction is consistent with the host peridotites being of either back-arc origin or abyssal peridotite origin. More distinctively, REE patterns in orthopyroxene and clinopyroxene from the Koro peridotites contrast strongly with residual abyssal peridotites that show little pyroxene LREE enrichment (e.g., Warren, 2016) compared to the extensively metasomatized Koro peridotites. Furthermore, while the calculated fO_2 values for Koro peridotites overlap with those of abyssal peridotites, $\text{Fe}^{3+}/\Sigma\text{Fe}$ ratios in the Koro peridotites are distinctly higher ($\text{Fe}^{3+}/\Sigma\text{Fe} > 0.2$) (Fig. 2.15). These elevated $\text{Fe}^{3+}/\Sigma\text{Fe}$ ratios are comparable to re-fertilized peridotite xenoliths that have been linked to back-arc spreading (e.g., Wood & Virgo, 1989; Satsukawa & Michibayashi, 2014). Recent experiments on the behaviour of Fe^{3+} by Stolper *et al.* (2020) also suggest that Cr^{3+} should preferentially substitute into spinel over Fe^{3+} in typical spinel facies conditions, which is not observed in the Koro peridotites. Increased spinel $\text{Fe}^{3+}/\Sigma\text{Fe}$ ratios, can be explained through metasomatic addition of clinopyroxene (Woodland *et al.*, 2006), higher equilibration temperatures (e.g., Canil & O’Neil, 1996), and/or interaction with more oxidised subduction-related melts (e.g., Bénard *et al.*, 2018). The negative Ce anomaly in olivine that is observed in most peridotites (Fig.

2.10) could also indicate formation under mantle oxidising conditions (e.g., arc-related environments). This signature is not observed in pyroxenes and is less prominent in wehrlite olivine, suggesting that it is easily overprinted by silicate metasomatism that reflect the current day intraplate surface volcanics. This could also explain why this negative Ce anomaly is not observed in the whole-rock REE as observed in a mantle peridotite from the Solomon Islands (Neal & Taylor, 1989). However, very little REE in olivine data currently exists, and further analyses are required to understand if this is linked to subduction or inherited from another process.

2.6.4. Evidence for a pre-existing thickened lithosphere

The present-day crustal thickness of the Fijian Plateau has been variously estimated to be ~25 km (Worthington, 1974), 15 to 20 km (Hamburger *et al.*, 1990), and 21 to 23.5 km (Chen *et al.*, 2019). Beneath the eastern islands of Fiji such as Koro Island, crustal thicknesses have been estimated to be as low as ~16 km (Chen *et al.*, 2019), in contrast to estimates of up to ~50 km beneath the northern Lau Ridge, to the east of Fiji (Wei *et al.*, 2016). In keeping with this, the lithospheric thickness (crust and mantle inclusive) beneath the eastern Fiji region is constrained to be on the order of 60 to 80 km thick from a recent seismic study in Wei *et al.* (2016), and it is evident, even from global tomography, that the lithospheric mantle in that region is likely to be thinner than that beneath the oldest parts of the oceans (e.g., Schaeffer & Lebedev, 2013). Additional constraints from this study on the thickness of the lithosphere beneath eastern Fiji can be added from peridotite petrology and geochemistry. Since all the Koro Group I peridotites are spinel-bearing, lithospheric depth constraints can be placed at no more than ~60 to 80 km thick depending on the Cr# of spinel (Klemme *et al.*, 2004; Ziberna *et al.*, 2013). Peridotite pressures calculated using the P_{KB} barometer from Köhler & Brey (1990), excluding peridotites with input temperatures that fall outside the 950–1250 °C experimental range of D’Souza *et al.* (2020), reveal very low pressures within the plagioclase stability field (Table 2.5). In combination with calculated temperatures using the T_{Al-ol-spl} thermometer from Wan *et al.* (2008), these P-T values do not follow a model oceanic geothermal gradient (Fig. 2.21). While some of the peridotites that plot within the plagioclase stability field have trace amounts of plagioclase, most resemble plagioclase-free spinel peridotites. These underestimated pressures are probably the result of disequilibrium resulting from the high diffusivity of Ca in olivine, possibly by a short-term heating event, such as host magma interaction (Köhler & Brey, 1990).

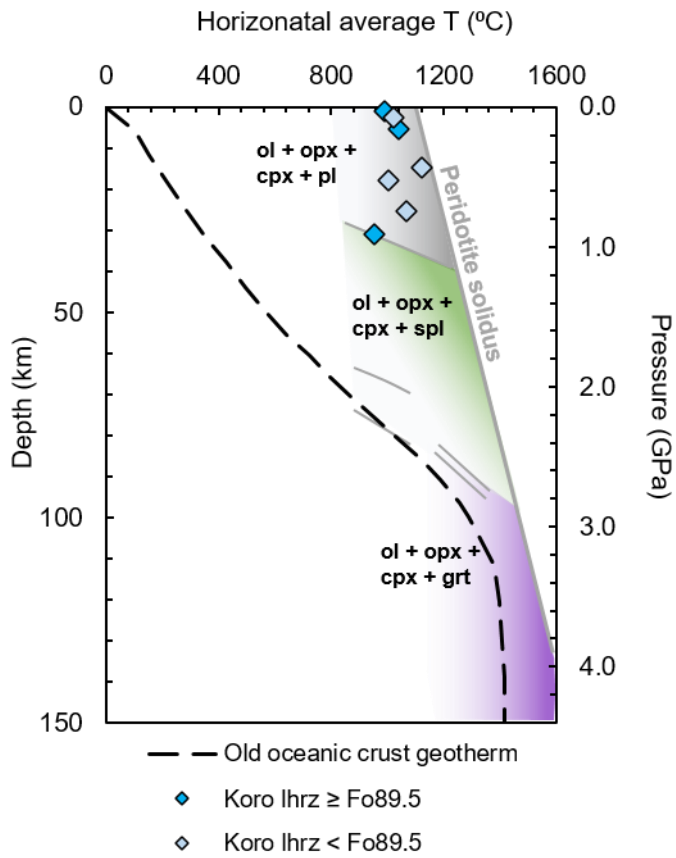


Figure 2.21. Pressure-temperature estimates using P[KB] barometer from Köhler & Brey (1990) in combination with the T[Al-in-ol-spl] thermometer from Wan *et al.* (2008) for selected Koro Iherzolites that fall within the experimental range of D’Souza *et al.* (2020) (see discussion in text). Peridotite solidus line and plagioclase-spinel-garnet facies parameters are from Koga *et al.* (1999) and Klemme (2004). Old oceanic geothermal gradient (geotherm) from McKenzie *et al.* (2005) is plotted for comparison.

The low clinopyroxene HREE abundances relative to orthopyroxene in Koro peridotites FJ167-2 and FJ167-3 (Fig. 2.13e) provide strong evidence that these xenoliths formed at greater depths within the garnet stability field as garnet is the only HREE compatible phase at shallow upper mantle conditions (e.g., Pearson *et al.*, 2003). Additional evidence for the presence of former garnet in these peridotites along with geochemical evidence in clinopyroxene comes from the presence of spinel symplectites (Fig. 2.3e), interpreted by Smith *et al.* (1977) as garnet breakdown textures, plus spinel exsolution lamellae within pyroxenes—a relationship that has also been interpreted to form under high temperatures during pressure changes in the mantle that may involve garnet breakdown. While the observed symplectite textures, could be related to products

of melt-infiltration from reaction with the host basaltic magma (e.g., Tracy, 1980), the REEs plus textural evidence provides compelling evidence for the presence of former garnet in some Koro peridotites. These peridotites may have been part of the lower-most garnet-bearing lithosphere indicating a vestige of thicker lithosphere that was possibly heated more recently to trigger the transformation of garnet to spinel.

2.6.5. SW Pacific regional tectonic implications

Seismic tomography studies have provided some constraints on the provenance of the lithosphere beneath eastern Fiji (e.g., Zhao *et al.*, 1997; Wei *et al.*, 2016; Chen *et al.*, 2019). These studies record a low-velocity region beneath the eastern Fijian Islands (20–80 km depths; Wei *et al.*, 2016) interpreted as regions of partial melt linked to back-arc development. In other words, eastern Fiji is underlain by lithosphere of very variable thickness. The same studies also observe other regions of partial melting beneath sections of the Lau Ridge, at shallower depths, suggesting that much of the pre-existing lithosphere has been removed (Wei *et al.*, 2016; Chen *et al.*, 2019). The possibility that these partial melt regions reflect the removal of thicker lithosphere beneath Koro could explain why the volcanics erupted onto Koro, along with most islands in eastern Fiji, resemble intraplate rather than arc-related volcanics, as noted in Gill & Whelan (1989). It is therefore conceivable that some of the Koro peridotites may represent fragments of this back-arc lithosphere and is consistent with the petrographic and chemical evidence presented here, that some Koro peridotites are samples of thicker, garnet facies lithospheric mantle that became heated and thinned, erupting as xenoliths above very thin present-day lithosphere. This could also explain that while geochemical signatures in the Koro peridotites represent typical oceanic mantle for the most part, a number of features are observed that require a more complex enrichment history to explain large amounts of silicate metasomatism/wehlitzination, and signatures that are more commonly observed in arc-related peridotites, such as elevated spinel $\text{Fe}^{3+}/\Sigma\text{Fe}$ ratios, negative Ce anomalies in olivine, and the severe disruption of I-PGEs in some peridotites.

The exact cause of this removal of lithosphere is unclear. Gill & Whelan (1989) proposed three possible scenarios to explain the transient switch from OIB to arc volcanism. These were: 1) the present-day OIBs represent volcanics sourced from Fijian lithosphere that was unaffected by arc magmatism, 2) Fijian OIBs are sourced from Indian Plate aesthenosphere by a process of “trench suction”, or 3) Fijian OIBs represent Pacific mantle that migrated with a change from convergent to transform plate style. The third scenario, favoured by Gill & Whelan (1989) based on the

existence of Type II FOIB in the North Fiji Basin. This scenario is supported by recent studies that suggest an influx of OIB material from the Samoan mantle plume resulted in the removal of oceanic lithosphere through heating and erosion (e.g., Price *et al.*, 2014, 2017; Wei *et al.*, 2016; Chen *et al.*, 2019). These studies support previous proposals suggesting that slab rollback of the subducting Pacific Plate may have allowed the entrance of Samoan plume material beneath the Lau Basin region (Turner & Hawkesworth, 1998; Conder & Wiens, 2007; Pearce *et al.*, 2007). The rapid destruction of garnet facies (i.e., transition to spinel facies) recorded in the Koro xenoliths, and anomalously high equilibration temperatures recorded by clinopyroxene, provide supporting evidence for the heating (likely coincident with extensive melt-related silicate metasomatism) and destruction of the pre-existing oceanic lithosphere that would fit the Samoan plume hypothesis (Fig. 2.22). The depleted clinopyroxene HREE concentrations that reflect garnet equilibration

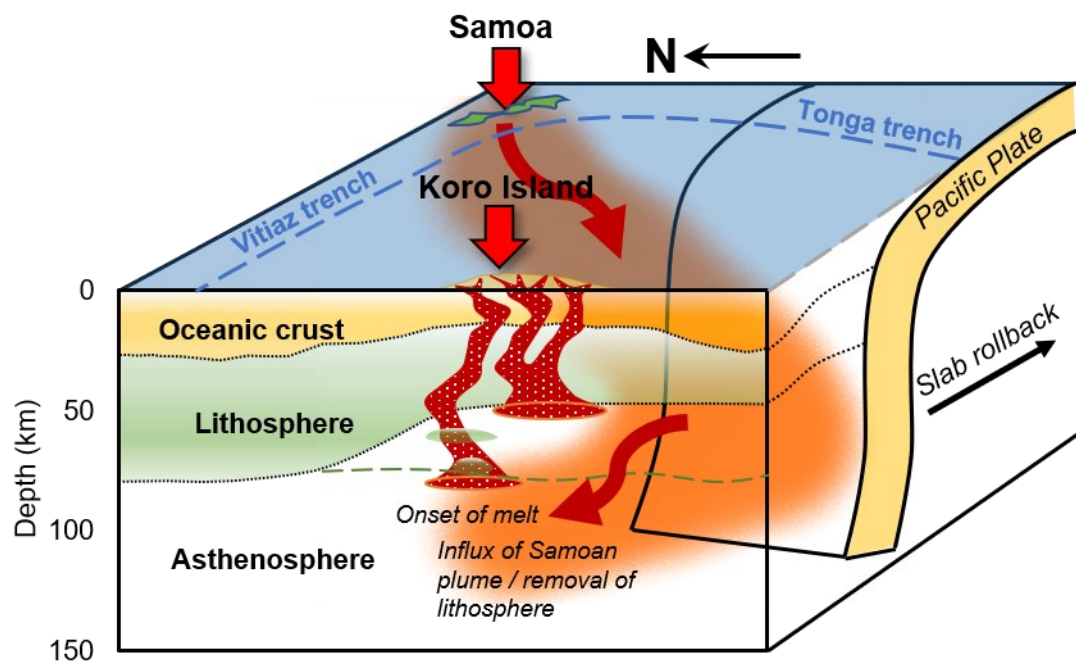


Figure 2.22. Schematic cartoon showing the influx of Samoan plume material resulting from slab rollback of the subducting Pacific Plate modified after Price *et al.* (2014) and Wei *et al.* (2016). Oceanic crust and lithospheric thickness are approximated from Wei *et al.* (2016). The horizontal distance between Koro Island and Samoa not to scale.

probably reflect peridotites that did not have enough time to re-equilibrate to the lower pressure/higher temperature spinel-facies assemblage before they were transported by volcanism to the surface. Interaction with Samoan plume material could be further supported by HSE and Os isotope signatures in the Koro peridotites. While the severe disruption of some HSE patterns, particularly the I-PGEs reflect sulfide destruction that seem to be most prevalent in arc environments, the distinctive P-PGE pattern observed in most peridotites supports the introduction metasomatic sulfides linked to silicate metasomatism. Furthermore, the average Koro peridotite $^{187}\text{Os}/^{188}\text{Os}$ ratio (0.1269 ± 0.0027) overlaps with the most recent peak recorded in the Samoan peridotite xenoliths from Jackson *et al.* (2016), suggesting a possible an overprint of the Samoan plume in both localities. Collectively, these features support existing geodynamic models for a pre-existing thick lithosphere beneath Koro that accreted beneath a former back-arc that has since been removed and severely overprinted by the influx of plume-related OIB volcanics that are prevalent in the present-day surface volcanics.

2.7. SUMMARY AND CONCLUSION

Peridotite xenoliths sampled from Koro Island in eastern Fiji represent fragments of oceanic mantle lithosphere that record a complex melt extraction history and extensive refertilization. Koro xenoliths resemble mantle residues following low to mid degrees of partial melting (~5% to <25%) as indicated by their olivine-spinel relationships and their whole-rock HREE abundances, that have been significantly overprinted by at least two separate metasomatic events. One of these metasomatic processes records the interaction with a low degree, and dominantly silicate-like melt that resulted in the formation of wehrellites via orthopyroxene dissolution. A separate metasomatic event, recorded in a small proportion of harzburgite and dunite xenoliths, resulted in an increase in spinel Cr#-Ti abundances via interaction with more arc-like melts. Supporting evidence for arc melt interaction includes elevated spinel $\text{Fe}^{3+}/\Sigma\text{Fe}$ ratios that are higher than those observed in abyssal peridotites, prominent negative Ce anomalies in residual olivines, a severe disruption in several PGEs, particularly the I-PGE, and the current tectonic framework of eastern Fiji that is in close proximity to both an extinct arc system (Lau-Colville Ridge) and the Lau back-arc Basin.

Together with the conspicuously low HREE in clinopyroxene from two peridotites that indicate prior equilibration with garnet, and spinel symplectite textures that suggest the breakdown of garnet, there is collective evidence that point towards a thickened mantle lithosphere that formed via back-arc accretion beneath Koro. To explain the absence of arc signatures in the present-day OIB surface volcanics and the thin (<20 km) lithosphere beneath eastern Fiji, a possibility is that this thicker lithosphere has since been removed and/or undergone significant metasomatic modification, with the pre-existing lithosphere only recorded in a few remnant xenoliths. Extensive silicate metasomatism, a perturbed geothermal gradient and rapid breakdown of former garnet, and $^{187}\text{Os}/^{188}\text{Os}$ ratios in the Koro peridotites that overlap with $^{187}\text{Os}/^{188}\text{Os}$ ratios from the Samoan peridotite xenoliths support lithospheric erosion/removal via the influx of Samoan plume material from slab roll-back of the subducting Pacific Plate. This peridotite xenolith study supports previous models and provides evidence that some of this plume material may have migrated throughout eastern Fiji.

Chapter 3

The formation of ultra-depleted residual mantle peridotites in ophiolites: The Papua New Guinea mantle tectonites

3.1. INTRODUCTION

Mantle-derived peridotites from ophiolites, with tectonite fabrics, provide an important geological archive for studying the melt-depletion processes responsible for creating oceanic lithosphere and are a key window into the evolution of the Earth's mantle (Bodinier & Godard, 2003). Since a connection between subduction processes and ophiolite formation was proposed by Miyashiro (1973), the mantle peridotites of ophiolite complexes have been further recognized as important samples to directly study partial melting processes and extents in subduction-influenced rift environments. Ophiolites that form in subduction environments are termed supra-subduction zone (SSZ) ophiolites (Pearce *et al.*, 1984), however, the relationship between ophiolite formation and subduction remains ambiguous. Papua New Guinea (PNG) hosts some of earliest identified ophiolite complexes in the world (Thompson & Fisher, 1965; Davies, 1968), with their discovery pre-dating the development of the Penrose stratigraphic model (Penrose, Participants 1972). The Marum and Papuan Ultramafic Belt (PUB) ophiolites in PNG are examples of SSZ ophiolites characterized by a well-preserved ultramafic complex dominated by tectonite peridotites with highly refractory compositions (Davies, 1971; England & Davies, 1973; Jaques & Chappell, 1980; Jaques, 1980; Kaczmarek *et al.*, 2015). The peridotites from these bodies have long-been recognized as representing some of the most melt-depleted residual peridotites found on Earth (Jaques, 1980) even compared with cratonic peridotites (Boyd, 1989). This study will focus on new geochemical, HSE and Os isotope data in mantle-derived peridotites from the PUB and Marum ophiolite massifs to better understand the pre-emplacement history of the depleted upper mantle preserved in the PNG lithosphere. Comparisons between new and existing hydrous and anhydrous mantle melting experiments were made to evaluate the melting conditions that might

have formed these ultra-depleted residues. Such highly refractory peridotites also provide an excellent opportunity to examine HSE behaviour in ultra-depleted mantle residues from subduction-influenced settings.

3.2. GEOLOGICAL CONTEXT AND SAMPLES

3.2.1. *Geological context*

Ophiolites form a discontinuous belt at the outer margin of the Australian continental mass in the island of New Guinea, which include the PUB in the southeast, the Marum ophiolite in the north, the April ultramafics in the west of PNG, the West Papua ophiolites in Irian Jaya-Indonesia that comprise the Central (or New Guinea) ophiolite belt in the far west, and the Cyclops ophiolite situated on the Indonesian-PNG boarder (Fig. 3.1; Davies & Jaques, 1984; Davies, 2012). All these ophiolite massifs are tilted away from the continental margin towards accreted remnants of Cenozoic island-arcs and are thought to have formed in an SSZ environment, and were emplaced as a result of early Cenozoic continent/island-arc collision between the Australian and the southward subducting Pacific Plate (Davies & Smith, 1971; Jaques & Robinson, 1977; Davies & Jaques, 1984; Davies, 2012). This study is focussed on the PUB and the Marum ophiolite which have unusually depleted mantle peridotites at their base.

3.2.1.1. *Papuan Ultramafic Belt (PUB)*

The PUB is the largest and most complete of the New Guinea ophiolites extending in a 400 km long by 40 km wide arcuate belt along the north-eastern side of the Owen Stanley Range in the Papuan Peninsula (Fig 3.1; Davies, 1971; Davies & Smith, 1971). The PUB comprises a layered sequence of 4 to 8 km of tectonite harzburgite and dunite overlain by about 4 km of gabbro (olivine gabbro, troctolite, norite-gabbro), overlain in turn by about 4 km of basalt. A discontinuous belt up to 0.5 km of cumulus ultramafics (lherzolite and plagioclase lherzolite) occurs at the ultramafic–gabbro boundary (England & Davies, 1973) and sheeted dykes are locally developed at the gabbro–basalt interface (Davies & Jaques, 1984). The ophiolite complex dips at 10 to 40° to the E and NE, and has been thrust to the SW over the Owen Stanley Metamorphics along the Owen Stanley Fault (Davies, 1971; Davies & Smith, 1971; Davies & Jaques, 1984). The PUB is intruded

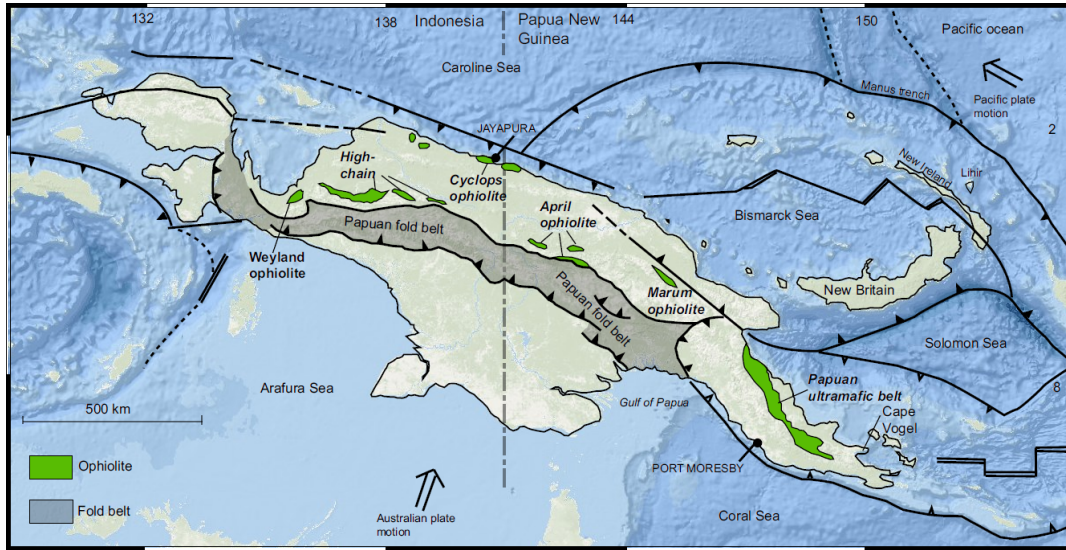


Figure 3.1. Simplified geological map of New Guinea showing the Marum and PUB ophiolites ophiolite localities, and Cape Vogel peninsula (boninite locality) after Kaczmarek *et al.* (2015)—a modified map based on Davies (2012). Map has been superimposed on the Esri Ocean Base map. The country border between Indonesia and Papua New Guinea is denoted by the dashed grey line.

by late Paleocene to Eocene (57–51 Ma) tonalites and diorites, and in the northwest is overlain by co-eval (57–55 Ma) and apparently co-magmatic andesitic to dacitic volcanics and associated sediments considered to represent the early stages of island arc magmatism (Jaques & Chappell, 1980; Davies & Jaques, 1984; Rogerson *et al.*, 1991). This suite is also considered to be both co-eval and chemically related to the late Paleocene (58–59 Ma; Walker & McDougall, 1982) submarine tholeiitic and boninitic lavas (Dabi Volcanics) of the Cape Vogel area (Fig. 3.1). The Cape Vogel volcanics are inferred to represent fore-arc or an early oceanic island arc which collided with the Australian continent resulting in emplacement of the PUB (Davies & Smith, 1971; Davies & Jaques, 1984; Whattam *et al.*, 2008; Whattam, 2009).

The PUB is faulted against metamorphic rocks of the Owen Stanley Terrane with the base of the ophiolite marked by a 300 m thick metamorphic sole of high grade metamorphics (granulites and amphibolites). A mean $^{40}\text{Ar}/^{39}\text{Ar}$ plateau age of 58.3 ± 0.4 Ma for amphiboles from the metamorphic sole is taken to be the age of cooling of the sole and emplacement of the PUB (Lus *et al.*, 2004). The underlying metamorphic rocks of the Owen Stanley sequence consist mostly of greenschist facies metamorphics (Kagi Metamorphics) derived, at least in part, from felsic and psammitic–pelitic protoliths of mid-Cretaceous age (Aptian–Cenomanian; Davies, 2012) and

thought to be an uplifted accretionary complex (Pieters, 1978). A prominent thrust sheet of blueschist to greenschist facies metabasite (Emo Metamorphics) forms a NE-dipping slab bounded by the Owen Stanley and Timeno faults that structurally overlay the Kagi Metamorphics (Pieters, 1978; Davies & Jaques, 1984; Rogerson *et al.*, 1991). The faults are thought to have developed as subduction thrust faults related to emplacement of the PUB and to have been reactivated as trans-tensional faults (Davies & Jaques, 1984). The Emo Metamorphics were derived from low-K oceanic tholeiites of Late Cretaceous (Maastrichtian) age with normal(N)-MORB to enriched(E)-MORB compositions and slightly negative Nb anomalies suggesting formation in a back-arc basin (Pieters, 1978; Worthing & Crawford, 1996). The age of formation of the PUB is not well established, however, it is reasonably constrained as late Cretaceous (Maastrichtian ~71–65 Ma based on fossil foraminifera; Smith & Davies, 1976; Belford, 1976), to early Paleocene (~60 Ma) based on the $^{40}\text{Ar}/^{39}\text{Ar}$ cooling ages for the metamorphic sole (Lus *et al.*, 2004) and age of the intrusive tonalites and diorites (Davies & Jaques, 1984; Davies, 2012).

3.2.1.2. Marum ophiolite

The Marum ophiolite consists of a shallow (~10°) N- to NE-dipping thrust sheet of peridotite and gabbro exposed for 90 km along the northern flank of the Bismarck Range, bounded to the north by the Ramu-Markham fault zone and to the south by the Bundi fault zone (Jaques, 1980; Davies & Jaques, 1984). The peridotite-gabbro massif forms a broadly folded thrust sheet ~4 km thick overlying a subsidiary thrust sheet of spilitic pillow lava, lava breccia, hyaloclastite and argillite up to 1 km thick (Tumu River Basalt). The peridotite–gabbro massif consists of a basal harzburgite–dunite unit overlain by a cumulate sequence which is grossly layered from peridotite to gabbro. Windows exposed in the river sections transecting the ophiolite show that the sole of the ophiolite is marked by a thin zone of serpentinite which rests on an imbricate zone of low-grade metasediments (Asai Shale) and metavolcanics. A basal cumulate dunite layer overlies the tectonites and is successively overlain by wehrlite, lherzolite, plagioclase lherzolite, pyroxenite, olivine norite-gabbro, and norite-gabbro and, finally, by minor anorthositic gabbro and ferronorite-gabbro near the top. Rare dykes of quartz dolerite intrude the uppermost gabbros, and narrow dykes and veins of pegmatitic gabbro cut all levels of the layered sequence (Jaques, 1981; Jaques *et al.*, 1983). In the Kurumbukari area dunite and orthopyroxene-poor harzburgite at the top of the tectonite unit are deeply weathered to form a thick laterite (average 15 m, locally up to 60 m) with Ni-rich limonite and saprolite that comprises the Ramu nickel-cobalt deposit (Holmes & Hall,

1975; Queen *et al.*, 2001) currently being mined. The Tumu River Basalts range from magnesian tholeiites to highly differentiated ferrobasalts, and are enriched in LREE, Ti, Zr, and other 'incompatible' elements relative to chondrite and similar to 'transitional' or E-MORB (Jaques *et al.*, 1978). The thrust sheets overlie low-grade metasediments, mostly dark calcareous shale, siltstone and limestone (Asai Shale), of late Cretaceous to Eocene age. In the southeast and east, both the ophiolite and the Asai Shale are faulted against graphitic slate and phyllite of the Mesozoic Goroka Formation. Both the age of formation and the age of emplacement of the Marum ophiolite are poorly constrained. The ophiolite is thought to have formed in the Paleocene based on a K–Ar age (59 ± 2.5 Ma) of hornblende in a granophyric diorite vein (Jaques, 1981), and have been tectonically emplaced prior to or during collision between the Australian continent and the Oligocene–early Miocene Finisiterre arc to the north (Jaques & Robinson, 1977).

3.2.2. *Geology and petrography of the peridotites*

Petrographic descriptions for all mantle-derived PNG peridotites, i.e., those with tectonite fabrics (hereafter referred to as tectonites) have been documented in England & Davies (1973), Jaques & Chappell (1980), and Jaques (1980). Tectonites were classified using petrographic evidence for solid-state recrystallization, whereas cumulate peridotites preserve evidence for primary crystal accumulation (England & Davies, 1973). Harzburgites are the dominant lithology in the tectonite unit, followed by dunites that occur in discrete lenses and discordant masses within the harzburgites. Four previously unclassified peridotites were added to this study. These include two harzburgites (KD1, MA4) and two dunites (KD2, KD3) that display granular textures with interlocking grains and interstitial spinels that are consistent with a tectonite origin despite high degrees of alteration. Dunite KD3 shows some sub- to euhedral spinels along with interstitial spinels, reflecting some possible recrystallization. Samples KD1, KD2, and KD3 were collected from the PUB ophiolite and MA4 collected from the Marum ophiolite.

3.2.2.1. *PUB tectonites*

The tectonite unit consists mostly of harzburgite with minor dunite intruded in places by veins, dykes and irregular bodies of orthopyroxenites (Davies, 1971). The harzburgite is commonly massive but some show fine-scale (cms) layering with alternating enstatite-rich and poor horizons. The harzburgites in this study contain more than 80 vol. % olivine, 10 to 20 vol % enstatite and ~1 vol. % spinel. These relatively uniform peridotites, while typical of the PUB harzburgite

generally (Davies, 1971), were collected from outcrop and boulders from one region (the Chirima and Mambare rivers) and may not represent the full mantle suite in the PUB as the data of England & Davies (1973) indicate a wider range in spinel compositions than encompassed by these samples. Studies of mantle peridotites in other ophiolites have shown a diversity of peridotites of varying composition are commonly present (e.g., Bodinier & Godard, 2003; Batanova & Sobolev, 2006; Pirard *et al.*, 2013). The degree of secondary alteration is low and limited to minor fine veinlets of serpentine and associated secondary magnetite. The samples are mildly to moderately deformed with a marked tectonite fabric characterized by undulose extinction and reduction in grainsize by dislocation and granulation of larger primary grains. Most have a coarse granular to weakly porphyroclastic texture. Olivine grains are typically ~4 mm across but range up to 10 mm in some samples. Orthopyroxene commonly forms partially dismembered porphyroclasts up to 10 mm and small strain-free neoblasts at the margin. Rare exsolved diopside lamellae were reported in enstatite for a few PUB harzburgites by England & Davies (1973) but none were found in samples from this study. The spinels have typically interstitial to subhedral forms 100 to 500 µm, with some up to 1 mm. The larger olivine and enstatite grains (~10 mm) with relic curvilinear grain boundaries are thought to be remnants of an earlier granular fabric (Jaques, 1980).

3.2.2.2. *Marum tectonites*

The Marum ultramafic tectonite unit consists predominantly of foliated, depleted harzburgite and dunite and is overlain by cumulate dunite and peridotite and the thick gabbro sequence (Jaques, 1980; 1981). The base of the tectonite unit is marked by a thin band (~1 m) of serpentinite that defines the sole of the ophiolite. The harzburgite has a discontinuous layering with alternating olivine- and pyroxene-rich layers 1 to 15 cms thick which in places are isoclinally folded or form boudins. The top of the unit is marked by a decrease in enstatite abundance and increase in intercalated lenses and pods of dunite (including Mg-rich dunite see below) passing into dunite with thin chromitite layers (mm) of inferred cumulate origin. Limited exposures in river sections and intersections in drill holes immediately below the Ni laterite at Kurumbukari indicate that the distribution of dunite pods and lenses and the variation in Fo contents in olivine in dunites and harzburgites occur on a scale of <1 m to tens of meters. The cumulate dunite passes into overlying cumulate peridotite with interstitial pyroxene and plagioclase that forms the base of cyclic units (10s to hundreds of m) of layered lherzolite, wehrlite, plagioclase lherzolite, troctolite and norite-gabbro with clear cumulate features (Jaques, 1981). The peridotites are intruded in places by

enstatite-rich veins and dykes 1 cm to 3 m wide (Jaques, 1980) and by clinopyroxene-rich veins and thin dykes of gabbro (Kaczmarek *et al.*, 2015). Although poorly exposed, this sequence of an ultramafic tectonite composed of harzburgite at the base overlain by a zone of highly depleted zone of dunite in the upper part of the mantle section, and a transition to layered peridotites, pyroxenites and gabbros is analogous to that found in many other ophiolites (e.g., Boudier & Nicolas, 1995; Suhr *et al.*, 2003; Pirard *et al.*, 2013; Dilek & Furnes, 2014). The transition from tectonite dunite to dunite interlayered with peridotite and gabbro is inferred to be the mantle–crust transition zone.

The harzburgites are coarse grained (2–7 mm, average 3–4 mm) with a granular to weakly porphyroclastic texture and comprised of more than 80 vol. % olivine, 8 to 20 vol. % enstatite, minor (<1 %) chrome diopside as exsolved lamellae in enstatite or recrystallized polygonal grains at grain boundaries, and accessory (1–2 vol %) chrome spinel. The dunites mostly have a similar grainsize to the harzburgites but typically have more abundant chrome spinel and include types with larger olivine porphyroclasts (up to 12 mm). A suite of Mg-rich dunites containing only minor enstatite (\leq 5 vol %) are transitional to the more orthopyroxene-poor harzburgites. Some of the Marum tectonites in this study and Kaczmarek *et al.* (2015) contain traces of diopside as interstitial phases, and as inclusions within orthopyroxene and spinel. Clinopyroxene appears to be confined to peridotites with olivine $<\text{Fo}_{93}$ and spinel Cr# ≤ 0.76 . Both the harzburgite and dunite have been plastically deformed as shown by weak elongation of olivine and enstatite to form a preferred orientation and undulatory extinction. In more deformed harzburgites, the enstatite forms rounded porphyroclasts with abundant deformation bands and small strain-free polygonal neoblasts at the margin. Chrome spinels in the harzburgites are typically small (100–500 μm), subhedral and interstitial, in places defining the foliation.

The microstructures in a suite of Marum tectonite and cumulate peridotites were examined using EBSD by Kaczmarek *et al.* (2015) who inferred from the strong olivine crystallographic preferred orientations in dunite and harzburgite that both (001)[100] and (010)[100] slip systems were activated, implying deformation under high-temperature and low-stress conditions. In addition, the crystallographic preferred orientations for clinopyroxene and orthopyroxene indicated activation of their (100)[001] and (010)[001] slip systems, which are common in pyroxenes deformed at high temperature. Kaczmarek *et al.* (2015) inferred that the plastic deformation probably occurred during formation rather than emplacement of the ophiolite, noting

that the foliation and olivine [100] slip directions parallel the volcanic arc which is inferred to have lain to the northeast prior to continent-arc collision.

3.3. ANALYTICAL METHODS

Whole-rock and in-situ major element (EPMA) data on some of the tectonites analyzed here from both the PUB and Marum ophiolites are reported in Jaques & Chappell (1980) and Jaques (1980), who detail their analytical methods. Peridotites with no previous whole-rock major element data (088, 090, 425, and 726), along with new peridotites (KD1, KD2, KD3 and MA4) were analyzed by X-ray fluorescence (XRF) using lithium tetraborate ($\text{Li}_2\text{B}_4\text{O}_7$) fused disks (Mertzman, 2015; Waterton *et al.*, 2020) at the X-ray Laboratory at Franklin and Marshall College, USA. A detailed description of the accuracy and repeatability of data using this measurement procedure is provided in Waterton *et al.* (2020), including compilations of ultramafic reference materials (RMs) run over the course of this study. Additional in-situ major elements were collected using two electron probe microanalyzers (EPMA) with attached wavelength-dispersive spectrometers (WDS). These includes a JEOL JXA-8900R EPMA operating at an accelerating voltage of 20 kV, beam current of 20 nA, count times of 30 secs on-peak, and fully-focused beam size ($<1 \mu\text{m}$) at the UofA and JEOL 8530F Plus EPMA operating at an accelerating voltage of 15 kV, beam current of 50 nA with 2 μm spot size at the Australian National University (ANU). In-situ trace elements were measured in olivine and orthopyroxene via LA-ICP-MS using a ThermoScientific Element XR and Resonetics RESOlution 193 nm excimer laser ablation system with two-volume Laurin Technic S155 sample cell at the UofA Arctic Resources Geochemistry Laboratory. Analytical methods and performance are documented by Bussweiler *et al.* (2019) and Scott *et al.* (2016) for olivine and orthopyroxene respectively. These data are supplemented by additional data collected using an Agilent Technologies 7700 ICP-MS coupled to an ANU HelEX laser-ablation system with a 193 nm wavelength EXCIMER laser (110 (ArF) COMPex, Lambda Physik) following the method of Eggins *et al.* (1997) and Jenner & O'Neill (2012) at the ANU using EPMA Si values as the internal standard and NIST glass SRM 612 (Jochum *et al.*, 2011) as the reference standard. Whole-rock trace element analyses were also measured on a ThermoScientific Element XR ICP-MS in solution mode at low and medium mass resolution at the UofA. Solutions were prepared by dissolving approximately 0.1 g of powder in 1 mL of concentrated HNO_3 , followed by 4 mL of

concentrated HF, and refluxed at 150 °C for 24 hours in Savillex PFA vials. Samples were dried down and an additional 1 mL of concentrated HNO₃ was added for refluxing a second time. This step was repeated, and an additional 2.5 mL of concentrated HNO₃ was added and refluxed overnight. Samples underwent a 5000x dilution in 3% HNO₃. Dissolutions of whole-rock powder RMs BCR-2, BHVO-2, BIR-1a, MUH-1, and OKUM (labelled OKUM724b in house), and a standard solution of known Pt, Ir, Ru, Pd, and Re concentration, and 3% HNO₃ blank solutions were included during analysis. Accuracy was generally better than 10%.

HSE were separated via high pressure Aqua Regia digestion, followed by isotope dilution. Os was extracted using CHCl₃ back-extracted into HBr (Cohen & Waters, 1996), and further purified via micro-distillation (Birck *et al.*, 1997). Pt, Ir, Ru, Pd, and Re were extracted via anion column chemistry described in Pearson & Woodland (2000). The purified Os was measured as OsO₃⁻ using negative-thermal ionization mass spectrometry (N-TIMS; Creaser *et al.*, 1991). All trace element and HSE solution chemistry were completed at the UofA Arctic Resources Geochemistry Laboratory. The accuracy and reproducibility of whole-rock RMs used in this study, over the analytical campaign, is reported in Waterton *et al.* (2020).

3.4. RESULTS

3.4.1. Mineral chemistry: major elements

Major elements measured in olivine, orthopyroxene, clinopyroxene, and spinel measured in the PNG tectonites from this study, along with select duplicate analyses from Jaques (1980) and Jaques & Chappell (1980) are summarized in Appendix 4.

3.4.1.1. Olivine

Olivine in the PNG tectonites in this study are very refractory with olivine Fo contents ranging between Fo_{91.2–94.6} in dunite tectonites and Fo_{91.8–93.3} in the harzburgite tectonites (Fig. 3.2a). The PUB harzburgite olivines in this study are characterized by high olivine Fo contents (Fo_{92.1–93.3}; median Fo_{92.8}) similar to the range (Fo_{91.6–93.6}) reported in the PUB tectonites by England & Davies (1973). The PUB harzburgite olivines also have high Ni (0.40–0.44 wt. % NiO) and very low Ca contents (<0.01 wt. %). Olivine crystals are uniform ($\leq \pm 0.2$ mol %) apart from rims adjacent to

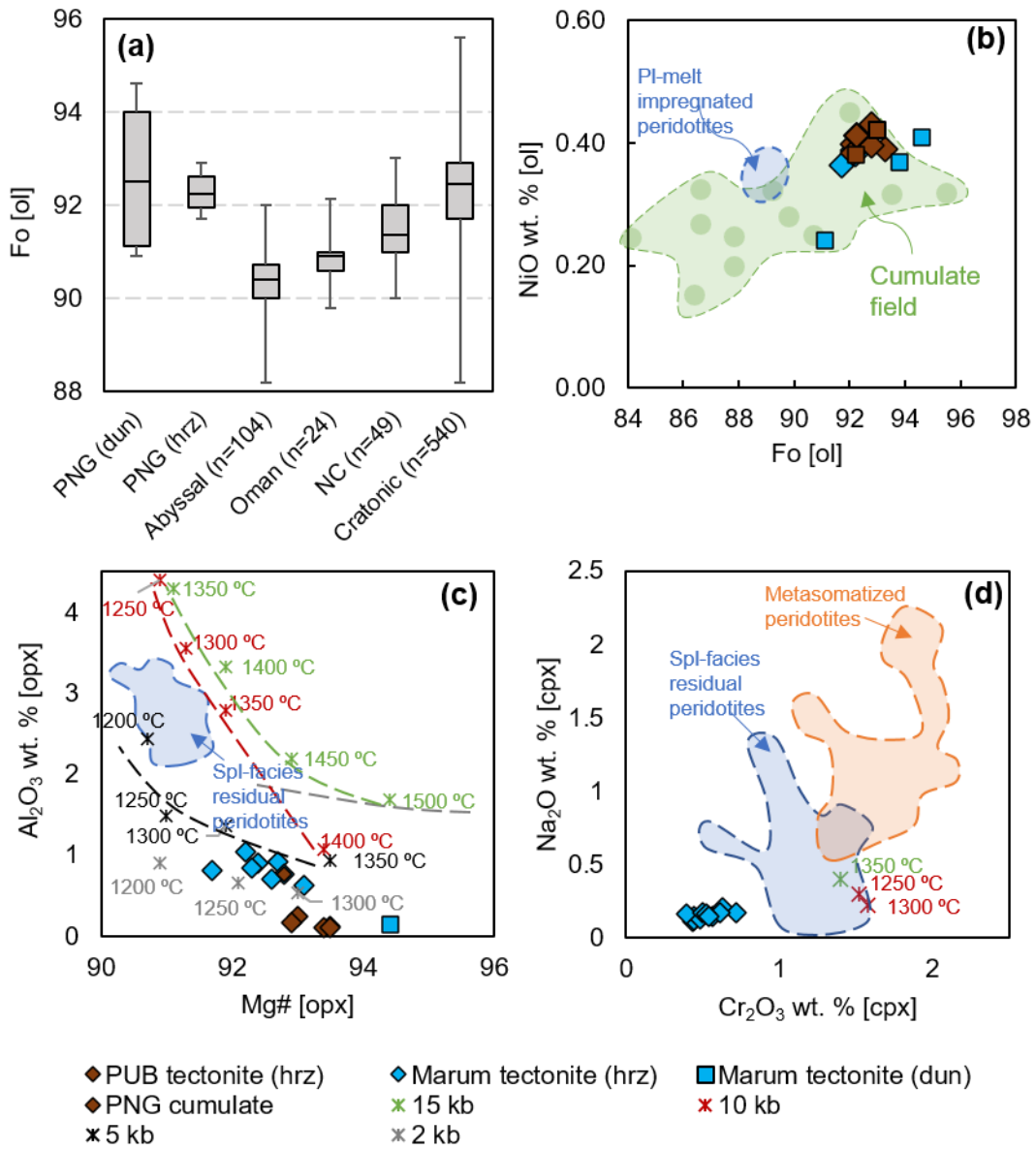


Figure 3.2. (a) Box and whisker plot showing olivine Fo contents in the PNG tectonites compared to abyssal peridotites, ophiolite peridotites from Oman and New Caledonia (Hanghøj *et al.*, 2010; Liu *et al.*, 2018; Xu & Liu, 2019; Secchiari *et al.*, 2016) and cratonic mantle peridotites (Pearson & Witting, 2008). (b) Olivine NiO wt. % vs. Fo in the PNG tectonites compared to cumulates from Jaques (1980) and Kaczmarek *et al.* (2015). Plagioclase-melt impregnated peridotites from Rampone *et al.* (2016) for comparison. (c) Al_2O_3 vs. Mg# in opx plotted against abyssal spl-facies peridotite residues from Seyler *et al.* (2007). Anhydrous spl-facies melt residues at 2–15 kb from experiments in Jaques & Green (1980). (d) Cpx Na_2O wt. % vs. Cr_2O_3 wt. % relationships in the Marum tectonite peridotites plotted against abyssal residual peridotites and abyssal metasomatic peridotites from Seyler *et al.* (2004).

spinels which, in some cases, have slightly higher Fo (up to 0.6 mol %) due to sub-solidus Fe-Mg exchange with spinel (see Appendix 4). Olivine in the Marum harzburgites is of uniform composition (\pm 0.1–0.2 mol %) within the Fo_{91.8–92.7} range. Olivine in the dunites form two groups: 1) a higher Mg group of Fo_{93–94.6} comprised of samples 087, 088 and KD2 with high Ni contents (~0.4 wt. % NiO) that includes the orthopyroxene-poor harzburgites interleaved with dunite, and 2) a lower Mg group (\leq Fo₉₁) comprised of peridotites 414 and KD3 with lower Ni contents (~0.3 wt. % NiO) similar to other low Ni (0.2–0.3 wt. % NiO) dunites described previously (Jaques, 1980; Kaczmarek *et al.*, 2015) (Fig. 3.2b). In addition, olivines in many of these tectonite peridotites overlap within the broad range of olivines in peridotite cumulates ranging from ~Fo₈₄ to >Fo₉₂ from Jaques (1980) and Kaczmarek *et al.* (2015) (Fig. 3.2a) and Ni contents (0.15–0.45 wt. % NiO) (Fig 3.2b).

3.4.1.2. Orthopyroxene

Orthopyroxene in the tectonite peridotites in both the Marum and PUB ophiolites is enstatite and is similarly refractory in its composition to the olivines. Orthopyroxene in the PUB has a limited compositional range with high Mg# (92.8–93.5), with very low Al₂O₃ and CaO contents (0.1–0.2 wt. %, both Al₂O₃ and CaO), with the exception of orthopyroxene in the harzburgite KD1 with slightly higher Al₂O₃ and CaO contents (0.77 wt. % and 0.43 wt. %, respectively). Orthopyroxene in the Marum harzburgites is mostly of similar composition but has slightly lower Mg#(91.8–93.1) and higher Al₂O₃ and CaO contents (0.6–1.0 and 0.6–0.9 wt. %, respectively) than those in the PUB (Fig. 3.2c). Orthopyroxene-bearing dunite sample 087 has the highest Mg# of all the samples (Mg#=94.4) and has very low Al₂O₃ of 0.15 wt. %, similar to the PUB orthopyroxene abundances, and CaO of 0.43 wt. %, roughly between the PUB and Marum values. All the tectonite orthopyroxenes contain significant Cr (Cr₂O₃ <0.4 wt. %) and have very low Na (Na₂O <0.02 wt. %).

3.4.1.3. Clinopyroxene

Clinopyroxene is inferred on textural grounds to have formed by sub-solidus exsolution from orthopyroxene on cooling, an interpretation supported by the low equilibration temperatures (700–800 °C, see section 3.5). Clinopyroxene in the Marum harzburgites have high Mg# (95–95.7) and Ca (Ca/(Mg+Ca+Fe) = 0.47–0.49) with Al and Cr contents of 0.6–0.9 wt. % Al₂O₃ and 0.4–0.6 wt. % Cr₂O₃, respectively. They also have very low Na₂O contents (<0.17–0.21 wt. %) and extremely low TiO₂ (<0.01 wt. %) that are notably lower than metasomatic clinopyroxene in

ophiolite peridotites (e.g., Marchesi *et al.*, 2009) that typically have much higher Ti contents ranging between 0.07 to 0.22 wt. %. Sodium contents in the PNG tectonite clinopyroxenes are significantly lower than both residual and metasomatic clinopyroxene recorded in abyssal peridotites (e.g., Seyler *et al.*, 2004), and have lower Cr₂O₃ abundances than metasomatic clinopyroxene (Fig. 3.2d). The clinopyroxene compositions reported in this study are similar to those found as interstitial grains by Kaczmarek *et al.* (2015). Clinopyroxene found in dunite tectonite (sample 414) as an inclusion in spinel has similarly low Na₂O (<0.17 wt. %) to the harzburgite tectonites, but slightly higher Ca (Ca/(Mg+Ca+Fe) = 0.5, and higher Cr and Al contents (Cr₂O₃ = 1.25 wt. %; Al₂O₃ = 1.13 wt. %), probably from exchange with the enclosing spinel (Jaques, 1980).

3.4.1.4. Cr-spinel

The spinels in the PNG tectonite peridotites are exceptionally Cr-rich magnesian chromites with very low calculated Fe³⁺ contents. The more Cr-rich spinels are generally associated with the most Mg-rich olivines (Fig. 3.3). Spinels (chromites) in the PUB harzburgite tectonites have very low Ti (<0.07, commonly ≤0.02 wt. %, TiO₂) and extremely high Cr# between 0.90 to 0.95, at the very high end of the 0.69 to 0.89 range indicated by the partial analyses in England & Davies (1973). Spinels in the Marum harzburgites, although slightly less refractory than those in the PUB, also have low Ti (<0.07 wt. %, TiO₂) and high Cr# (0.71–0.77). Spinels in the dunite tectonites from both PUB and Marum have a spinel Cr# ranging between 0.70 to 0.92; spinels in the high-Mg olivine dunite tectonites (087 and 088) have similar Cr-rich spinel (Cr# >0.85) to those in the PUB harzburgites. Spinels in the dunite tectonites with olivine <Fo₉₂ (414 and KD3) are less Cr-rich (Cr# ~0.70) and more comparable with spinels in the Marum harzburgites. Ti contents in the chromites from the high-Mg olivine dunite tectonites are low (≤0.03 wt. %), whereas those in the lower Mg-olivine dunite tectonites (414 and KD3) reach slightly higher values (up to 0.16 wt. % TiO₂). Similar to Fo in olivine, there is some overlap between spinel Cr# in the peridotite tectonites from this study and cumulates from Jaques (1980) and Kaczmarek *et al.* (2015), however, only in tectonites do spinels exceed values greater than Cr# ~0.85 (Fig. 3.3a). Cumulate olivine and spinel show a trend to decreasing Cr# (and increasing Fe³⁺, Jaques, 1981) in spinel with decreasing Fo in olivine that is distinct from the melt-residue olivine spinel mantle array (OSMA) defined by Arai (1994) and is consistent with falling crystallization temperatures with magmatic differentiation (Fig. 3.3a). The most depleted spinels occur in the PUB harzburgites and the Marum dunites, and

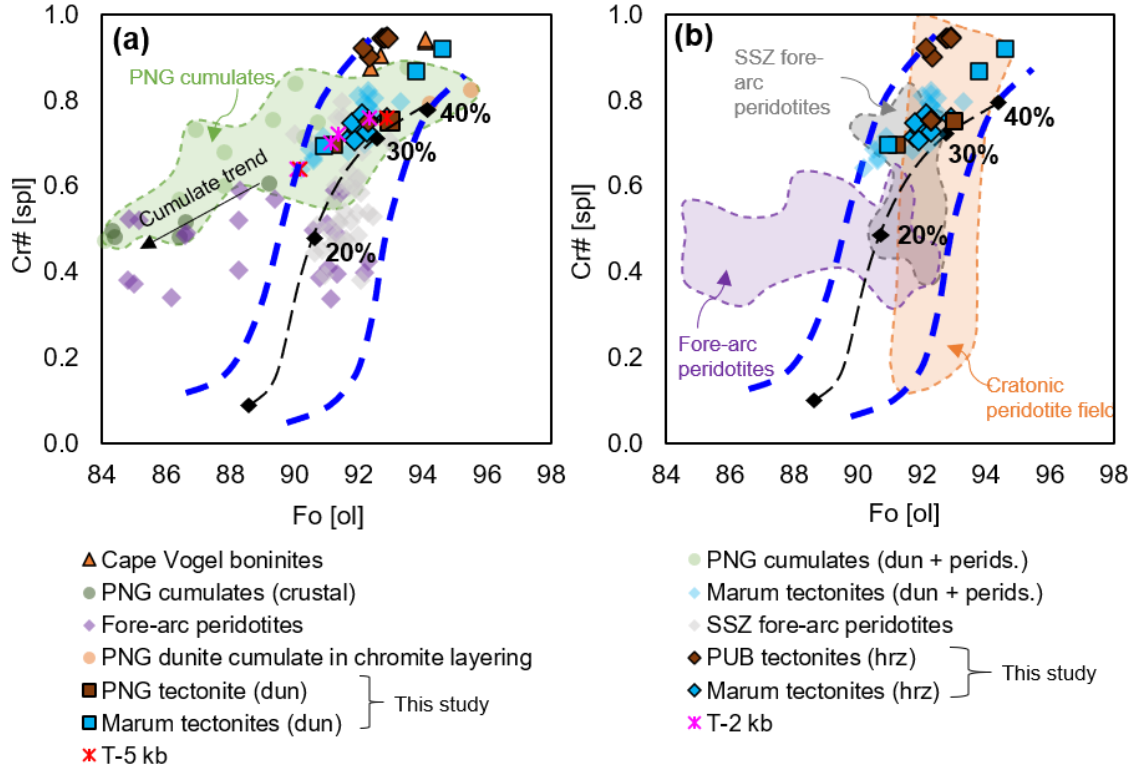


Figure 3.3. (a) and (b) show variations in spinel Cr# vs. olivine Fo content. Olivine spinel mantle array (OSMA) and anhydrous melt estimates (black dashed lines) are from Arai (1994). T-2 and T-5 represent residual spinel between 1150–1300 °C at 2 kb and 1150–1350°C at 5 kb from Jaques & Green (1980). PUB data is from Jaques & Chappell (1980), and England & Davies (1973). Marum data is from Jaques (1980) and Kaczmarek *et al.* (2015). Cape Vogel boninites from Walker & Cameron (1983). Fore-arc peridotites from Franz *et al.* (2002), SSZ fore-arc peridotites from Ishii *et al.* (1992), and cratonic peridotite field drawn from Scott *et al.* (2019 and references therein).

plot at the extreme end of the OSMA trend overlapping the most refractory spinels and olivines (highest Cr# and Fo) in cratonic peridotite residues (Fig. 3.3b). The Marum tectonites cluster around similar spinel Cr# and olivine Fo compositions to those observed in SSZ fore-arc peridotites from Ishii *et al.* (1992), whereas fore-arc peridotites from Franz *et al.* (2002) span a much lower spinel Cr# and olivine Fo range and do not overlap with any of the PNG tectonite peridotites (Fig. 3.3b). Exceptionally Cr-rich spinels (Cr# = 0.80–0.90) like those in the PUB harzburgites are also found in the Cape Vogel boninites (Walker & Cameron, 1983).

3.4.2. Whole-rock major and trace elements

Whole-rock major element abundances from this study and Jaques (1980) are reported in Table 3.1. The PNG mantle tectonites have high Cr/Al ratios ranging from 1.3 to 3.1 in the Marum harzburgite tectonites and to higher values in the PUB harzburgite tectonites (3.5–12.7), exceeding values in other depleted ophiolite peridotites (e.g., Marchesi *et al.*, 2009). The extreme Cr/Al ratios in the PUB harzburgite tectonites exceed also those of the highly depleted Murowa cratonic peridotites (Pearson *et al.*, 2018) (Fig. 3.4a). Fe contents in the PUB and Marum harzburgite tectonites show a narrow range between 6.9 and 7.5 wt. % FeO, whereas the dunite tectonites show a larger range between 5.8 and 9.3 wt. % FeO. Al and Ca contents in all PNG tectonites are highly depleted with $\text{Al}_2\text{O}_3 < 0.35$ wt. %; median 0.22 wt. %, and $\text{CaO} < 0.31$ wt. %; median 0.19 wt. % (Fig. 3.4b). These median values, along with those found in the ultra-depleted peridotites of the Iwanadake massif, Japan (Kubo, 2002) are the lowest of any terrestrial peridotites, being considerably more depleted than average cratonic peridotite (Pearson & Wittig, 2014), or even the most depleted cratonic peridotites such as those from East Greenland (Hanghøj *et al.*, 2001) and Zimbabwe (Pearson *et al.*, 2018). As with their in-situ major elements, the Al and Ca contents in the PUB harzburgite tectonites are noticeably more depleted than the Marum harzburgite tectonites (Fig. 3.4c).

Whole-rock trace element abundances from this study are reported in Table 3.2. Most of the trace element abundances in the PNG mantle tectonites are exceptionally low (but above ICP-MS detection limits) with, for example, bulk Ti concentrations <5 ppm excluding dunites 414, KD3, and harzburgite 489 which have 21.3, 14.5, and 13.3 ppm Ti, respectively. Two peridotites in this study (KD1 and KD2) show anomalously high incompatible trace element abundances to other PNG tectonites (Fig. 3.5). KD1 and KD2 show very high degrees of alteration (LOIs of 9.38 and 12.50 wt. %, respectively; Table 3.1), however, dunite KD3, that also shows high degrees of alteration (9.47 wt. % LOI), show distinct incompatible element abundances to KD1 and KD2, but are similar to the typical PNG tectonites patterns (Fig. 3.5). These more elevated Ti values in KD1 and KD2 (49.4–55.6 ppm) are still well below layered cumulate peridotites and pyroxenites from both ophiolites which typically lie in the range 60–300 ppm Ti (Jaques & Chappell, 1980; Jaques *et al.*, 1983). Excluding KD1 and KD2, the PNG mantle tectonites show similar trace element

Table 3.1: Whole-rock major and trace element abundances in the PNG tectonites

Location: Marum ophiolite												
Sample:	MA4	088	090	425	#087	#414	#423	#473	#488	#489	#490	#492
Rock type:	Hrz	Dun	Hrz	Hrz	Dun	Dun	Hrz	Hrz	Hrz	Hrz	Hrz	Hrz
<i>XRF (wt.%)</i>												
SiO ₂	45.64	42.48	44.61	44.50	42.10	40.66	43.98	44.80	43.72	44.65	42.72	43.68
TiO ₂	–	0.01	–	–	<0.002	0.004	0.002	0.002	<0.002	0.003	<0.002	<0.002
Al ₂ O ₃	0.28	0.35	0.33	0.32	0.03	0.31	0.25	0.34	0.23	0.25	0.09	0.18
FeO*	7.32	5.76	7.51	7.06	6.25	9.26	7.49	7.43	7.27	7.44	7.45	7.50
MnO	0.11	0.09	0.12	0.11	0.10	0.15	0.12	0.12	0.13	0.13	0.12	0.13
MgO	46.42	51.01	47.19	47.75	51.47	49.42	47.97	47.05	48.47	47.21	49.52	48.33
CaO	0.18	0.24	0.20	0.20	0.05	0.19	0.19	0.25	0.17	0.31	0.09	0.19
Na ₂ O	0.03	0.06	0.05	0.05	0.01	<0.01	<0.01	<0.01	<0.01	<0.01	<0.01	<0.01
P ₂ O ₅	0.01	–	–	–	<0.001	<0.001	<0.001	<0.001	<0.001	<0.001	<0.001	<0.001
SUM	100	100	100	100	100	100	100	100	100	100	100	100
LOI	5.57	2.60	-0.03	1.12	2.83	2.15	2.90	2.06	4.69	3.80	3.06	5.07
Cr/Al	2.2	3.7	1.6	1.3	13.7	2.8	1.7	1.5	1.5	1.9	3.1	2.6
Ca/Al	1.2	1.2	1.1	1.1	3.0	1.2	1.4	1.4	1.3	2.3	1.8	1.9
<i>XRF (ppm)</i>												
Rb	<0.5	<0.5	<0.5	<0.5	<0.1	<0.1	<0.1	<0.1	<0.1	<0.1	<0.1	<0.1
Sr	<1	<1	<1	<1	<0.1	<0.1	<0.1	<0.2	<0.1	<0.1	<0.1	<0.1
Y	<1	<0.5	<0.5	<0.5	<1	<1	<1	<1	<1	<1	<1	<1
Zr	<1	8	7	7	<1	<1	<1	1	<1	1	<1	<1
V	14	7	19	7	4	14	11	19	8	17	5	15
Ni	2662	3274	2346	2654	2710	1850	2500	2410	2540	2400	2680	2630
Cr	3093	6552	2766	2154	2140	4460	2210	2560	1790	2420	1490	2390
Nb	<0.5	<0.5	<0.5	<0.5	<1	<1	<1	1	<1	<1	<1	<1
Ga	<1	<1	<1	<1	–	–	–	–	–	–	–	–
Cu	6	<1	<1	<1	4	5	4	3	3	4	6	3
Zn	29	38	48	45	38	47	45	48	44	46	46	44
Co	94	119	119	118	–	–	–	–	–	–	–	–
Ba	<3	13	13	12	–	–	–	–	–	–	–	–

La	<2	<2	<2	<2	-	-	-	-	-	-	-	-
Ce	<1	<2	<2	<2	-	-	-	-	-	-	-	-
U	<0.5	<0.5	<0.5	<0.5	-	-	-	-	-	-	-	-
Th	<0.5	<0.5	<0.5	<0.5	-	-	-	-	-	-	-	-
Sc	<1	<1	5	5	2	6	6	7	6	8	4	6
Pb	<1	<1	<1	1	-	-	-	-	-	-	-	-

Table 3.1: Continued

Location:	Papuan ultramafic belt							
Sample:	KD1	KD2	KD3	*714	*715	*716	*720	726
Rock type:	Hrz	Dun	Dun	Hz	Hz	Hz	Hz	Hz
<i>XRF (wt.%)</i>								
SiO ₂	45.50	42.19	41.59	43.84	43.99	43.83	43.82	44.97
TiO ₂	–	–	–	<0.002	<0.002	<0.002	<0.002	–
Al ₂ O ₃	0.26	0.11	0.20	0.05	0.06	0.04	0.03	0.14
FeO*	7.64	7.40	9.16	7.48	6.92	6.95	6.90	7.18
MnO	0.11	0.10	0.14	0.12	0.11	0.12	0.11	0.11
MgO	46.18	50.09	48.75	48.46	48.88	49.02	49.09	47.48
CaO	0.27	0.06	0.09	0.04	0.03	0.03	0.04	0.06
Na ₂ O	0.04	0.03	0.05	<0.01	<0.01	<0.01	<0.01	0.05
P ₂ O ₅	0.01	0.01	0.01	<0.001	<0.001	<0.001	<0.001	0.00
SUM	100	100	100	100	100	100	100	100
LOI	9.38	12.50	9.47	2.2	1.98	1.66	1.81	0.67
Cr/Al	2.1	3.7	4.1	10.3	6.9	11.7	12.7	3.5
Ca/Al	1.9	1.0	0.8	1.5	0.9	1.4	2.4	0.8
<i>XRF (ppm)</i>								
Rb	<0.5	<0.5	<0.5	<0.1	<0.1	<0.1	<0.1	<0.5
Sr	<1	<1	<1	<0.1	<0.1	<0.1	<0.1	<1
Y	<1	<1	<1	<1	<1	<1	<1	<0.5
Zr	<1	<1	<1	<1	<1	<1	<1	7
V	17	14	20	9	9	8	8	12
Ni	2530	3447	2862	2740	2760	2740	2790	2580
Cr	2771	2063	4226	2680	2150	2410	1980	2494
Nb	<0.5	<0.5	<0.5	<0.5	<0.5	0.5	<0.5	<0.5
Ga	<1	<1	<1	–	–	–	–	<1
Cu	<2	<2	4	<1	<1	<1	<1	<1
Zn	23	22	38	44	42	42	42	47
Co	116	102	133	–	–	–	–	121
Ba	<3	<3	<3	–	–	–	–	9
La	<2	<2	<2	–	–	–	–	<2
Ce	1	<1	<1	–	–	–	–	<2

U	<0.5	<0.5	<0.5	—	—	—	—	<0.5
Th	<0.5	<0.5	<0.5	—	—	—	—	<0.5
Sc	1	<1	<1	4	3	3	3	2
Pb	<1	<1	<1	—	—	—	—	<1

Major elements (wt. %) are measured by XRF and values anhydrous normalized to 100. Trace elements (ppm) are measured on pressed powder pellets. FeO* = Total Fe₂O₃ and FeO. ‡ = samples values from Jaques & Chappell (1980) and Jaques (1980). LOI = Loss on ignition.

Table 3.2: Whole-rock trace element abundances via solution ICP-MS for PNG tectonites

Zr	—	0.0046	0.0475	—	0.0043	—	0.0047	—	—	0.0190	—	—
Nb	0.001	0.001	0.002	0.004	0.010	0.004	0.004	0.004	0.002	0.003	0.002	0.002
Rb	0.034	—	0.001	—	0.009	—	0.009	—	—	0.005	0.001	—
Y	—	0.0059	0.0121	0.0021	0.0118	0.0013	0.0056	0.0021	0.0060	0.0263	—	—
Mo	0.426	0.531	0.595	0.430	0.355	0.476	0.512	0.445	0.458	0.423	0.475	0.430
Cs	0.004	0.000	0.001	—	0.001	—	0.001	—	0.001	0.004	0.006	0.000
Ba	0.358	0.025	0.025	—	0.140	—	0.083	0.002	—	0.012	0.008	—
Hf	—	—	0.001	—	—	—	—	—	—	0.001	—	—
Pb	—	0.011	0.010	—	—	—	0.006	—	—	—	—	—
Mn	728	643	572	888	1064	816	831	861	775	814	775	758
Fe	62386	62101	53594	75644	90988	69968	73217	71470	67021	68261	68114	65381
Ni	2324	2628	2949	2201	1784	2368	2464	2296	2386	2219	2502	2261

Table 3.2: Continued

Location: Papuan ultramafic belt										
Sample:	KD1	KD2	KD3	714	715	716	720	726		
Rock type:	Hrz	Dun	Dun	Hzr	Hzr	Hzr	Hzr	Hzr		
<i>ICP-MS (ppm)</i>										
La	0.04051	0.07724	0.00365	0.00015	0.00128	0.00091	0.00137	–		
Ce	0.06009	0.21071	0.00175	0.00055	0.00279	0.00188	0.00313	0.00025		
Pr	0.00635	0.03069	–	0.00007	0.00027	0.00023	0.00025	–		
Nd	0.02526	0.15000	–	0.00029	0.00118	0.00082	0.00121	–		
Sm	0.00699	0.04103	–	–	0.00020	0.00012	0.00029	–		
Eu	0.00425	0.01141	0.00016	–	–	–	–	–		
Gd	0.00294	0.04531	–	–	–	–	–	–		
Tb	0.00194	0.00966	–	–	0.00003	0.00004	0.00004	–		
Dy	0.01484	0.06112	0.00040	–	0.00018	0.00029	0.00025	–		
Ho	0.00329	0.01334	0.00033	0.00002	0.00007	0.00007	0.00010	0.00003		
Er	0.01089	0.03865	0.00194	0.00011	0.00035	0.00027	0.00023	0.00004		
Yb	0.01214	0.03641	0.00609	0.00054	0.00037	0.00099	0.00062	0.00067		
Lu	0.00214	0.00573	0.00155	0.00024	0.00014	0.00015	0.00016	0.00014		
Location: Marum ophiolite										
Sample:	MA4	087	088	090	414	423	425	473	488	489
Rock type:	Hrz	Dun	Dun	Hzr	Dun	Hzr	Hzr	Hzr	Hzr	Hzr
<i>ICP-MS (ppm)</i>										
La	–	0.00009	0.00125	–	–	–	0.00018	–	–	–
Ce	–	0.00047	0.00368	–	–	–	0.00080	–	–	–
Pr	–	0.00005	0.00050	–	–	–	0.00007	–	–	–
Nd	–	0.00033	0.00248	–	–	–	0.00043	–	–	–
Sm	–	0.00010	0.00084	–	–	–	–	–	–	–
Eu	–	–	0.00010	–	–	–	–	–	–	–
Tb	–	0.00005	0.00026	–	–	–	0.00005	–	0.00039	–
Dy	–	0.00057	0.00179	–	0.00015	–	0.00052	–	0.00001	0.00322
Ho	–	0.00017	0.00042	–	0.00032	0.00005	0.00015	0.00013	0.00025	0.00109
Er	0.00037	0.00104	0.00182	0.00063	0.00281	0.00073	0.00110	0.00075	0.00143	0.00437
Yb	0.00150	0.00198	0.00322	0.00233	0.00954	0.00353	0.00320	0.00294	0.00431	0.00928
Lu	0.00062	0.00054	0.00064	0.00078	0.00216	0.00100	0.00074	0.00096	0.00119	0.00200
										0.00050
										0.00057

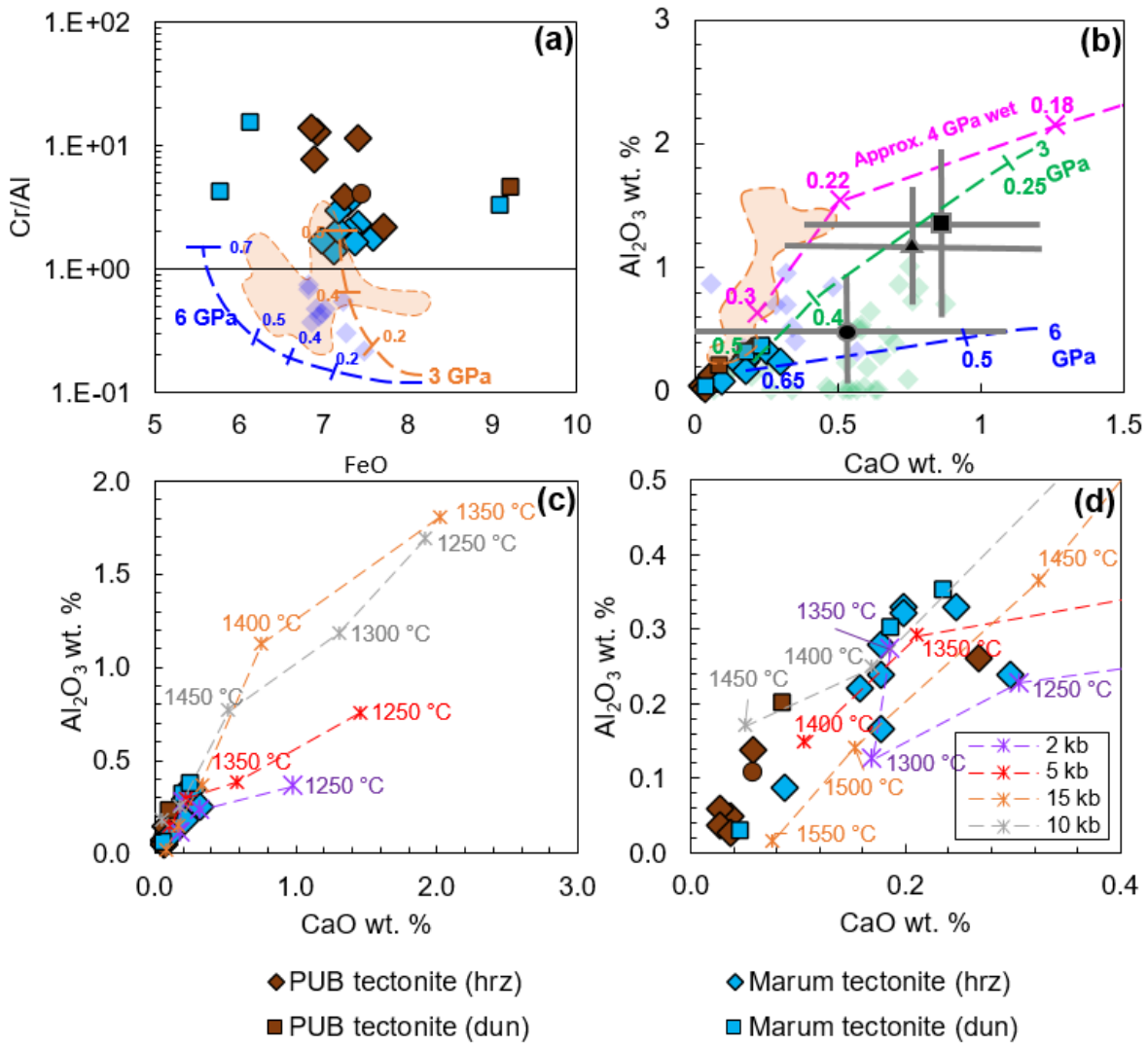


Figure 3.4. Select whole-rock major elements abundances in the PNG tectonites showing extremely high levels of melt depletion. (a) Cr/Al atomic ratios vs. FeO wt. % and (b) Al_2O_3 wt. % vs. CaO wt. % plotted against depleted ophiolite peridotites (transparent blue diamonds) from Marchesi *et al.* (2006), highly depleted abyssal peridotites (transparent green diamonds) (Harvey *et al.*, 2006; Godard *et al.*, 2008), and depleted cratonic peridotites from Murowa (orange field) from Pearson *et al.* (2018). Grey crosses with black symbols in (b) represent average cratonic peridotite (triangle = Kaapvaal, circle = North Atlantic, square = Venetia; Pearson *et al.*, 2018). Anhydrous batch melting trends at 3 GPa (orange/green dashed lines) and 6 GPa (dark blue dashed line) from Walter (1998) and hydrous melting resides at 4 GPa (pink dashed line) from Wang *et al.* (2020). (c) and (d) show compositions of melt residues between 2–15 kb from peridotite experiments in Jaques & Green (1980) plotted against the PNG data from (b).

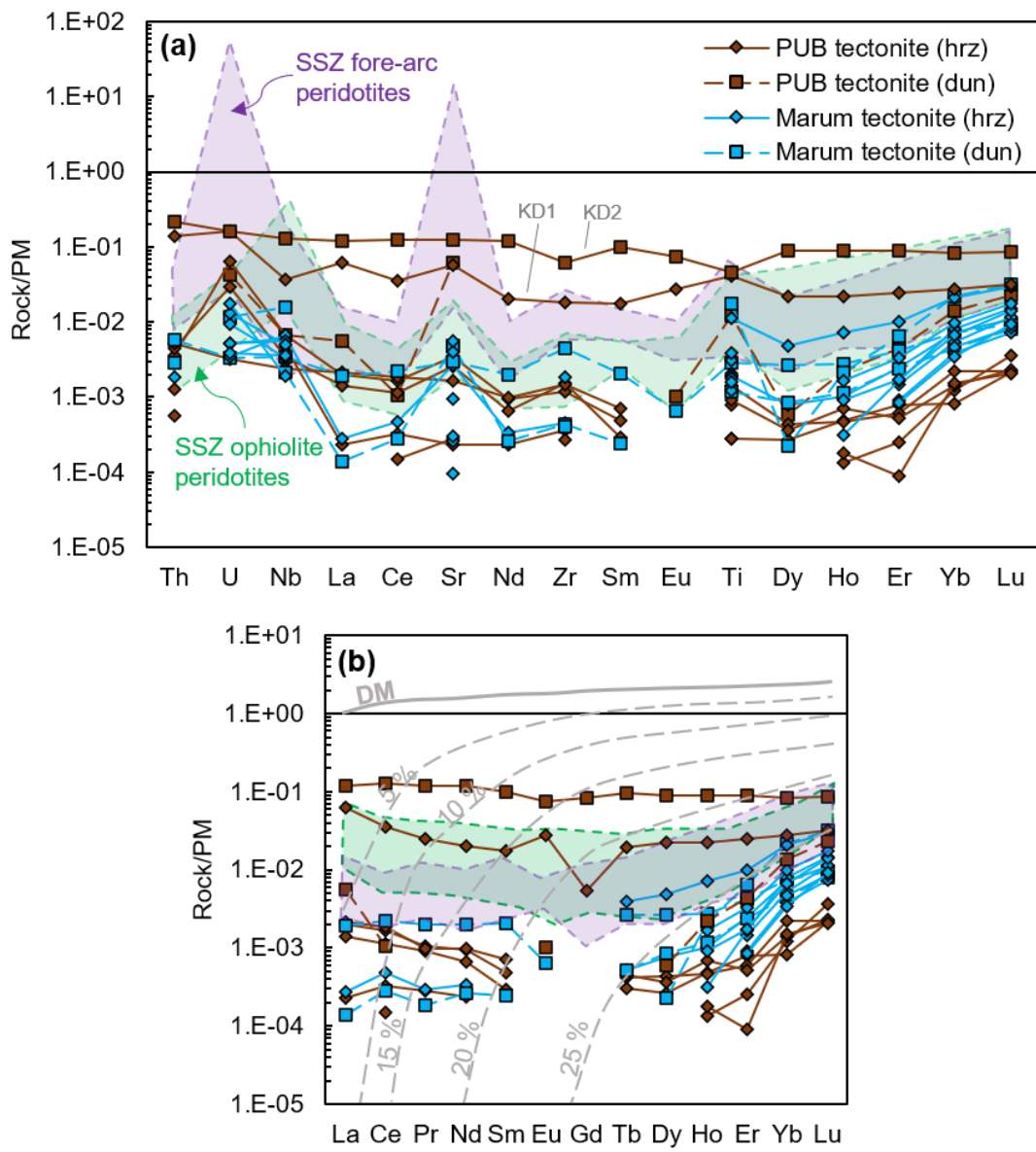


Figure 3.5. Plots of extended whole-rock REE (a) and REE only (b) normalized to primitive mantle (McDonough & Sun, 1995). The purple field represents fore-arc peridotites (Parkinson & Pearce, 1998), and green fields represents suprasubduction zone (SSZ) ophiolite peridotites from Uysal *et al.* (2012) in (a) and New Caledonia (Secchiari *et al.*, 2020) in (b). Anhydrous partial melt-estimates between 0–25 % in (b) calculated following method in Hellebrand *et al.* (2002) in the spinel stability field using partition coefficients from Ionov *et al.* (2002). DM starting compositions are from Salters & Stracke (2004).

patterns to SSZ-type ophiolite and fore-arc peridotites (e.g., Parkinson & Pearce, 1998; Uysal *et al.*, 2012; Secchiari *et al.*, 2020), aside from the large positive Sr and U anomalies observed in the fore-arc samples. The Marum and PUB mantle tectonites display lower incompatible trace element abundances compared to other SSZ tectonites, with the lowest values observed in the PUB samples. This is shown by their low total HREE abundances that exhibit steep HREE to MREE depletions in Fig. 3.5a. The PUB tectonites can be further distinguished from the Marum tectonites by their slightly positive LREE enrichment and resulting “U-shaped” REE pattern in most of these peridotites. Similar U-shaped REE patterns are observed in SSZ mantle harzburgites from New Caledonia (Secchiari *et al.*, 2020), however, the total REE abundance in these peridotites are higher than the PNG tectonites. In the PNG mantle tectonites, whole-rock Ti is positively correlated with Yb across all samples (Fig. 3.6a) and whole-rock V vs. Yb trends span the spectrum from normal mantle (\sim FMQ) to more oxidized ($\text{FMQ}+1$) $f\text{O}_2$ conditions as found in SSZ peridotites (Fig. 3.6b). Titanium and V contents are also positively correlated in the mantle peridotites and with the overlying cumulate peridotites and gabbros in both the PUB and Marum ophiolites. This is most defined in the Marum ophiolite which shows a linear relationship from the low abundances in the mantle rocks to increasing V and Ti levels over a wide compositional range in the cumulates (Appendix 2), with the exception of fractionated MgO-poor quartz dolerite dykes and gabbro pegmatoids in the Marum gabbro sequence which show a relative depletion in V at high Ti levels (\geq 5000 ppm Ti). A correlation of Ti and V for tectonites, cumulates and basalts for the PUB was interpreted as suggesting a genetic link between all units (Jaques & Chappell, 1980) as the partition coefficients for Ti and V in the major phases during both mantle melting (olivine, pyroxene, spinel, garnet) and crystallizing from basaltic magma (olivine, pyroxene, plagioclase) at high temperature are less than unity and approximately similar (e.g., Duke, 1976; Mallmann & O’Neill, 2009). However, the new ICP-MS analyses of Ti indicate displacement of some PUB tectonites from this trend to lower Ti values.

3.4.3. Mineral Chemistry: *in-situ* trace elements

Select trace elements in olivine and orthopyroxene were measured in the harzburgite and dunite tectonites (Appendix 4).

3.4.3.1. Olivine

The PUB and Marum olivines in the tectonite peridotites have very low abundances of lithophile

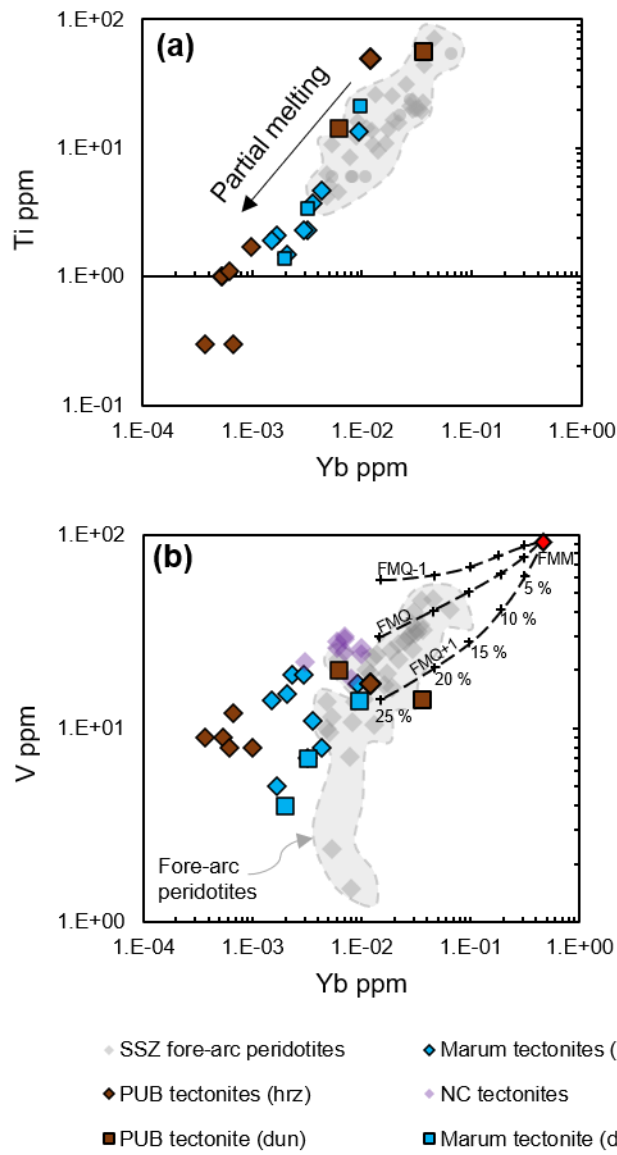


Figure 3.6. Whole-rock variation plots of Ti vs. Yb and V vs. Yb plotted against SSZ fore-arc peridotites from Uysal *et al.* (2012) in (a) and SSZ fore-arc peridotites from Parkinson & Pearce (1998) and New Caledonia SSZ peridotites from Secchiari *et al.* (2020) in (b). Partial melting estimates, oxygen fugacity (FMQ) values and fertile MORB mantle (FMM) are from Pearce *et al.* (2000) and references therein.

trace elements. Olivine in the PUB harzburgites have average values: 1.3–2.2 ppm Al, 62–124 ppm Ca, 0.1–0.4 Ti, 0.4–0.9 V, 16–46 ppm Cr. Olivine in the Marum harzburgites have very similar to or slightly higher average abundances: 3.3–4.8 ppm Al, 106–140 ppm Ca, 0.4–2.1 ppm

Ti, 0.2–0.6 ppm V, 12–21 ppm Cr. Abundances of incompatible elements such as REE in olivine are very low in both the PUB and Marum peridotites and, even with the enhanced detection limits offered by sector-field LA-ICP-MS, many REE are below detection limits and lower than the average olivine compositions reported for the depleted New Caledonia harzburgites by Secchiari *et al.* (2020) (Fig. 3.7). HREE abundances in olivine, primarily Tm, Yb, and Lu in Fig. 3.7a, are distinctly higher in the Marum dunite tectonites (414, 087, 088) than both in the Marum and PUB harzburgites. Olivine in the high-Mg Marum dunite tectonites (088 and 087) have slightly higher Ca and similar Ti abundances (147–243 ppm Ca, 1.1–1.5 ppm Ti) to olivine from both the Marum (106–140 ppm Ca, 0.4–2.1 ppm Ti) and PUB harzburgites (62–124 ppm Ca, 0.1–0.4 ppm). Olivine in low-Mg Marum dunite (414) has markedly higher Ca and Ti (662 ppm Ca, 3.1 ppm Ti) abundances than the high-Mg Marum dunite tectonites and the Marum and PUB harzburgites which are extremely depleted. Trace elements in PUB dunite olivine KD3 were not analyzed in this study.

3.4.3.2. Orthopyroxene

Orthopyroxene in the PUB and Marum harzburgites also have very low abundances of lithophile elements. Orthopyroxene in the PUB harzburgites have averages of 534–1285 ppm Al, 892–1445 ppm Ca, 3–8 ppm Ti, 8–12 ppm V, 705–744 ppm Ni, 840–1427 ppm Cr. Orthopyroxene in the Marum harzburgites have very similar to or slightly higher average abundances of lithophile trace elements: 8–42 ppm Ti, 36–48 ppm V, 595–702 ppm Ni, but significantly higher Al (3715–5654 ppm), Ca (4967–6906 ppm), and Cr (2656–3248 ppm), reflecting the higher degrees of depletion observed in the major element abundances in the PUB harzburgites. Similar low trace element abundances in orthopyroxene to the PNG mantle tectonites are observed in orthopyroxene from previously reported depleted harzburgites including Moana Lake peridotite xenoliths from New Zealand (Ti = 0.2–32.9 ppm, V = 29–45 ppm, Ni = 644–794 ppm; Scott *et al.*, 2016) and Kopeto and Yaté ophiolite peridotites from New Caledonia (Ti = 1.1–7.0 ppm; V = 50–88 ppm; Ni = 612–734 ppm; Secchiari *et al.*, 2020). The entire REE suite in the orthopyroxenes was not able to be measured in a fully quantifiable way as for olivine due to very low abundances. However, proxies for HREE and Ga in orthopyroxene display lower values in the PUB tectonites compared to the Marum tectonites, similar to their whole-rock REE compositions (Fig. 2.4). Orthopyroxene in the Marum harzburgite reported by Kaczmarek *et al.* (2015) shows strong depletion in LREE in relation to both middle and HREE.

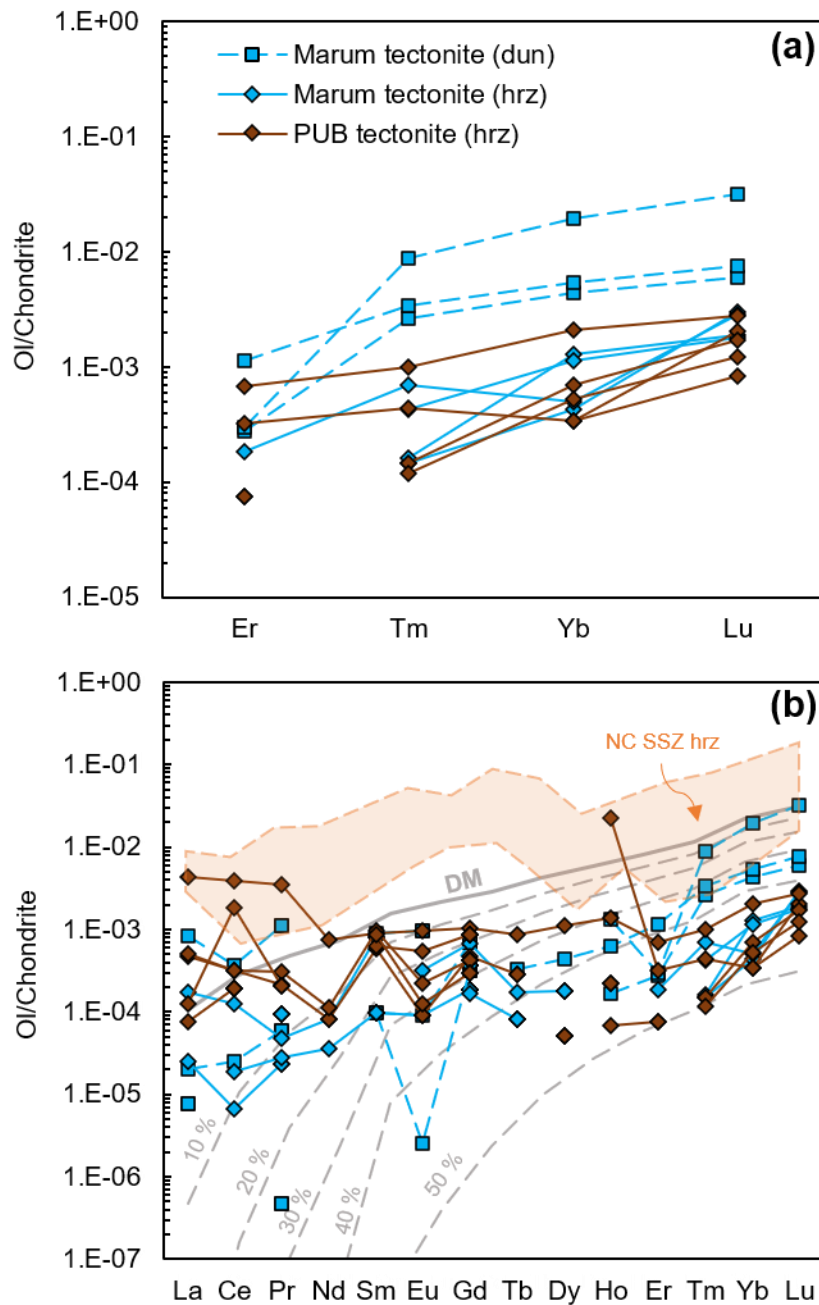


Figure 3.7. (a) Select HREE and (b) total REE abundances normalized to chondrite (McDonough & Sun, 1995). Orange shaded field represents REE in olivines from New Caledonian ophiolite peridotites (Secchiari *et al.* 2020). Grey lines represent modelled partial melting of olivine in the spinel stability field assuming 2% melting in the garnet stability field. DM values from Salters & Stracke (2004) and olivine (forsterite) partition coefficients from Burnham & O'Neill (2020). Olivines in KD1, KD2, and KD3 were not measured for REE.

3.4.4. Whole-rock HSE and Os isotope signatures

HSE abundances and $^{187}\text{Os}/^{188}\text{Os}$ ratios in the PNG tectonites are summarized in Table 3.3. Chondrite-normalized HSE patterns in the mantle tectonites from the PUB and Marum ophiolites are distinctive, characterized by very low Os, Ir and Pt abundances that are depleted relative primitive upper mantle (PUM; Becker *et al.*, 2006) estimates (Fig. 3.8). In particular, Os abundances in the PNG tectonites are extremely variable and low for mantle tectonites (<1.1 ng/g). Os, Ir and Pt are also depleted relative to Ru, producing a pronounced Ru anomaly, however, Ru abundances are also slightly lower compared to PUM estimates. Ru abundances show very little variation, whereas Pd shows considerable variability, with values ranging from significantly lower than, to comparable with PUM. These very low abundances in Os, Ir and Pt are rarely observed in fore-arc mantle peridotites, or other mantle peridotites generally (Fig. 3.8a). However, some highly depleted mantle harzburgites from New Zealand and New Caledonia record similarly low Os, Ir, and Pt values and broadly similar PGE patterns (Fig. 3.8b). Pd abundances in the PNG mantle tectonites are similar to the large range shown by fore-arc peridotites in Fig. 3.8a, whereas the very low Pd levels observed in the New Zealand mantle peridotites in Fig. 3.8b are not observed in the PNG mantle peridotites and New Caledonia peridotites. The HSE patterns of the PUB tectonites therefore differ from the typical HSE patterns of large degree melt residues such as those observed in cratonic peridotites, with PUM-like, relatively unfractionated I-PGE (Ir, Os, Ru) and from the variably depleted P-PGE (Pd, Pt) abundances (e.g., Pearson *et al.*, 2004; Aulbach *et al.*, 2016), or flat HSE patterns that resemble PUM estimates (i.e., normal to mildly depleted oceanic mantle, e.g. Luguet *et al.*, 2003; Luguet & Reisberg, 2016). Unlike several major and trace elements in the PNG tectonites, there is no noticeable difference in PGE patterns between the PUB and Marum mantle tectonites and, therefore, the PGE abundances do not simply reflect varying degrees of melt depletion. PGE patterns also show no clear differences between PNG harzburgite or dunite tectonites apart from the higher Os content of KD1(4.4 ppb), which also has an Ir content closer to PUM estimates and hence an $[\text{Os}/\text{Ir}]_{\text{N}}$ value that is less fractionated than the residues (Fig. 3.8c).

Most PNG mantle tectonites fall within the $^{187}\text{Os}/^{188}\text{Os}$ range from sub-chondritic to PUM-like values (~ 0.130). Three of the tectonite peridotites (KD3, 715, and MA4) have whole-rock $^{187}\text{Os}/^{188}\text{Os}$ ratios that are significantly higher than this range, and overlap with the range shown

Table 3.3: Os isotopes and HSE abundances for PNG tectonites

Sample	Location	Rock type	$^{187}\text{Os}/^{188}\text{Os}$	Abs. 2σ	$^{187}\text{Re}/^{188}\text{Os}$	Abs. 2σ	T_{RD} (Ma)	Abs. 2σ (Ma)
KD1	PUB	Hrz	0.1284	0.0003	—	—	—	—
KD2		Dun	0.1207	0.0005	1.5744	0.2303	1072	496
KD3		Dun	0.1611	0.0049	0.0575	0.0391	—	—
*714		Hrz	0.1231	0.0004	0.0147	0.0015	737	488
*715		Hrz	0.1574	0.0060	3.8713	0.2829	—	—
716		Hrz	0.1214	0.0019	0.6963	0.0746	894	556
‡720		Hrz	0.1220	0.0026	7.2780	1.0453	—	—
†726		Hrz	0.1298	0.0002	—	—	—	—
MA4	MO	Dun	0.1577	0.0035	0.5972	0.1796	—	—
414		Dun (\pm cpx)	0.1280	0.0004	0.0356	0.0013	47	486
087		Dun (\pm opx)	0.1222	0.0002	0.0832	0.0047	857	488
088		Hrz	0.1227	0.0004	0.0874	0.0053	785	489
090		Hrz	0.1260	0.0006	0.1299	0.0062	324	490
423		Hrz	0.1204	0.0007	0.2546	0.0319	1107	502
473		Hrz	0.1289	0.0012	0.0204	0.0008	—	—
488		Hrz	0.1220	0.0005	0.0850	0.0044	885	493
489		Hrz	0.1244	0.0004	0.0281	0.0010	549	486
490		Hrz	0.1349	0.0033	0.2737	0.0762	—	—
492		Hrz	0.1246	0.0004	0.0122	0.0005	524	486

Table 3.3: Continued

Sample	Loc- ation	Rock type	Os (ppb)	Abs. 2σ	Ir (ppb)	Abs. 2σ	Ru (ppb)	Abs. 2σ	Pt (ppb)	Abs. 2σ	Pd (ppb)	Abs. 2σ	Re (ppb)	Abs. 2σ	$[Os/Ir]_N$	$[Pt/Pd]_N$
KD1	PUB	Hz	4.414	0.034	2.9674	0.0942	4.0778	0.1157	6.0308	0.1867	0.1015	0.0025	—	—	1.4	38.7
KD2		Dun	0.091	0.009	0.0855	0.0163	1.7906	0.0723	0.0874	0.0234	0.0216	0.0009	0.03	0.0033	1.0	2.6
KD3		Dun	0.476	0.011	0.6132	0.0397	3.0584	0.1173	¹⁸ 620 ₁	0.9947	0.255	0.0061	0.0056	0.0038	0.7	47.6
714		Hz	0.171	0.009	0.2473	0.0608	1.4702	0.0335	¹⁰ 071 ₆	0.3787	0.2992	0.0073	0.0032	0.0003	0.6	21.9
§715		Hz	0.024	0.002	0.0161	0.0161	1.5276	0.0331	0.1365	0.0089	0.0265	0.0036	0.0186	0.0004	1.4	3.4
716		Hz	0.085	0.009	0.0811	0.0210	1.5983	0.0345	0.1985	0.0092	0.0904	0.0030	0.0123	0.0003	1.0	1.4
§720		Hz	0.011	0.002	0.0361	0.0181	1.3444	0.029	0.1608	0.0083	0.038	0.0027	0.0164	0.0004	0.3	2.8
§726		Hz	0.004	0.001	0.0287	0.0102	0.9048	0.0196	0.175	0.0061	0.0198	0.008	0.0046	0.0001	0.1	5.8
MA4	MO	Hz	0.087	0.009	0.0859	0.0163	0.8700	0.0599	0.0436	0.0233	0.0496	0.0014	0.0103	0.0029	0.9	0.6
087		Dun (\pm opx)	0.224	0.009	0.4232	0.0202	1.9264	0.0465	0.4581	0.0144	0.0353	0.0018	0.0039	0.0001	0.5	8.5
088		Dun	0.179	0.009	0.2954	0.0196	1.6976	0.0369	0.2711	0.0129	0.0451	0.0022	0.0033	0.0001	0.6	3.9
090		Hz	0.233	0.009	0.382	0.0163	0.4739	0.0107	0.2533	0.0101	0.0278	0.0013	0.0063	0.0002	0.6	5.9
414		Dun (\pm cpx)	0.518	0.011	0.7633	0.0300	1.5839	0.0343	¹² 183 ₃	0.4761	0.5252	0.0127	0.0038	0.0001	0.6	15.1
423		Hz	0.073	0.009	0.0629	0.0177	1.4072	0.0306	0.2318	0.0128	0.0144	0.0026	0.0039	0.0001	1.1	10.5
473		Hz	0.639	0.011	0.127	0.0436	0.8901	0.0194	0.5344	0.0314	0.0186	0.0028	0.0027	0.0001	4.6	18.7
488		Hz	0.219	0.009	0.4698	0.025	1.1427	0.0247	0.8097	0.0244	0.0246	0.0026	0.0039	0.0001	0.4	21.4
489		Hz	0.638	0.011	0.507	0.0189	1.2426	0.0277	2.6400	0.0652	0.1669	0.0042	0.0037	0.0001	1.1	10.3
§490		Hz	0.009	0.001	0.0423	0.0114	0.8264	0.0182	0.1306	0.009	0.0055	0.0028	0.0018	0.0001	0.2	15.5
492		Hz	0.875	0.012	0.414	0.0200	0.3103	0.0074	2.2589	0.0563	0.0687	0.0028	0.0022	0.0001	1.9	21.4

* = $^{187}\text{Os}/^{188}\text{Os}$ values from ~0.005 ng of P3 spike (instead of ~ 0.03 ng). † = no spike added. ‡ = Re corrected $^{187}\text{Os}/^{188}\text{Os}$ value.

T_{RD} = Re depletion model age (assuming no Re addition) § = Os values taken from run with ~0.005 ng of P3 spike (instead of ~ 0.03 ng). N = PGEs normalized to chondrite (Fischer-Gödde *et al.*, 2010).

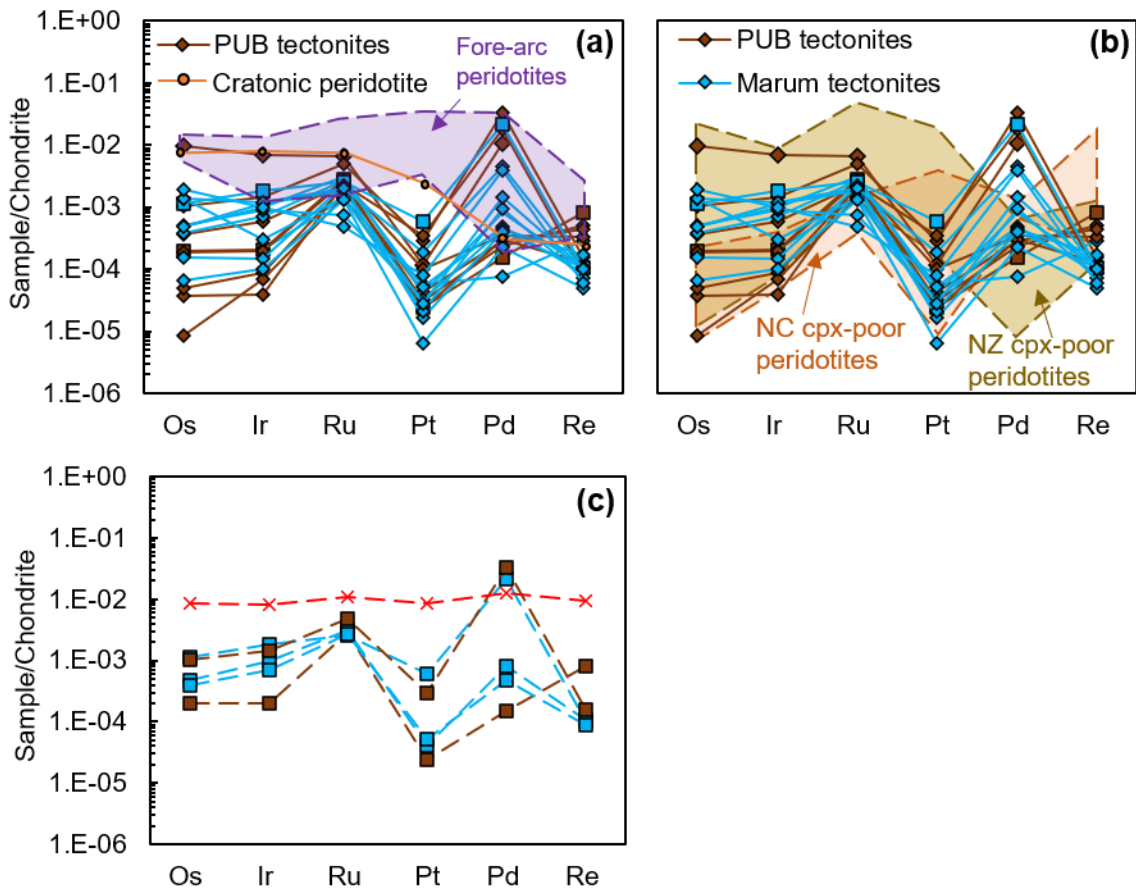


Figure 3.8. PGEs normalized to chondrite (Fischer-Gödde *et al.*, 2010). (a) and (b) show PNG tectonite harzburgites plotted against fore-arc peridotites (purple) and average cratonic peridotite xenoliths from Pearson *et al.* (2004) in (a) and cpx-poor tectonite peridotites from New Caledonia (Secchiari *et al.*, 2020) and New Zealand (Scott *et al.*, 2019) in (b). (c) PGE abundances in the PNG dunite tectonites. Red dashed line = primitive upper mantle.

by the more radiogenic end of the mid-ocean ridge peridotites (e.g., Snow & Reisberg, 1995; Lassiter *et al.*, 2014). Like fore-arc peridotites and global ophiolite peridotites, the $^{187}\text{Os}/^{188}\text{Os}$ ratios in the PNG tectonites show no correlation with whole-rock Al_2O_3 or Os abundances, or to Pt_N/Pd_N ratios (Figs. 3.9a–b).

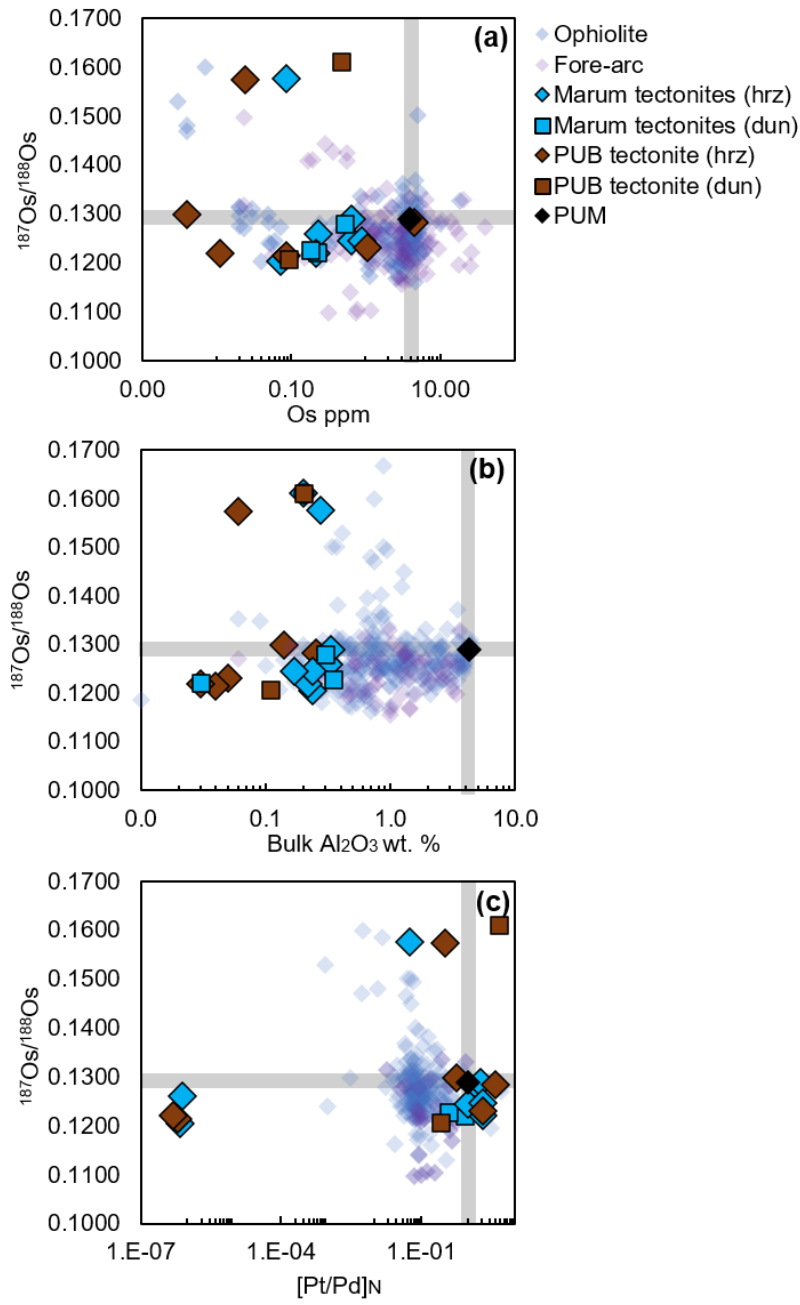


Figure 3.9. Variation plots showing (a) $^{187}\text{Os}/^{188}\text{Os}$ vs. Os, (b) $^{187}\text{Os}/^{188}\text{Os}$ vs. Al_2O_3 wt. %, and (c) $^{187}\text{Os}/^{188}\text{Os}$ vs. $[\text{Pt}/\text{Pd}]_N$, plotted against fore-arc peridotites (purple) and ophiolite peridotites (blue). See Appendix 6 for references. The grey crosses intersecting the black diamond represent the PUM value of Becker *et al.* (2016).

3.5. DISCUSSION

3.5.1. Equilibration conditions

Both the Marum and PUB tectonite peridotites preserve high-temperature deformation fabrics, with their granular to weakly porphyroclastic textures implying plastic deformation at high temperature (≥ 1200 °C, Mercier & Nicolas, 1975). Kaczmarek *et al.* (2015) inferred from the activation of A- and E-type slip systems in olivine in the Marum peridotites that the fabrics were consistent with a high-temperature and low-stress origin in the mantle, and likely resulted from plastic deformation during partial melting. Equilibration temperatures for the peridotites were calculated at 10 kbar using the two-pyroxene geothermometers of Brey & Köhler (1990) and Taylor (1998), and the Ca-in-enstatite (Köhler & Brey, 1990 with the Nimis & Grutter, 2010 modification for temperatures < 900 °C), the enstatite-in-diopside (Nimis & Taylor, 2000), and the olivine-spinel Fe-Mg (O'Neill & Wall, 1987) geothermometers. All gave temperatures of ~ 700 to 830 °C for the Marum harzburgites and dunites except for the Ca-in-enstatite geothermometer which gave higher disequilibrium temperatures (800–1000 °C). The PUB harzburgites gave similar or slightly lower temperatures (~ 640 –800 °C). These temperatures are well below the high magmatic crystallization temperatures (1100–1200 °C) recorded by relic primary pyroxenes in the overlying Marum cumulate peridotites and gabbro (Jaques, 1981) and indicate sub-solidus cooling. The sub-solidus pyroxenes in the Marum cumulate rocks have similar equilibration temperatures to the mantle peridotites.

3.5.2. Extent and environment of melt depletion in the PNG ophiolite peridotites

The rock fabrics, Mg-rich olivines, Mg-rich and Al-orthopyroxenes, and the Cr-rich spinels in the PNG tectonites are all consistent with an origin as depleted residues of large degrees of partial melting of mantle peridotite. The PNG tectonites are characterized by very high olivine Fo contents reaching Fo_{94.6} in the dunites and Fo_{92.6} in the harzburgites (Fig. 3.2a). Such high olivine Fo contents previously reported in ophiolite peridotites are typically confined to olivine in dunite lenses, often within or in contact with chromitite layers or seams (e.g., Rollinson, 2008), where high Fo contents are generated via Fe-Mg partitioning between olivine and spinel upon cooling (e.g., Fabriès, 1979). For this study, analyses of mineral rims and mineral inclusions have been excluded to ensure that interpretations reflect primary olivine compositions rather than similar late-

stage cooling processes. Rim and inclusion analyses are included in supplementary data for comparison. After excluding the rim and inclusion analyses, the primary olivine compositions in the PNG mantle tectonites still show high olivine Fo contents in association with extremely high spinel Cr# (0.70–0.95), confirming that these signatures resemble very high degrees of melt depletion compared to other ophiolitic peridotites.

3.5.2.1. Melt estimates from experimental studies

Experimental studies on a range of model mantle peridotites have shown that harzburgite assemblages, like several Marum harzburgites, characterized by olivine Fo_{91–92}, low alumina enstatite (<1.5 wt. % Al₂O₃) and high spinel Cr# (0.7–0.8), can form by large degrees (~15–30 %) of partial melting of depleted spinel lherzolite at low pressures (<1 GPa) under anhydrous conditions (e.g., Jaques & Green, 1980; Herzberg, 2004). Partial melting studies at higher pressures have also shown that spinels and orthopyroxenes in harzburgite (ol + opx + spl) and lherzolite (ol + opx + cpx + spl) residues from melting under both anhydrous and hydrous conditions have higher bulk Al contents (Jaques & Green, 1980; Falloon & Green, 1987; Gaetani & Grove, 1998; Walter, 1998; Falloon *et al.*, 1999; Green *et al.*, 2014) than the Al contents observed in harzburgites from this study (Figs. 3.2b & 3.3). An origin as residues of low-pressure melting is also supported by the major element compositions of the harzburgites which match the whole-rock compositions of experimental residues at low pressure (Figs. 3.4a & 3.4b). However, the PNG harzburgites with olivine >Fo₉₂ and chromite with Cr# >0.8, coupled with their extremely depleted major element and HREE chemistry, require higher degrees of partial melting, ~25 to >40 %, if derived from melting of fertile mantle peridotite (Fig. 3.3). The formation of such refractory compositions by melt fractions >30% for fertile peridotite sources or (re-) melting of a strongly depleted peridotite, under anhydrous conditions requires temperatures \geq 1300 °C and melting conditions close to the opx-out curve (Jaques & Green, 1980; Duncan & Green, 1987; Walter, 1998; Falloon & Danushevsky, 2000; Herzberg, 2004). Melting temperatures would be lowered by the presence of water (Katz *et al.*, 2003; Green *et al.*, 2014; Foley & Pinter, 2018) with experiments indicating that at ~1 GPa the opx-out melting curve lies up to 100 °C (depending on water content) below the anhydrous position.

Spinel Cr# compositions similar to those in the Marum harzburgite tectonites (e.g., spinel Cr# = 0.7–0.8) co-existing with olivine Fo_{90–92} is found in SSZ mantle harzburgites such as the Izu-Bonin Mariana (IBM) fore-arc (Fig. 3.3b; Ishii *et al.*, 1992), in refractory harzburgites from

New Caledonian ophiolites (Pirard *et al.*, 2013), and ophiolites from northern Oman (Tamura & Arai, 2006). Based on the experimental considerations above, spinel with Cr# up to ~0.8 can be produced by anhydrous melting of refractory peridotite with high Cr/Al beyond the opx-out boundary (Jaques & Green, 1980), or a water-fluxed melting environment (e.g., Arai, 1994; Mitchell & Grove, 2015; Scott *et al.*, 2019) to enhance the melt production, allowing total incremental melt fractions removed from these residual rocks to approach 40 %. Harzburgites from this study with spinel Cr# >0.85 to 0.95 have not been replicated by anhydrous melting experiments and are more likely residues from high levels of water-saturated melting at low pressures. This is supported by the high Cr# abundances in spinels (0.8–0.9) and high magnesian olivines (~Fo₉₄) from low-Ca PNG boninites reported in Walker & Cameron (1983) and 1–2 wt. % H₂O in melt inclusions from Kamenetsky *et al.* (2001). Despite this evidence, the co-existence of high temperatures with production of hydrous magmas in the mantle wedge is still not well-understood, and is often referred to as the “boninite paradox” (Sobolev & Chaussidon, 1996). In a recent experimental study of the water-saturated solidus of mantle peridotite Wang *et al.* (2020) suggested that boninite magmas may be produced by partial melting of mantle peridotite at lower temperature (1000–1200 °C) but higher pressure (3–4 GPa). Their experimental data suggest that refractory harzburgitic residues characterized by Mg-rich olivine (\geq Fo₉₂) and Al-poor orthopyroxene ± garnet could be produced by ≥25 % partial melting at 1150–1200 °C at these pressures (Fig. 3.4b). As the experimental starting composition did not include Cr, comparison of residual chromite compositions is not possible. This model might, as suggested by Wang *et al.* (2020), be applicable to more mature island arcs such as Japan, but is unlikely to apply to the PNG ophiolites given the petrological and experimental evidence in favour of formation of the peridotites (and overlying boninites in the case of the PUB) at low pressure. Moreover, the cumulate peridotites and gabbros that directly overlie the PNG mantle tectonite harzburgites crystallized at low pressure (~1–2 kb; Jaques, 1981), making it difficult to envisage a geological scenario where residual mantle tectonites are derived from much deeper processes (i.e., pressures of 4 GPa or more).

Highly depleted subduction-related peridotites such as the Lake Wanaka suite from New Zealand (Liu *et al.*, 2015), show a similar range in olivine and whole-rock Al compositions (Fo_{91.8–93.3}; Al₂O₃ = 0.05–0.47 wt. %) to the PUB and Marum tectonite harzburgites (Fo_{90.9–94.6}; Al₂O₃ = 0.03–0.35 wt. %). Spinel Cr# and whole-rock Ca in the Lake Wanaka suite (Cr# = 0.64–0.79; CaO

= 0.26–1.29 wt. %), which would otherwise be considered ultra-refractory, are noticeably less depleted than the most depleted PNG tectonites (PUB harzburgites) with spinel Cr# 0.90–0.95 and whole-rock CaO 0.03–0.06 wt. %. These mantle tectonites are lower in whole-rock Ca and Al contents than average cratonic residues, excepting the most depleted peridotites (e.g., Murowa; Pearson *et al.*, 2018), however, in terms of olivine Fo and spinel Cr#, the PNG tectonites are similar to typical cratonic residues (i.e., Fig. 3.3b). The very low whole-rock Ca and Al contents and high whole-rock Cr/Al ratios at generally low FeO (Fig. 3.4a & 3.4b; factoring in some scatter from melt-rock reaction) in all the PNG tectonites plot at the most depleted end, or exceed anhydrous melt experiments on such mantle whole-rock compositions (Jaques & Green, 1980; Falloon & Green, 1987; Walter, 1998). Globally, magnesian spinels with Cr# values of ≥ 0.85 , excluding chromite inclusions in diamonds, diamondiferous kimberlites and diamond-facies peridotites, are limited mostly to boninites, some komatiites (Barnes & Roedder, 2001), and to a small number of ophiolites (New Caledonia, Oman, Bay of Islands) where they mostly occur in discordant/replacive dunites (Pirard *et al.*, 2013; Arai *et al.*, 2006; Suhr *et al.*, 2003).

3.5.2.2. Melt-rock interaction and origin of dunites

Some replacive dunites from Suhr *et al.* (2003) that record olivine contents $>\text{Fo}_{93}$, are as high as Fo contents recorded in olivine from some Marum dunite tectonites in this study. While the PUB and Marum harzburgite tectonites have an upper olivine limit of $\text{Fo}_{92.6}$, the Marum dunite tectonites (samples 087 and 088) exceed Fo_{93} ($\text{Fo}_{93.8}$ and $\text{Fo}_{94.6}$, respectively), and probably experienced a similar process of melt interaction to the Bay of Islands dunites. Further evidence that dunite tectonites in this study formed through orthopyroxene dissolution rather than melt-depletion is best supported by their HREE in olivine abundances, where the most melt-depleted olivine HREE signatures are recorded in the harzburgite tectonites rather than the dunite tectonites (Figs. 3.7a & 3.7b). If these dunite tectonites represented high degree melt residues formed by greater amounts of depletion to harzburgites, their HREE abundances in olivine would be lowered to greater levels of melt depletion than olivine in the harzburgite tectonites, which is not what is observed. This distinction is not recognized in all melt-sensitive major elements such as spinel Cr#, olivine Fo and bulk Cr/Al, Ca and Al, suggesting that HREE may be more reliable for tracing true melt depletion in peridotites.

The depleted whole-rock HREE to MREE signatures in the dunite tectonites, except dunite KD2 (that will be discussed below), indicate that these dunites represent residues that were likely

overprinted during orthopyroxene dissolution. This process of orthopyroxene dissolution, is further supported by the presence of orthopyroxenite dykes with close to pure enstatite compositions that cross-cut the Marum and PUB harzburgites (Jaques & Chappell, 1980; Kaczmarek *et al.*, 2015). These enstatite dykes have depleted orthopyroxene LREE patterns that are similar to LREE patterns in orthopyroxene from co-existing harzburgites, except are higher in abundance (Kaczmarek *et al.*, 2015), suggesting they were derived from the harzburgites. This process may resemble melting of an already depleted harzburgite, initiated by the interaction with an olivine-saturated (possibly hydrous) melt (e.g., Aldanmaz *et al.*, 2020), resulting in incongruent melting of orthopyroxene, and leaving behind high Fo dunites. Such dunite–orthopyroxenite field relationships are commonly observed in ophiolite peridotites globally (e.g., Tamura & Arai, 2006; Le Roux, 2019; Lawley *et al.*, 2020). The difference between the high-Mg olivine ($>\text{Fo}_{93}$) and low-Mg olivine ($\leq\text{Fo}_{92}$) dunite tectonites in the PNG suite may be explained different degrees of melting recorded in the depleted harzburgites, possibly from varying amounts of water fluxing in the source prior to overprinting/orthopyroxene-dissolution, or by interaction with late-stage melts of different compositions (e.g., high Mg boninite vs. tholeiitic melts). The significantly higher olivine HREE abundances in the low-Mg olivine dunite tectonite (414) compared to the high-Mg olivine dunite tectonites (087 and 088), suggests that dunite 414 has only experienced lower degrees of partial melting (~10 %) prior to melt-rock interaction, and could also account for the small amounts of residual clinopyroxene present in this sample. The dunite tectonite 414 is probably similar to the clinopyroxene-bearing dunite bodies described in Kaczmarek *et al.* (2015) that were also attributed to refertilization of the depleted residual peridotite by a percolating silica- and Mg-rich melt.

For the PUB harzburgites, the very high spinel Cr# values and low Ti may also arise by “up-grading” of spinel Cr# by the interaction with high-Cr# and low Ti boninite melts (e.g., Fig. 3.10; Pearce *et al.*, 2000). While it is plausible that the percolation of such depleted boninitic melts from the second stage of melting may have acted to increase the Cr# of spinel without noticeably increasing the Ti abundances in spinel in the PUB harzburgites, the low HREE abundances in olivine from the PUB harzburgites are consistent with high degree hydrous melt residues, rather than melt-rock interaction. Three PNG mantle peridotites (including two dunites) that show

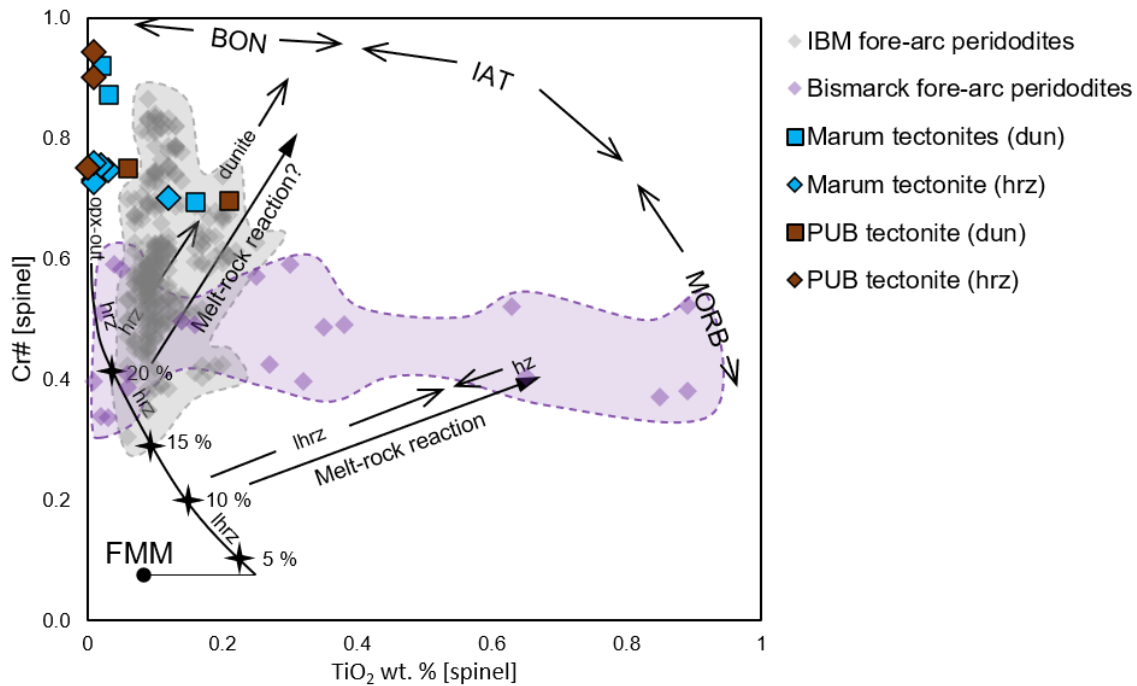


Figure 3.10. Plot of melt-rock reaction and partial melting trends using spinel Cr# vs. Ti. Annotations are adapted from Pearce *et al.* (2000). BON = boninite, IAT = island arc tholeiite, MORB = mid ocean ridge basalt, FMM = fertile MORB mantle. Izu-Bonin Mariana (IBM) fore-arc peridotites from Parkinson & Pearce (1998) and Bismarck fore-arc peridotites from Franz *et al.* (2000).

slightly elevated Ti spinel contents in Fig. 3.10, may support some melt-rock interaction with a lower Cr# and higher Ti melt. Excluding these dunites that have already been accounted for through melt-rock interaction, the Marum harzburgite with elevated spinel Ti may suggest this harzburgite has experienced a small amount of melt-rock interaction, but not to the extent of orthopyroxene dissolution. Most Marum harzburgites have very low Ti in spinel, suggesting that there was little to no melt-rock interaction in these samples. The anomalously high incompatible trace element abundances in harzburgite KD1 and dunite KD2 that show flat HREE to LREE patterns (Fig. 5b), could reflect the higher degrees of secondary alteration in these samples. While low temperature alteration cannot be ruled out, sample KD3, that displays similar high degrees of alteration does not exhibit unusually high incompatible trace elements abundances, suggesting that alteration is unlikely to be the source of these enrichments. KD1 and KD2 most probably resemble recrystallized tectonites or contain trapped melt phases. The remaining PNG mantle harzburgite and dunite tectonites all show HREE to MREE depletions, and have either whole-rock REE patterns that are flattened at the LREE end, with higher La/Nd ratios than expected for the large

degrees of melting suggested by their HREE depletions, or have LREE enrichment leading to U-shaped patterns (Fig. 3.5b). Such REE variability have been observed previously in ophiolitic and SSZ peridotites (e.g., Bodinier & Godard, 2003; Pearce *et al.*, 2000; Secchiari *et al.*, 2020). These observed whole-rock LREE enrichments relative to theoretical melting trends may indicate clinopyroxene re-addition from crystallizing interstitial melts (e.g., Simon *et al.*, 2003). However, clinopyroxene textures and major element chemistry points to exsolution from co-existing orthopyroxene rather than a metasomatic origin (Fig. 3.2d), indicating that the whole-rock REE enrichment is more likely due to the incomplete removal of melts in residual pore spaces that do not crystalize as clinopyroxene (e.g., Vernierès *et al.*, 1997). Instead of clinopyroxene addition, the REE patterns appear to be well modelled by the “plate model” of Vernierès *et al.* (1997) for the fractionation of trace elements during partial melting and melt percolation. In an open system melting model such as that likely to be present in the mantle, peridotites undergoing melting will also likely re-equilibrate with percolating incompatible-element-enriched melts generated within the same melting column. Within the context of such a model, the whole-rock REE patterns of the PNG residues appear to best resemble those produced in a model of two-phase porous flow with melt infiltration into the base of the melting column, that may have occurred during second stage melting in a mantle wedge being fluxed with water and producing hydrous melts. The LREE-enriched melts could be similar to those identified in the melt-inclusions in Cape Vogel boninites from Kamenetsky *et al.* (2002), which are surprisingly LREE-enriched considering their refractory major element characteristics.

3.5.3. Evidence for a multi-stage melting model

3.5.3.1. Relationship to overlying cumulates and lavas

The crystallization sequence of ol + spl + cpx + opx + pl and mineral compositional range of the cumulate minerals of both the PUB and Marum ophiolites indicate that these sequences formed by fractional crystallization and accumulation from magma(s) that differ from MORB in several important parameters. The Mg-rich nature of the cumulus olivine and its limited compositional range compared to MORB ($\geq\text{Fo}_{92-78}$ compared with Fo_{91-60}), the early and abundant crystallization of cumulus Mg-rich opx (Mg_{90-60}), the high Cr# values of early-formed cumulus spinel ($\text{Cr}\#\geq0.7-0.8$), the highly calcic nature of the plagioclase (An_{92-67}), and the very Ti- and Na-poor nature of the cumulus pyroxenes all point to crystallization from a Mg-rich tholeiitic magma with high Mg#

(>74), high Ni and Cr, and low TiO₂ and alkali contents (Jaques & Chappell, 1980; Jaques, 1981). Experimental studies have shown that the compositions of spinel crystalizing from a magma is governed by the composition of the melt (e.g., Barnes & Roedder, 2001; Kamenetsky *et al.*, 2001). Using the relationships defined for Al₂O₃ and TiO₂ by Rollinson (2008), spinels in PUB and Marum cumulate peridotites suggest their parental magma(s) had low TiO₂ (≤ 0.8 wt. %) and moderate Al₂O₃ (~10–12 wt. %) contents. The water content of the magma is unknown. An absence of primary amphibole (apart from in rare residual feldspar–quartz veins) suggests very low water contents but amphibole crystallization could have been suppressed by the high magmatic temperatures (1100–1200 °C) indicated by pyroxene thermometry (Jaques, 1981).

Peridotites and gabbros from both ophiolites have very low abundances LIL (Ba, Rb, K) of and high field strength elements (HFSE—Ti, Zr, Nb), and strongly LREE-depleted REE patterns (Jaques & Chappell, 1980; Jaques *et al.*, 1983). Parental magmas for both ophiolites were inferred from modelling of trace element partitioning between cumulates and co-existing melts to have been strongly depleted in LIL elements and LREE ($\text{La}_N/\text{Sm}_N \leq 0.6$) with $< 10 \times$ chondritic abundance of HREE, and lower abundances Ti and Zr than most MORB (Jaques & Chappell, 1989; Jaques *et al.*, 1983). PUB ophiolite basalts typically have very low (N-MORB-like) abundances of LIL elements (excluding those affected by sea-floor alteration), and lower Ti, Zr and Nb than N-MORB at equivalent Mg#, and are either strongly LREE-depleted ($\text{La}_N/\text{Sm}_N \leq 0.6$) or have slightly higher Ti and $\text{La}_N/\text{Sm}_N \sim 1$ similar to T-MORB (Jaques & Chappell, 1980; Rogerson *et al.*, 1991). In addition to these depletion signatures, many of the PUB lavas have high V and low Ti/V ratios (10–20; Appendix 2), a feature characteristic of fore-arc basalts (FAB; Reagan *et al.*, 2010; Hickey-Vargas *et al.*, 2018). The parent magma(s) for both the PUB and Marum cumulate sequences differed from MORB, being more depleted in Ti and LREE and higher in silica (Jaques & Chappell, 1980; Jaques *et al.* 1983). It differed from the LREE-enriched low-Ca boninites like those of Cape Vogel overlying the PUB but shared some of the geochemical features of the LREE-depleted tholeiitic basalts underlying the boninites (cf. Konig *et al.*, 2010). The absence of primary amphibole in the overlying PUB basalts and pillow lavas (Davies, 1971; Jaques & Chappell, 1980) suggests their mantle source regions did not necessarily require a highly water-fluxed environment during the initial stages of subduction. The anhydrous melting experiments by Jaques & Green (1980) demonstrate that Marum tectonites, reflecting more moderate levels of melt-depletion compared to the PUB tectonites, can be replicated through

anhydrous melting at low pressures and high temperatures (Figs. 3.2c, 3.3a, 3.3b, & 3.4c). These experiments show that low pressure (2–5 kb) conditions satisfy more Cr-rich spinel compositions compared to higher pressure (10–15 kb) conditions (Fig. 3.3a) and that, while Al_2O_3 in orthopyroxene decreases with increasing temperature, Al_2O_3 is consistently lower at low pressure (2–5 kb) conditions than at the higher pressures (Fig. 3.2c). Both of these features indicate that higher spinel Cr and lower Al_2O_3 compositions in orthopyroxene are favoured at low pressures (2–5 kb,) and temperatures ≤ 1300 °C, whereas higher pressures would require temperatures > 1300 °C. The extremely depleted mineral chemistry observed in the PUB tectonites, however, was not replicated in the Jaques & Green (1980) experiments indicating further depletion either by more extreme melting at lower pressure or through addition of a fluid or melt. Evidence for later hydrous, low pressure, high-temperature melt depletion of an already depleted mantle source is provided by the highly refractory Cape Vogel low-Ca boninites which contain similar high Cr# spinels and Fo-rich olivine similar to those in the PUB harzburgites in a pyroxene-rich glass with clinoenstatite, enstatite-pigeonite and quenched amphibole, and are inferred from olivine–spinel thermometry to have crystallized at ~ 1280 – 1240 °C (Walker & Cameron, 1983) or higher temperatures (> 1370 °C) based on melt inclusions in chromite (Kamenetsky *et al.*, 2002).

The varying levels of depletion in residual peridotites recorded in the PNG mantle tectonites studied here thus support a multi-stage geodynamic melting environment, that require a hydrous melting regime, in at least one stage, that is sufficiently water-fluxed enough to drive excess melting and boninite production. Based on the relationships to overlying cumulates and lavas discussed above, this study proposes that the ultra-depleted Marum harzburgite tectonites resemble residues of fore-arc basalt (FAB) melts, whereas the even more ultra-depleted PUB harzburgite tectonites are residues of boninite melts. These findings support previously suggested multi-stage melt depletion models for the PNG ophiolites (Kamenetsky *et al.*, 2002; Kaczmarek *et al.*, 2015), whereby a first stage of melting occurred during the initial stages of subduction to produced tholeiitic fore-arc basalts, followed by a later stage of melting (and possible melt interaction in the mantle wedge) as subduction continued under low-P hydrous conditions, to produce boninite magmas (Shervais, 2001; Reagan *et al.*, 2010; Whattam & Stern, 2011; Stern *et al.*, 2012; Whattam *et al.*, 2020). The Cape Vogel boninites are among the most “depleted” recorded boninites (spinel $\text{TiO}_2 \sim 0.04$ wt. %, spinel Cr# ~ 0.94 , and whole-rock $\text{CaO}/\text{Al}_2\text{O}_3 \sim 0.3$; Walker & Cameron, 1983; Kamenetsky *et al.*, 2002), requiring their origin from an exceptionally

depleted source—a source that would fit well with the PUB tectonite compositions. Hydrous flux-melting at mantle potential temperatures ~50 to 100 °C hotter than the MORB source were appealed to for the genesis of the Cape Vogel boninites by Kamenetsky *et al.* (2002) and would be consistent with the ultra-depleted PNG mantle tectonite compositions.

3.5.3.2. Timing of melt depletion

Unlike some very depleted abyssal peridotites that have old Os depletion ages from sulfides (e.g., IODP Leg 209; Harvey *et al.*, 2006), the most depleted PNG samples show no evidence of the ancient Paleoproterozoic melt depletion. Apart from the very radiogenic Os isotope ratios in three mantle-derived peridotites (KD3, 715, and MA4), that will be discussed separately, the relatively low $^{187}\text{Os}/^{188}\text{Os}$ ratios (0.1204–0.1349) compared to other Phanerozoic ophiolites and peaks at around ~0.1238 and ~0.1286 (Fig. 3.11) may support multi-stage melting, with a first stage of melting in the Late Mesoproterozoic or Neoproterozoic. However, the uncertainties in the Os evolution curve in the last 1 Ga or more of Earth history preclude any accurate estimation of the melting age, with some of the isotopic ratios overlap the range in other Phanerozoic ophiolites. Overall, the Os isotope data from the main suite of PNG mantle-described peridotites suggest that whatever the cause of the extreme melt depletion that they reflect, it involved removing melt to the stage of quantitative Re-removal that arrests the radiogenic ingrowth of Os isotopes, and likely operated in the Late Mesoproterozoic to Phanerozoic Earth.

The peridotites with $^{187}\text{Os}/^{188}\text{Os} > 0.15$ may attain their Os isotope signatures from interaction with percolating basaltic melts, either in stage-one of the melting model during subduction initiation, or in the second-stage melting environment in a developed subduction setting. Such basaltic melts typically have higher $^{187}\text{Os}/^{188}\text{Os}$ compositions than residual peridotites especially in subduction settings (e.g., Dale *et al.*, 2008), although the few studies of Os isotopes on boninites indicate that they resemble sub-arc mantle peridotite with unradiogenic Os (Senda *et al.*, 2016). The relationship between the addition of radiogenic Os and evidence for melt-rock reaction is complex. Peridotites that show the clearest evidence for having experienced melt-rock interaction such as the dunite tectonites with greater olivine HREE enrichment, or peridotites with higher spinel Ti compositions, do not show more radiogenic $^{187}\text{Os}/^{188}\text{Os}$ ratios.

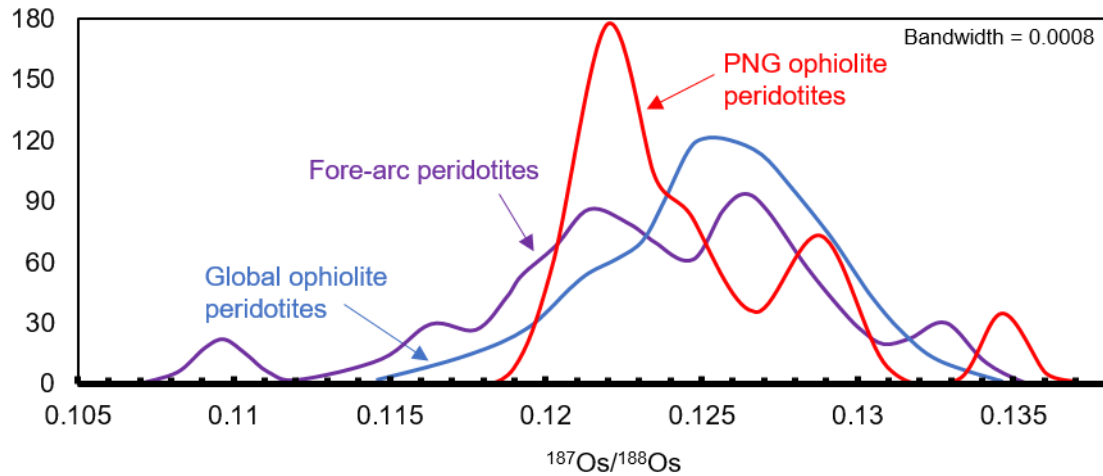


Figure 3.11. Kernel density estimate for $^{187}\text{Os}/^{188}\text{Os}$ plotted against literature values for ophiolite and fore-arc peridotites (see references in Appendix 6).

3.5.4. Reconciling the extreme HSE variability in the PNG mantle with melting and melt-rock reaction processes

3.5.4.1. HSE systematics

The extended PGE patterns of the PNG tectonites are distinctive and different from those associated with low to moderate degrees of partial melting such as abyssal peridotites (e.g., Luguet *et al.*, 2003; Becker & Dale, 2016). On one level, this is unsurprising given the highly melt-depleted nature of the PNG mantle tectonites. On another level, very few mantle peridotites have been observed with these distinctive highly fractionated HSE patterns. In other extremely melt-depleted mantle residues such as cratonic peridotites, Os averages are $\sim 3.5 \text{ ng/g}$, $[\text{Os}/\text{Ir}]_N \sim 1$, and P-PGEs are systematically depleted (Aulbach *et al.*, 2016). In cratonic peridotites, the P-PGEs and Re are significantly fractionated from I-PGEs, to much lower concentrations due to breakdown of the sulfide phase that hosts all these elements in fertile peridotites, and stabilization of alloys phases that are thought to host the I-PGEs in highly melt depleted peridotites (e.g., Pearson *et al.*, 2004; Aulbach *et al.*, 2016; Luguet & Pearson, 2019). However, the extended PGE patterns of the PNG mantle peridotites contrast strongly with cratonic peridotites, especially with respect to depletion of Os and Ir to very low levels, variable Os/Ir ratios, and strong depletion of both these elements relative to Ru (Fig. 3.7a). In the PNG mantle tectonites, Pt has also been lowered to very

low abundances—in some cases (over two-orders of magnitude lower than PUM; Becker *et al.*, 2006)—and is consistently more depleted in the PNG tectonites than in cratonic peridotites. The large variations in Pd, varying from very low (0.0055 ng/g) to high values (0.3 ng/g), and appears to be independent of Os and Ir behaviour, reflecting multiple processes affecting PGE.

The origin of these highly heterogeneous extended PGE patterns is unclear but such low Os and Ir abundances are increasingly being recognized in harzburgites from other ophiolites and SSZ peridotites, notably from New Caledonia (Secchiari *et al.*, 2020) and in a few very depleted peridotite xenoliths from continental subduction-related regions (e.g., Liu *et al.*, 2015; Scott *et al.*, 2019). Irregular PGE patterns with fractionated Os/Ir and Pt anomalies have also been increasingly recognized as features of melt residues from some SSZ ophiolites (e.g., Büchl *et al.*, 2002; Lorand *et al.*, 2004). The HSE systematics in such melt-depleted peridotites are thought to be controlled by the formation of Ir-Pt-rich alloy phases during the total removal of sulfide from the melt residue at high melt fractions (e.g., Brenan & Andrews, 2001; Fonseca *et al.*, 2009). However, these residues have positive Pt anomalies in contrast to the striking negative Pt anomalies observed in the PNG melt residues, and do not have the consistently low Os and Ir seen in the PNG tectonites. The very low Os, Ir and Pt in most of the PNG mantle tectonites analyzed here do not correlate to any melt depletion index and seem instead to point to extreme melt depletion, under conditions where the Os-Ir and Pt alloys that usually stabilize these elements (e.g., Luguet *et al.*, 2007) have broken down, likely via dissolution, allowing these elements to enter the melt. An exemption could be harzburgite KD1 that shows both higher I-PGE abundances and higher whole-rock trace elements compared to the other PNG tectonites, however, a correlation between I-PGEs and incompatible trace elements cannot be determined from one sample alone. For the remaining tectonites that show low Os and Ir, a potential melt composition that may be responsible might be the high liquidus temperature ultra-depleted melts found as inclusions in olivines within Cape Vogel boninites. As such melts require a very depleted mantle source (similar to the PNG tectonites in terms of major elements), they would be hot and highly S-undersaturated. These properties could make them agents for sulfide dissolution while percolating through the mantle, and contenders to dissolve residual alloy phases if their oxygen fugacity was sufficiently high, which is observed in the PNG tectonites as inferred from whole-rock V-Yb relationships ($\text{Log } \Delta\text{FMQ} = 0$ to +1; Fig. 3.6b). The New Caledonia and New Zealand harzburgites that have similar HSE characteristics are among the most melt-depleted of their respective suites (Liu *et al.*, 2015; Scott

et al., 2019; Secchiari *et al.*, 2020), and these residues were produced in tectonic settings where hydrous melting and melt-percolation likely played a role.

Whereas the low Os, Ir and Pt seem to indicate PGE removal, the more elevated Pd and Re concentrations in Fig. 3.8 seem to indicate later enrichment/metasomatism via a Pd and Re-enriched fluid, though this did not increase Pt concentrations, nor did it result in the formation of obvious metasomatic sulfides. While the extremely fractionated HSE patterns in the PNG mantle peridotites seem most like a product of melt-rock reaction, the levels of Os-Ir-Pt depletion and Os isotope ratios do not correlate with mineral or lithophile element indications of melt interaction, such as LREE enrichment. This likely reflects a decoupling of lithophile from HSE behaviour, but also the action of multiple mantle processes, that may have involved the interaction with more than a single type of percolating melt, to generate this complex behaviour. It seems likely that Re and Pd have been variably re-added to the PNG mantle since the loss of their sulfides and alloys.

3.5.4.2. *Role of fluids*

The complex whole-rock HSE patterns are not related in a straightforward way to partial melting. Even though they may be caused by percolating fluids that could have been either instrumental in the melting process, or resulted from the melting process, a lack of experiments on PGE partitioning during hydrous mantle melting makes it difficult to rule out a partial melting origin for these highly fractionated HSE patterns. Other suites such as the New Zealand peridotites and the type- “B” clinopyroxene-free harzburgites from New Caledonia, are not quite as melt-depleted as the average PNG mantle peridotites, but show similar PGE patterns, and lack any correlation between Os content and bulk Al_2O_3 , HREE depletion, or spinel Cr#. Since there is no clear relationship between the complex HSE patterns with the introduction of components via melt or fluid enrichment, perhaps the most likely explanation is that the very low Os, Ir and Pt represent a dissolution process by a high temperature (mantle-derived) fluid or melt that is aggressive enough to dissolve and/or mobilize the alloys that typically host these phases in very melt-depleted peridotites. The relatively minor variation in Ru abundances suggest that Ru has largely withstood this process if Ru-rich sulfides or alloys were preferentially hosted in residual spinel, protecting them from dissolution, whereas, re-enrichment of Pd and Re seems to be required to create the higher (up to PUM-level) concentrations of these PGEs in rocks that should be highly depleted in Pd and Re. The fluids that may have been responsible for the removal of I-PGE and Pt could have been similar to those responsible for water-fluxed melting of the PNG mantle in a second-stage

melting regime proposed to create highly melt-depleted compositions, with continued fluid-fluxing by removing HSEs at low pressures (e.g., ≤ 2 GPa; Jaques & Green, 1980) and higher temperature conditions (e.g., 1150–1200 °C; Crawford *et al.*, 1989). These fluids must have been more aggressive than Cl-rich fluids that have been proposed to explain low Os contents in subduction zone peridotites (e.g., Brandon *et al.*, 1996) due to the removal of Ir, which is often resistant to the Cl-rich fluids proposed to complex and transport Os (e.g., Wood *et al.*, 1990). These fluids are, therefore, unlikely to be related to low temperature serpentinization processes as the varied Os isotope ratios and HSE systematics would require unfeasibly high water-rock ratios (>100) to disturb Os isotopes at visible % levels (e.g., Becker & Dale, 2016). This is further supported by similar features are also observed in much fresher peridotites (some with 0% LOI) from New Caledonia (Secchiari *et al.*, 2020). From a mineral exploration standpoint, future studies related to how these fluids interact with depleted peridotite to mobilized some PGE and not others may have important implications for understanding of the widespread occurrence of alluvial PGE alloys and associated mineralization within PNG (e.g., Weiser & Bachmann, 1999; Johan *et al.*, 2000; Malitch & Thalhammer, 2002; González-Álvarez *et al.*, 2013).

3.5.5. *Origin of the PNG mantle tectonites*

Geological and geochemical data indicate that the PNG ophiolite peridotites represent sub-oceanic lithospheric mantle that formed in a subduction-related (i.e., SSZ) tectonic environment. The principal evidence for this SSZ origin includes: 1) a thick mantle tectonite section dominated by harzburgite as the main lithology, 2) highly refractory major and trace element compositions are consistent with those observed in SSZ ophiolites, 3) the existence of a metamorphic sole or thrust (PUB) on which the ophiolite was emplaced (Davies, 1978; Lus *et al.*, 2004), 4) the occurrence of high-Mg arc lavas (Dabi Volcanics) derived from hydrous melts (i.e., boninites) overlying the PUB on the Cape Vogel peninsula (Dallwitz *et al.*, 1966; Dallwitz, 1968; Jenner, 1981; Walker & Cameron, 1983), and 5) presence of almost pure-enstatite orthopyroxenite dykes (Kaczmarek *et al.*, 2015) cross-cutting the PUB and Marum harzburgites that resembling products of subduction-related hydrous fluid melting. In current plate tectonic models (Whattam, 2009) the PUB and Marum ophiolites represent fore-arc basement formed in an SSZ setting above a NE-dipping subduction zone during the earliest stages of formation of an early Paleocene intra-oceanic arc. The young newly-formed ophiolites, and a segment of the Cretaceous-early Paleocene subducting lithosphere (Emo Metamorphics, Tumu River Basalt), were accreted onto a rifted fragment of the

Australian continent at the eastern margin of the Australian Plate through collision with the intra-oceanic arc (Davies & Jaques, 1984; Whattam, 2009). New data presented in this study from the PNG mantle peridotites, along with the previous petrology and geochemistry of the cumulate sequence rocks and the PUB lavas, are consistent with formation in an SSZ environment by fore-arc spreading caused by upwelling of the asthenospheric mantle and decompression melting in response to the initiation of subduction. A second stage of melting, at higher temperature and in a water-fluxed environment appears necessary to explain the extreme melt-depletion recorded in these mantle residues. This model of formation of the PUB and Marum ophiolites as fore-arc lithosphere is analogous to the initiation of subduction and early arc development in the Izu-Bonin-Mariana fore-arc (Ishizuka *et al.*, 2014; Hickey-Vargas *et al.*, 2018) and intra-oceanic SSZ ophiolites more generally (e.g., Stern & Bloomer, 1992; Dilek & Furnes, 2014; Pearce, 2014). However, the exceptionally refractory signatures in the PNG mantle tectonites are uniquely depleted in contrast to previously studied SSZ ophiolite peridotites in terms of their very low whole-rock lithophile elements contents and high spinel Cr#. Their PUM-like $^{187}\text{Os}/^{188}\text{Os}$ ratios rule out an origin as ancient residues from long-term Re depletion, as observed in melt-depleted cratonic residues, or even suggested for some of the Izu-Bonin peridotites (Parkinson & Pearce, 1998) but rather fall within the range of modern convecting oceanic mantle (e.g., 0.12809 ± 0.00085 ; Walker *et al.*, 2002), indicating that the melting processes were recent.

3.6. SUMMARY AND CONCLUSIONS

The mantle tectonites of Marum and PUB ophiolite complex record some of the most depleted peridotite signatures in mantle residues. Major element abundances, particularly whole-rock Ca and Al, and spinel Cr# exceed those recorded in most ophiolite and cratonic peridotite residues. To justify these highly depleted signatures and the regional geology of the ophiolite complex, a two- or multi-stage melting process is favored in order to achieve such high levels of melt depletion (>40 %), whereby the first stage was linked to the formation of FAB-like lavas during subduction initiation, and a second stage that formed the low-Ca Cape Vogel boninites in a water-fluxed environment as subduction continued. Some samples show evidence of melt–rock interaction, however, there is no clear indication of a single process, but rather multiple melt–rock interaction processes. One of these processes formed replacive dunite tectonites through the interaction with

a hydrous high-Mg, orthopyroxene-undersaturated melt, resulting in higher olivine Fo contents compared to the harzburgites.

The very low Os, Ir and Pt that are not typical of mantle residues, but are also observed in similar hydrous melt-depleted geodynamic settings, and probably reflect the scavenging of these elements via interaction with a high temperature fluid, possibly linked to the production of boninites. The ultimate cause of these highly fractionated HSE patterns is unclear and may only be resolved by new experimental studies of HSE behavior during water-saturated peridotite melting and HSE mobility in high-temperature hydrothermal fluids. The $^{187}\text{Os}/^{188}\text{Os}$ isotope systematics and unusual HSE patterns indicate that these extremely high levels of melt depletion are not linked to ancient melt extraction events as observed in cratonic residues, or even the most depleted oceanic peridotites.

Chapter 4

Conclusions

The aim of this thesis was to focus on new petrological, geochemical and isotopic data in peridotites from well-exposed localities of oceanic mantle lithosphere in the SW Pacific region. These peridotites resemble two different geodynamic environments, one sampled via erupted xenoliths, and the second exposed through tectonically emplaced ophiolites, with both aiming to better understand how mantle evolution may differ beneath subduction zones, back-arc settings and intraplate environments. Peridotite xenoliths from Fiji and ophiolites from Papua New Guinea (PNG) provide opportunities to study direct fragments of mantle lithosphere and are important additions for understanding the composition and processes operating in the mantle beneath SW Pacific region and globally. The collective findings from this thesis are summarized below.

4.1. Relationships between mantle melting, HSE and Os isotope systematics

Peridotites are important archives for understanding partial melting in the Earth's mantle. In this thesis a number of geochemical "proxies" have been applied to measure the extent of partial melting. An important outcome of this study is that these major or trace element indicators of melt depletion do not correlate with the whole-rock $^{187}\text{Os}/^{188}\text{Os}$ isotope signatures which should track the long-term effects of melting. Based on Al_2O_3 versus $^{187}\text{Os}/^{188}\text{Os}$ systematics from both peridotite suites studied here—one highly depleted and one mildly depleted—there is no evidence for an "aluminachron" relationship of the type often observed in non-cratonic peridotites (Reisberg & Lorand, 1995). Such scattered Al-Os isotope relationships are the norm in suites of sub-oceanic peridotites (e.g., Brandon *et al.*, 2000; Harvey *et al.*, 2006) and indicate a complex history of multi-stage mantle melting and mixing, to a much greater extent than observed for peridotite suites comprising old continental lithosphere. For the Fijian Koro peridotite suite, $^{187}\text{Os}/^{188}\text{Os}$ isotope ratios range between 0.1201–0.1306 (median 0.1273) whereas the PNG ophiolitic peridotite suite is more varied 0.1204–0.1611 (median 0.1246). The Os isotope variability in both these samples of oceanic mantle reflect the heterogeneity within modern convecting mantle (with some addition

of radiogenic crustal Os evident in the PNG tectonites) rather than discrete melt-extraction events that could be easily related to their isolation as lithosphere. Furthermore, the extremely depleted peridotites from the Papuan Ultramafic Belt (PUB) do not record any evidence of the ancient melting events recorded in some New Zealand peridotites (e.g., $^{187}\text{Os}/^{188}\text{Os} = 0.1098$; $T_{\text{RD}} = 2.6$ Ga; Liu *et al.*, 2015), though young highly depleted melt residues were also incorporated into the lithosphere beneath New Zealand. This indicates that while highly depleted geochemical signatures can be produced in the modern Earth through multi-stage ridge and subduction-related hydrous melting, the mantle sampled by the obduction of the PNG ophiolites is significantly less varied in the spectrum of melting events it reflects than that accreted beneath New Zealand to the South.

Koro peridotite HSE patterns are generally unfractionated apart from some slight Pt-Pd decoupling, and are consistent with OIB-hosted peridotites and abyssal peridotites reflecting metasomatic sulfides. However, a number of “outlier” samples characterized by very low I-PGEs show a closer resemblance to HSE patterns observed in the PNG ophiolite peridotites. In the PNG tectonites, highly fractionated HSE patterns are similar to the depleted peridotites from New Zealand (Liu *et al.*, 2015) and New Caledonia (Secchiari *et al.*, 2020) that show unusually low I-PGE abundances and strong Pt-Pd decoupling that are not observed in typical mantle residues (e.g., cratonic peridotites), but could reflect scavenging/mobilization of PGEs by fluids that are specific to arc-related environments. This signature is being increasingly observed in arc-related highly depleted mantle peridotites and further micro- to nano-scale petrological study of such samples could yield important data on the mechanisms of HSE mobilisation in Earth’s mantle and possible mineralisation processes.

4.2. Mantle metasomatism / melt-rock interaction

Metasomatic processes in the mantle lithosphere beneath Fiji and PNG record very different melt-rock interaction processes. This is shown by the lithological diversity between the Fijian peridotites in Chapter 2 that are dominated by clinopyroxene-rich peridotites (lherzolites and wehrlites), while the PNG tectonites in Chapter 3 are dominated by harzburgites and some likely replacive dunites with minimal evidence for patent metasomatism, i.e., the introduction of new mineral phases, in the latter suite. These different metasomatic styles likely reflect the diverse geodynamic environments in the SW Pacific oceanic mantle.

In the Fijian peridotites, there is a clear dominance of silicate metasomatism, possibly sourced from ingress of the Samoan mantle plume beneath eastern Fiji as a result of slab rollback of the Pacific Plate. This event heated the lithosphere and produced peridotites of varied metasomatic intensity, culminating in wehrellites at the highest melt-rock ratios. In contrast, in the oceanic mantle lithosphere represented by the PNG tectonite suite, the dominant metasomatic process is sourced from arc-related melts that resulted in opx-dissolution to produce dunites and orthopyroxenite dykes. Results from this thesis also show that olivine REE, particularly olivine HREE, is potentially a useful proxy to discriminate dunites that formed through melt-rock interaction from harzburgites in the same suite that formed via melt depletion, particularly when this cannot be discerned based on major element proxies.

4.3. SW Pacific mantle evolution in the context of the Pacific

Although the Pacific oceanic crust is geologically young (<200 Ma; Müller *et al.*, 2008), peridotites resembling fragments of oceanic mantle lithosphere have been shown to be significantly older in several regions of the Pacific (e.g., Ishikawa *et al.*, 2011; Liu *et al.*, 2015; Jackson *et al.*, 2016; Scott *et al.*, 2019). This de-coupling of mantle lithosphere from the surface volcanics provides an opportunity to better understand past geological processes that may have not been well-preserved in the oceanic crust record.

Findings from Chapter 2 demonstrate the diversity and complex nature of the SW Pacific mantle in the xenolith record, but importantly provide evidence for multiple metasomatic interactions within the mantle. The evidence for heating and removal of lithospheric material beneath eastern Fiji via intense silicate metasomatism can also be viewed as weakening of the underlying mantle lithosphere. This is important because it could suggest that erosion of lithosphere via the influx of plume material elsewhere in the Pacific could act as a barrier to lithospheric stabilization, and potentially the growth of oceanic islands and continents such as Zealandia. Such a processes could contribute to explaining why the Fijian archipelago and the so-called “Fijian Platform” region has yet to develop into an elevated continent like Zealandia. Another reason may be the relative weakness of the mildly depleted peridotites that appear to under-pin Fiji, if those beneath Koro are representative.

The PNG ophiolite peridotites described in Chapter 3 record the most incompatible element depleted sections of mantle lithosphere in the Pacific and possibly on Earth. Elsewhere in the

Pacific, the Izu-Bonin-Mariana (IBM) arc is a well-studied modern SSZ ophiolite analogue, and has been used as the basis for the subduction initiation model that explains the transition from tholeiitic to boninitic volcanism above subduction zones (e.g., Whatman & Stern, 2011), however, little is known about how the underlying mantle may respond to such processes. The multi-stage melt evolution recorded in the mantle sections of the Marum and PUB ophiolite in Chapter 3 may record the underlying mantle processes of this subduction initiation model based on the IBM arc, providing a more complete picture of the SSZ ophiolite evolution. However, more research needs to be done to understand why these ultra-depleted peridotite compositions are preserved in PNG but not elsewhere, with the possible exception of Japan (Kubo, 2002).

4.4. Recommendations for future work

The oceanic mantle lithosphere plays an important role in controlling global geodynamics and volcanism; however, its characterization and understanding the processes involved in its formation and evolution is limited by difficulties in accessing direct samples of this region compared to the more accessible crustal portion of the lithosphere. While this study provides a useful snapshot of the mantle lithosphere beneath the SW Pacific region, much remains unknown about the composition and processes in the mantle beneath the Pacific. Some of these knowledge gaps can be addressed through additional sampling in both arc-related and intraplate peridotites through erupted xenoliths and dredging, along with interdisciplinary studies related to the rheology and mechanical properties of the lithosphere though seismic investigations.

As this thesis is the first detailed geochemical study on peridotite xenoliths from Fiji, there are many further studies that can be conducted on these samples. The results from spinel Mössbauer spectroscopy provided some key evidence for the main conclusions in Chapter 2, however, only a limited number of samples constrained to the lherzolites were analysed in this study. Additional Mössbauer spectroscopy on spinels will help constrain redox conditions of the Fijian mantle and aid the association with a back-arc origin. New studies that could be conducted on the Fijian samples include the application of other radiogenic isotope systems (e.g., Sr-Nd-Hf) on picked pyroxene grains (e.g., Liu *et al.*, 2020). Following the suggested link between the introduced clinopyroxene and silicate metasomatism in Chapter 2, radiogenic isotopes in picked clinopyroxene separates should be compared to signatures from the Samoan OIBs and metasomatized peridotites (e.g., Hauri *et al.*, 1993) to further investigate the relationship proposed

in Chapter 2. Other follow-up studies could include an assessment of diffusion rates between the xenoliths and the host basalt melt or crystals within host basalt (i.e., diffusion chronometry) to calculate magma eruption rates (e.g., Costa et al., 2020), and measuring water concentrations in nominally anhydrous phases via FTIR (e.g., Peslier & Bizimis, 2015). All samples from Koro Island have been catalogued, photographed and will remain stored at the UofA for future studies on peridotite xenoliths and their host basalts, and additional peridotite xenoliths will be collected from Moala Island in eastern Fiji during 2021/22 to build on the Koro Island peridotite study. Moala Island volcano (Fig 4.1) is also part of the eastern Fijian OIB group of islands, but is geologically older than Koro and may record the thinnest oceanic lithosphere in eastern Fiji (≤ 16 km; Chen *et al.*, 2019), perhaps representing a lithosphere more extensively thinned by the Samoan plume.

While previous work has been conducted on the PNG ophiolite peridotites (England & Davies, 1973; Jaques, 1980; Jaques & Chappell, 1980; Kaczmarek *et al.*, 2015), there are fewer studies of these peridotites compared to other ophiolite complexes such as the Semail ophiolite in Oman, Troodos ophiolite in Cyprus, and Bay of Islands ophiolite in Canada. Improved constraints on emplacement age of the PNG ophiolite could be attempted by applying the ^{190}Pt - ^{186}Os isotope system to platinum group alloys (e.g., Coggon *et al.*, 2011), and further geochemical studies on ultramafic cumulates, along with the gabbros and basalts of the ophiolite sequence, will better constrain relationships between these ophiolite units and the erupted volcanic sequence. Future work that can be applied to both the Fijian peridotites and PNG tectonites include microstructural EBSD, particularly on the Fijian and PUB peridotites (similar to the detailed EBSD study conducted on Marum peridotites in Kaczmarek *et al.*, 2015), and high-resolution thin section mapping of PGE alloys. Based on the affinity between PGEs and sulfide phases along with metal alloys, measurements of whole-rock chalcophile element abundances (e.g., S, Se, Te) will help better understand whether sulfur contents are responsible for the low I-PGE abundances and highly fractionated PGE patterns in general.

In addition to continuing analytical work on the PNG tectonites and Koro peridotites, both studies will benefit largely from experiments that aim to better understand the behaviour of PGE and REE during hydrous partial melting at high degrees of melt extraction. Recent improvements in measuring REEs in olivine has shown to be particularly useful in this study to identify peridotites that formed via partial melting versus peridotites formed through melt-rock interaction. Continued

application of REE in olivine, coupled with other melt depletion tracers may provide an additional tool to discriminate peridotite residues, melt-rock reaction products and cumulate peridotites.

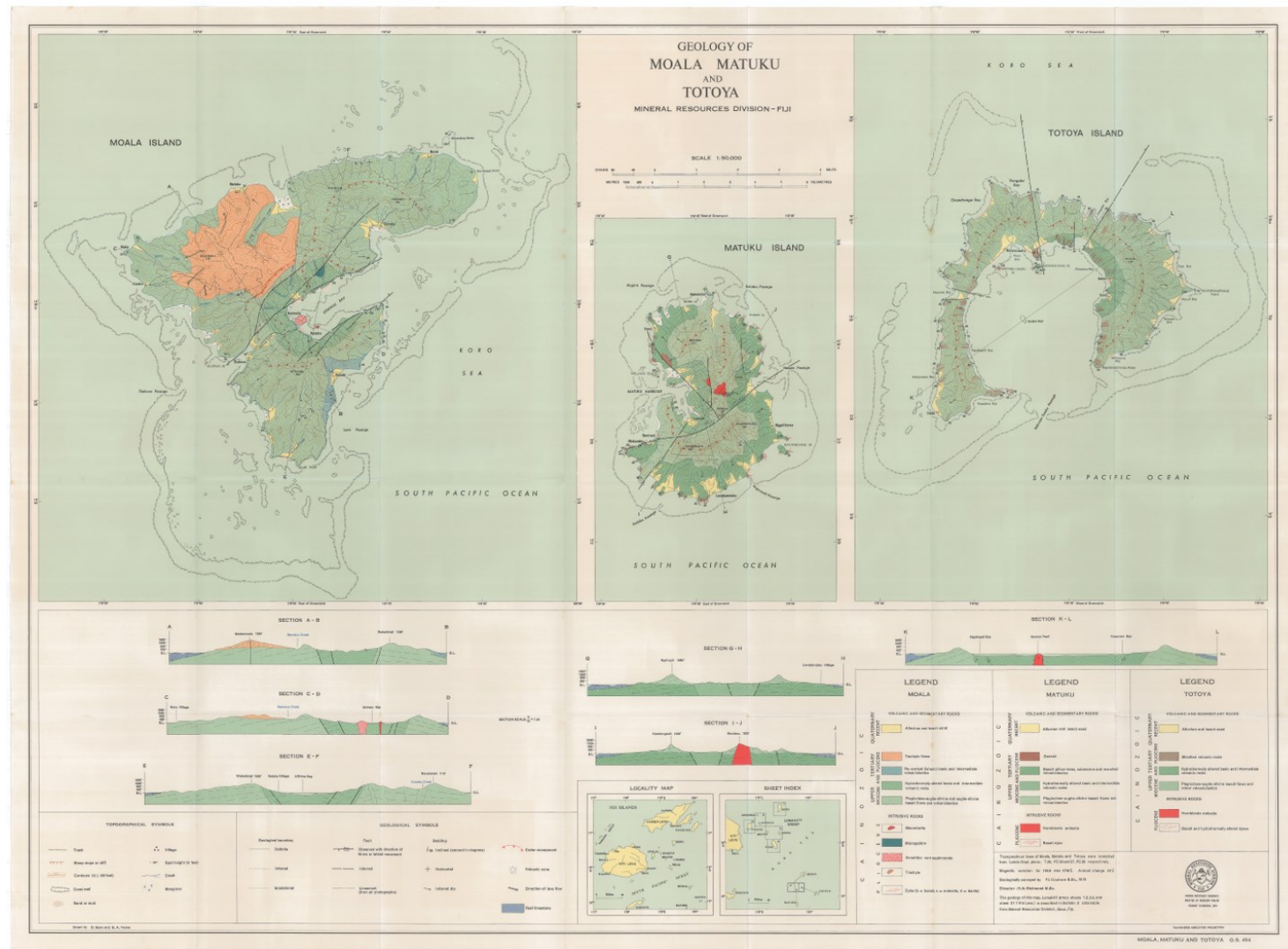


Figure 4.1. Geological map of Moala, Matuku and Totoya Islands after Coulson (1970).

BIBLIOGRAPHY

- Abe, N., Arai, S., & Yurimoto, H. (1998). Geochemical characteristics of the uppermost mantle beneath the Japan island arcs: implications for upper mantle evolution. *Physics of the Earth and Planetary Interiors*, 107(1-3), 233-248.
- Alard, O., Griffin, W. L., Lorand, J. P., Jackson, S. E., & O'Reilly, S. Y. (2000). Non-chondritic distribution of the highly siderophile elements in mantle sulphides. *Nature*, 407(6806), 891-894.
- Aldanmaz, E., van Hinsbergen, D. J., Yıldız-Yüksekol, Ö., Schmidt, M. W., McPhee, P. J., Meisel, T., ... & Mason, P. R. (2020). Effects of reactive dissolution of orthopyroxene in producing incompatible element depleted melts and refractory mantle residues during early fore-arc spreading: constraints from ophiolites in eastern Mediterranean. *Lithos*, 360, 105438.
- Anderson, D. L. (2007). New theory of the Earth. Cambridge University Press.
- Arai, S. (1994). Characterization of spinel peridotites by olivine-spinel compositional relationships: review and interpretation. *Chemical Geology*, 113(3-4), 191-204.
- Arai, S., & Takemoto, Y. (2007). Mantle wehrlite from Hess Deep as a crystal cumulate from an ultra-depleted primary melt in East Pacific Rise. *Geophysical Research Letters*, 34(8).
- Arai, S., Kadoshima, K., & Morishita, T. (2006). Widespread arc-related melting in the mantle section of the northern Oman ophiolite as inferred from detrital chromian spinels. *Journal of the Geological Society*, 163(5), 869-879.
- Artemieva, I. (2011). Lithosphere: an interdisciplinary approach. Cambridge University Press.
- Aulbach, S., Luchs, T., & Brey, G. P. (2014). Distribution and behaviour during metasomatism of PGE-Re and Os isotopes in off-craton mantle xenoliths from Namibia. *Lithos*, 184, 478-490.
- Aulbach, S., Mungall, J. E., & Pearson, D. G. (2016). Distribution and processing of highly siderophile elements in cratonic mantle lithosphere. *Reviews in Mineralogy and Geochemistry*, 81(1), 239-304.
- Auzende, J. M., Lafay, Y., & Marsset, B. (1988). Recent geodynamic evolution of the north Fiji basin (southwest Pacific). *Geology*, 16(10), 925-929.
- Auzende, J. M., Pelletier, B., & Eissen, J. P. (1995). The North Fiji Basin geology, structure, and geodynamic evolution. In *Backarc Basins* (pp. 139-175). Springer, Boston, MA.
- Auzende, J. M., Rissen, J. P., Lafay, Y., Gente, P., & Charlou, J. L. (1988). Seafloor spreading in the north Fiji basin (Southwest Pacific). *Tectonophysics*, 146(1-4), 317-352.
- Baker, M. B., & Stolper, E. M. (1994). Determining the composition of high-pressure mantle melts using diamond aggregates. *Geochimica et Cosmochimica Acta*, 58(13), 2811-2827.
- Ballhaus, C., & Sylvester, P. (2000). Noble metal enrichment processes in the Merensky Reef, Bushveld Complex. *Journal of Petrology*, 41(4), 545-561.
- Barnes, S. J., & Roeder, P. L. (2001). The range of spinel compositions in terrestrial mafic and ultramafic rocks. *Journal of Petrology*, 42(12), 2279-2302.
- Barnes, S. J., Mungall, J. E., & Maier, W. D. (2015). Platinum group elements in mantle melts and mantle samples. *Lithos*, 232, 395-417.
- Barsdell, M., & Smith, I. E. (1989). Petrology of recrystallized ultramafic xenoliths from Merelava volcano, Vanuatu. *Contributions to Mineralogy and Petrology*, 102(2), 230-241.

- Batanova, V. G., & Sobolev, A. V. (2000). Compositional heterogeneity in subduction-related mantle peridotites, Troodos massif, Cyprus. *Geology*, 28(1), 55-58.
- Becker, H., & Dale, C. W. (2016). Re–Pt–Os isotopic and highly siderophile element behavior in oceanic and continental mantle tectonites. *Reviews in Mineralogy and Geochemistry*, 81(1), 369-440.
- Becker, H., Horan, M. F., Walker, R. J., Gao, S., Lorand, J. P., & Rudnick, R. L. (2006). Highly siderophile element composition of the Earth's primitive upper mantle: constraints from new data on peridotite massifs and xenoliths. *Geochimica et Cosmochimica Acta*, 70(17), 4528-4550.
- Begg, G., & Gray, D. R. (2002). Arc dynamics and tectonic history of Fiji based on stress and kinematic analysis of dikes and faults of the Tavua Volcano, Viti Levu Island, Fiji. *Tectonics*, 21(4), 5-1.
- Belford, D. (1976). Appendix: foraminifera and age of samples from south-eastern Papua. *Geology of the South-eastern Papuan mainland. Bulletin. Bureau of Mineral Resources. Geology and Geophysics (Australia)*, 165, 73-82.
- Bénard, A., Le Losq, C., Nebel, O., & Arculus, R. J. (2018). Low-Ca boninite formation by second-stage melting of spinel harzburgite residues at mature subduction zones: new evidence from veined mantle xenoliths from the West Bismarck Arc. *Contributions to Mineralogy and Petrology*, 173(12), 105.
- Birck, J. L., Barman, M. R., & Capmas, F. (1997). Re-Os isotopic measurements at the femtomole level in natural samples. *Geostandards Newsletter*, 21(1), 19-27.
- Birner, S. K., Warren, J. M., Cottrell, E., Davis, F. A., Kelley, K. A., & Falloon, T. J. (2017). Forearc peridotites from Tonga record heterogeneous oxidation of the mantle following subduction initiation. *Journal of Petrology*, 58(9), 1755-1780.
- Bizimis, M., Griselin, M., Lassiter, J. C., Salters, V. J., & Sen, G. (2007). Ancient recycled mantle lithosphere in the Hawaiian plume: osmium–hafnium isotopic evidence from peridotite mantle xenoliths. *Earth and Planetary Science Letters*, 257(1-2), 259-273.
- Bodinier, J. L., & Godard, M. (2003). Orogenic, ophiolitic, and abyssal peridotites. *Treatise on Geochemistry*, 2, 568.
- Bodinier, J. L., Menzies, M. A., Shimizu, N., Frey, F. A., & McPHERSON, E. L. A. I. N. E. (2004). Silicate, hydrous and carbonate metasomatism at Lherz, France: contemporaneous derivatives of silicate melt–harzburgite reaction. *Journal of Petrology*, 45(2), 299-320.
- Boudier, F., & Nicolas, A. (1995). Nature of the Moho transition zone in the Oman ophiolite. *Journal of Petrology*, 36(3), 777-796.
- Boyd, F. R. (1973). A pyroxene geotherm. *Geochimica et Cosmochimica Acta*, 37(12), 2533-2546.
- Boyd, F. R. (1989). Compositional distinction between oceanic and cratonic lithosphere. *Earth and Planetary Science Letters*, 96(1-2), 15-26.
- Brandon, A. D., & Draper, D. S. (1996). Constraints on the origin of the oxidation state of mantle overlying subduction zones: an example from Simcoe, Washington, USA. *Geochimica et Cosmochimica Acta*, 60(10), 1739-1749.
- Brandon, A. D., Creaser, R. A., Shirey, S. B., & Carlson, R. W. (1996). Osmium recycling in subduction zones. *Science*, 272(5263), 861-863.

- Brandon, A. D., Snow, J. E., Walker, R. J., Morgan, J. W., & Mock, T. D. (2000). ^{190}Pt - ^{186}Os and ^{187}Re - ^{187}Os systematics of abyssal peridotites. *Earth and Planetary Science Letters*, 177(3-4), 319-335.
- Brenan, J. M., & Andrews, D. (2001). High-temperature stability of laurite and Ru-Os-Ir alloy and their role in PGE fractionation in mafic magmas. *The Canadian Mineralogist*, 39(2), 341-360.
- Brey, G. P., & Köhler, T. (1990). Geothermobarometry in four-phase Iherzolites II. New thermobarometers, and practical assessment of existing thermobarometers. *Journal of Petrology*, 31(6), 1353-1378.
- Bryndzia, L. T., & Wood, B. J. (1990). Oxygen thermobarometry of abyssal spinel peridotites: the redox state and C-O-H volatile composition of the Earth's sub-oceanic upper mantle. *American Journal of Science*, 290(10), 1093-1116.
- Büchl, A., Brügmann, G., Batanova, V. G., Münker, C., & Hofmann, A. W. (2002). Melt percolation monitored by Os isotopes and HSE abundances: a case study from the mantle section of the Troodos Ophiolite. *Earth and Planetary Science Letters*, 204(3-4), 385-402.
- Burnham, A. D., & O'Neill, H. S. C. (2020). Mineral-melt partition coefficients and the problem of multiple substitution mechanisms: insights from the rare earths in forsterite and protoenstatite. *Contributions to Mineralogy and Petrology*, 175(1), 7.
- Bussweiler, Y., Brey, G. P., Pearson, D. G., Stachel, T., Stern, R. A., Hardman, M. F., ... & Jackson, S. E. (2017). The aluminum-in-olivine thermometer for mantle peridotites—Experimental versus empirical calibration and potential applications. *Lithos*, 272, 301-314.
- Bussweiler, Y., Giuliani, A., Greig, A., Kjarsgaard, B. A., Petts, D., Jackson, S. E., ... & Pearson, D. G. (2019). Trace element analysis of high-Mg olivine by LA-ICP-MS—Characterization of natural olivine standards for matrix-matched calibration and application to mantle peridotites. *Chemical Geology*, 524, 136-157.
- Canil, D., & O'Neill, H. S. C. (1996). Distribution of ferric iron in some upper-mantle assemblages. *Journal of Petrology*, 37(3), 609-635.
- Chase, C. G. (1971). Tectonic history of the Fiji Plateau. *Geological Society of America Bulletin*, 82(11), 3087-3110.
- Chen, J., Chen, Y. J., Wiens, D. A., Wei, S. S., Zha, Y., Julià, J., & Cai, C. (2019). Crustal and lithospheric structure of inactive volcanic arc terrains in Fiji. *Tectonophysics*, 750, 394-403.
- Chou, C. L. (1978). Abundances of Noble Metals in the Earth's Upper Mantle: Evidence for Late Heavy Bombardment After Core Formation. *Meteoritics*, 13, 407.
- Clague, D. A. (1988). Petrology of ultramafic xenoliths from Loihi Seamount, Hawaii. *Journal of Petrology*, 29(6), 1161-1186.
- Clague, D. A., & Straley, P. F. (1977). Petrologic nature of the oceanic Moho. *Geology*, 5(3), 133-136.
- Coggon, J. A., Nowell, G. M., Pearson, D. G., & Parman, S. W. (2011). Application of the ^{190}Pt - ^{186}Os isotope system to dating platinum mineralization and ophiolite formation: an example from the Meratus Mountains, Borneo. *Economic Geology*, 106(1), 93-117.
- Cohen, A. S., & Waters, F. G. (1996). Separation of osmium from geological materials by solvent extraction for analysis by thermal ionisation mass spectrometry. *Analytica Chimica Acta*, 332(2-3), 269-275.

- Cole, J. W., Graham, I. J., & Gibson, I. L. (1990). Magmatic evolution of Late Cenozoic volcanic rocks of the Lau Ridge, Fiji. *Contributions to Mineralogy and Petrology*, 104(5), 540-554.
- Coleman, P. J., & Packham, G. H. (1976). The Melanesian Borderlands and India—Pacific plates' boundary. *Earth-Science Reviews*, 12(2-3), 197-233.
- Coltorti, M., Bonadiman, C., Hinton, R. W., Siena, F., & Upton, B. G. J. (1999). Carbonatite metasomatism of the oceanic upper mantle: evidence from clinopyroxenes and glasses in ultramafic xenoliths of Grande Comore, Indian Ocean. *Journal of Petrology*, 40(1), 133-165.
- Conder, J. A., & Wiens, D. A. (2007). Rapid mantle flow beneath the Tonga volcanic arc. *Earth and Planetary Science Letters*, 264(1-2), 299-307.
- Conference Participants. (1972). Penrose field conference: ophiolites. *Geotimes*, 17, 24-25.
- Coogan, L. A., Saunders, A. D., & Wilson, R. N. (2014). Aluminum-in-olivine thermometry of primitive basalts: Evidence of an anomalously hot mantle source for large igneous provinces. *Chemical Geology*, 368, 1-10.
- Costa, F., Shea, T., & Ubide, T. (2020). Diffusion chronometry and the timescales of magmatic processes. *Nature Reviews Earth & Environment*, 1-14.
- Coulson, F. I. E. (1976). Geology of the Lomaiviti and Moala island groups. Government of Fiji, Ministry of Lands and Mineral Resources, Mineral Resources Division.
- Crawford, A. J., Falloon, T. J., & Green, D. H. (1989). Classification, petrogenesis and tectonic setting of boninites, in Crawford, A. J., ed., *Boninites and Related Rocks*. Boston, Massachusetts, Unwin Hyman pp. 1-49.
- Creaser, R. A., Papanastassiou, D. A., & Wasserburg, G. J. (1991). Negative thermal ion mass spectrometry of osmium, rhenium and iridium. *Geochimica et Cosmochimica Acta*, 55(1), 397-401.
- Crocket, J. H. (1979). Platinum-group elements in mafic and ultramafic rocks: a survey. *Canadian Mineralogist*, 17(2), 391-402.
- D'Souza, R. J., Canil, D., & Coogan, L. A. (2020). Geobarometry for spinel peridotites using Ca and Al in olivine. *Contributions to Mineralogy and Petrology*, 175(1), 5.
- Dale, C. W., Luguet, A., Macpherson, C. G., Pearson, D. G., & Hickey-Vargas, R. (2008). Extreme platinum-group element fractionation and variable Os isotope compositions in Philippine Sea Plate basalts: tracing mantle source heterogeneity. *Chemical Geology*, 248(3-4), 213-238.
- Dallwitz, W. B. (1968). Chemical composition and genesis of clinoenstatite-bearing volcanic rocks from Cape Vogel, Papua: a discussion. In Proc. 23rd Int. Geol. Congr. (Vol. 2, pp. 229-242).
- Dallwitz, W. B., Green, D. H., & Thompson, J. E. (1966). Clinoenstatite in a volcanic rock from the Cape Vogel area, Papua. *Journal of Petrology*, 7(3), 375-403.
- Davey, F. J. (1982). The structure of the South Fiji basin. *Tectonophysics*, 87(1-4), 185-241.
- Davies, H. L. (1968). Papuan ultramafic belt. In Abstract volume of the 21st International Geological Congress, Prague (Vol. 1, pp. 209-220).
- Davies, H. L. (1971). Peridotite-gabbro-basalt complex in eastern Papua: an overthrust plate of oceanic mantle and crust. *Bull. Bureau Min. Res. Geol. Geophys.*, 118, 48.
- Davies, H. L. (1978). Folded thrust fault and associated metamorphism in the Suckling-Dayman massif, Papua New Guinea. *Geological Survey of Papua New Guinea*.

- Davies, H. L. (2012). The geology of New Guinea—the cordilleran margin of the Australian continent. *Episodes-Newsmagazine of the International Union of Geological Sciences*, 35(1), 87.
- Davies, H. L., & Jaques, A. L. (1984). Emplacement of ophiolite in Papua New Guinea. *Geological Society, London, Special Publications*, 13(1), 341-349.
- Davies, H. L., & Smith, I. E. (1971). Geology of eastern Papua. *Geological Society of America Bulletin*, 82(12), 3299-3312.
- Day, J. M., Walker, R. J., & Warren, J. M. (2017). 186Os–187Os and highly siderophile element abundance systematics of the mantle revealed by abyssal peridotites and Os-rich alloys. *Geochimica et Cosmochimica Acta*, 200, 232-254.
- Demouchy, S., Ishikawa, A., Tommasi, A., Alard, O., & Keshav, S. (2015). Characterization of hydration in the mantle lithosphere: Peridotite xenoliths from the Ontong Java Plateau as an example. *Lithos*, 212, 189-201.
- Dick, H. J., & Bullen, T. (1984). Chromian spinel as a petrogenetic indicator in abyssal and alpine-type peridotites and spatially associated lavas. *Contributions to Mineralogy and Petrology*, 86(1), 54-76.
- Dilek, Y. (2003). Ophiolite concept and its evolution. *Special Papers-Geological Society of America*, 1-16.
- Dilek, Y., & Furnes, H. (2014). Ophiolites and their origins. *Elements*, 10(2), 93-100.
- Douville, E., Bienvenu, P., Charlou, J. L., Donval, J. P., Fouquet, Y., Appriou, P., & Gamo, T. (1999). Yttrium and rare earth elements in fluids from various deep-sea hydrothermal systems. *Geochimica et Cosmochimica Acta*, 63(5), 627-643.
- Duke, J. M. (1976). Distribution of the period four transition elements among olivine, calcic clinopyroxene and mafic silicate liquid: experimental results. *Journal of Petrology*, 17(4), 499-521.
- Duncan, R. A., & Green, D. H. (1987). The genesis of refractory melts in the formation of oceanic crust. *Contributions to Mineralogy and Petrology*, 96(3), 326-342.
- Dupré, B., & Allègre, C. J. (1983). Pb–Sr isotope variation in Indian Ocean basalts and mixing phenomena. *Nature*, 303(5913), 142-146.
- Eggins, S. M., Woodhead, J. D., Kinsley, L. P. J., Mortimer, G. E., Sylvester, P., McCulloch, M. T., ... & Handler, M. R. (1997). A simple method for the precise determination of ≥ 40 trace elements in geological samples by ICPMS using enriched isotope internal standardisation. *Chemical Geology*, 134(4), 311-326.
- Eggler, D. H. (1987). Solubility of major and trace elements in mantle metasomatic fluids: experimental constraints, in: Menzies, M.A., Hawkesworth, C.J. (Eds.), *Mantle Metasomatism*. Academic Press, London, 21-41.
- England, R. N., & Davies, H. L. (1973). Mineralogy of ultramafic cumulates and tectonites from eastern Papua. *Earth and Planetary Science Letters*, 17(2), 416-425.
- Ernst, T. (1936). The melilite basalt of the west mountain near Hofgeismar, north of Kassel, an assimilation product of ultrabasic rocks . *Chem. Erde*, 10, 631-666.
- Esri, GEBCO, DeLorme, NaturalVue | Esri, GEBCO, IHO-IOC GEBCO, DeLorme, NGS
- Eugster, O., Tera, F., & Wasserburg, G. J. (1969). Isotopic analyses of barium in meteorites and in terrestrial samples. *Journal of Geophysical Research*, 74(15), 3897-3908.

- Fabriès, J. (1979). Spinel-olivine geothermometry in peridotites from ultramafic complexes. *Contributions to Mineralogy and Petrology*, 69(4), 329-336.
- Falloon, T. J., & Danyushevsky, L. V. (2000). Melting of refractory mantle at 1.5, 2 and 2.5 GPa under anhydrous and H₂O-undersaturated conditions: Implications for the petrogenesis of high-Ca boninites and the influence of subduction components on mantle melting. *Journal of Petrology*, 41(2), 257-283.
- Falloon, T. J., & Green, D. H. (1987). Anhydrous partial melting of MORB pyrolite and other peridotite compositions at 10 kbar: implications for the origin of primitive MORB glasses. *Mineralogy and Petrology*, 37(3-4), 181-219.
- Falloon, T. J., Green, D. H., Danyushevsky, L. V., & Faul, U. H. (1999). Peridotite melting at 1.0 and 1.5 GPa: an experimental evaluation of techniques using diamond aggregates and mineral mixes for determination of near-solidus melts. *Journal of Petrology*, 40(9), 1343-1375.
- Falloon, T. J., & Danyushevsky, L. V. (2000). Melting of refractory mantle at 1.5, 2 and 2.5 GPa under anhydrous and H₂O-undersaturated conditions: Implications for the petrogenesis of high-Ca boninites and the influence of subduction components on mantle melting. *Journal of Petrology*, 41(2), 257-283
- Fischer, K. M., Ford, H. A., Abt, D. L., & Rychert, C. A. (2010). The lithosphere-asthenosphere boundary. *Annual Review of Earth and Planetary Sciences*, 38, 551-575.
- Fischer-Gödde, M., Becker, H., & Wombacher, F. (2010). Rhodium, gold and other highly siderophile element abundances in chondritic meteorites. *Geochimica et Cosmochimica Acta*, 74(1), 356-379.
- Foley, S. F., & Pintér, Z. (2018). Primary melt compositions in the Earth's mantle. In *Magmas Under Pressure* (pp. 3-42). Elsevier.
- Foley, S. F., Prelevic, D., Rehfeldt, T., & Jacob, D. E. (2013). Minor and trace elements in olivines as probes into early igneous and mantle melting processes. *Earth and Planetary Science Letters*, 363, 181-191.
- Fonseca, R. O., Campbell, I. H., O'Neill, H. S. C., & Allen, C. M. (2009). Solubility of Pt in sulphide mattes: Implications for the genesis of PGE-rich horizons in layered intrusions. *Geochimica et Cosmochimica Acta*, 73(19), 5764-5777.
- Franz, L., & Wirth, R. (2000). Spinel inclusions in olivine of peridotite xenoliths from TUBAF seamount (Bismarck Archipelago/Papua New Guinea): evidence for the thermal and tectonic evolution of the oceanic lithosphere. *Contributions to Mineralogy and Petrology*, 140(3), 283-295.
- Franz, L., Becker, K. P., Kramer, W., & Herzig, P. M. (2002). Metasomatic mantle xenoliths from the Bismarck microplate (Papua New Guinea)—thermal evolution, geochemistry and extent of slab-induced metasomatism. *Journal of Petrology*, 43(2), 315-343.
- Frechen, J. (1948). Die Genese der Olivinausscheidungen von Dreiser Weiher (Eifel) und Finkenberg (Siebengebirge): Neues Jahrb. Mineral. Geol, 79, 317-406.
- Frey, F. A., & Prinz, M. (1978). Ultramafic inclusions from San Carlos, Arizona: petrologic and geochemical data bearing on their petrogenesis. *Earth and Planetary Science Letters*, 38(1), 129-176.
- Gaetani, G. A., & Grove, T. L. (1998). The influence of water on melting of mantle peridotite. *Contributions to Mineralogy and Petrology*, 131(4), 323-346.

- Gale, A., Dalton, C. A., Langmuir, C. H., Su, Y., & Schilling, J. G. (2013). The mean composition of ocean ridge basalts. *Geochemistry, Geophysics, Geosystems*, 14(3), 489-518.
- Garrido, C. J., Bodinier, J. L., & Alard, O. (2000). Incompatible trace element partitioning and residence in anhydrous spinel peridotites and websterites from the Ronda orogenic peridotite. *Earth and Planetary Science Letters*, 181(3), 341-358.
- Gill, J. B. (1970). Geochemistry of Viti Levu, Fiji, and its evolution as an island arc. *Contributions to Mineralogy and Petrology*, 27(3), 179-203.
- Gill, J. B. (1976). Composition and age of Lau Basin and Ridge volcanic rocks: Implications for evolution of an interarc basin and remnant arc. *Geological Society of America Bulletin*, 87(10), 1384-1395.
- Gill, J. B. (1984). Sr-Pb-Nd isotopic evidence that both MORB and OIB sources contribute to oceanic island arc magmas in Fiji. *Earth and Planetary Science Letters*, 68(3), 443-458.
- Gill, J. B. (1987). Early geochemical evolution of an oceanic island arc and backarc: Fiji and the South Fiji Basin. *The Journal of Geology*, 95(5), 589-615.
- Gill, J. B., & McDougall, I. (1973). Biostratigraphic and geological significance of Miocene-Pliocene volcanism in Fiji. *Nature*, 241(5386), 176-180.
- Gill, J., & Whelan, P. (1989). Postsubduction ocean island alkali basalts in Fiji. *Journal of Geophysical Research: Solid Earth*, 94(B4), 4579-4588.
- Glaser, S. M., Foley, S. F., & Günther, D. (1999). Trace element compositions of minerals in garnet and spinel peridotite xenoliths from the Vitim volcanic field, Transbaikalia, eastern Siberia. In *Developments in Geotectonics* (Vol. 24, pp. 263-285). Elsevier.
- Godard, M., Lagabrielle, Y., Alard, O., & Harvey, J. (2008). Geochemistry of the highly depleted peridotites drilled at ODP Sites 1272 and 1274 (Fifteen-Twenty Fracture Zone, Mid-Atlantic Ridge): Implications for mantle dynamics beneath a slow spreading ridge. *Earth and Planetary Science Letters*, 267(3-4), 410-425.
- Gonzalez-Alvarez, I., Sweetapple, M., Lindley, I. D., & Kirakar, J. (2013). Hydrothermal Ni: Doriri Creek, Papua New Guinea. *Ore Geology Reviews*, 52, 37-57.
- Green, D. H., Hibberson, W. O., Kovács, I., & Rosenthal, A. (2010). Water and its influence on the lithosphere–asthenosphere boundary. *Nature*, 467(7314), 448-451.
- Green, D. H., Hibberson, W. O., Rosenthal, A., Kovács, I., Yaxley, G. M., Falloon, T. J., & Brink, F. (2014). Experimental study of the influence of water on melting and phase assemblages in the upper mantle. *Journal of Petrology*, 55(10), 2067-2096.
- Green, H. W. (1988). Pyroxene-spinel symplectites; origin by decomposition of garnet confirmed. *Am. Geophys. Union EOS*, 69, 1514.
- Grégoire, M., Moine, B. N., O'Reilly, S. Y., Cottin, J. Y., & Giret, A. (2000). Trace element residence and partitioning in mantle xenoliths metasomatized by highly alkaline, silicate-and carbonate-rich melts (Kerguelen Islands, Indian Ocean). *Journal of Petrology*, 41(4), 477-509.
- Hall, R. (2002). Cenozoic geological and plate tectonic evolution of SE Asia and the SW Pacific: computer-based reconstructions, model and animations. *Journal of Asian Earth Sciences*, 20(4), 353-431.
- Hamburger, M. W., Everingham, I. B., Isacks, B. L., & Barazangi, M. (1990). Seismicity and crustal structure of the Fiji Platform, Southwest Pacific. *Journal of Geophysical Research: Solid Earth*, 95(B3), 2553-2573.

- Hanghøj, K., Kelemen, P., Bernstein, S., Blusztajn, J., & Frei, R. (2001). Osmium isotopes in the Wiedemann Fjord mantle xenoliths: a unique record of cratonic mantle formation by melt depletion in the Archaean. *Geochemistry, Geophysics, Geosystems*, 2(1).
- Hanghøj, K., Kelemen, PB, Hassler, D., & Godard, M. (2010). Composition and genesis of depleted mantle peridotites from the Wadi Tayin Massif, Oman Ophiolite; major and trace element geochemistry, and Os isotope and PGE systematics. *Journal of Petrology*, 51 (1-2), 201-227.
- Hart, S. R. (1984). A large-scale isotope anomaly in the Southern Hemisphere mantle. *Nature*, 309(5971), 753-757.
- Harvey, J., Gannoun, A., Burton, K. W., Rogers, N. W., Alard, O., & Parkinson, I. J. (2006). Ancient melt extraction from the oceanic upper mantle revealed by Re-Os isotopes in abyssal peridotites from the Mid-Atlantic ridge. *Earth and Planetary Science Letters*, 244(3-4), 606-621.
- Hathway, B. (1993). The Nadi Basin: Neogene strike-slip faulting and sedimentation in a fragmented arc, western Viti Levu, Fiji. *Journal of the Geological Society*, 150(3), 563-581.
- Hauri, E. H., & Hart, S. R. (1994). Constraints on melt migration from mantle plumes: a trace element study of peridotite xenoliths from Savai'i, Western Samoa. *Journal of Geophysical Research: Solid Earth*, 99(B12), 24301-24321.
- Hauri, E. H., Shimizu, N., Dieu, J. J., & Hart, S. R. (1993). Evidence for hotspot-related carbonatite metasomatism in the oceanic upper mantle. *Nature*, 365(6443), 221-227.
- Hellebrand, E., Snow, J. E., Dick, H. J., & Hofmann, A. W. (2001). Coupled major and trace elements as indicators of the extent of melting in mid-ocean-ridge peridotites. *Nature*, 410(6829), 677-681.
- Hellebrand, E., Snow, J. E., Hoppe, P., & Hofmann, A. W. (2002). Garnet-field melting and late-stage refertilization in 'residual' abyssal peridotites from the Central Indian Ridge. *Journal of Petrology*, 43(12), 2305-2338.
- Herzberg, C. (2004). Geodynamic information in peridotite petrology. *Journal of Petrology*, 45(12), 2507-2530.
- Hickey-Vargas, R., Yogodzinski, G. M., Ishizuka, O., McCarthy, A., Bizimis, M., Kusano, Y., ... & Arculus, R. (2018). Origin of depleted basalts during subduction initiation and early development of the Izu-Bonin-Mariana island arc: Evidence from IODP expedition 351 site U1438, Amami-Sankaku basin. *Geochimica et Cosmochimica Acta*, 229, 85-111.
- Hindle, W. H., & Colley, H. (1981). An oceanic volcano in an island arc setting—Seatura Volcano, Fiji. *Geological Magazine*, 118(1), 1-14.
- Hofmann, A. W. (1988). Chemical differentiation of the Earth: the relationship between mantle, continental crust, and oceanic crust. *Earth and Planetary Science Letters*, 90(3), 297-314.
- Holmes, K. D., & Hall, R. J. (1975). Marum nickeliferous laterite, Madang District, PNG. *Economic geology of Australia and Papua New Guinea*, 1, 1011-1017.
- Hughes, H. S., McDonald, I., Faithfull, J. W., Upton, B. G., & Loocke, M. (2016). Cobalt and precious metals in sulphides of peridotite xenoliths and inferences concerning their distribution according to geodynamic environment: a case study from the Scottish lithospheric mantle. *Lithos*, 240, 202-227.
- Hunter, R. H. (1987). Textural equilibrium in layered igneous rocks. In: *Origins of igneous layering* (pp. 473-503). Springer, Dordrecht.

- IAG, 2015. IAG certified reference materials. Available at: <http://www.iageo.com/index.php/certified-reference-materials.html>.
- Ionov, D. A., Bodinier, J. L., Mukasa, S. B., & Zanetti, A. (2002). Mechanisms and sources of mantle metasomatism: major and trace element compositions of peridotite xenoliths from Spitsbergen in the context of numerical modelling. *Journal of Petrology*, 43(12), 2219-2259.
- Irvine, T. N. (1982). Terminology for layered intrusions. *Journal of Petrology*, 23(2), 127-162.
- Ishii, T., Robinson, P. T., Maekawa, H., & Fiske, R. (1992). Petrological studies of peridotites from diapiric serpentinite seamounts in the Izu-Ogasawara-Mariana forearc, Leg 125. In *Proceedings of the ocean drilling program, scientific results* (Vol. 125, No. 445-485). College Station: Ocean Drilling Program.
- Ishikawa, A., Kuritani, T., Makishima, A., & Nakamura, E. (2007). Ancient recycled crust beneath the Ontong Java Plateau: Isotopic evidence from the garnet clinopyroxenite xenoliths, Malaita, Solomon Islands. *Earth and Planetary Science Letters*, 259(1-2), 134-148.
- Ishikawa, A., Maruyama, S., & Komiya, T. (2004). Layered lithospheric mantle beneath the Ontong Java Plateau: implications from xenoliths in alnöite, Malaita, Solomon Islands. *Journal of Petrology*, 45(10), 2011-2044.
- Ishikawa, A., Pearson, D. G., & Dale, C. W. (2011). Ancient Os isotope signatures from the Ontong Java Plateau lithosphere: Tracing lithospheric accretion history. *Earth and Planetary Science Letters*, 301(1-2), 159-170.
- Ishizuka, O., Tani, K., & Reagan, M. K. (2014). Izu-Bonin-Mariana forearc crust as a modern ophiolite analogue. *Elements*, 10(2), 115-120.
- Jackson, E. D., Green, H. W., & Moores, E. M. (1975). The Vourinos ophiolite, Greece: cyclic units of lineated cumulates overlying harzburgite tectonite. *Geological Society of America Bulletin*, 86(3), 390-398.
- Jackson, M. G., Shirey, S. B., Hauri, E. H., Kurz, M. D., & Rizo, H. (2016). Peridotite xenoliths from the Polynesian Austral and Samoa hotspots: Implications for the destruction of ancient 187Os and 142Nd isotopic domains and the preservation of Hadean 129Xe in the modern convecting mantle. *Geochimica et Cosmochimica Acta*, 185, 21-43.
- Jaques, A. L. (1980). Petrologic and experimental studies on the petrogenesis of Papua New Guinea ophiolites (Doctoral dissertation, University of Tasmania).
- Jaques, A. L. (1981). Petrology and petrogenesis of cumulate peridotites and gabbros from the Marum ophiolite complex, northern Papua New Guinea. *Journal of Petrology*, 22(1), 1-40.
- Jaques, A. L., & Chappell, B. W. (1980). Petrology and trace element geochemistry of the Papuan ultramafic belt. *Contributions to Mineralogy and Petrology*, 75(1), 55-70.
- Jaques, A. L., & Green, D. H. (1980). Anhydrous melting of peridotite at 0–15 kb pressure and the genesis of tholeiitic basalts. *Contributions to Mineralogy and Petrology*, 73(3), 287-310.
- Jaques, A. L., Chappell, B. W., & Taylor, S. R. (1983). Geochemistry of cumulus peridotites and gabbros from the Marum ophiolite complex, northern Papua New Guinea. *Contributions to Mineralogy and Petrology*, 82(2-3), 154-164.
- Jaques, A. L., Chappell, B. W., & Taylor, S.R. (1978). Geochemistry of LIL-element enriched tholeiites from the Marum ophiolite complex, northern Papua New Guinea. *B.M.R.J. Austral. Geol. Geophys.*, 3(4), 297-310.

- Jaques, A. L., Robinson, G.P. (1977). The continent/island-arc collision in northern Papua New Guinea. *B.M.R.J. Austral. Geol. Geophys.*, 2, 289-303.
- Jenner, F. E., & O'Neill, H. S. C. (2012). Major and trace analysis of basaltic glasses by laser-ablation ICP-MS. *Geochemistry, Geophysics, Geosystems*, 13(3).
- Jenner, G. A. (1981). Geochemistry of high-Mg andesites from Cape Vogel, Papua New Guinea. *Chemical Geology*, 33(1-4), 307-332.
- Jochum, K. P., Nohl, U., Herwig, K., Lammel, E., Stoll, B., & Hofmann, A. W. (2005). GeoReM: a new geochemical database for reference materials and isotopic standards. *Geostandards and Geoanalytical Research*, 29(3), 333-338.
- Jochum, K. P., Weis, U., Stoll, B., Kuzmin, D., Yang, Q., Raczek, I., ... & Günther, D. (2011). Determination of reference values for NIST SRM 610-617 glasses following ISO guidelines. *Geostandards and Geoanalytical Research*, 35(4), 397-429.
- Jochum, K. P., Willbold, M., Raczek, I., Stoll, B., & Herwig, K. (2005). Chemical Characterisation of the USGS Reference Glasses GSA-1G, GSC-1G, GSD-1G, GSE-1G, BCR-2G, BHVO-2G and BIR-1G Using EPMA, ID-TIMS, ID-ICP-MS and LA-ICP-MS. *Geostandards and Geoanalytical Research*, 29(3), 285-302.
- Johan, Z., Slansky, E., & Kelly, D. A. (2000). Platinum nuggets from the Kompiam area, Enga Province, Papua New Guinea: evidence for an Alaskan-type complex. *Mineralogy and Petrology*, 68(1-3), 159-176.
- Johnson, K. T., Dick, H. J., & Shimizu, N. (1990). Melting in the oceanic upper mantle: an ion microprobe study of diopsides in abyssal peridotites. *Journal of Geophysical Research: Solid Earth*, 95(B3), 2661-2678.
- Johnston, S. T. (2004). The New Caledonia-D'Entrecasteaux orocline and its role in clockwise rotation of the Vanuatu-New Hebrides Arc and formation of the North Fiji Basin. *Orogenic Curvature: Integrating Paleomagnetic and Structural Analyses: Geological Society of America Special Paper*, 383, 225-236.
- Kaczmarek, M. A., Jonda, L., & Davies, H. L. (2015). Evidence of melting, melt percolation and deformation in a supra-subduction zone (Marum ophiolite complex, Papua New Guinea). *Contributions to Mineralogy and Petrology*, 170(2), 19.
- Kamenetsky, V. S., Crawford, A. J., & Meffre, S. (2001). Factors controlling chemistry of magmatic spinel: an empirical study of associated olivine, Cr-spinel and melt inclusions from primitive rocks. *Journal of Petrology*, 42(4), 655-671.
- Kamenetsky, V. S., Sobolev, A. V., Eggins, S. M., Crawford, A. J., & Arculus, R. J. (2002). Olivine-enriched melt inclusions in chromites from low-Ca boninites, Cape Vogel, Papua New Guinea: evidence for ultramafic primary magma, refractory mantle source and enriched components. *Chemical Geology*, 183(1-4), 287-303.
- Katz, R. F., Spiegelman, M., & Langmuir, C. H. (2003). A new parameterization of hydrous mantle melting. *Geochemistry, Geophysics, Geosystems*, 4(9).
- Kelemen, P. B. (1990). Reaction between ultramafic rock and fractionating basaltic magma I. Phase relations, the origin of calc-alkaline magma series, and the formation of discordant dunite. *Journal of Petrology*, 31(1), 51-98.
- Kelemen, P. B., Dick, H. J., & Quick, J. E. (1992). Formation of harzburgite by pervasive melt/rock reaction in the upper mantle. *Nature*, 358(6388), 635-641.

- Kelemen, P. B., Shimizu, N., & Salters, V. J. (1995). Extraction of mid-ocean-ridge basalt from the upwelling mantle by focused flow of melt in dunite channels. *Nature*, 375(6534), 747-753.
- Kepezhinskas, P., Defant, M. J., & Widom, E. (2002). Abundance and distribution of PGE and Au in the island-arc mantle: implications for sub-arc metasomatism. *Lithos*, 60(3-4), 113-128.
- Klemme, S. (2004). The influence of Cr on the garnet–spinel transition in the Earth's mantle: experiments in the system MgO–Cr₂O₃–SiO₂ and thermodynamic modelling. *Lithos*, 77(1-4), 639-646.
- Koga, K. T., Shimizu, N., & Grove, T. L. (1999). Experimental Determination of Garnet-Spinel Coexisting Lherzolite Facies and Trace Element Distribution. *Ofioliti*, 24(1b), 114-115.
- Kogarko, L., Kurat, G., & Ntaflos, T. (2001). Carbonate metasomatism of the oceanic mantle beneath Fernando de Noronha Island, Brazil. *Contributions to Mineralogy and Petrology*, 140(5), 577-587.
- Köhler, T. P., & Brey, G. (1990). Calcium exchange between olivine and clinopyroxene calibrated as a geothermobarometer for natural peridotites from 2 to 60 kb with applications. *Geochimica et Cosmochimica Acta*, 54(9), 2375-2388.
- König, S., Münker, C., Schuth, S., Luguet, A., Hoffmann, J. E., & Kuduon, J. (2010). Boninites as windows into trace element mobility in subduction zones. *Geochimica et Cosmochimica Acta*, 74(2), 684-704.
- Kubo, K. (2002). Dunite formation processes in highly depleted peridotite: case study of the Iwanaidake peridotite, Hokkaido, Japan. *Journal of Petrology*, 43(3), 423-448.
- Lassiter, J. C., Byerly, B. L., Snow, J. E., & Hellebrand, E. (2014). Constraints from Os-isotope variations on the origin of Lena Trough abyssal peridotites and implications for the composition and evolution of the depleted upper mantle. *Earth and Planetary Science Letters*, 403, 178-187.
- Latkoczy, C., & Günther, D. (2002). Enhanced sensitivity in inductively coupled plasma sector field mass spectrometry for direct solid analysis using laser ablation (LA-ICP-SFMS). *Journal of Analytical Atomic Spectrometry*, 17(10), 1264-1270.
- Lawley, C. J., Pearson, D. G., Waterton, P., Zagorevski, A., Bédard, J. H., Jackson, S. E., ... & Wright, D. (2020). Element and isotopic signature of re-fertilized mantle peridotite as determined by nanopowder and olivine LA-ICPMS analyses. *Chemical Geology*, 536, 119464.
- Le Bas, M. L., Maitre, R. L., Streckeisen, A., Zanettin, B., & IUGS Subcommission on the Systematics of Igneous Rocks. (1986). A chemical classification of volcanic rocks based on the total alkali-silica diagram. *Journal of Petrology*, 27(3), 745-750.
- Le Roux, V., & Liang, Y. (2019). Ophiolitic pyroxenites record boninite percolation in subduction zone mantle. *Minerals*, 9(9), 565.
- Leslie, R. A., Danyushevsky, L. V., Crawford, A. J., & Verbeeten, A. C. (2009). Primitive shoshonites from Fiji: Geochemistry and source components. *Geochemistry, Geophysics, Geosystems*, 10(7).
- Lian, D., Yang, J., Dilek, Y., & Rocholl, A. (2019). Mineralogy and geochemistry of peridotites and chromitites in the Aladag Ophiolite (southern Turkey): melt evolution of the Cretaceous Neotethyan mantle. *Journal of the Geological Society*, 176(5), 958-974.
- Liang, Y., Sun, C., & Yao, L. (2013). A REE-in-two-pyroxene thermometer for mafic and ultramafic rocks. *Geochimica et Cosmochimica Acta*, 102, 246-260.

- Liu, C. Z., Snow, J. E., Brügmann, G., Hellebrand, E., & Hofmann, A. W. (2009). Non-chondritic HSE budget in Earth's upper mantle evidenced by abyssal peridotites from Gakkel ridge (Arctic Ocean). *Earth and Planetary Science Letters*, 283(1-4), 122-132.
- Liu, C. Z., Xu, Y., & Wu, F. Y. (2018). Limited recycling of crustal osmium in forearc mantle during slab dehydration. *Geology*, 46(3), 239-242.
- Liu, J., & Pearson, D. G. (2014). Rapid, precise and accurate Os isotope ratio measurements of nanogram to sub-nanogram amounts using multiple Faraday collectors and amplifiers equipped with $1012\ \Omega$ resistors by N-TIMS. *Chemical Geology*, 363, 301-311.
- Liu, J., Pearson, D. G., Shu, Q., Sigurdsson, H., Thomassot, E., & Alard, O. (2020). Dating post-Archean lithospheric mantle: Insights from Re-Os and Lu-Hf isotopic systematics of the Cameroon Volcanic Line peridotites. *Geochimica et Cosmochimica Acta*, 278, 177-198.
- Liu, J., Scott, J. M., Martin, C. E., & Pearson, D. G. (2015). The longevity of Archean mantle residues in the convecting upper mantle and their role in young continent formation. *Earth and Planetary Science Letters*, 424, 109-118.
- Lorand, J. P., Delpech, G., Grégoire, M., Moine, B., O'Reilly, S. Y., & Cottin, J. Y. (2004). Platinum-group elements and the multistage metasomatic history of Kerguelen lithospheric mantle (South Indian Ocean). *Chemical Geology*, 208(1-4), 195-215.
- Lorand, J. P., & Luguet, A. (2016). Chalcophile and siderophile elements in mantle rocks: Trace elements controlled by trace minerals. *Reviews in Mineralogy and Geochemistry*, 81(1), 441-488.
- Luck, J. M., & Allègre, C. J. (1983). $^{187}\text{Re}-^{187}\text{Os}$ systematics in meteorites and cosmochemical consequences. *Nature*, 302(5904), 130-132.
- Luguet, A., & Pearson, G. (2019). Dating mantle peridotites using Re-Os isotopes: The complex message from whole rocks, base metal sulfides, and platinum group minerals. *American Mineralogist*, 104(2), 165-189.
- Luguet, A., Alard, O., Lorand, J. P., Pearson, N. J., Ryan, C., & O'Reilly, S. Y. (2001). Laser-ablation microprobe (LAM)-ICPMS unravels the highly siderophile element geochemistry of the oceanic mantle. *Earth and Planetary Science Letters*, 189(3-4), 285-294.
- Luguet, A., Lorand, J. P., & Seyler, M. (2003). Sulfide petrology and highly siderophile element geochemistry of abyssal peridotites: A coupled study of samples from the Kane Fracture Zone (45°W 23°20'N, MARK area, Atlantic Ocean). *Geochimica et Cosmochimica Acta*, 67(8), 1553-1570.
- Luguet, A., Lorand, J. P., Alard, O., & Cottin, J. Y. (2004). A multi-technique study of platinum group element systematic in some Ligurian ophiolitic peridotites, Italy. *Chemical Geology*, 208(1-4), 175-194.
- Luguet, A., Nowell, G. M., & Pearson, D. G. (2008). $^{184}\text{Os}/^{188}\text{Os}$ and $^{186}\text{Os}/^{188}\text{Os}$ measurements by Negative Thermal Ionisation Mass Spectrometry (N-TIMS): effects of interfering element and mass fractionation corrections on data accuracy and precision. *Chemical Geology*, 248(3-4), 342-362.
- Luguet, A., Shirey, S. B., Lorand, J. P., Horan, M. F., & Carlson, R. W. (2007). Residual platinum-group minerals from highly depleted harzburgites of the Lherz massif (France) and their role in HSE fractionation of the mantle. *Geochimica et Cosmochimica Acta*, 71(12), 3082-3097.

- Lus, W. Y., McDougall, I., & Davies, H. L. (2004). Age of the metamorphic sole of the Papuan Ultramafic Belt ophiolite, Papua New Guinea. *Tectonophysics*, 392(1-4), 85-101.
- Luth, R. W., & Stachel, T. (2014). The buffering capacity of lithospheric mantle: implications for diamond formation. *Contributions to Mineralogy and Petrology*, 168(5), 1083.
- Malitch, K. N., & Thalhammer, O. A. (2002). Pt–Fe nuggets derived from clinopyroxenite–dunite massifs, Russia: a structural, compositional and osmium-isotope study. *The Canadian Mineralogist*, 40(2), 395-418.
- Mallmann, G., & O'Neill, H. S. C. (2009). The crystal/melt partitioning of V during mantle melting as a function of oxygen fugacity compared with some other elements (Al, P, Ca, Sc, Ti, Cr, Fe, Ga, Y, Zr and Nb). *Journal of Petrology*, 50(9), 1765-1794.
- Marchesi, C., Garrido, C. J., Godard, M., Belley, F., & Ferré, E. (2009). Migration and accumulation of ultra-depleted subduction-related melts in the Massif du Sud ophiolite (New Caledonia). *Chemical Geology*, 266(3-4), 171-186.
- Maury, R. C., Defant, M. J., & Joron, J. L. (1992). Metasomatism of the sub-arc mantle inferred from trace elements in Philippine xenoliths. *Nature*, 360(6405), 661-663.
- McDonough, W. F., & Rudnick, R. L. (1998). Mineralogy and composition of the upper mantle. *Reviews in Mineralogy*, 37, 139-164.
- McDonough, W. F., & Sun, S. S. (1995). The composition of the Earth. *Chemical Geology*, 120(3-4), 223-253.
- McDougall, I. (1963). Potassium–argon ages of some rocks from Viti Levu, Fiji. *Nature*, 198(4881), 677-677.
- McInnes, B. I., Gregoire, M., Binns, R. A., Herzig, P. M., & Hannington, M. D. (2001). Hydrous metasomatism of oceanic sub-arc mantle, Lihir, Papua New Guinea: petrology and geochemistry of fluid-metasomatised mantle wedge xenoliths. *Earth and Planetary Science Letters*, 188(1-2), 169-183.
- McInnes, B. I., McBride, J. S., Evans, N. J., Lambert, D. D., & Andrew, A. S. (1999). Osmium isotope constraints on ore metal recycling in subduction zones. *Science*, 286(5439), 512-516.
- McKenzie, D. (1989). Some remarks on the movement of small melt fractions in the mantle. *Earth and Planetary Science Letters*, 95(1-2), 53-72.
- McKenzie, D., Jackson, J., & Priestley, K. (2005). Thermal structure of oceanic and continental lithosphere. *Earth and Planetary Science Letters*, 233(3-4), 337-349.
- Meisel, T., Walker, R. J., Irving, A. J., & Lorand, J. P. (2001). Osmium isotopic compositions of mantle xenoliths: a global perspective. *Geochimica et Cosmochimica Acta*, 65(8), 1311-1323.
- Mercier, J. C., & Nicolas, A. (1975). Textures and fabrics of upper-mantle peridotites as illustrated by xenoliths from basalts. *Journal of Petrology*, 16(1), 454-487.
- Merle, R., Kaczmarek, M. A., Tronche, E., & Girardeau, J. (2012). Occurrence of inherited supra-subduction zone mantle in the oceanic lithosphere as inferred from mantle xenoliths from Dragon Seamount (southern Tore–Madeira Rise). *Journal of the Geological Society*, 169(3), 251-267.
- Mertzman, S. A. (2015). XRF laboratory: overview and analytical procedures.
- Miller, W. G., Holland, T. J., & Gibson, S. A. (2016). Garnet and spinel oxybarometers: new internally consistent multi-equilibria models with applications to the oxidation state of the lithospheric mantle. *Journal of Petrology*, 57(6), 1199-1222.

- Mitchell, A. L., & Grove, T. L. (2015). Melting the hydrous, subarc mantle: the origin of primitive andesites. *Contributions to Mineralogy and Petrology*, 170(2), 13.
- Miyashiro, A. (1973). The Troodos ophiolitic complex was probably formed in an island arc. *Earth and Planetary Science Letters*, 19(2), 218-224.
- Morgan, J. W. (1986). Ultramafic xenoliths: clues to Earth's late accretionary history. *Journal of Geophysical Research: Solid Earth*, 91(B12), 12375-12387.
- Morrison, G. W. (1980). Characteristics and tectonic setting of the shoshonite rock association. *Lithos*, 13(1), 97-108.
- Mortimer, N., Herzer, R. H., Gans, P. B., Laporte-Magoni, C., Calvert, A. T., & Bosch, D. (2007). Oligocene–Miocene tectonic evolution of the South Fiji Basin and Northland Plateau, SW Pacific Ocean: Evidence from petrology and dating of dredged rocks. *Marine Geology*, 237(1-2), 1-24.
- Neal, C. R., & Taylor, L. A. (1989). A negative Ce anomaly in a peridotite xenolith: evidence for crustal recycling into the mantle or mantle metasomatism?. *Geochimica et Cosmochimica Acta*, 53(5), 1035-1040.
- Neumann, E. R. (1991). Ultramafic and mafic xenoliths from Hierro, Canary Islands: evidence for melt infiltration in the upper mantle. *Contributions to Mineralogy and Petrology*, 106(2), 236-252.
- Neumann, E. R., Wulff-Pedersen, E., Johnsen, K., Andersen, T., & Krogh, E. (1995). Petrogenesis of spinel harzburgite and dunite suite xenoliths from Lanzarote, eastern Canary Islands: implications for the upper mantle. *Lithos*, 35(1-2), 83-107.
- Neumann, E. R., Wulff-Pedersen, E., Pearson, N. J., & Spencer, E. A. (2002). Mantle xenoliths from Tenerife (Canary Islands): evidence for reactions between mantle peridotites and silicic carbonatite melts inducing Ca metasomatism. *Journal of Petrology*, 43(5), 825-857.
- Nimis, P., & Grütter, H. (2010). Internally consistent geothermometers for garnet peridotites and pyroxenites. *Contributions to Mineralogy and Petrology*, 159(3), 411-427.
- Nimis, P., & Taylor, W. R. (2000). Single clinopyroxene thermobarometry for garnet peridotites. Part I. Calibration and testing of a Cr-in-Cpx barometer and an enstatite-in-Cpx thermometer. *Contributions to Mineralogy and Petrology*, 139(5), 541-554.
- Niu, Y. (1997). Mantle melting and melt extraction processes beneath ocean ridges: evidence from abyssal peridotites. *Journal of Petrology*, 38(8), 1047-1074.
- Niu, Y., & Green, D. H. (2018). The petrological control on the lithosphere-asthenosphere boundary (LAB) beneath ocean basins. *Earth-Science Reviews*, 185, 301-307.
- Nixon, P. H. (1987). Mantle xenoliths. John Wiley & Sons Ltd., Chichester.
- Nixon, P. H., & Boyd, F. R. (1979). Garnet bearing lherzolites and discrete nodule suites from the Malaita alnoite, Solomon Islands, SW Pacific, and their bearing on oceanic mantle composition and geotherm. *The Mantle Sample: Inclusion in Kimberlites and Other Volcanics*, 16, 400-423.
- Nixon, P. H., & Coleman, P. J. (1978). Garnet-bearing lherzolites and discrete nodule suites from the Malaita alnoite, Solomon Islands, and their bearing on the nature and origin of the Ontong Java Plateau. *Exploration Geophysics*, 9(3), 103-107.
- National Oceanic and Atmospheric Administration (NOAA). ""How big is the Pacific Ocean?""". [oceanexplorer.noaa.gov.](http://oceanexplorer.noaa.gov/)"

- O'Driscoll, B., Emeleus, C. H., Donaldson, C. H., & Daly, J. S. (2010). Cr-spinel seam petrogenesis in the Rum Layered Suite, NW Scotland: cumulate assimilation and in situ crystallization in a deforming crystal mush. *Journal of Petrology*, 51(6), 1171-1201.
- O'Neill, H. S. (1987). Quartz-fayalite-iron and quartz-fayalite-magnetite equilibria and the free energy of formation of fayalite (Fe_2SiO_4) and magnetite (Fe_3O_4). *American Mineralogist*, 72(1-2), 67-75.
- O'Neill, H. S. C., & Wall, V. J. (1987). The Olivine—Orthopyroxene—Spinel oxygen geobarometer, the nickel precipitation curve, and the oxygen fugacity of the Earth's Upper Mantle. *Journal of Petrology*, 28(6), 1169-1191.
- Parkinson, I. J., & Pearce, J. A. (1998). Peridotites from the Izu–Bonin–Mariana forearc (ODP Leg 125): evidence for mantle melting and melt–mantle interaction in a supra-subduction zone setting. *Journal of Petrology*, 39(9), 1577-1618.
- Patkó, L., Liptai, N., Aradi, L. E., Klébesz, R., Sendula, E., Bodnar, R. J., ... & Trásy, B. (2020). Metasomatism-induced wehrlite formation in the upper mantle beneath the Nograd-Gömör Volcanic Field (Northern Pannonian Basin): Evidence from xenoliths. *Geoscience Frontiers*, 11(3), 943-964.
- Paton, C., Hellstrom, J., Paul, B., Woodhead, J., & Hergt, J. (2011). Iolite: Freeware for the visualisation and processing of mass spectrometric data. *Journal of Analytical Atomic Spectrometry*, 26(12), 2508-2518.
- Pearce, J. A. (2014). Immobile element fingerprinting of ophiolites. *Elements*, 10(2), 101-108.
- Pearce, J. A., & Robinson, P. T. (2010). The Troodos ophiolitic complex probably formed in a subduction initiation, slab edge setting. *Gondwana Research*, 18(1), 60-81.
- Pearce, J. A., Barker, P. F., Edwards, S. J., Parkinson, I. J., & Leat, P. T. (2000). Geochemistry and tectonic significance of peridotites from the South Sandwich arc–basin system, South Atlantic. *Contributions to Mineralogy and Petrology*, 139(1), 36-53.
- Pearce, J. A., Kempton, P. D., & Gill, J. B. (2007). Hf–Nd evidence for the origin and distribution of mantle domains in the SW Pacific. *Earth and Planetary Science Letters*, 260(1-2), 98-114.
- Pearce, J. A., Lippard, S. J., & Roberts, S. (1984). Characteristics and tectonic significance of supra-subduction zone ophiolites. *Geological Society, London, Special Publications*, 16(1), 77-94.
- Pearson, D. G., & Wittig, N. (2008). Formation of Archaean continental lithosphere and its diamonds: the root of the problem. *Journal of the Geological Society*, 165(5), 895-914.
- Pearson, D. G., & Wittig, N. (2014). The formation and evolution of cratonic mantle lithosphere—evidence from mantle xenoliths, in: Holland, H.D., Turekian, K.K. (Eds.), *Treatise on Geochemistry*. Elsevier Ltd., Amsterdam, 255-292.
- Pearson, D. G., & Woodland, S. J. (2000). Solvent extraction/anion exchange separation and determination of PGEs (Os, Ir, Pt, Pd, Ru) and Re–Os isotopes in geological samples by isotope dilution ICP-MS. *Chemical Geology*, 165(1-2), 87-107.
- Pearson, D. G., Canil, D., & Shirey, S. B. (2003). Mantle samples included in volcanic rocks: xenoliths and diamonds. *Treatise on Geochemistry*, 2, 568.
- Pearson, D. G., Irvine, G. J., Ionov, D. A., Boyd, F. R., & Dreibus, G. E. (2004). Re–Os isotope systematics and platinum group element fractionation during mantle melt extraction: a study of massif and xenolith peridotite suites. *Chemical Geology*, 208(1-4), 29-59.
- Pearson, D. G., Parman, S. W., & Nowell, G. M. (2007). A link between large mantle melting events and continent growth seen in osmium isotopes. *Nature*, 449(7159), 202-205.

- Pearson, D. G., Smith, C. B., Liu, J., Mather, K. A., Krebs, M. Y., Bulanova, G. P., & Kobussen, A. (2018). Characteristics and origin of the mantle root beneath the Murowa diamond mine: Implications for craton and diamond formation. *Society of Economic Geologists Special Publication*, 20, 403-424.
- Peters, B. J., Day, J. M., & Taylor, L. A. (2016). Early mantle heterogeneities in the Réunion hotspot source inferred from highly siderophile elements in cumulate xenoliths. *Earth and Planetary Science Letters*, 448, 150-160.
- Peters, D., & Pettke, T. (2017). Evaluation of major to ultra trace element bulk rock chemical analysis of nanoparticulate pressed powder pellets by LA-ICP-MS. *Geostandards and Geoanalytical Research*, 41(1), 5-28.
- Pieters, P. E. (1978). Port Moresby-Kalo-Aroa-1: 250,000 Geological Series. Explanatory notes to accompany Port Moresby-Kalo-Aroa, 250, 55-6.
- Pirard, C., Hermann, J., & O'Neill, H. S. C. (2013). Petrology and geochemistry of the crust–mantle boundary in a nascent arc, Massif du Sud ophiolite, New Caledonia, SW Pacific. *Journal of Petrology*, 54(9), 1759-1792.
- Pirnia, T., Saccani, E., & Arai, S. (2018). Spinel and plagioclase peridotites of the Nain ophiolite (Central Iran): Evidence for the incipient stage of oceanic basin formation. *Lithos*, 310, 1-19.
- Price, A. A., Jackson, M. G., Blichert-Toft, J., Hall, P. S., Sinton, J. M., Kurz, M. D., & Blusztajn, J. (2014). Evidence for a broadly distributed Samoan-plume signature in the northern Lau and North Fiji Basins. *Geochemistry, Geophysics, Geosystems*, 15(4), 986-1008.
- Price, A. A., Jackson, M. G., Blichert-Toft, J., Kurz, M. D., Gill, J., Blusztajn, J., ... & Arculus, R. (2017). Geodynamic implications for zonal and meridional isotopic patterns across the northern Lau and North Fiji Basins. *Geochemistry, Geophysics, Geosystems*, 18(3), 1013-1042.
- Quick, J. E. (1981). Petrology and petrogenesis of the Trinity peridotite, an upper mantle diapir in the eastern Klamath Mountains, northern California. *Journal of Geophysical Research: Solid Earth*, 86(B12), 11837-11863.
- Raczek, I., Stoll, B., Hofmann, A. W., & Peter Jochum, K. (2001). High-Precision Trace Element Data for the USGS Reference Materials BCR-1, BCR-2, BHVO-1, BHVO-2, AGV-1, AGV-2, DTS-1, DTS-2, GSP-1 and GSP-2 by ID-TIMS and MIC-SSMS. *Geostandards Newsletter*, 25(1), 77-86.
- Rampone, E., Borghini, G., Godard, M., Ildefonse, B., Crispini, L., & Fumagalli, P. (2016). Melt/rock reaction at oceanic peridotite/gabbro transition as revealed by trace element chemistry of olivine. *Geochimica et Cosmochimica Acta*, 190, 309-331.
- Rampone, E., Hofmann, A. W., & Raczek, I. (1998). Isotopic contrasts within the Internal Liguride ophiolite (N. Italy): the lack of a genetic mantle–crust link. *Earth and Planetary Science Letters*, 163(1-4), 175-189.
- Reagan, M. K., Ishizuka, O., Stern, R. J., Kelley, K. A., Ohara, Y., Blichert-Toft, J., ... & Hickey-Vargas, R. (2010). Fore-arc basalts and subduction initiation in the Izu-Bonin-Mariana system. *Geochemistry, Geophysics, Geosystems*, 11(3).
- Reisberg, L., & Meisel, T. (2002). The Re-Os isotopic system: A review of analytical techniques. *Geostandards Newsletter*, 26(3), 249-267.
- Rodda, P. (1994). Geology in Fiji. *Geology and submarine resources of Tonga-Lau-Fiji region*. South Pacific Applied Geoscience Commission, 131-151.

- Rogers, N. W., & Setterfield, T. N. (1994). Potassium and incompatible-element enrichment in shoshonitic lavas from the Tavua volcano, Fiji. *Chemical Geology*, 118(1-4), 43-62.
- Rogerson, R. (1991). New stratigraphic and whole-rock geochemical data from the Waria River area, northern Papuan Peninsula. *Geological Survey of Papua New Guinea Report*, 91 (7).
- Rollinson, H. (2008). The geochemistry of mantle chromitites from the northern part of the Oman ophiolite: inferred parental melt compositions. *Contributions to Mineralogy and Petrology*, 156(3), 273-288.
- Rollinson, H. (2017). Masirah—the other Oman ophiolite: A better analogue for mid-ocean ridge processes?. *Geoscience Frontiers*, 8(6), 1253-1262.
- Ross, C. S., Foster, M. D., & Myers, A. T. (1954). Origin of dunites and of olivine-rich inclusions in basaltic rocks. *American Mineralogist: Journal of Earth and Planetary Materials*, 39(9-10), 693-737.
- Rudnick, R. L., & Nyblade, A. A. (1999). The thickness and heat production of Archean lithosphere: constraints from xenolith thermobarometry and surface heat flow. *Mantle petrology: field observations and high pressure experimentation: a tribute to Francis R. (Joe) Boyd*, 6, 3-12.
- Rudnick, R. L., McDonough, W. F., & Chappell, B. W. (1993). Carbonatite metasomatism in the northern Tanzanian mantle: petrographic and geochemical characteristics. *Earth and Planetary Science Letters*, 114(4), 463-475.
- Rychert, C. A., & Shearer, P. M. (2009). A global view of the lithosphere-asthenosphere boundary. *Science*, 324(5926), 495-498.
- Salters, V. J., & Stracke, A. (2004). Composition of the depleted mantle. *Geochemistry, Geophysics, Geosystems*, 5(5).
- Satsukawa, T., & Michibayashi, K. (2014). Flow in the uppermost mantle during back-arc spreading revealed by Ichinomegata peridotite xenoliths, NE Japan. *Lithos*, 189, 89-104.
- Schaefer, B. F., Turner, S., Parkinson, I., Rogers, N., & Hawkesworth, C. (2002). Evidence for recycled Archean oceanic mantle lithosphere in the Azores plume. *Nature*, 420(6913), 304-307.
- Schaeffer, A. J., & Lebedev, S. (2013). Global shear speed structure of the upper mantle and transition zone. *Geophysical Journal International*, 194(1), 417-449.
- Scott, J. M., Liu, J., Pearson, D. G., & Waight, T. E. (2016). Mantle depletion and metasomatism recorded in orthopyroxene in highly depleted peridotites. *Chemical Geology*, 441, 280-291.
- Scott, J. M., Liu, J., Pearson, D. G., Harris, G. A., Czertowicz, T. A., Woodland, S. J., ... & Luth, R. W. (2019). Continent stabilisation by lateral accretion of subduction zone-processed depleted mantle residues; insights from Zealandia. *Earth and Planetary Science Letters*, 507, 175-186.
- Scott, V.D. & Love, G. (1983) Quantitative electron-probe microanalysis. Wiley, New York.
- Secchiari, A., Montanini, A., Bosch, D., Macera, P., & Cluzel, D. (2016). Melt extraction and enrichment processes in the New Caledonia Iherzolites: Evidence from geochemical and Sr-Nd isotope data. *Lithos*, 260, 28-43.
- Secchiari, A., Gleissner, P., Li, C., Goncharov, A., Milke, R., Becker, H., ... & Montanini, A. (2020). Highly siderophile and chalcophile element behaviour in abyssal-type and supra-

- subduction zone mantle: New insights from the New Caledonia ophiolite. *Lithos*, 354, 105338.
- Segev, A., Rybakov, M., & Mortimer, N. (2012). A crustal model for Zealandia and Fiji. *Geophysical Journal International*, 189(3), 1277-1292.
- Sen, G., & Jones, R. E. (1990). Cumulate xenolith in Oahu, Hawaii: implications for deep magma chambers and Hawaiian volcanism. *Science*, 249(4973), 1154-1157.
- Sen, G., & Presnall, D. C. (1986). Petrogenesis of dunite xenoliths from Koolau volcano, Oahu, Hawaii: implications for Hawaiian volcanism. *Journal of Petrology*, 27(1), 197-217.
- Sen, G., Frey, F. A., Shimizu, N., & Leeman, W. P. (1993). Evolution of the lithosphere beneath Oahu, Hawaii: rare earth element abundances in mantle xenoliths. *Earth and Planetary Science Letters*, 119(1-2), 53-69.
- Senda, R., Shimizu, K., & Suzuki, K. (2016). Ancient depleted mantle as a source of boninites in the Izu-Bonin-Mariana arc: evidence from Os isotopes in Cr-spinel and magnetite. *Chemical Geology*, 439, 110-119.
- Senda, R., Tanaka, T., & Suzuki, K. (2007). Os, Nd, and Sr isotopic and chemical compositions of ultramafic xenoliths from Kurose, SW Japan: Implications for contribution of slab-derived material to wedge mantle. *Lithos*, 95(3-4), 229-242.
- Seyler, M., Lorand, J. P., Dick, H. J., & Drouin, M. (2007). Pervasive melt percolation reactions in ultra-depleted refractory harzburgites at the Mid-Atlantic Ridge, 15° 20' N: ODP Hole 1274A. *Contributions to Mineralogy and Petrology*, 153(3), 303.
- Seyler, M., Lorand, J. P., Toplis, M. J., & Godard, G. (2004). Asthenospheric metasomatism beneath the mid-ocean ridge: Evidence from depleted abyssal peridotites. *Geology*, 32(4), 301-304.
- Shervais, J. W. (2001). Birth, death, and resurrection: The life cycle of suprasubduction zone ophiolites. *Geochemistry, Geophysics, Geosystems*, 2(1).
- Shirey, S. B., & Walker, R. J. (1998). The Re-Os isotope system in cosmochemistry and high-temperature geochemistry. *Annual Review of Earth and Planetary Sciences*, 26(1), 423-500.
- Simon, N. S. C., Neumann, E. R., & Widom, E. (2008). Ultra-depleted domains in the oceanic mantle lithosphere: Evidence from major element and modal relationships in mantle xenoliths from ocean islands. *Journal of Petrology*, 49, 1223-1251.
- Simon, N. S., Irvine, G. J., Davies, G. R., Pearson, D. G., & Carlson, R. W. (2003). The origin of garnet and clinopyroxene in "depleted" Kaapvaal peridotites. *Lithos*, 71(2-4), 289-322.
- Smith, D. (1977). The origin and interpretation of spinel-pyroxene clusters in peridotite. *The Journal of Geology*, 85(4), 476-482.
- Smith, I. E. M., & Davies, H. L. (1976). The geology of the southeast Papuan mainland: Aust. Bur. Miner. Resourc., Geol. Geophys., Bull., 165, 86, with Appendix on Foraminifera and Age of Samples by D.J. Belford.
- Smith, W. H., & Sandwell, D. T. (1997). Global sea floor topography from satellite altimetry and ship depth soundings. *Science*, 277(5334), 1956-1962.
- Snortum, E., Day, J. M., & Jackson, M. G. (2019). Pacific lithosphere evolution inferred from Aitutaki mantle xenoliths. *Journal of Petrology*, 60(9), 1753-1772.
- Snow, J. E., & Reisberg, L. (1995). Os isotopic systematics of the MORB mantle: results from altered abyssal peridotites. *Earth and Planetary Science Letters*, 133(3-4), 411-421.

- Sobolev, A. V., & Chaussidon, M. (1996). H₂O concentrations in primary melts from supra-subduction zones and mid-ocean ridges: implications for H₂O storage and recycling in the mantle. *Earth and Planetary Science Letters*, 137(1-4), 45-55.
- Soustelle, V., Tommasi, A., Demouchy, S., & Franz, L. (2013). Melt-rock interactions, deformation, hydration and seismic properties in the sub-arc lithospheric mantle inferred from xenoliths from seamounts near Lihir, Papua New Guinea. *Tectonophysics*, 608, 330-345.
- Standish, J. J., Hart, S. R., Blusztajn, J., Dick, H. J. B., & Lee, K. L. (2002). Abyssal peridotite osmium isotopic compositions from cr-spinel. *Geochemistry, Geophysics, Geosystems*, 3(1), 1-24.
- Stein, C. A., & Stein, S. (1992). A model for the global variation in oceanic depth and heat flow with lithospheric age. *Nature*, 359(6391), 123-129.
- Stern, R. J., & Bloomer, S. H. (1992). Subduction zone infancy: examples from the Eocene Izu-Bonin-Mariana and Jurassic California arcs. *Geological Society of America Bulletin*, 104(12), 1621-1636.
- Stern, R. J., Reagan, M., Ishizuka, O., Ohara, Y., & Whattam, S. (2012). To understand subduction initiation, study forearc crust: To understand forearc crust, study ophiolites. *Lithosphere*, 4(6), 469-483.
- Stolper, E. M., Shortle, O., Antoshechkina, P. M., & Asimow, P. D. (2020). The effects of solid-solid phase equilibria on the oxygen fugacity of the upper mantle. *American Mineralogist*, 105(10), 1445-1471.
- Suhr, G., Hellebrand, E., Snow, J. E., Seck, H. A., & Hofmann, A. W. (2003). Significance of large, refractory dunite bodies in the upper mantle of the Bay of Islands Ophiolite. *Geochemistry, Geophysics, Geosystems*, 4(3).
- Sun, S. S., & McDonough, W. F. (1989). Chemical and isotopic systematics of oceanic basalts: implications for mantle composition and processes. *Geological Society, London, Special Publications*, 42(1), 313-345.
- Tamura, A., & Arai, S. (2006). Harzburgite-dunite-orthopyroxenite suite as a record of supra-subduction zone setting for the Oman ophiolite mantle. *Lithos*, 90(1-2), 43-56.
- Taylor, G. K., Gascoyne, J., & Colley, H. (2000). Rapid rotation of Fiji: paleomagnetic evidence and tectonic implications. *Journal of Geophysical Research: Solid Earth*, 105(B3), 5771-5781.
- Taylor, W. R. (1998). An experimental test of some geothermometer and geobarometer formulations for upper mantle peridotites with application to the ther-mobarometry of fertile Iherzolite and garnet websterite. *Neues Jahrbuch für Mineralogie-Abhandlungen*, 381-408.
- Thompson, J. E., & Fisher, N. H. (1965). Mineral deposits of New Guinea and Papua and their tectonic setting, Commonwealth of Australia: Australia Bur. Mineral Resources Record 10, 40.
- Tollan, P. M. E., Dale, C. W., Hermann, J., Davidson, J. P., & Arculus, R. J. (2017). Generation and modification of the mantle wedge and lithosphere beneath the West Bismarck island arc: melting, metasomatism and thermal history of peridotite xenoliths from Ritter island. *Journal of Petrology*, 58(8), 1475-1510.
- Tollan, P. M. E., O'Neill, H. S. C., Hermann, J., Benedictus, A., & Arculus, R. J. (2015). Frozen melt-rock reaction in a peridotite xenolith from sub-arc mantle recorded by diffusion of trace elements and water in olivine. *Earth and Planetary Science Letters*, 422, 169-181.

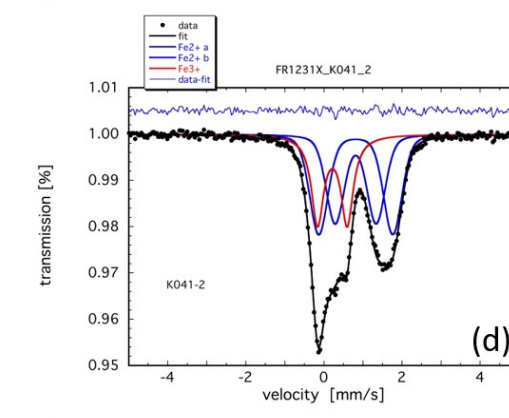
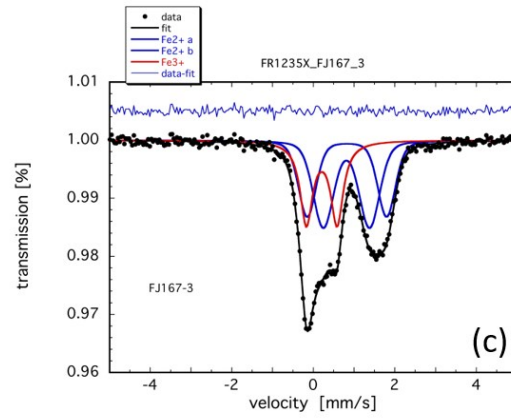
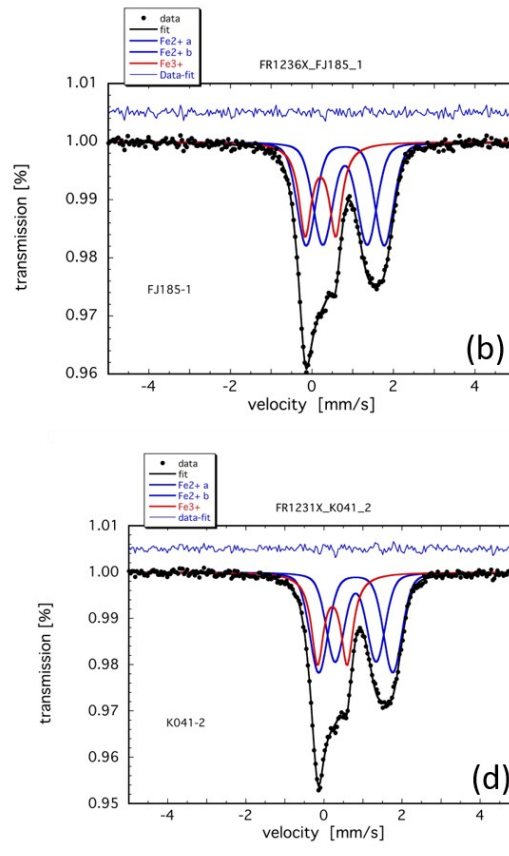
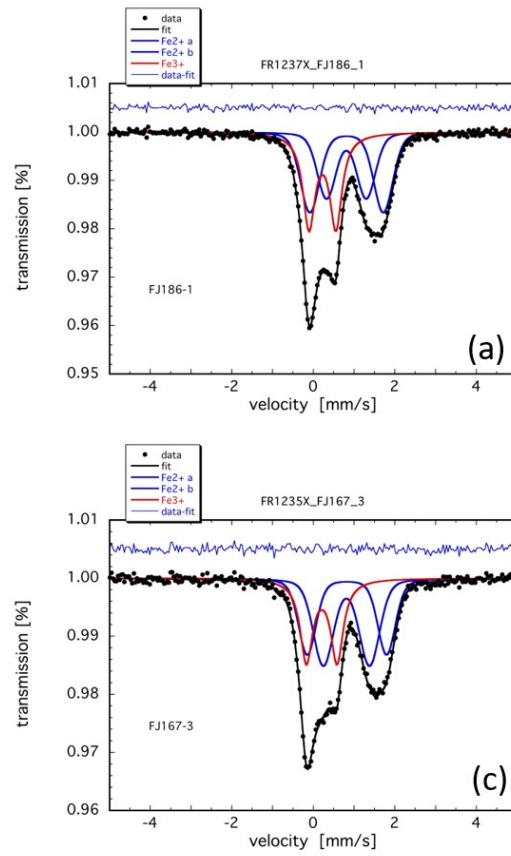
- Tracy, R. J. (1980). Petrology and genetic significance of an ultramafic xenolith suite from Tahiti. *Earth and Planetary Science Letters*, 48(1), 80-96.
- Turner, F. J., & Bartrum, J. A. (1928). The Geology of the Takapuna-Silverdale District, Waitemata County, Auckland.
- Turner, S., & Hawkesworth, C. (1998). Using geochemistry to map mantle flow beneath the Lau Basin. *Geology*, 26(11), 1019-1022.
- Uenver-Thiele, L., Woodland, A. B., Downes, H., & Altherr, R. (2014). Oxidation state of the lithospheric mantle below the Massif Central, France. *Journal of Petrology*, 55(12), 2457-2480.
- Uysal, İ., Ersoy, E. Y., Karslı, O., Dilek, Y., Sadıkclar, M. B., Ottley, C. J., ... & Meisel, T. (2012). Coexistence of abyssal and ultra-depleted SSZ type mantle peridotites in a Neo-Tethyan Ophiolite in SW Turkey: Constraints from mineral composition, whole-rock geochemistry (major-trace-REE-PGE), and Re-Os isotope systematics. *Lithos*, 132, 50-69.
- Vernières, J., Godard, M., & Bodinier, J. L. (1997). A plate model for the simulation of trace element fractionation during partial melting and magma transport in the Earth's upper mantle. *Journal of Geophysical Research: Solid Earth*, 102(B11), 24771-24784.
- Vine, F. J., & Moores, E. M. (1972). A model for the gross structure, petrology, and magnetic properties of oceanic crust. *Studies in Earth and Space Sciences: A Memoir in Honor of Harry Hammond Hess*, 195-205.
- Wager, L. R., Brown, G. M., & Wadsworth, W. J. (1960). Types of igneous cumulates. *Journal of Petrology*, 1(1), 73-85.
- Wainwright, A. N., Luguet, A., Schreiber, A., Fonseca, R. O., Nowell, G. M., Lorand, J. P., ... & Janney, P. E. (2016). Nanoscale variations in ^{187}Os isotopic composition and HSE systematics in a Bultfontein peridotite. *Earth and Planetary Science Letters*, 447, 60-71.
- Walker, D. A., & Cameron, W. E. (1983). Boninite primary magmas: evidence from the Cape Vogel Peninsula, PNG. *Contributions to Mineralogy and Petrology*, 83(1-2), 150-158.
- Walker, R. J., Prichard, H. M., Ishiwatari, A., & Pimentel, M. (2002). The osmium isotopic composition of convecting upper mantle deduced from ophiolite chromites. *Geochimica et Cosmochimica Acta*, 66(2), 329-345.
- Walker, D. A., & McDougall, I. (1982). ^{40}Ar - ^{39}Ar and K-Ar dating of altered glassy volcanic rocks: the Dabi Volcanics, PNG. *Geochimica et Cosmochimica Acta*, 46(11), 2181-2190.
- Walker, R. J., Carlson, R. W., Shirey, S. B., & Boyd, F. R. (1989). Os, Sr, Nd, and Pb isotope systematics of southern African peridotite xenoliths: implications for the chemical evolution of subcontinental mantle. *Geochimica et Cosmochimica Acta*, 53(7), 1583-1595.
- Walter, M. J. (1998). Melting of garnet peridotite and the origin of komatiite and depleted lithosphere. *Journal of Petrology*, 39(1), 29-60.
- Wan, Z., Coogan, L. A., & Canil, D. (2008). Experimental calibration of aluminum partitioning between olivine and spinel as a geothermometer. *American Mineralogist*, 93(7), 1142-1147.
- Wang, J., Takahashi, E., Xiong, X., Chen, L., Li, L., Suzuki, T., & Walter, M. J. (2020). The Water-Saturated Solidus and Second Critical Endpoint of Peridotite: Implications for Magma Genesis Within the Mantle Wedge. *Journal of Geophysical Research: Solid Earth*, 125(8), e2020JB019452.
- Warren, J. M. (2016). Global variations in abyssal peridotite compositions. *Lithos*, 248, 193-219.

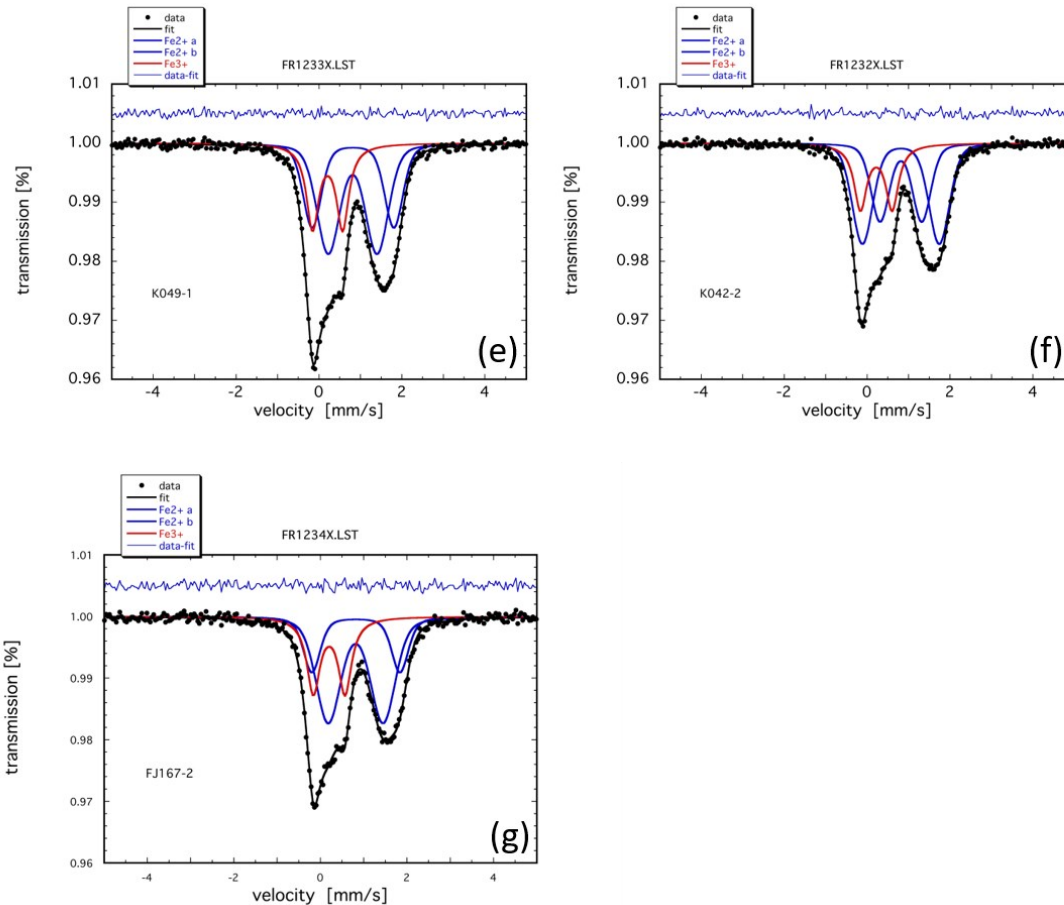
- Waterton, P., Pearson, D. G., Mertzman, S. A., Mertzman, K. R., & Kjarsgaard, B. A. (2020). A fractional crystallisation link between komatiites, basalts, and dunites of the Palaeoproterozoic Winnipegosis Komatiite Belt, Manitoba, Canada. *Journal of Petrology*, 61(5), egaa052.
- Wei, S. S., Zha, Y., Shen, W., Wiens, D. A., Conder, J. A., & Webb, S. C. (2016). Upper mantle structure of the Tonga-Lau-Fiji region from Rayleigh wave tomography. *Geochemistry, Geophysics, Geosystems*, 17(11), 4705-4724.
- Weiser, T. W., & Bachmann, H. G. (1999). Platinum-group minerals from the Aikora river area, Papua New Guinea. *The Canadian Mineralogist*, 37(5), 1131-1145.
- Whattam, S. A. (2009). Arc-continent collisional orogenesis in the SW Pacific and the nature, source and correlation of emplaced ophiolitic nappe components. *Lithos*, 113(1-2), 88-114.
- Whattam, S. A., & Stern, R. J. (2011). The 'subduction initiation rule': a key for linking ophiolites, intra-oceanic forearcs, and subduction initiation. *Contributions to Mineralogy and Petrology*, 162(5), 1031-1045.
- Whattam, S. A., Malpas, J., Ali, J. R., & Smith, I. E. (2008). New SW Pacific tectonic model: Cyclical intraoceanic magmatic arc construction and near-coeval emplacement along the Australia-Pacific margin in the Cenozoic. *Geochemistry, Geophysics, Geosystems*, 9(3).
- Whattam, S. A., Shervais, J. W., Reagan, M. K., Coulthard Jr, D. A., Pearce, J. A., Jones, P., ... & Li, H. (2020). Mineral compositions and thermobarometry of basalts and boninites recovered during IODP Expedition 352 to the Bonin forearc. *American Mineralogist: Journal of Earth and Planetary Materials*, 105(10), 1490-1507.
- Whelan, P. M., Gill, J. B., Kollman, E., Duncan, R. A. & Drake, R. E. (1985). Radiometric dating of magmatic stages in Fiji. In: Scholl, D. W. & Vallier, T. L. (eds) *Geology and Offshore Resources of Pacific Island Arcs—Tonga Region*. Circum-Pacific Council for Energy and Mineral Resources Earth Science Series 2, 415–435.
- White, W. M., Klein, E. M., Holland, H. D., & Turekian, K. K. (2014). 4.13-Composition of the oceanic crust. *Treatise on Geochemistry*, 4, 457-496.
- Widom, E., Kepezhinskas, P., & Defant, M. (2003). The nature of metasomatism in the sub-arc mantle wedge: evidence from Re-Os isotopes in Kamchatka peridotite xenoliths. *Chemical Geology*, 196(1-4), 283-306.
- Wilshire, H. G., & Shervais, J. W. (1975). Al-augite and Cr-diopside ultramafic xenoliths in basaltic rocks from western United States. In *Physics and Chemistry of the Earth* (pp. 257-272). Pergamon.
- Wood, B. J., & Virgo, D. (1989). Upper mantle oxidation state: Ferric iron contents of Iherzolite spinels by ^{57}Fe Mössbauer spectroscopy and resultant oxygen fugacities. *Geochimica et Cosmochimica Acta*, 53(6), 1277-1291.
- Wood, B. J., Bryndzia, L. T., & Johnson, K. E. (1990). Mantle oxidation state and its relationship to tectonic environment and fluid speciation. *Science*, 248(4953), 337-345.
- Woodhall, D. (1985). *Geology of the Lau Ridge*.
- Woodland, A. B., Kornprobst, J., & Tabit, A. (2006). Ferric iron in orogenic Iherzolite massifs and controls of oxygen fugacity in the upper mantle. *Lithos*, 89(1-2), 222-241.
- Workman, R. K., & Hart, S. R. (2005). Major and trace element composition of the depleted MORB mantle (DMM). *Earth and Planetary Science Letters*, 231(1-2), 53-72.

- Worthing, M. A., & Crawford, A. J. (1996). The igneous geochemistry and tectonic setting of metabasites from the Emo Metamorphics, Papua New Guinea; a record of the evolution and destruction of a backarc basin. *Mineralogy and Petrology*, 58(1-2), 79-100.
- Worthington, G. A. (1974). Crustal studies in the Fiji Island area using gravity and magnetic survey data.
- Xu, Y., & Liu, C. Z. (2019). Subduction-Induced Fractionated Highly Siderophile Element Patterns in Forearc Mantle. *Minerals*, 9(6), 339.
- Yaxley, G. M., Green, D. H., & Kamenetsky, V. (1998). Carbonatite metasomatism in the southeastern Australian lithosphere. *Journal of Petrology*, 39(11-12), 1917-1930.
- Zhao, D., Xu, Y., Wiens, D. A., Dorman, L., Hildebrand, J., & Webb, S. (1997). Depth extent of the Lau back-arc spreading center and its relation to subduction processes. *Science*, 278(5336), 254-257.
- Zharikov V. A. (2007). 9. Metasomatism and metasomatic rocks. A classification of metamorphic rocks and glossary of terms. Recommendations of the International Union of Geological Sciences Subcommission on the Systematics of Metamorphic Rocks.
- Ziberna, L., Klemme, S., & Nimis, P. (2013). Garnet and spinel in fertile and depleted mantle: insights from thermodynamic modelling. *Contributions to Mineralogy and Petrology*, 166(2), 411-421.
- Zindler, A., & Jagoutz, E. (1988). Lead isotope systematics in spinel Iherzolite nodules. *Chem. Geo.*, 70(1-2), 58.
- Zinngrebe, E., & Foley, S. F. (1995). Metasomatism in mantle xenoliths from Gees, West Eifel, Germany: evidence for the genesis of calc-alkaline glasses and metasomatic Ca-enrichment. *Contributions to Mineralogy and Petrology*, 122(1-2), 79-96.

APPENDICES

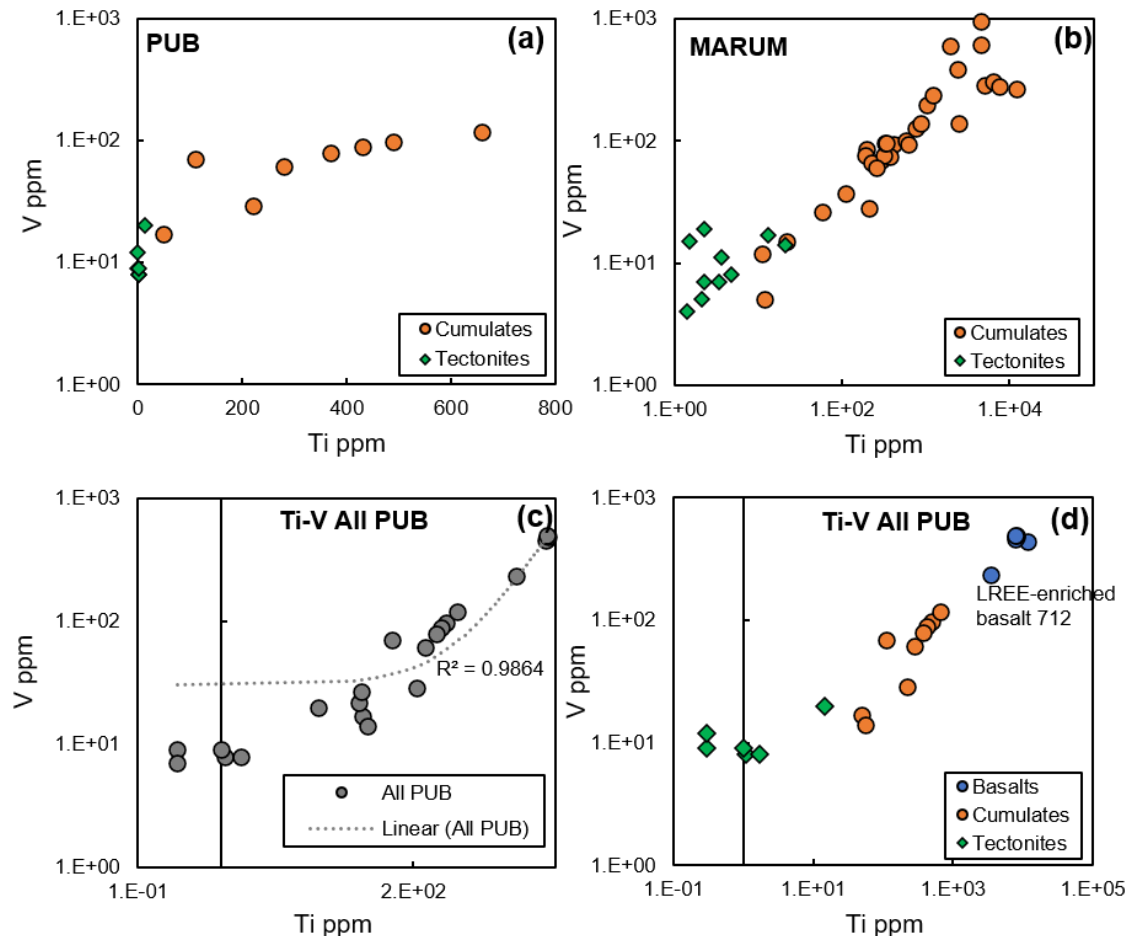
Appendix 1. Chapter 2 supplementary figures





Supplementary Figure 1. Mössbauer spectra for select Koro Iherzolites. (a) FJ186-1 (b) FJ185-1 (c) FJ167-3 (d) K041-2 (e) K049-1 (f) K042-2 (g) FJ167-1.

Appendix 2. Chapter 3 supplementary figures



Supplementary Figure 2. Whole-rock basalt V-Ti relationships between tectonites, cumulates and basalts from Jaques & Chappell (1980) and this study.

Appendix 3. Chapter 2 supplementary tables

Supplementary Table 1: Average wt.% oxide values from Electron Probe Microanalysis (EPMA) in olivine (thin section)

Sample:	K008	K159	FJ024	K048A-2	FJ063	FJ186	K045	K011-1	K015A-2	K041-2	K042-2	K047-2
Rock type:	Dun	Dun	Dun	Hrz	Hrz	Hrz	Lhrz	Lhrz	Lhrz	Lhrz	Lhrz	Lhrz
Analyses:n=11	n=14	n=7	n=3	n=6	n=20	n=18	n=6	n=9	n=6	n=8	n=5	
<i>EPMA (wt.%)</i>												
SiO ₂	40.32	40.09	40.75	40.60	40.51	40.37	39.55	40.92	40.83	40.86	40.77	40.29
TiO ₂	0.01	0.01	–	–	–	–	0.01	–	–	–	–	0.01
Al ₂ O ₃	0.01	0.09	–	–	0.01	0.03	0.02	–	–	–	0.01	–
V ₂ O ₃	–	–	–	0.01	–	–	–	–	–	–	–	–
Cr ₂ O ₃	0.02	0.06	0.02	–	0.04	0.10	0.15	–	–	–	–	0.01
FeO	8.46	10.70	9.45	10.38	9.66	9.10	12.68	9.47	9.87	9.83	9.51	11.64
NiO	0.35	0.37	0.38	0.39	0.36	0.34	0.28	0.38	0.38	0.38	0.38	0.31
MnO	0.15	0.17	0.14	0.16	0.15	0.14	0.18	0.14	0.14	0.14	0.14	0.17
MgO	48.92	47.12	48.75	48.63	48.51	48.58	45.55	49.25	49.08	49.04	48.70	47.50
CaO	0.11	0.07	0.05	0.04	0.11	0.10	0.17	0.02	0.05	0.06	0.07	0.10
Na ₂ O	0.01	–	–	–	–	0.01	–	–	–	–	–	–
P ₂ O ₅	0.01	0.01	0.01	–	0.01	–	0.01	–	–	–	–	–
Total	98.37	98.70	99.55	100.21	99.37	98.77	98.61	100.20	100.37	100.32	99.58	100.05
Mg#	91.2	88.7	90.2	89.3	90.0	90.4	86.5	90.3	89.9	89.9	90.1	87.9
Sample:	K049-1	K050A-1	K050A-2	K067-1	FJ167-2	FJ167-3	FJ181	FJ185-1	FJ185-2	FJ188-1	FJ188-2	FJ190A-1
Rock type:	Lhrz	Lhrz	Lhrz	Lhrz	Lhrz	Lhrz	Lhrz	Lhrz	Lhrz	Lhrz	Lhrz	Lhrz
Analyses:n=7	n=3	n=17	n=3	n=4	n=4	n=11	n=4	n=5	n=5	n=5	n=5	n=7
<i>EPMA (wt.%)</i>												
SiO ₂	40.22	40.36	40.17	40.79	39.94	40.06	40.98	40.83	40.30	40.49	40.62	40.70
TiO ₂	0.01	0.01	0.01	–	0.01	0.01	–	–	–	–	–	–
Al ₂ O ₃	0.02	0.01	0.02	–	0.02	0.02	–	0.02	0.02	0.02	0.01	–

Cr ₂ O ₃	0.09	0.09	0.04	–	0.02	0.01	0.02	–	0.01	0.01	–	0.02
FeO	9.53	9.22	10.51	9.52	9.77	10.04	9.43	9.43	11.70	10.08	10.29	10.37
NiO	0.36	0.36	0.35	0.37	0.37	0.38	0.38	0.38	0.32	0.38	0.38	0.36
MnO	0.14	0.14	0.16	0.14	0.14	0.15	0.14	0.14	0.17	0.15	0.15	0.15
MgO	48.24	48.59	47.50	49.27	47.77	47.72	49.32	48.59	46.78	48.08	48.02	48.51
CaO	0.10	0.08	0.12	0.01	0.10	0.08	0.04	0.07	0.10	0.07	0.08	0.07
Na ₂ O	–	–	–	–	–	0.01	–	–	–	–	–	–
K ₂ O	–	–	–	–	–	–	–	–	–	–	–	–
P ₂ O ₅	–	0.01	0.01	–	0.02	0.02	–	–	–	0.01	0.03	N/A
Total	98.72	98.88	98.89	100.11	98.16	98.48	100.33	99.47	99.41	99.28	99.57	100.20
Mg#	90.0	90.4	88.9	90.2	89.7	89.4	90.3	90.2	87.7	89.5	89.3	89.3

Supplementary Table 1: Continued

Sample:	FJ205	K014-1	K046	K047-1	K048A-1	FJ194	K049-2 Ol-gabbro (crustal)	B-FJ024 Ol phenocryst (volcanic)
Rock type:	Lhrz	Whr	Whr	Whr	Whr	Whr	Ol-gabbro (crustal) n=5	Ol phenocryst (volcanic) n=2
Analyses:	n=12	n=9	n=18	n=7	n=4	n=5		
<i>EPMA (wt.%)</i>								
SiO ₂	40.36	40.09	39.85	40.63	40.08	40.08	39.08	40.78
TiO ₂	—	—	0.02	—	0.01	—	0.01	—
Al ₂ O ₃	—	—	0.04	0.01	0.00	—	0.02	0.05
V ₂ O ₃	—	—	—	—	—	—	0.01	0.01
Cr ₂ O ₃	0.01	—	0.05	0.01	0.01	—	0.01	0.06
FeO	9.32	13.72	11.71	11.52	14.26	13.96	15.84	10.41
NiO	0.39	0.24	0.33	0.30	0.26	0.24	0.19	0.34
MnO	0.13	0.21	0.17	0.17	0.20	0.22	0.22	0.15
MgO	48.54	45.83	46.48	47.22	45.53	45.52	43.08	47.31
CaO	0.02	0.06	0.18	0.09	0.13	0.06	0.17	0.23
Na ₂ O	—	—	0.01	—	—	—	0.01	0.01
P ₂ O ₅	0.01	—	0.01	0.01	—	—	0.03	0.01
Total	98.79	100.18	98.85	99.98	100.49	100.09	98.65	99.38
Mg#	90.3	85.6	87.6	88.0	85.1	85.3	82.9	89.0

Supplementary Table 2: Average wt.% oxide values from Electron Probe Microanalysis (EPMA) in orthopyroxene

Sample:	K048A-2	FJ063	FJ186-1	K011-1	K015A-2	K041-2	K042-2	K045	K047-2	K049-1	K050A-2
Rock type:	Hrz	Hrz	Hrz	Lhrz	Lhrz	Lhrz	Lhrz	Lhrz	Lhrz	Lhrz	Lhrz
Analyses:	n=3	n=6	n=13	n=6	n=9	n=5	n=8	n=4	n=3	n=6	n=9
<i>EPMA (wt.%)</i>											
SiO ₂	54.91	55.84	56.60	55.56	55.63	52.30	54.29	53.23	54.11	56.49	56.11
TiO ₂	0.03	0.07	0.04	0.03	0.04	0.03	0.05	0.18	0.13	0.03	0.05
Al ₂ O ₃	3.60	1.72	2.13	2.83	2.95	6.03	3.70	4.42	4.12	2.69	3.11
V ₂ O ₃	0.02	0.01	0.01	0.02	0.02	0.02	0.02	0.01	0.02	0.01	0.01
Cr ₂ O ₃	0.57	0.41	0.44	0.49	0.37	1.21	0.42	0.51	0.56	0.42	0.44
FeO	6.54	6.18	6.12	6.41	6.35	6.70	6.06	8.81	6.98	6.24	6.13
NiO	0.08	0.08	0.08	0.08	0.09	0.11	0.09	0.08	0.09	0.09	0.09
MnO	0.15	0.16	0.15	0.16	0.15	0.14	0.14	0.19	0.15	0.14	0.14
MgO	33.37	34.87	34.94	34.10	33.99	32.88	33.55	30.91	31.83	34.68	34.38
CaO	0.62	0.49	0.49	0.44	0.58	0.63	0.83	1.32	1.57	0.55	0.74
Na ₂ O	–	0.01	0.01	–	–	–	0.02	0.07	0.03	0.01	0.04
P ₂ O ₅	–	0.01	–	–	–	–	0.01	0.01	–	0.01	–
Total	99.92	99.85	101.01	100.13	100.18	100.08	99.17	99.75	99.61	101.37	101.23
Sample:	K067-1	FJ167-2	FJ167-3	FJ181	FJ185-1	FJ185-2	FJ188-1	FJ188-2	FJ190A-1	FJ205	
Rock type:	Lhrz	Lhrz	Lhrz	Lhrz	Lhrz	Lhrz	Lhrz	Lhrz	Lhrz	Lhrz	
Analyses:	n=3	n=6	n=6	n=6	n=4	n=4	n=5	n=4	n=8	n=13	
<i>EPMA (wt.%)</i>											
SiO ₂	54.98	54.37	54.86	55.53	54.22	53.49	53.56	53.73	54.86	54.73	
TiO ₂	0.03	0.06	0.12	0.03	0.05	0.12	0.09	0.13	0.06	0.03	
Al ₂ O ₃	3.49	4.15	3.53	3.16	3.81	4.21	4.07	4.15	3.82	2.87	
V ₂ O ₃	0.01	0.01	0.01	0.02	0.01	0.02	0.01	0.01	0.02	0.02	
Cr ₂ O ₃	0.58	0.51	0.56	0.52	0.43	0.39	0.43	0.49	0.47	0.37	
FeO	6.33	6.23	6.63	6.25	6.08	7.58	6.55	6.65	6.62	6.14	
NiO	0.07	0.25	0.10	0.08	0.10	0.09	0.11	0.10	0.09	0.08	
MnO	0.15	0.14	0.15	0.15	0.14	0.17	0.15	0.15	0.15	0.14	
MgO	33.71	33.08	33.18	34.02	33.54	32.19	32.86	32.78	32.98	34.17	
CaO	0.55	0.99	1.03	0.52	0.85	0.92	0.90	1.00	0.86	0.42	
Na ₂ O	–	0.06	0.06	–	0.02	0.06	0.06	0.06	–	–	

P ₂ O ₅	-	-	0.01	-	0.01	-	0.01	-	-	0.02
Total	99.90	99.85	100.25	100.28	99.25	99.25	98.78	99.26	99.94	98.99

Supplementary Table 2: Continued

Sample:	K159	K014-1	FJ194	FJ194
Rock type:	Dun	Whr	Whr	Whr
Analyses:	n=11	n=4	n=1	(opx in cpx grain)
<i>EPMA (wt.%)</i>				
SiO ₂	55.47	54.10	53.85	39.95
TiO ₂	0.05	0.08	0.13	0.01
Al ₂ O ₃	5.25	3.91	4.21	0.22
V ₂ O ₃	0.01	0.01	0.02	0.00
Cr ₂ O ₃	0.31	0.30	0.35	0.02
FeO	6.49	8.91	9.10	12.61
NiO	0.08	0.06	0.05	0.26
MnO	0.16	0.20	0.22	0.20
MgO	30.94	31.31	31.09	46.24
CaO	1.70	0.91	0.85	0.29
Na ₂ O	0.41	—	—	—
K ₂ O	0.04	—	—	—
P ₂ O ₅	0.01	—	—	—
Total	100.91	99.79	99.87	99.82

Supplementary Table 3: Average wt.% oxide values from Electron Probe Microanalysis (EPMA) in clinopyroxene

Sample:	K008	K159	FJ024	K048A-2	FJ063	FJ186-1	K011-1	K015A-2	K041-2	K042-2	K045	K047-2	K049-1
Rock type:	Dun	Dun	Dun	Hrzs	Hrzs	Hrzs	Lhrzs	Lhrzs	Lhrzs	Lhrzs	Lhrzs	Lhrzs	Lhrzs
Analyses:	n=9	n=3	n=4	n=4	n=4	n=11	n=9	n=11	n=6	n=8	n=13	n=4	n=2
<i>EPMA (wt.%)</i>													
SiO ₂	54.29	51.89	52.89	52.59	53.32	54.43	53.09	53.00	52.60	52.28	50.13	51.19	53.74
TiO ₂	0.16	0.11	0.16	0.10	0.14	0.07	0.10	0.14	0.10	0.15	0.59	0.55	0.09
Al ₂ O ₃	1.29	3.05	2.68	3.33	1.85	1.45	2.60	3.03	3.67	3.93	5.78	5.54	2.67
V ₂ O ₃	0.01	0.02	0.04	0.03	0.02	0.01	0.02	0.03	0.03	0.03	0.03	0.03	0.02
Cr ₂ O ₃	0.50	0.52	0.43	0.72	0.69	0.33	0.62	0.61	0.54	0.62	0.91	1.11	0.53
FeO _{tot}	1.92	3.09	2.27	2.3	2.24	2.22	2.42	2.49	2.74	2.7	4.43	3.9	2.42
Fe ₂ O ₃	1.11	2.61	2.08	1.11	2.00	0.75	0.62	0.44	0.59	1.10	1.66	1.03	0.72
FeO	0.92	0.74	0.40	1.30	0.44	1.54	1.86	2.09	2.21	1.71	2.93	2.97	1.77
NiO	0.04	0.05	0.04	0.05	0.04	0.04	0.05	0.05	0.05	0.05	0.05	0.04	0.04
MnO	0.08	0.10	0.04	0.07	0.08	0.07	0.08	0.08	0.09	0.09	0.12	0.12	0.07
MgO	17.45	16.71	16.77	16.91	17.29	17.61	17.39	17.29	17.24	16.95	16.15	16.53	17.11
CaO	25.07	23.12	25.04	23.29	24.39	24.51	23.33	22.80	22.51	22.61	19.85	19.42	24.0
Na ₂ O	0.18	0.41	0.21	0.35	0.28	0.16	0.16	0.28	0.24	0.36	0.69	0.92	0.27
P ₂ O ₅	0.01	0.01	0.02	—	0.01	0.01	—	—	—	0.01	0.03	—	0.01
Total	101.1	99.3	100.7	99.8	100.5	100.9	99.9	99.8	99.8	99.8	98.8	99.4	101.0
Ca/Al [cpx]	26.2	10.2	12.6	9.4	17.8	22.8	12.1	10.2	8.3	7.8	4.6	4.7	12.1
Mg# [cpx]	97.1	97.6	98.7	95.9	98.6	95.3	94.3	93.6	93.3	94.7	90.8	90.8	94.5
Mg# [ol]	91.2	88.7	90.2	89.3	90.0	90.4	90.3	89.9	89.9	90.1	86.5	87.9	90.0

Sample:	K050A-1	K050A-2	K067-1	FJ167-2	FJ167-3	FJ181	FJ185-1	FJ185-2	FJ188-1	FJ188-2	FJ190A-1	FJ205
Rock type:	Lhrz	Lhrz	Lhrz	Lhrz	Lhrz	Lhrz	Lhrz	Lhrz	Lhrz	Lhrz	Lhrz	Lhrz
Analyses:	n=8	n=11	n=4	n=6	n=6	n=7	n=5	n=6	n=5	n=6	n=8	n=12

<i>EPMA (wt.%)</i>													
SiO ₂	53.40	52.60	51.58	52.06	52.00	52.88	52.17	51.47	51.19	51.86	52.34	52.70	
TiO ₂	0.10	0.35	0.10	0.20	0.22	0.08	0.15	0.38	0.34	0.39	0.19	0.11	
Al ₂ O ₃	3.23	4.22	4.28	4.39	4.84	3.61	4.01	5.26	5.44	4.82	4.56	2.50	
V ₂ O ₃	0.04	0.03	0.05	0.03	0.03	0.03	0.03	0.04	0.04	0.04	0.04	0.03	
Cr ₂ O ₃	0.64	0.66	1.09	0.73	0.81	0.58	0.60	0.66	0.76	0.70	0.71	0.48	

FeO_{tot}	2.44	3.07	2.37	3.0	3.22	3	2.78	3.66	3.27	3.34	3.15	2.14
Fe_2O_3	1.22	1.44	1.46	1.33	1.80	0.23	1.31	1.65	1.60	1.15	0.87	1.89
FeO	1.34	1.78	1.05	1.80	1.60	2.79	1.61	2.17	1.83	2.31	2.37	0.44
NiO	0.05	0.05	0.04	0.05	0.05	0.05	0.05	0.04	0.06	0.05	0.05	0.04
MnO	0.07	0.09	0.08	0.09	0.10	0.09	0.08	0.10	0.10	0.11	0.09	0.07
MgO	16.98	16.36	17.06	16.50	16.01	18.25	16.92	15.84	15.79	16.42	16.61	16.98
CaO	23.81	22.55	22.72	21.98	21.61	20.90	22.60	20.98	21.10	20.72	21.13	24.55
Na_2O	0.38	0.71	0.24	0.64	0.96	0.24	0.37	0.97	0.95	0.89	0.78	0.19
P_2O_5	0.01	0.02	–	0.01	0.02	–	0.01	0.04	0.03	0.02	–	0.02
Total	101.2	100.8	99.7	99.7	100.0	99.7	99.8	99.5	99.1	99.4	99.6	99.9
Ca/Al [cpx]	10.0	7.2	7.2	6.8	6.0	7.8	7.6	5.4	5.2	5.8	6.3	13.3
Mg# [cpx]	95.8	94.3	96.6	94.2	94.7	92.1	94.9	92.9	93.9	92.7	92.6	98.6
Mg# [ol]	90.4	88.9	90.2	89.7	89.4	90.3	90.2	87.7	89.5	89.3	89.3	90.3

Supplementary Table 3: Continued

Sample:	K014-1	K046	K047-1	K048-1	FJ194	K049-2	K048-1 Augite cpx Whr n=3
Rock type:	Whr n=4	Whr n=2	Whr n=5	Whr n=6	Whr n=7	OI-gabbro n=9	
<i>EPMA (wt.%)</i>							
SiO ₂	50.76	49.94	50.32	50.86	49.41	50.33	48.27
TiO ₂	0.52	1.12	1.04	0.53	1.14	0.75	1.81
Al ₂ O ₃	4.98	5.30	6.27	5.74	6.14	11.15	9.06
V ₂ O ₃	0.03	0.05	0.05	0.03	0.05	0.03	0.06
Cr ₂ O ₃	0.88	1.34	1.13	0.94	0.74	0.3	0.22
FeO _{tot}	4.35	3.35	3.84	4.56	4.59	3.63	4.70
Fe ₂ O ₃	1.38	1.10	1.45	1.30	1.37	—	1.44
FeO	3.11	2.36	2.54	3.39	3.36	—	3.41
NiO	0.03	0.03	0.04	0.04	0.03	0.02	0.04
MnO	0.11	0.09	0.11	0.12	0.12	0.09	0.12
MgO	15.98	15.52	15.64	16.08	14.91	11.71	14.77
CaO	21.33	21.50	19.85	19.87	21.43	20.46	19.47
Na ₂ O	0.46	0.66	1.11	0.79	0.56	1.26	0.98
K ₂ O	—	—	—	—	—	0.01	—
P ₂ O ₅	—	0.01	0.02	—	—	0.02	—
Total	99.5	98.9	99.5	99.6	99.2	100.19	99.5
Ca/Al [cpx]	5.8	5.5	4.3	4.7	4.7	2.5	2.9
Mg# [cpx]	90.2	92.1	91.7	89.4	88.8	85.2	88.5
Mg# [ol]	85.6	87.6	88.0	85.1	85.3	82.9	85.3

FeO and Fe₂O₃ calculated stoichiometrically. Mg# in cpx = Mg/(Mg + Fe²⁺)

Supplementary Table 4: Average wt.% oxide values from Electron Probe Microanalysis (EPMA) in spinel

Sample:	K008	FJ024	FJ063	K048A-2	K159	FJ186-1	K011-1
Rock type:	Dun	Dun	Hrz	Hrz	Hrz	Hrz	Lhrz
Analyses:	n=12	n=3	n=4	n=3	n=8	n=8	n=7
<i>EPMA (wt.%)</i>							
SiO ₂	—	—	—	0.01	—	—	0.01
TiO ₂	0.45	0.13	0.38	0.03	0.09	0.09	0.09
Al ₂ O ₃	21.82	40.08	25.34	44.94	46.18	31.02	39.46
V ₂ O ₃	0.11	0.28	0.19	0.14	0.11	0.16	0.15
Cr ₂ O ₃	40.84	25.87	38.91	22.20	18.44	32.51	26.42
FeO _{tot}	19.36	15.56	19.64	15.11	14.48	19.62	17.37
Fe ₂ O ₃	7.57	3.56	5.91	3.34	3.73	6.73	4.57
FeO	12.55	12.35	14.32	12.10	11.13	13.56	13.26
NiO	0.20	0.26	0.19	0.27	0.34	0.20	0.25
MnO	0.23	0.13	0.17	0.14	0.15	0.20	0.16
MgO	14.65	16.73	14.08	17.67	17.85	14.95	16.33
CaO	0.01	—	—	—	—	—	—
K ₂ O	—	—	0.01	—	—	—	—
P ₂ O ₅	—	—	0.01	—	—	—	—
Total	97.69	99.04	98.93	100.71	97.64	98.77	100.39
Cr#	55.66	30.23	50.73	24.89	21.15	41.29	31
Fe ³⁺ /ΣFe (calc.)	0.35	0.21	0.27	0.20	0.23	0.31	0.24
Fe ³⁺ /ΣFe (Moss.)	—	—	—	—	—	—	—
Fo [ol]	91.2	90.2	90	89.3	88.7	90.4	90.3
Sample:	K015A-2	K041-2	K042-2	K045	K047-2	K049-1	
Rock type:	Lhrz	Lhrz	Lhrz	Lhrz	Lhrz	Lhrz	
Analyses:	n=4	n=6	n=6	n=13	n=3	n=3	
<i>EPMA (wt.%)</i>							
SiO ₂	0.02	0.03	0.00	0.00	0.05	0.00	
TiO ₂	0.08	0.06	0.08	0.42	0.53	0.04	
Al ₂ O ₃	47.72	49.96	50.68	45.09	49.58	45.81	
V ₂ O ₃	0.13	0.10	0.11	0.12	0.12	0.14	
Cr ₂ O ₃	20.20	17.62	17.41	18.03	16.46	19.49	

FeO_{tot}	13.48	13.37	11.28	16.84	14.15	13.35
Fe_2O_3	2.39	2.94	1.46	5.10	2.94	3.94
FeO	11.33	10.72	9.97	12.25	11.50	9.81
NiO	0.30	0.33	0.31	0.27	0.31	0.29
MnO	0.12	0.12	0.10	0.15	0.13	0.12
MgO	18.51	19.18	19.45	17.36	18.78	18.74
CaO	–	0.01	0.01	0.01	–	0.07
Na_2O	–	–	–	–	–	0.01
K_2O	0.01	–	–	–	–	–
P_2O_5	–	–	0.01	–	–	–
Total	100.7	100.89	99.44	98.3	100.22	98.06
Cr#	22.11	19.13	18.73	21.14	18.22	22.2
$\text{Fe}^{3+}/\Sigma \text{Fe}$ (calc.)	0.16	0.20	0.12	0.27	0.19	0.27
$\text{Fe}^{3+}/\Sigma \text{Fe}$ (Moss.)	–	0.291 ± 0.004	–	–	–	0.249 ± 0.005
Fo [ol]	89.9	89.9	90.1	86.5	87.9	90

Supplementary Table 4: Continued

Sample:	K050A-1	K050A-2	K067-1	FJ167-2	FJ167-3	FJ181	FJ181 (rim)
Rock type:	Lhrz	Lhrz	Lhrz	Lhrz	Lhrz	Lhrz	Lhrz
Analyses:	n=6	n=11	n=3	n=5	n=8	n=7	n=2
<i>EPMA (wt.%)</i>							
SiO ₂	—	—	—	—	—	0.01	0.07
TiO ₂	0.03	0.28	0.02	0.11	0.12	0.04	0.05
Al ₂ O ₃	45.27	41.31	44.87	47.78	46.76	44.94	37.71
V ₂ O ₃	0.12	0.13	0.13	0.09	0.10	0.16	0.21
Cr ₂ O ₃	21.69	24.30	23.34	17.80	18.25	23.52	32.04
FeO _{tot}	13.19	14.84	13.82	12.32	13.51	12.77	11.79
Fe ₂ O ₃	3.59	4.28	2.11	3.49	4.13	2.36	1.51
FeO	9.96	10.98	11.92	9.18	9.79	10.65	10.43
NiO	0.28	0.28	0.24	0.33	0.32	0.26	0.18
MnO	0.13	0.15	0.13	0.12	0.13	0.12	0.14
MgO	18.92	17.89	17.72	19.38	18.92	18.61	18.00
CaO	0.03	0.04	—	—	0.01	0.01	0.04
P ₂ O ₅	—	—	—	0.01	—	—	—
Total	99.67	99.22	100.5	97.95	98.12	100.59	100.43
Cr#	24.39	28.32	25.87	20.00	20.75	25.99	36.31
Fe ³⁺ /ΣFe (calc.)	0.24	0.26	0.14	0.25	0.28	0.17	0.12
Fe ³⁺ /ΣFe (Moss.)	—	—	—	0.263 ± 0.006	0.301 ± 0.006	—	—
Fo [ol]	90.4	88.9	90.2	89.7	89.4	90.3	—
Sample:	FJ185-1	FJ185-2	FJ188-1	FJ188-2	FJ190A-1	FJ205	
Rock type:	Lhrz	Lhrz	Lhrz	Lhrz	Lhrz	Lhrz	
Analyses:	n=4	n=4	n=4	n=3	n=4	n=10	
<i>EPMA (wt.%)</i>							
SiO ₂	—	—	—	—	0.05	0.00	
TiO ₂	0.08	0.18	0.13	0.28	0.10	0.05	
Al ₂ O ₃	49.84	51.38	51.18	47.20	47.88	46.90	
V ₂ O ₃	0.11	0.08	0.08	0.09	0.10	0.12	
Cr ₂ O ₃	17.37	13.68	15.00	19.01	18.79	19.84	
FeO _{tot}	12.40	15.36	12.82	13.99	13.91	14.08	

Fe_2O_3	2.05	3.71	2.85	3.00	3.25	1.31
FeO	10.55	12.03	10.25	11.29	10.99	12.90
NiO	0.33	0.35	0.37	0.31	0.31	0.28
MnO	0.10	0.12	0.10	0.11	0.13	0.11
MgO	18.93	18.24	19.25	18.34	18.66	16.88
CaO	—	—	0.02	0.05	0.01	—
K_2O	—	—	—	—	0.01	—
P_2O_5	0.01	0.01	0.01	—	—	—
Total	99.17	99.41	98.96	99.39	100.07	98.28
Cr#	18.95	15.15	16.45	21.29	20.84	22.11
$Fe^{3+}/\Sigma Fe$ (calc.)	0.15	0.22	0.20	0.19	0.21	0.08
$Fe^{3+}/\Sigma Fe$ (Moss.)	0.276 ± 0.006	—	—	—	—	—
Fo [ol]	90.2	87.7	89.5	89.3	89.3	90.3

Supplementary Table 4: Continued

Sample:	K014-1	K046	K047-1	K048A-1	K048A-1 (in aug vein)	FJ194	FJ194 (spl in cpx)
Rock type:	Whr	Whr	Whr	Whr	Whr	Whr	Whr
Analyses:	n=3	n=20	n=7	n=2	n=3	n=3	n=2
<i>EPMA (wt.%)</i>							
SiO ₂	0.03	—	—	0.07	0.07	0.04	0.74
TiO ₂	0.42	1.00	0.66	0.43	0.45	0.25	1.27
Al ₂ O ₃	44.73	42.71	47.24	43.72	62.49	51.13	32.83
V ₂ O ₃	0.07	0.13	0.12	0.13	0.08	0.07	0.15
Cr ₂ O ₃	18.66	20.20	17.95	20.05	1.90	11.52	24.74
FeO _{tot}	19.60	16.41	15.18	19.60	14.95	18.52	23.91
Fe ₂ O ₃	5.82	4.73	3.29	5.51	3.82	6.47	7.44
FeO	14.36	12.16	12.22	14.65	11.51	12.69	17.22
NiO	0.23	0.31	0.28	0.25	0.33	0.28	0.18
MnO	0.17	0.16	0.13	0.16	0.11	0.15	0.23
MgO	16.41	17.53	18.00	16.21	20.20	18.00	13.90
CaO	—	0.01	0.01	0.01	—	—	0.42
P ₂ O ₅	—	—	0.01	—	—	—	—
Total	100.49	98.46	99.58	100.76	100.71	100.09	98.44
Cr#	21.87	24.09	20.37	23.53	2.01	13.13	33.65
Fe ³⁺ /ΣFe (calc.)	0.27	0.26	0.19	0.25	0.23	0.31	0.28
Fe ³⁺ /ΣFe (Moss.)	—	—	—	—	—	—	—
Fo [ol]	85.6	87.6	88	85.1	—	85.3	—
Cr# = Cr/(Cr+Al) molar.							

Supplementary Table 5: Average wt.% values from Electron Probe Microanalysis (EPMA) in Koro sulfides

Sample:	FJ167-3	FJ167-2	K050A-2	K050A-2							
Rock type:	Lhrz	Lhrz		Lhrz		Lhrz		Lhrz	Lhrz	Lhrz	
Sulfide number:	S1	S2		S2		S3		S4	S5	S2	
Phase:			Phase a	Phase b	Phase a	Phase b	Spot a	Spot b			
EPMA spot number:	121	123	124	125	127	128	129	130	131	133	134
<i>EPMA (wt.%)</i>											
Fe	30.5	52.4	33.6	58.3	26.0	27.4	28.2	28.5	24.5	29.4	38.2
Co	0.1	0.2	0.5	0.0	0.3	0.0	0.4	0.0	0.3	0.3	0.3
Ni	34.1	8.2	29.0	0.7	35.3	7.2	31.4	0.8	31.7	28.2	22.6
Cu	0.0	0.0	0.2	0.0	1.4	24.2	0.2	28.6	2.6	1.7	1.4
S	33.2	37.3	33.1	38.5	33.2	31.8	33.7	32.4	31.5	31.4	33.9
Total	97.9	98.1	96.2	97.5	96.2	90.6	93.8	90.4	90.7	90.9	96.4
Sample:	K050A-2	K050A-2	K050A-2	K050A-2	K050A-1	K050A-1	K046	K046			
Rock type:	Lhrz		Lhrz	Lhrz	Lhrz	Lhrz	Whr	Whr			
Sulfide number:		S4		S5	S9	S6	S8	S1	S1		
Phase:	Phase a	Phase b	Phase a					Phase b			
EPMA spot number:	135	136	137	141	138	140	146	147			
<i>EPMA (wt.%)</i>											
Fe	39.0	60.3	24.8	39.3	38.3	24.5	26.7	47.8			
Co	0.4	0.0	0.4	0.3	0.3	0.4	0.6	0.1			
Ni	22.5	0.4	25.2	19.5	23.2	33.5	37.4	11.6			
Cu	2.0	0.0	1.3	3.3	1.7	0.3	0.0	0.1			
S	33.6	37.8	31.6	34.1	33.7	35.4	33.0	38.5			
Total	97.4	98.5	83.3	96.5	97.1	94.1	97.8	98.2			

Supplementary Table 5: Continued

Sample:	FJ024	K008	FJ186-1	FJ186-1	FJ186-1	FJ186-1	FJ186-1	FJ186-1	FJ186-1	FJ185-1	FJ185-1
Rock type:	Dun	Dun	Hz	Hz	Hz	Hz	Hz	Hz	Hz	Lhrz	Lhrz
Sulfide number:	Ni-Cu1	S1	S1	S2	S3	S4	S5	S6	S7	S1	S2
Phase:											
EPMA spot number:	49	62	52	53	54	55	57	59	60	49	50
<i>EPMA (wt.%)</i>											
Fe	1.3	33.3	29.6	30.8	36.1	23.0	33.7	29.8	36.2	39.2	33.4
Co	0.0	0.4	0.3	0.3	0.4	0.5	0.4	0.4	0.3	0.2	0.2
Ni	46.3	24.2	32.2	32.7	23.6	37.5	29.5	33.6	26.7	14.8	18.6
Cu	54.0	0.1	0.1	0.1	1.0	0.1	0.4	0.1	1.8	1.0	0.4
S	0.0	38.7	33.5	33.8	32.0	31.3	34.2	33.1	33.3	28.6	27.8
Total	101.6	96.8	95.7	97.7	93.1	92.2	98.2	96.9	98.3	83.8	80.4
Sample:	FJ185-1	FJ185-1	FJ185-1	FJ185-1	FJ185-1	FJ185-1	FJ185-2	FJ185-2	FJ185-2	FJ185-2	FJ185-2
Rock type:	Lhrz	Lhrz	Lhrz	Lhrz	Lhrz	Lhrz	Lhrz	Lhrz	Lhrz	Lhrz	Lhrz
Sulfide number:	S3	S4 (in opx)	S5 (in spl)	S6 (in cpx)	S7 (in opx)	S1	S2	S3	S4	S5	
Phase:			Phase a								
EPMA spot number:	51	52	53	54	55	56	57	58	59	60	61
<i>EPMA (wt.%)</i>											
Fe	39.1	40.1	38.2	38.3	30.4	37.8	48.2	57.3	36.6	50.7	48.0
Co	0.3	0.3	0.4	0.4	0.4	0.3	0.2	0.0	0.3	0.1	0.2
Ni	22.4	18.1	23.5	25.6	30.3	24.1	11.0	1.8	22.7	3.3	10.0
Cu	2.7	0.3	1.6	0.6	0.0	1.0	0.0	0.1	4.5	0.5	0.0
S	33.9	39.2	32.6	34.2	32.7	34.5	39.1	38.0	32.9	35.4	39.1
Total	98.4	97.9	96.3	99.2	93.8	97.7	98.6	97.3	96.9	89.9	97.3

Supplementary Table 5: Continued

Sample:	FJ188-2	FJ188-2	FJ188-2	FJ188-2	FJ188-2	FJ188-1	FJ188-1	FJ188-1	FJ188-1	FJ188-1	K049-1
Rock type:	Lhrz										
Sulfide number:	S1	S2	S3		S4	S1	S2		S3	S4	S1
Phase:	–	–	Phase a	Phase b	–	–	Phase a	Phase b	–	–	–
EPMA spot number:	62	63	64	65	66	67	68	69	70	71	72
<i>EPMA (wt.%)</i>											
Fe	40.7	38.3	30.9	42.0	38.6	52.6	59.5	37.7	38.2	37.1	21.6
Co	0.2	0.3	0.1	0.2	0.3	0.0	0.0	0.4	0.3	0.4	0.3
Ni	15.3	18.1	2.4	16.2	21.8	1.7	0.8	24.9	22.6	25.9	42.5
Cu	0.2	0.9	28.7	0.2	3.2	0.1	0.0	1.6	2.4	1.3	0.0
S	36.6	32.0	35.5	39.0	34.3	34.3	37.9	34.0	34.2	33.9	33.1
Total	93.1	89.6	97.5	97.7	98.2	88.8	98.3	98.6	97.7	98.6	97.5
Sample:	K049-1	K049-1	K049-1	K049-1	FJ205						
Rock type:	Lhrz	Lhrz	Lhrz	Lhrz	Lhrz						
Sulfide number:	S2	S3	S4	S5	S1						
Phase:	–	–	–	–	–						
EPMA spot number:	73	74	75	76	77						
<i>EPMA (wt.%)</i>											
Fe	32.1	38.5	38.9	39.1	21.0						
Co	0.4	0.3	0.3	0.3	0.1						
Ni	32.3	22.1	22.3	23.5	14.3						
Cu	0.0	3.7	2.9	2.4	18.0						
S	33.2	34.1	33.9	34.2	28.5						
Total	98.1	98.7	98.2	99.5	81.9						

Supplementary Table 6: Olivine core-rim EPMA analyses on picked grains

	Core/SiO ₂ Rim (wt.%)	Al ₂ O ₃ (wt.%)	Cr ₂ O ₃ (wt.%)	FeO _{tot} (wt.%)	CoO (wt.%)	NiO (wt.%)	MnO (wt.%)	MgO (wt.%)	CaO (wt.%)	TOTAL Fo	Co ppm	Mn ppm	Ni ppm	Ca ppm	Al ppm	
<i>Lherzolite (olivine \geqFo_{89.5})</i>																
FJ009	C 40.90	0.00	0.00	9.65	0.02	0.34	0.15	48.25	0.02	99.33	89.9	118	1150	2706	119	11
	R 40.93	0.00	0.00	9.67	0.01	0.34	0.15	48.22	0.02	99.35	89.9	102	1143	2686	156	11
FJ013	C 40.83	0.00	0.00	9.23	0.02	0.39	0.13	48.54	0.02	99.15	90.4	123	997	3030	112	10
	R 40.76	0.00	0.00	9.17	0.02	0.38	0.13	48.49	0.02	98.98	90.4	121	1032	3022	119	15
FJ017	C 40.61	0.03	0.02	10.00	0.01	0.36	0.14	47.84	0.09	99.10	89.5	113	1108	2818	651	179
	R 40.59	0.03	0.02	9.76	0.02	0.36	0.14	48.01	0.09	99.01	89.8	128	1106	2839	616	154
FJ020	C 40.71	0.01	0.01	9.43	0.01	0.38	0.14	48.27	0.04	98.99	90.1	107	1078	2958	287	37
	R 40.93	0.00	0.00	9.37	0.02	0.37	0.14	48.34	0.03	99.20	90.2	136	1066	2913	237	23
FJ021	C 40.76	0.01	0.00	9.49	0.01	0.38	0.14	48.27	0.04	99.10	90.1	106	1093	2948	312	31
	R 40.80	0.01	0.00	9.48	0.02	0.36	0.14	48.28	0.04	99.14	90.1	135	1081	2866	301	41
FJ031	C 40.79	0.02	0.01	9.97	0.02	0.38	0.15	47.79	0.09	99.22	89.5	135	1139	3008	608	89
	R 40.83	0.02	0.01	10.01	0.02	0.38	0.15	47.75	0.09	99.26	89.5	127	1173	3005	616	96
FJ053-1	C 40.83	0.00	0.00	9.15	0.01	0.37	0.13	48.62	0.04	99.16	90.4	106	1012	2942	265	16
	R 40.97	0.00	0.00	9.15	0.01	0.37	0.13	48.55	0.04	99.23	90.4	114	1038	2928	271	25
FJ055-1	C 40.71	0.00	0.00	9.25	0.02	0.38	0.14	48.32	0.02	98.83	90.3	125	1048	2991	164	11
	R 40.83	0.00	0.00	9.23	0.02	0.38	0.14	48.30	0.02	98.92	90.3	130	1057	2999	165	15
FJ060	C 40.99	0.00	0.00	9.35	0.01	0.37	0.14	48.42	0.01	99.30	90.2	117	1080	2918	106	9
FJ066-2	C 40.82	0.00	0.00	9.48	0.02	0.38	0.13	48.30	0.02	99.16	90.1	138	1027	3008	165	20
	R 40.85	0.00	0.00	9.41	0.02	0.37	0.14	48.29	0.04	99.13	90.1	133	1098	2922	261	20
FJ067	C 40.79	0.01	0.00	9.97	0.02	0.36	0.14	48.07	0.03	99.38	89.6	121	1080	2840	196	27
	R 40.75	0.00	0.00	9.89	0.02	0.37	0.15	48.02	0.02	99.22	89.6	118	1157	2917	151	17
FJ104	C 40.98	0.01	0.00	9.06	0.02	0.39	0.13	48.50	0.03	99.10	90.5	153	993	3028	195	31
	R 40.87	0.01	0.00	9.04	0.02	0.38	0.13	48.51	0.02	98.99	90.5	139	1037	2997	178	27
FJ140	C 40.81	0.00	0.00	9.29	0.02	0.38	0.14	48.52	0.04	99.20	90.3	146	1065	3002	256	16
	R 40.88	0.00	0.01	9.30	0.01	0.39	0.14	48.53	0.03	99.29	90.3	114	1080	3055	247	19
FJ143	C 40.94	0.00	0.00	9.31	0.02	0.39	0.14	48.48	0.03	99.31	90.3	125	1097	3099	183	13
	R 40.87	0.01	0.00	9.30	0.02	0.39	0.14	48.42	0.03	99.17	90.3	147	1097	3055	201	31
FJ145	C 40.95	0.01	0.00	9.75	0.02	0.38	0.14	48.28	0.05	99.57	89.8	125	1097	2969	363	45
	R 40.80	0.01	0.00	9.70	0.02	0.38	0.14	48.08	0.05	99.18	89.8	122	1094	2965	373	38
FJ154	C 40.85	0.00	0.00	9.54	0.02	0.38	0.13	48.08	0.03	99.03	90.0	121	1035	3020	192	19
	R 40.85	0.00	0.00	9.53	0.02	0.38	0.14	48.18	0.02	99.12	90.0	138	1076	2965	147	17

FJ155-1	C	40.90	0.00	0.00	9.00	0.02	0.41	0.13	48.81	0.02	99.29	90.6	130	972	3228	133	12
FJ166	C	40.78	0.01	0.01	9.45	0.02	0.39	0.14	48.51	0.05	99.33	90.2	134	1054	3041	342	40
	R	40.76	0.01	0.00	9.39	0.01	0.39	0.14	48.35	0.05	99.11	90.2	96	1046	3073	347	41
FJ171	C	40.94	0.01	0.00	9.55	0.01	0.38	0.14	48.43	0.05	99.52	90.0	109	1076	3024	372	52
	R	40.74	0.01	0.00	9.58	0.02	0.39	0.14	48.27	0.05	99.19	90.0	125	1084	3038	352	47
FJ177	C	40.60	0.01	0.00	9.66	0.02	0.37	0.14	48.03	0.05	98.89	89.9	121	1112	2894	381	36
	R	40.77	0.01	0.00	9.68	0.01	0.37	0.14	48.09	0.05	99.13	89.8	118	1076	2912	368	43
FJ180	C	40.98	0.00	0.00	9.09	0.01	0.39	0.13	48.66	0.03	99.30	90.5	113	1013	3076	193	14
FJ181	C	40.75	0.00	0.00	9.46	0.01	0.38	0.14	48.40	0.04	99.20	90.1	100	1105	3019	251	21
	R	40.80	0.00	0.00	9.41	0.01	0.38	0.14	48.42	0.04	99.21	90.2	109	1084	2995	252	18
FJ183	C	40.72	0.01	0.00	9.41	0.01	0.39	0.14	48.36	0.03	99.07	90.2	113	1061	3090	227	28
	R	40.79	0.00	0.00	9.41	0.01	0.39	0.14	48.40	0.03	99.18	90.2	116	1062	3099	220	21
FJ184-1	C	40.89	0.00	0.00	9.54	0.02	0.38	0.14	48.31	0.01	99.29	90.0	137	1053	2987	91	12
FJ198B-1	C	40.74	0.01	0.00	9.61	0.02	0.40	0.14	48.18	0.06	99.15	89.9	133	1095	3120	414	45
	R	40.78	0.01	0.01	9.60	0.01	0.39	0.14	48.08	0.05	99.08	89.9	98	1102	3065	378	45
FJ199	C	40.73	0.01	0.01	9.53	0.01	0.38	0.13	48.17	0.07	99.04	90.0	114	1015	2966	483	75
	R	40.80	0.02	0.01	9.52	0.02	0.37	0.14	48.27	0.07	99.22	90.0	128	1088	2945	473	80
FJ200	C	40.96	0.01	0.01	9.42	0.02	0.39	0.13	48.31	0.06	99.31	90.1	147	1025	3090	401	46
	R	41.03	0.01	0.00	9.43	0.01	0.39	0.13	48.34	0.06	99.39	90.1	115	1001	3054	406	51

Supplementary Table 6: Continued

	Core/ Rim	SiO ₂ (wt.%)	Al ₂ O ₃ (wt.%)	Cr ₂ O ₃ (wt.%)	FeO _{tot} (wt.%)	CoO (wt.%)	NiO (wt.%)	MnO (wt.%)	MgO (wt.%)	CaO (wt.%)	TOTALFo	Co ppm	Mn ppm	Ni ppm	Ca ppm	Al ppm	
<i>Lherzolite (olivine $\geq Fo_{89.5}$)</i>																	
FJ215	C	40.81	0.01	0.01	9.33	0.01	0.39	0.14	48.36	0.07	99.13	90.2	88	1047	3052	498	64
	R	40.81	0.01	0.01	9.34	0.01	0.38	0.14	48.31	0.07	99.09	90.2	105	1071	2996	505	55
K001	C	41.00	0.00	0.00	9.29	0.01	0.40	0.13	48.43	0.03	99.30	90.3	117	1036	3119	198	18
	R	41.40	0.00	0.00	9.26	0.02	0.39	0.14	48.45	0.03	99.69	90.3	141	1069	3046	189	18
K002	C	41.38	0.01	0.00	8.75	0.02	0.35	0.14	48.81	0.06	99.51	90.9	128	1084	2782	450	30
	R	41.30	0.01	0.00	8.69	0.01	0.36	0.14	48.78	0.06	99.35	90.9	115	1082	2819	440	38
K011-1	C	41.19	0.00	0.00	9.34	0.02	0.39	0.13	48.23	0.03	99.32	90.2	119	1037	3045	180	12
	R	41.21	0.00	0.00	9.33	0.02	0.38	0.14	48.27	0.02	99.37	90.2	127	1068	2990	174	17
K012-1	C	41.16	0.01	0.01	9.47	0.01	0.38	0.14	48.13	0.04	99.34	90.1	118	1085	2981	297	35
	R	41.09	0.00	0.01	9.42	0.01	0.38	0.15	48.09	0.04	99.19	90.1	115	1144	2972	298	26
K012-3	C	41.32	0.01	0.00	9.40	0.02	0.39	0.14	48.34	0.05	99.66	90.2	135	1054	3073	349	42
	R	41.10	0.01	0.00	9.39	0.02	0.39	0.14	48.22	0.05	99.30	90.1	122	1084	3036	342	44
K015A-2	C	40.94	0.02	0.01	9.64	0.01	0.39	0.14	48.00	0.08	99.22	89.9	106	1073	3057	561	107
	R	41.25	0.02	0.01	9.67	0.01	0.38	0.14	48.14	0.08	99.71	89.9	109	1087	3000	560	111
K022	C	41.06	0.00	0.00	9.26	0.02	0.38	0.13	48.27	0.02	99.14	90.3	127	982	3005	165	24
	R	40.93	0.00	0.00	9.23	0.02	0.38	0.13	48.28	0.02	99.00	90.3	155	1016	2978	165	18
K025-1	C	41.09	0.00	0.00	9.32	0.02	0.38	0.14	48.44	0.02	99.41	90.3	132	1097	2963	139	12
K026	C	41.14	0.00	0.00	9.26	0.01	0.39	0.14	48.43	0.01	99.38	90.3	105	1057	3074	82	16
K030	C	41.13	0.01	0.00	9.27	0.01	0.39	0.13	48.41	0.02	99.37	90.3	104	1034	3063	115	39
	R	41.02	0.01	0.00	9.28	0.02	0.39	0.13	48.47	0.06	99.39	90.3	134	1024	3083	456	48
K031	C	41.47	0.00	0.00	9.20	0.01	0.39	0.13	48.57	0.02	99.80	90.4	114	1022	3069	110	16
	R	41.08	0.01	0.00	9.22	0.01	0.39	0.13	48.34	0.01	99.19	90.3	102	990	3094	65	39
K033-1	C	41.27	0.00	0.00	9.69	0.02	0.37	0.14	48.11	0.01	99.60	89.9	122	1096	2874	68	10
	R	41.19	0.00	0.00	9.71	0.01	0.36	0.14	47.96	0.01	99.38	89.8	115	1114	2838	76	11
K039-1	C	40.22	0.00	0.01	9.27	0.01	0.39	0.13	48.25	0.03	98.32	90.3	110	1021	3028	248	13
	R	40.18	0.00	0.00	9.26	0.02	0.39	0.13	48.21	0.03	98.23	90.3	131	1024	3047	244	23
K039-2	C	40.72	0.01	0.01	9.48	0.02	0.38	0.14	48.18	0.07	99.02	90.1	137	1099	3014	469	59
	R	40.37	0.01	0.01	9.45	0.02	0.39	0.14	48.13	0.07	98.58	90.1	134	1056	3054	487	48
K040	C	40.30	0.01	0.01	9.61	0.02	0.38	0.14	48.00	0.06	98.53	89.9	129	1082	2996	440	59
	R	40.40	0.01	0.01	9.58	0.02	0.37	0.14	48.05	0.06	98.64	89.9	142	1066	2906	451	61
K041-1	C	40.35	0.01	0.01	9.67	0.01	0.38	0.13	47.93	0.06	98.55	89.8	101	1030	2969	401	51

	R	40.51	0.01	0.01	9.69	0.01	0.38	0.14	47.95	0.05	98.74	89.8	114	1071	2951	386	49
K042-1	C	40.03	0.01	0.00	9.64	0.01	0.39	0.14	47.74	0.06	98.02	89.8	108	1073	3067	396	52
	R	40.34	0.01	0.01	9.63	0.01	0.38	0.14	47.89	0.05	98.46	89.9	117	1093	2947	388	54
K043	C	40.54	0.00	0.00	9.38	0.02	0.39	0.13	48.18	0.02	98.66	90.2	143	1035	3093	127	11
K044-1	C	40.79	0.03	0.02	9.45	0.02	0.38	0.13	48.24	0.11	99.17	90.1	119	1045	2994	763	140
	R	40.76	0.02	0.02	9.44	0.02	0.38	0.13	48.16	0.11	99.03	90.1	124	1015	2973	769	122
K044-2	C	40.79	0.01	0.01	9.73	0.02	0.39	0.14	47.84	0.06	99.01	89.8	142	1083	3070	463	58
	R	40.67	0.01	0.01	9.48	0.02	0.38	0.14	47.95	0.06	98.72	90.0	127	1051	3022	445	50
K048-4	C	40.64	0.01	0.00	9.51	0.02	0.39	0.14	48.04	0.06	98.80	90.0	123	1108	3041	411	60
	R	40.54	0.01	0.01	9.51	0.01	0.38	0.13	47.93	0.06	98.58	90.0	116	1014	2993	404	68
K050A-1	C	40.57	0.01	0.00	9.48	0.02	0.38	0.14	48.02	0.06	98.68	90.0	131	1054	3014	397	56
	R	40.50	0.01	0.00	9.50	0.01	0.39	0.14	48.07	0.06	98.68	90.0	91	1067	3085	399	62
K051	C	40.29	0.01	0.00	9.55	0.02	0.39	0.14	48.17	0.05	98.62	90.0	125	1071	3064	349	39
	R	40.05	0.01	0.00	9.54	0.01	0.38	0.14	48.31	0.05	98.49	90.0	118	1074	2983	348	62
K052	C	40.08	0.01	0.01	9.43	0.02	0.38	0.14	48.26	0.07	98.40	90.1	119	1065	3021	485	77
	R	40.19	0.01	0.01	9.45	0.01	0.38	0.14	48.28	0.07	98.56	90.1	116	1060	3011	485	75
K053-1	C	40.72	0.01	0.00	8.98	0.01	0.40	0.13	48.77	0.03	99.06	90.6	118	985	3135	234	27

Supplementary Table 6: Continued

		SiO ₂ Core/Rim (wt.%)	Al ₂ O ₃ (wt.%)	Cr ₂ O ₃ (wt.%)	FeO _{tot} (wt.%)	CoO (wt.%)	NiO (wt.%)	MnO (wt.%)	MgO (wt.%)	CaO (wt.%)	TOTAL Fo	Co ppm	Mn ppm	Ni ppm	Ca ppm	Al ppm	
Lherzolite (olivine \geq Fo _{89.5})																	
	R	40.58	0.01	0.00	9.13	0.02	0.39	0.13	48.63	0.03	98.92	90.5	131	1003	3083	236	34
K055-1	C	40.35	0.00	0.00	9.34	0.01	0.39	0.13	48.44	0.03	98.70	90.2	107	986	3052	195	13
K056	C	40.11	0.00	0.00	9.34	0.02	0.38	0.14	48.47	0.03	98.48	90.2	136	1046	2957	194	18
K060-2	C	40.00	0.00	0.00	9.51	0.02	0.37	0.14	48.33	0.02	98.38	90.1	124	1078	2890	132	11
	R	40.37	0.00	0.00	9.51	0.02	0.37	0.14	48.24	0.02	98.66	90.0	126	1049	2880	159	18
K064	C	40.38	0.02	0.01	9.53	0.02	0.39	0.14	48.15	0.10	98.73	90.0	123	1099	3043	738	92
	R	40.29	0.02	0.02	9.49	0.01	0.38	0.14	48.04	0.10	98.49	90.0	107	1076	2994	735	102
K066	C	40.47	0.00	0.00	9.30	0.01	0.39	0.13	48.52	0.02	98.85	90.3	111	1025	3055	118	16
	R	40.14	0.00	0.00	9.33	0.02	0.39	0.14	48.48	0.02	98.51	90.3	119	1051	3066	119	16
K067-1	C	40.16	0.00	0.00	9.43	0.02	0.38	0.14	48.35	0.02	98.49	90.1	139	1065	2960	165	22
	R	40.47	0.00	0.00	9.41	0.02	0.38	0.14	48.46	0.02	98.89	90.2	142	1068	2962	173	9
K070	C	40.33	0.00	0.01	9.50	0.02	0.39	0.14	48.32	0.04	98.75	90.1	126	1050	3092	267	26
	R	40.38	0.00	0.00	9.46	0.01	0.39	0.14	48.19	0.04	98.62	90.1	106	1055	3095	266	23
K072	C	40.51	0.02	0.01	9.68	0.01	0.38	0.14	48.06	0.08	98.90	89.9	111	1063	2989	597	104
	R	40.35	0.02	0.01	9.65	0.01	0.38	0.14	48.00	0.08	98.65	89.9	116	1098	2957	589	105
K074	C	40.49	0.02	0.01	9.39	0.02	0.39	0.14	48.16	0.09	98.70	90.1	152	1050	3036	634	104
	R	40.55	0.02	0.01	9.43	0.01	0.38	0.14	48.34	0.09	98.98	90.1	117	1056	3007	617	96
K076	C	40.71	0.01	0.00	9.29	0.01	0.40	0.13	48.47	0.03	99.04	90.3	111	1027	3140	219	29
	R	40.70	0.01	0.00	9.24	0.02	0.39	0.13	48.43	0.03	98.96	90.3	134	1041	3064	234	45
K077	C	40.70	0.00	0.00	9.24	0.01	0.39	0.13	48.58	0.03	99.09	90.4	112	1016	3069	232	24
	R	40.47	0.00	0.00	9.27	0.02	0.39	0.13	48.54	0.03	98.85	90.3	126	979	3032	238	20
K083	C	40.50	0.00	0.00	9.23	0.02	0.40	0.14	48.36	0.02	98.67	90.3	122	1062	3125	169	17
	R	40.27	0.00	0.00	9.22	0.01	0.39	0.14	48.28	0.03	98.35	90.3	117	1089	3034	195	14
K085	C	40.34	0.01	0.00	9.31	0.01	0.39	0.13	48.48	0.04	98.71	90.3	107	1002	3081	304	42
	R	40.38	0.01	0.00	9.29	0.02	0.39	0.14	48.42	0.07	98.70	90.3	120	1110	3063	471	28
K090	C	40.48	0.00	0.00	9.75	0.02	0.34	0.15	48.12	0.03	98.88	89.8	137	1178	2639	180	18
	R	40.44	0.00	0.00	9.69	0.02	0.33	0.14	48.11	0.03	98.77	89.8	132	1115	2606	189	12
K099	C	40.64	0.00	0.00	9.27	0.02	0.40	0.13	48.50	0.03	98.98	90.3	121	1027	3114	210	16
	R	40.33	0.01	0.00	9.30	0.01	0.40	0.14	48.32	0.04	98.55	90.3	117	1093	3108	262	54
K102	C	40.88	0.01	0.00	9.67	0.02	0.38	0.14	48.20	0.05	99.34	89.9	126	1122	2988	333	44
	R	40.82	0.01	0.00	9.63	0.02	0.37	0.15	48.09	0.05	99.13	89.9	127	1148	2944	337	34

K103	C	41.14	0.00	0.00	9.25	0.02	0.39	0.13	48.52	0.02	99.47	90.3	127	1027	3043	128	11
	R	40.98	0.00	0.00	9.28	0.02	0.39	0.13	48.51	0.02	99.33	90.3	129	1045	3028	129	13
K106	C	41.09	0.01	0.01	9.42	0.02	0.38	0.14	48.41	0.06	99.55	90.2	122	1082	3024	428	71
	R	41.03	0.01	0.01	9.42	0.02	0.38	0.14	48.40	0.06	99.46	90.2	131	1062	2955	422	69
K107	C	40.98	0.00	0.00	9.57	0.02	0.39	0.14	48.08	0.03	99.21	90.0	123	1049	3050	243	21
	R	40.76	0.00	0.00	9.49	0.01	0.40	0.13	48.22	0.03	99.05	90.1	105	1041	3126	243	20
K109-2	C	41.08	0.00	0.00	9.22	0.02	0.39	0.13	48.49	0.02	99.36	90.4	128	999	3063	159	22
K110	C	40.99	0.00	0.00	9.36	0.02	0.38	0.14	48.50	0.02	99.39	90.2	118	1050	2971	131	12
	R	41.00	0.00	0.00	9.31	0.02	0.39	0.13	48.46	0.03	99.34	90.3	120	1011	3104	196	10
K121	C	41.03	0.01	0.00	9.22	0.02	0.39	0.13	48.63	0.04	99.48	90.4	127	1029	3078	299	36
	R	40.88	0.01	0.00	9.17	0.02	0.40	0.13	48.53	0.05	99.18	90.4	124	1020	3161	358	37
K122	C	41.12	0.01	0.00	9.28	0.01	0.40	0.14	48.44	0.06	99.45	90.3	110	1069	3123	405	31
	R	41.09	0.01	0.00	9.29	0.01	0.39	0.14	48.41	0.06	99.41	90.3	110	1104	3092	410	39
K127	C	40.83	0.00	0.00	9.54	0.01	0.38	0.13	48.24	0.03	99.16	90.0	111	1020	2968	206	16
	R	40.88	0.00	0.00	9.55	0.02	0.38	0.15	48.26	0.03	99.28	90.0	127	1133	3013	199	19
K131	C	41.17	0.01	0.00	9.05	0.02	0.39	0.13	48.69	0.05	99.50	90.6	120	979	3066	364	27
	R	41.20	0.01	0.01	9.06	0.01	0.41	0.13	48.66	0.05	99.54	90.5	114	1021	3200	356	27
K132	C	41.06	0.01	0.01	9.13	0.02	0.40	0.13	48.58	0.05	99.39	90.5	145	1040	3127	389	52
	R	40.97	0.01	0.00	9.14	0.02	0.39	0.13	48.45	0.06	99.17	90.4	132	1008	3027	403	58

Supplementary Table 6: Continued

	Core/ Rim	SiO ₂ (wt.%)	Al ₂ O ₃ (wt.%)	Cr ₂ O ₃ (wt.%)	FeO _{tot} (wt.%)	CoO (wt.%)	NiO (wt.%)	MnO (wt.%)	MgO (wt.%)	CaO (wt.%)	TOTALFo	Co ppm	Mn ppm	Ni ppm	Ca ppm	Al ppm	
Lherzolite (olivine \geq Fo _{89.5})																	
K137	C	40.91	0.01	0.01	9.23	0.01	0.39	0.14	48.46	0.05	99.19	90.3	110	1057	3035	323	39
	R	40.97	0.01	0.00	9.29	0.02	0.39	0.14	48.39	0.04	99.24	90.3	121	1062	3039	321	37
K138	C	40.93	0.00	0.00	9.40	0.02	0.40	0.14	48.37	0.04	99.29	90.2	141	1079	3161	252	22
	R	40.95	0.00	0.00	9.43	0.01	0.39	0.14	48.48	0.04	99.45	90.2	113	1064	3067	268	11
K146	C	41.12	0.00	0.00	9.34	0.02	0.38	0.13	48.37	0.02	99.38	90.2	123	1043	2966	166	20
	R	41.16	0.00	0.00	9.31	0.02	0.38	0.13	48.41	0.02	99.43	90.3	143	1026	2984	145	14
K147	C	41.12	0.01	0.00	8.60	0.02	0.40	0.13	48.95	0.05	99.28	91.0	124	970	3136	367	46
	R	41.13	0.01	0.00	8.60	0.02	0.40	0.12	48.94	0.05	99.26	91.0	122	964	3105	367	44
K154	C	40.86	0.01	0.00	9.13	0.02	0.40	0.14	48.48	0.05	99.08	90.4	133	1046	3145	338	31
	R	40.86	0.01	0.00	9.12	0.02	0.40	0.13	48.42	0.05	99.01	90.4	119	1018	3174	344	42
K163	C	41.00	0.01	0.01	9.89	0.01	0.38	0.16	47.71	0.05	99.22	89.6	110	1208	2970	375	42
	R	41.06	0.01	0.00	10.04	0.01	0.38	0.16	47.68	0.05	99.40	89.4	82	1240	3009	371	39
K164	C	41.11	0.01	0.01	9.49	0.02	0.38	0.14	48.00	0.05	99.19	90.0	129	1061	2978	355	36
	R	41.13	0.01	0.00	9.48	0.01	0.38	0.14	47.85	0.05	99.05	90.0	108	1051	3007	354	54
K166	C	41.05	0.01	0.00	9.44	0.02	0.39	0.13	47.98	0.05	99.07	90.1	151	1036	3078	348	38
	R	41.05	0.01	0.00	9.47	0.02	0.39	0.13	48.13	0.05	99.24	90.1	138	1042	3027	348	32
K170	C	41.11	0.01	0.00	9.37	0.02	0.38	0.14	48.14	0.05	99.22	90.2	133	1079	3018	353	39
	R	41.12	0.01	0.00	9.41	0.02	0.40	0.14	48.19	0.05	99.34	90.1	141	1074	3148	369	42
K175-1	C	41.09	0.01	0.00	9.51	0.02	0.39	0.14	48.18	0.05	99.37	90.0	119	1051	3047	352	40
	R	40.96	0.01	0.00	9.42	0.01	0.38	0.13	48.01	0.05	98.97	90.1	113	1023	2976	366	46
K176	C	40.89	0.01	0.00	9.54	0.01	0.38	0.13	47.97	0.05	98.99	90.0	118	1035	3006	348	39
	R	40.77	0.01	0.00	9.48	0.02	0.38	0.13	47.94	0.05	98.78	90.0	139	1017	2957	350	46
K176-2	C	40.91	0.01	0.01	9.45	0.02	0.39	0.14	47.90	0.07	98.89	90.0	143	1055	3083	480	67
	R	40.93	0.01	0.01	9.44	0.02	0.39	0.14	48.03	0.07	99.05	90.1	125	1104	3104	485	67
K179	C	40.81	0.01	0.00	9.46	0.02	0.39	0.13	48.00	0.05	98.85	90.0	123	1023	3028	331	41
	R	40.88	0.01	0.00	9.45	0.01	0.39	0.13	48.09	0.05	99.01	90.1	106	1044	3027	333	34
K180	C	40.96	0.01	0.00	9.38	0.02	0.39	0.13	48.16	0.06	99.11	90.1	138	1023	3101	426	51
	R	40.93	0.01	0.01	9.37	0.01	0.40	0.13	48.26	0.06	99.18	90.2	115	1039	3114	448	49
K181-1	C	40.84	0.01	0.00	9.15	0.01	0.39	0.13	48.24	0.06	98.84	90.4	117	1043	3085	402	57
	R	40.84	0.01	0.01	9.15	0.02	0.39	0.13	48.27	0.06	98.88	90.4	120	1039	3049	415	66
K182	C	40.81	0.00	0.00	9.29	0.02	0.38	0.13	48.26	0.03	98.93	90.2	122	1007	3024	234	22

	R	40.86	0.01	0.00	9.29	0.02	0.38	0.13	48.16	0.03	98.88	90.2	127	982	3012	233	27
K183	C	40.79	0.02	0.01	9.67	0.02	0.37	0.14	47.91	0.09	99.03	89.8	137	1117	2926	641	106
	R	40.77	0.02	0.01	9.66	0.01	0.36	0.14	47.83	0.09	98.89	89.8	117	1082	2860	633	80
K185	C	40.85	0.01	0.01	9.55	0.01	0.38	0.14	47.82	0.07	98.84	89.9	116	1061	2998	523	72
	R	40.77	0.01	0.01	9.49	0.02	0.37	0.14	47.83	0.07	98.71	90.0	123	1047	2924	529	73
K187	C	40.89	0.01	0.00	9.36	0.02	0.40	0.14	48.14	0.05	99.01	90.2	138	1072	3162	342	36
	R	40.89	0.01	0.00	9.36	0.01	0.40	0.14	48.02	0.05	98.88	90.1	118	1068	3131	345	46
K188	C	40.94	0.01	0.01	9.11	0.01	0.40	0.13	48.15	0.06	98.82	90.4	110	1037	3142	414	40
	R	40.87	0.01	0.01	9.08	0.01	0.40	0.13	48.18	0.06	98.75	90.4	111	1030	3165	397	61
K196	C	40.70	0.01	0.00	9.31	0.01	0.39	0.14	48.09	0.03	98.67	90.2	108	1048	3084	187	38
	R	40.56	0.01	0.00	9.29	0.01	0.39	0.14	47.98	0.03	98.40	90.2	95	1061	3026	205	37
K198	C	40.86	0.01	0.00	9.65	0.02	0.42	0.14	47.92	0.04	99.05	89.9	120	1119	3263	262	31
	R	40.93	0.01	0.00	9.38	0.02	0.39	0.13	48.21	0.04	99.10	90.2	140	998	3050	307	29
K199	C	40.97	0.01	0.00	9.33	0.02	0.39	0.14	48.32	0.05	99.21	90.2	121	1088	3073	327	37
	R	40.67	0.01	0.00	9.31	0.02	0.39	0.14	48.09	0.04	98.67	90.2	141	1049	3067	318	36
K202	C	40.50	0.01	0.00	9.52	0.02	0.39	0.14	47.88	0.04	98.48	90.0	124	1055	3080	272	29
	R	40.60	0.01	0.00	9.52	0.02	0.39	0.13	47.85	0.04	98.55	90.0	139	1040	3072	304	43
K205	C	40.88	0.01	0.00	9.38	0.02	0.39	0.14	47.95	0.04	98.80	90.1	121	1062	3051	282	32
	R	40.74	0.01	0.00	9.36	0.02	0.38	0.14	47.99	0.04	98.67	90.1	143	1070	2971	290	30

Supplementary Table 6: Continued

	Core/ Rim	SiO ₂ (wt.%)	Al ₂ O ₃ (wt.%)	Cr ₂ O ₃ (wt.%)	FeO _{tot} (wt.%)	CoO (wt.%)	NiO (wt.%)	MnO (wt.%)	MgO (wt.%)	CaO (wt.%)	TOTAL Fo	Co ppm	Mn ppm	Ni ppm	Ca ppm	Al ppm	
Lherzolite (olivine <Fo _{89.5})																	
FJ032	C	40.66	0.02	0.01	10.33	0.02	0.38	0.15	47.55	0.08	99.19	89.1	133	1125	2958	591	95
	R	40.62	0.02	0.01	10.30	0.02	0.38	0.14	47.47	0.08	99.03	89.1	147	1082	2950	604	98
FJ155-2	C	40.28	0.02	0.01	12.29	0.01	0.30	0.18	45.99	0.10	99.20	87.0	112	1431	2393	708	116
	R	40.17	0.02	0.01	12.27	0.02	0.30	0.18	45.85	0.10	98.92	87.0	133	1430	2364	711	114
FJ178	C	40.44	0.02	0.01	11.11	0.02	0.36	0.16	46.92	0.07	99.10	88.3	149	1222	2862	520	92
	R	40.49	0.02	0.01	11.13	0.02	0.36	0.16	46.87	0.08	99.13	88.2	120	1233	2832	537	89
FJ190A-1	C	40.39	0.02	0.01	10.84	0.02	0.36	0.16	47.13	0.07	98.98	88.6	120	1221	2826	484	85
	R	40.45	0.02	0.01	10.80	0.02	0.36	0.16	47.19	0.07	99.07	88.6	132	1238	2848	485	90
K006	C	40.52	0.00	0.00	12.08	0.01	0.34	0.19	46.00	0.02	99.16	87.2	113	1451	2687	147	14
	R	40.96	0.00	0.00	12.06	0.01	0.35	0.20	46.19	0.02	99.80	87.2	108	1521	2722	151	20
K015-1	C	40.89	0.02	0.01	11.39	0.01	0.36	0.17	46.74	0.09	99.68	88.0	115	1306	2836	609	117
	R	40.79	0.02	0.01	11.50	0.02	0.35	0.16	46.54	0.08	99.48	87.8	121	1275	2786	602	115
K037-2	C	39.70	0.01	0.00	13.18	0.02	0.35	0.20	44.89	0.06	98.41	85.9	136	1518	2728	451	74
	R	39.75	0.01	0.00	13.34	0.01	0.35	0.19	44.97	0.06	98.70	85.7	114	1464	2750	453	72
K038-1	C	40.32	0.01	0.01	10.29	0.02	0.38	0.15	47.37	0.07	98.61	89.1	130	1164	2956	471	71
	R	40.10	0.01	0.00	10.26	0.02	0.37	0.15	47.28	0.06	98.25	89.1	121	1160	2890	437	67
K038-2	C	40.07	0.01	0.00	11.93	0.01	0.35	0.17	46.12	0.07	98.75	87.3	110	1352	2734	495	70
	R	39.86	0.01	0.01	12.00	0.02	0.36	0.17	45.96	0.07	98.45	87.2	131	1342	2794	508	64
K039-4	C	39.82	0.05	0.03	11.87	0.02	0.29	0.15	46.06	0.20	98.50	87.4	123	1178	2266	1454	272
	R	39.68	0.11	0.03	11.85	0.02	0.29	0.16	45.92	0.22	98.27	87.4	140	1251	2282	1548	564
K060-1	C	40.02	0.02	0.02	11.01	0.02	0.34	0.16	47.02	0.09	98.70	88.4	120	1233	2647	673	88
	R	39.81	0.02	0.02	10.95	0.01	0.35	0.16	47.00	0.10	98.41	88.4	84	1226	2712	716	86
K062	C	39.94	0.00	0.00	10.29	0.02	0.31	0.15	47.49	0.02	98.21	89.2	124	1191	2427	120	12
	R	40.18	0.00	0.00	10.32	0.01	0.31	0.16	47.54	0.02	98.53	89.1	96	1202	2421	126	13
K068	C	39.77	0.01	0.01	13.39	0.01	0.32	0.18	45.14	0.08	98.92	85.7	107	1418	2482	581	78
	R	39.76	0.02	0.01	13.39	0.02	0.31	0.19	45.01	0.08	98.79	85.7	162	1453	2462	605	81
K075-1	C	40.28	0.02	0.01	10.38	0.02	0.36	0.15	47.51	0.08	98.82	89.1	125	1200	2849	603	107
	R	40.11	0.02	0.01	10.35	0.02	0.36	0.16	47.37	0.08	98.48	89.1	139	1216	2817	600	106
K081-1	C	40.09	0.02	0.01	10.82	0.02	0.36	0.17	47.06	0.08	98.63	88.6	123	1297	2861	594	99
	R	40.21	0.01	0.01	10.85	0.02	0.36	0.17	47.08	0.09	98.80	88.6	126	1335	2837	625	76
K087	C	39.44	0.02	0.00	14.79	0.02	0.26	0.21	43.92	0.09	98.76	84.1	124	1651	2069	656	117

	R	39.57	0.02	0.01	14.72	0.02	0.27	0.21	43.94	0.09	98.85	84.2	158	1655	2143	666	122
K094	C	39.93	0.01	0.00	12.66	0.02	0.30	0.19	45.58	0.08	98.77	86.5	131	1488	2378	595	59
	R	39.77	0.02	0.00	12.98	0.02	0.26	0.19	45.27	0.06	98.57	86.1	133	1499	2049	464	87
K105	C	40.89	0.01	0.01	10.44	0.02	0.36	0.16	47.69	0.06	99.63	89.1	130	1228	2797	464	58
	R	40.75	0.01	0.01	10.38	0.02	0.36	0.16	47.62	0.07	99.38	89.1	125	1246	2830	480	53
K108	C	40.43	0.02	0.01	11.59	0.02	0.35	0.18	46.56	0.09	99.24	87.7	140	1359	2760	618	102
	R	40.19	0.02	0.01	11.76	0.01	0.34	0.18	46.38	0.09	98.98	87.5	105	1360	2660	611	95
K165	C	41.08	0.01	0.00	10.02	0.02	0.39	0.16	47.64	0.05	99.38	89.4	128	1251	3057	361	51
	R	40.97	0.01	0.00	9.96	0.02	0.39	0.16	47.49	0.05	99.05	89.5	138	1256	3026	373	49
K191	C	40.44	0.02	0.00	12.17	0.01	0.35	0.18	45.62	0.09	98.88	87.0	113	1390	2775	609	90
	R	40.44	0.02	0.01	12.24	0.02	0.34	0.18	45.81	0.09	99.14	87.0	121	1409	2673	613	88

Supplementary Table 6: Continued

	Core/ Rim	SiO ₂ (wt.%)	Al ₂ O ₃ (wt.%)	Cr ₂ O ₃ (wt.%)	FeO _{tot} (wt.%)	CoO (wt.%)	NiO (wt.%)	MnO (wt.%)	MgO (wt.%)	CaO (wt.%)	TOTAL Fo	Co ppm	Mn ppm	Ni ppm	Ca ppm	Al ppm	
<i>Harzburgite</i>																	
FJ186B	C	41.16	0.05	0.00	9.17	0.01	0.38	0.14	48.35	0.06	99.32	90.4	95	1078	2975	429	276
	R	40.89	0.00	0.00	9.08	0.02	0.39	0.14	48.54	0.03	99.08	90.5	130	1058	3041	199	12
K010	C	41.40	0.01	0.00	9.75	0.02	0.37	0.14	48.01	0.03	99.73	89.8	119	1120	2896	229	27
	R	41.20	0.00	0.00	9.83	0.02	0.36	0.15	48.06	0.03	99.65	89.7	139	1140	2831	232	15
K025-2	C	41.28	0.00	0.00	9.54	0.02	0.37	0.14	48.24	0.01	99.61	90.0	131	1093	2934	97	24
	R	41.26	0.00	0.00	9.54	0.02	0.37	0.14	48.25	0.01	99.60	90.0	127	1117	2935	90	11
K048A-2	C	40.61	0.00	0.00	9.37	0.02	0.39	0.13	48.14	0.04	98.70	90.2	121	1008	3033	287	22
	R	40.51	0.01	0.00	9.40	0.02	0.39	0.13	48.14	0.03	98.63	90.1	124	1006	3057	230	39
K129	C	40.97	0.00	0.00	9.33	0.02	0.39	0.13	48.59	0.03	99.46	90.3	129	1031	3039	194	12
	R	41.03	0.00	0.00	9.34	0.02	0.39	0.14	48.58	0.03	99.53	90.3	127	1071	3063	235	14
K152	C	40.86	0.00	0.00	9.32	0.02	0.38	0.13	48.32	0.04	99.08	90.2	122	1012	2973	284	25
	R	40.87	0.01	0.00	9.36	0.02	0.38	0.14	48.39	0.04	99.21	90.2	133	1046	3002	314	43
K193	C	40.84	0.01	0.01	9.27	0.02	0.39	0.14	48.26	0.06	99.00	90.3	129	1065	3063	407	51
	R	40.97	0.01	0.00	9.26	0.01	0.40	0.13	48.26	0.06	99.11	90.3	118	1006	3146	413	54
<i>Dunite</i>																	
FJ106	C	40.89	0.01	0.00	9.22	0.01	0.37	0.15	48.44	0.06	99.15	90.4	97	1144	2878	419	44
	R	40.96	0.01	0.01	9.22	0.01	0.36	0.14	48.56	0.06	99.35	90.4	107	1117	2867	423	38
FJ198A-1	C	40.49	0.00	0.00	10.72	0.01	0.33	0.17	47.53	0.02	99.27	88.8	111	1302	2604	118	14
K003	C	40.62	0.00	0.00	12.04	0.02	0.34	0.20	46.08	0.03	99.32	87.2	129	1520	2648	193	21
	R	40.92	0.00	0.00	12.04	0.01	0.34	0.19	46.15	0.03	99.69	87.2	109	1504	2644	199	26
K008	C	41.50	0.00	0.01	8.47	0.02	0.36	0.14	49.27	0.03	99.81	91.2	118	1113	2853	247	19
	R	41.80	0.00	0.02	8.38	0.01	0.37	0.15	49.41	0.05	100.19	91.3	117	1168	2901	325	26
K012-2	C	41.00	0.00	0.00	10.34	0.01	0.37	0.16	47.48	0.03	99.39	89.1	100	1275	2884	206	22
	R	41.08	0.00	0.00	10.43	0.02	0.37	0.16	47.48	0.04	99.58	89.0	125	1227	2898	290	25
K037-1	C	39.81	0.07	0.04	11.87	0.02	0.30	0.16	45.95	0.22	98.43	87.3	132	1251	2344	1539	353
	R	39.81	0.05	0.03	11.84	0.01	0.29	0.16	45.87	0.22	98.28	87.4	116	1253	2297	1549	284
K109-1	C	40.28	0.02	0.01	13.48	0.02	0.27	0.21	45.16	0.11	99.55	85.7	137	1590	2143	816	83
	R	40.12	0.01	0.01	13.87	0.01	0.25	0.21	44.84	0.11	99.43	85.2	111	1614	1977	780	75
K112	C	40.79	0.01	0.01	10.39	0.01	0.36	0.15	47.49	0.06	99.29	89.1	112	1196	2864	462	72
	R	40.74	0.01	0.02	10.48	0.02	0.36	0.16	47.51	0.08	99.37	89.0	134	1226	2819	567	43
K119	C	40.99	0.01	0.01	8.93	0.01	0.40	0.14	48.74	0.06	99.28	90.7	96	1083	3134	397	38

	R	40.94	0.01	0.01	8.88	0.01	0.39	0.14	48.66	0.05	99.10	90.7	118	1107	3070	382	40
K124	C	40.34	0.01	0.00	12.49	0.02	0.32	0.21	45.85	0.08	99.33	86.7	129	1658	2545	573	57
	R	40.45	0.01	0.01	12.32	0.02	0.32	0.21	45.85	0.08	99.26	86.9	120	1608	2519	560	63
K186	C	41.05	0.01	0.01	9.25	0.02	0.40	0.14	48.19	0.06	99.13	90.3	126	1065	3149	420	58
	R	41.04	0.01	0.00	9.27	0.01	0.39	0.14	48.19	0.06	99.12	90.3	106	1071	3095	424	59
<i>Wehrlite</i>																	
FJ194	C	40.11	0.01	0.00	13.43	0.02	0.24	0.20	45.08	0.07	99.17	85.7	144	1572	1864	491	76
	R	40.10	0.01	0.00	13.41	0.02	0.24	0.20	45.17	0.07	99.22	85.7	125	1585	1866	501	75
K014-1	C	40.76	0.01	0.00	13.49	0.02	0.25	0.21	45.20	0.06	77.02	85.7	129	1590	1959	449	79
	R	40.70	0.02	0.00	13.50	0.02	0.24	0.20	45.13	0.06	99.86	85.6	139	1556	1871	445	80
K047-1	C	40.14	0.03	0.01	11.55	0.01	0.31	0.18	46.55	0.09	98.87	87.8	97	1384	2437	657	135
	R	40.12	0.03	0.01	11.56	0.02	0.31	0.17	46.48	0.09	98.79	87.8	142	1341	2399	669	145
K171-1	C	40.60	0.02	0.03	11.80	0.02	0.28	0.17	46.21	0.09	99.21	87.5	135	1317	2239	610	106
	R	40.58	0.02	0.01	11.73	0.02	0.28	0.18	46.21	0.09	99.11	87.5	148	1387	2221	612	102

Supplementary Table 7: Average trace element concentrations in Koro xenolith orthopyroxenes

Comments	# of analyses	Sc	Ti	V	Co	Ni	Cu	Zn	Ga	Y	Zr	Nb
<i>LA-ICP-MS (ppm)</i>												
<i>Lherzolite (olivine $\geq Fo_{89.5}$)</i>												
K011-1	n=1	24.0	222	116	57	678						
K015A-2	n= 4	41.9	490	180	96	937						
SD		1.8	20	8	2	23						
K041-2	n= 4	12.4	113	57	141	2270						
SD		13.6	130	61	30	777						
K042-2	n= 4	25.0	357	133	70	903	2.4	46.3	4.3	1.0	12.2	0.04
SD		5.7	62	19	13	179	1.5	4.4	0.1	0.2	4.0	0.01
K049-1	n= 2	33.0	236	144	66	803	3.0	41.4	2.8	0.6	0.3	0.07
SD		1.3	1	6	1	25	1.5	0.1	0.1	0.0	0.1	0.02
K067-1	n= 2	27.8	210	124	51	595						
SD		0.8	7	3	0	11						
FJ167-2	n= 2	40.4	616	179	98	1287	6.6	65.7	5.3	1.9	1.3	0.06
SD		0.3	32	8	7	114	4.8	3.7	0.7	0.3	0.5	0.01
FJ181	n= 4	44.2	302	166	82	836						
SD		11.1	94	37	4	35						
FJ185-1	n= 4	24.2	352	129	72	923	2.5	41.5	4.7	1.0	12.6	0.03
SD		0.4	7	4	1	15	0.2	1.5	0.1	0.0	0.3	0.00
FJ188-1	n= 5	20.9	597	108	69	876	8.7	43.0	6.0	1.4	18.7	0.11
SD		1.2	170	7	5	99	8.3	4.7	0.7	0.2	1.6	0.08
FJ205	n= 4	54.0	516	251	140	1615	1.8	71.5	5.8	1.1	10.1	0.02
SD		3.9	38	12	11	136	0.1	5.6	0.4	0.1	0.5	0.00

Supplementary Table 7: Continued

Comments	# of analyses	Sc	Ti	V	Co	Ni	Cu	Zn	Ga	Y	Zr	Nb
<i>LA-ICP-MS (ppm)</i>												
<i>Lherzolite (olivine <Fo_{89.5})</i>												
K045-1	n= 4	25.9	1232	135	86	1009	131.3	71.8	6.8	1.2	2.1	0.04
SD		0.4	191	2	5	378	99.3	1.6	0.3	0.1	0.4	0.01
K047-2	n= 6	20.3	525	96	57	677						
SD		0.8	76	7	1	17						
FJ167-3	n= 2	48.0	722	218	120	1500	2.2	76.8	6.8	2.1	8.0	0.08
SD		1.9	95	17	5	73	0.8	2.2	0.0	0.2	3.4	0.02
FJ185-2	n= 4	19.9	728	107	70	855	1.8	54.5	6.4	1.6	18.7	0.04
SD		1.1	96	10	1	27	0.4	2.9	0.3	0.0	2.5	0.01
FJ188-2	n= 4	15.8	705	89	58	760	2.8	38.4	5.3	1.3	15.8	0.06
SD		0.5	244	3	2	19	0.8	1.0	0.4	0.1	1.2	0.02
FJ190A-1	n= 5	31.7	537	154	83	877						
SD		3.3	52	16	8	61						

Supplementary Table 7: Continued

Comments	# of analyses	Sc	Ti	V	Co	Ni	Cu	Zn	Ga	Y	Zr	Nb
<i>LA-ICP-MS (ppm)</i>												
<i>Dunite</i>												
K159	n=4	48.1	642	240	168	2131	5.3	136.1	7.5	1.6	3.8	0.04
SD		8.2	78	45	16	208	0.4	13.2	0.8	0.2	3.4	0.02
<i>Harzburgite</i>												
K048-2	n=5	26.8	199	123	49	578						
SD		1.5	7	3	1	14						
FJ063	n= 2	49.9	999	144	146	1700	5.6	102.0	4.9	1.2	1.7	0.02
SD		8.9	169	25	27	310	1.5	17.0	1.3	0.2	0.3	0.00
FJ186B	n= 7	56.2	688	212	127	1432	5.9	84.0	6.0	0.6	9.3	0.04
SD		4.3	79	21	26	312	6.9	18.4	0.9	0.1	5.4	0.02
<i>Wehrlite</i>												
K046	n= 2	41.1	945	70	1360	25850	80.0	626.0	2.2	3.1	3.4	1.58
SD		4.5	25	3	70	1750	55.0	16.0	0.0	0.3	0.7	0.66
K047-1	n= 2	29.3	2900	192	99	1022	20.5	69.5	8.9	2.1	5.1	0.12

Supplementary Table 8: Average REE concentrations of orthopyroxene

Comments	# of analyses	La	Ce	Pr	Nd	Sm	Eu	Gd	Tb
<i>LA-ICP-MS (ppm)</i>									
<i>Lherzolite (olivine \geqFo_{89.5})</i>									
K011-1	n=1	0.0199	0.0455	0.0055	0.0220	0.0041	0.0021	0.0132	0.0030
K015A-2	n= 4	0.0001	0.0002	0.0000	0.0007	0.0028	0.0029	0.0202	0.0093
SD		0.0001	0.0001	0.0001	0.0003	0.0005	0.0010	0.0028	0.0009
K041-2	n= 4	0.1437	0.2549	0.0385	0.1431	0.0211	0.0080	0.0295	0.0063
SD		0.1833	0.3534	0.0475	0.1685	0.0220	0.0079	0.0298	0.0058
K042-2	n= 4	0.1143	0.1988	0.0217	0.0895	0.0179	0.0152	0.0410	0.0074
SD		0.0363	0.0550	0.0066	0.0330	0.0032	0.0031	0.0035	0.0017
K049-1	n= 2	0.0085	0.0313	0.0016	0.0058	0.0028	0.0014	0.0108	0.0047
SD		0.0014	0.0158	0.0002	0.0004	0.0001	0.0002	0.0002	0.0002
K067-1	n= 2	0.0029	0.0050	0.0005	0.0020	0.0016	0.0016	0.0146	0.0052
SD		0.0010	0.0024	0.0002	0.0013	0.0014	0.0004	0.0047	0.0012
FJ167-2	n= 2	0.0235	0.0839	0.0110	0.0563	0.0271	0.0128	0.0742	0.0225
SD		0.0039	0.0231	0.0034	0.0214	0.0099	0.0046	0.0209	0.0050
FJ181	n= 4	0.2240	0.2878	0.0195	0.0482	0.0093	0.0057	0.0339	0.0103
SD		0.2176	0.2820	0.0172	0.0395	0.0091	0.0059	0.0394	0.0125
FJ185-1	n= 4	0.1155	0.2035	0.0227	0.0823	0.0142	0.0184	0.0473	0.0096
SD		0.0057	0.0083	0.0009	0.0108	0.0031	0.0060	0.0178	0.0007
FJ188-1	n= 5	0.1624	0.3376	0.0439	0.1830	0.0546	0.0361	0.1122	0.0192
SD		0.0560	0.1219	0.0132	0.0343	0.0114	0.0042	0.0288	0.0041
FJ205	n= 4	0.0978	0.1700	0.0195	0.0670	0.0078	0.0067	0.0174	0.0072
SD		0.0086	0.0031	0.0027	0.0127	0.0034	0.0007	0.0109	0.0017

Supplementary Table 8: Continued

Comments	# of analyses	Dy	Ho	Er	Tm	Yb	Lu
<i>LA-ICP-MS (ppm)</i>							
<i>Lherzolite (olivine \geqFo_{89.5})</i>							
K011-1	n=1	0.0414	0.0163	0.0725	0.0161	0.1440	0.0264
K015A-2	n= 4	0.1114	0.0443	0.1990	0.0396	0.4138	0.0745
SD		0.0069	0.0016	0.0052	0.0014	0.0202	0.0014
K041-2	n= 4	0.0553	0.0168	0.0637	0.0113	0.1159	0.0204
SD		0.0432	0.0132	0.0538	0.0097	0.1143	0.0202
K042-2	n= 4	0.1015	0.0349	0.1290	0.0249	0.2440	0.0498
SD		0.0137	0.0082	0.0341	0.0081	0.0564	0.0108
K049-1	n= 2	0.0564	0.0225	0.0996	0.0229	0.2054	0.0437
SD		0.0028	0.0011	0.0019	0.0008	0.0014	0.0012
K067-1	n= 2	0.0595	0.0235	0.0978	0.0197	0.1830	0.0371
SD		0.0120	0.0030	0.0054	0.0009	0.0070	0.0003
FJ167-2	n= 2	0.2196	0.0675	0.2706	0.0506	0.4560	0.0870
SD		0.0414	0.0110	0.0314	0.0078	0.0490	0.0107
FJ181	n= 4	0.1156	0.0423	0.1759	0.0343	0.3370	0.0616
SD		0.1117	0.0366	0.1215	0.0185	0.1341	0.0190
FJ185-1	n= 4	0.0975	0.0306	0.1433	0.0280	0.2633	0.0463
SD		0.0208	0.0035	0.0131	0.0043	0.0262	0.0026
FJ188-1	n= 5	0.1776	0.0484	0.1940	0.0367	0.3114	0.0552
SD		0.0278	0.0051	0.0274	0.0049	0.0543	0.0118
FJ205	n= 4	0.1083	0.0420	0.1630	0.0440	0.4085	0.0918
SD		0.0116	0.0055	0.0196	0.0074	0.0227	0.0062

Supplementary Table 8: Continued

Comments	# of analyses	La	Ce	Pr	Nd	Sm	Eu	Gd	Tb
<i>LA-ICP-MS (ppm)</i>									
<i>Lherzolite (olivine <Fo_{89.5})</i>									
K045-1	n= 4	0.0133	0.0598	0.0102	0.0870	0.0378	0.0219	0.0735	0.0192
SD		0.0032	0.0111	0.0029	0.0214	0.0155	0.0060	0.0243	0.0028
K047-2	n= 6	0.0244	0.0742	0.0129	0.0746	0.0379	0.0169	0.0705	0.0168
SD		0.0124	0.0334	0.0048	0.0219	0.0094	0.0031	0.0083	0.0014
FJ167-3	n= 2	0.0389	0.1783	0.0320	0.1860	0.0668	0.0295	0.1105	0.0256
SD		0.0056	0.0168	0.0004	0.0020	0.0061	0.0020	0.0115	0.0019
FJ185-2	n= 4	0.1295	0.2738	0.0339	0.1985	0.0663	0.0388	0.1580	0.0261
SD		0.0131	0.0340	0.0038	0.0372	0.0069	0.0053	0.0593	0.0039
FJ188-2	n= 4	0.1328	0.2573	0.0335	0.1535	0.0590	0.0325	0.0935	0.0185
SD		0.0116	0.0159	0.0018	0.0075	0.0094	0.0056	0.0159	0.0028
FJ190A-1	n= 5	0.0139	0.0562	0.0107	0.0572	0.0240	0.0135	0.0527	0.0130
SD		0.0014	0.0046	0.0009	0.0043	0.0050	0.0034	0.0100	0.0017
<i>Dunite</i>									
K159	n=4	0.0298	0.1298	0.0164	0.1328	0.0260	0.0180	0.0770	0.0177
SD		0.0178	0.0717	0.0097	0.0748	0.0300	0.0108	0.0442	0.0043
<i>Harzburgite</i>									
K048-2	n=5	0.0611	0.1007	0.0083	0.0192	0.0029	0.0014	0.0088	0.0032
SD		0.0385	0.0682	0.0056	0.0134	0.0014	0.0006	0.0037	0.0009
FJ063	n= 2	0.0226	0.0565	0.0084	0.0445	0.0165	0.0128	0.0490	0.0135
SD		0.0034	0.0115	0.0027	0.0035	0.0035	0.0018	0.0180	0.0013
FJ186B	n= 7	0.1109	0.1961	0.0184	0.0680	0.0082	0.0100	0.0159	0.0034
SD		0.0473	0.0849	0.0113	0.0371	0.0072	0.0070	0.0167	0.0017
<i>Wehrlite</i>									
K046	n= 2	0.5500	0.2005	0.1365	0.6450	0.0685	0.0325	0.1935	0.0415
SD		0.1400	0.0895	0.0385	0.3750	0.0315	0.0135	0.1465	0.0025
K047-1	n= 2	0.0315	0.1270	0.0229	0.1310	0.0800	0.0330	0.1680	0.0371

Supplementary Table 8: Continued

Comments	# of analyses	Dy	Ho	Er	Tm	Yb	Lu
<i>LA-ICP-MS (ppm)</i>							
<i>Lherzolite (olivine <Fo_{89.5})</i>							
K045-1	n= 4	0.1710	0.0457	0.1475	0.0312	0.2625	0.0393
SD		0.0132	0.0041	0.0306	0.0028	0.0283	0.0053
K047-2	n= 6	0.1385	0.0379	0.1390	0.0253	0.2013	0.0360
SD		0.0110	0.0025	0.0103	0.0020	0.0151	0.0037
FJ167-3	n= 2	0.2335	0.0737	0.2940	0.0551	0.4890	0.0957
SD		0.0165	0.0053	0.0250	0.0058	0.0320	0.0058
FJ185-2	n= 4	0.2115	0.0600	0.2093	0.0403	0.3408	0.0623
SD		0.0198	0.0035	0.0223	0.0044	0.0370	0.0045
FJ188-2	n= 4	0.1803	0.0501	0.1775	0.0336	0.2905	0.0538
SD		0.0102	0.0047	0.0123	0.0006	0.0307	0.0056
FJ190A-1	n= 5	0.1302	0.0408	0.1649	0.0325	0.2916	0.0541
SD		0.0167	0.0050	0.0169	0.0028	0.0224	0.0031
<i>Dunite</i>							
K159	n=4	0.1580	0.0628	0.2428	0.0548	0.5178	0.1003
SD		0.0586	0.0093	0.0409	0.0120	0.1051	0.0225
<i>Harzburgite</i>							
K048-2	n=5	0.0458	0.0180	0.0800	0.0184	0.1732	0.0344
SD		0.0067	0.0014	0.0082	0.0019	0.0122	0.0024
FJ063	n= 2	0.1255	0.0455	0.1950	0.0310	0.4065	0.0645
SD		0.0105	0.0095	0.0620	0.0060	0.0965	0.0115
FJ186B	n= 7	0.0539	0.0218	0.1049	0.0218	0.2873	0.0586
SD		0.0159	0.0060	0.0179	0.0029	0.0386	0.0109
<i>Wehrlite</i>							
K046	n= 2	0.3350	0.1095	0.5500	0.0625	0.6400	0.1355
SD		0.0150	0.0075	0.0600	0.0135	0.1400	0.0625
K047-1	n= 2	0.3030	0.0930	0.2710	0.0590	0.3930	0.0656

Supplementary Table 9: Average trace element concentrations of clinopyroxene

Comments	# of analyses	Sc	Ti	V	Mn	Co	Ni	Cu	Zn	Ga	Sr	Y	Zr	Nb
<i>LA-ICP-MS (ppm)</i>														
<i>Lherzolite (olivine $\geq Fo_{89.5}$)</i>														
FJ167-2	n= 2	3.6	63	13	43	1.5	23	0.1	0.7	0.2	3	0.6	0.2	0.02
SD		0.1	2	0	0	0.1	1	0.0	0.1	0.0	1	0.0	0.0	0.01
K015A-2	n= 9	65.7	882	219	645	28.5	417							
SD		2.0	58	14	42	5.2	85							
FJ205	n= 6	46.4	582	153	473	17.5	265	5.3	20.6	12.3	38	5.7	162.5	0.34
SD		3.1	71	18	26	1.8	15	1.3	10.5	2.1	5	0.4	24.6	0.04
FJ188-1	n= 5	47.2	1569	193	635	19.7	306	9.1	15.1	17.4	127	12.1	188.2	0.73
SD		1.6	697	5	31	1.1	9	5.7	0.6	1.8	2	3.0	17.7	0.11
K011-1	n= 2	62.4	671	202	629	29.4	413							
SD		1.1	8	1	9	0.2	1							
K041-2	n= 5	55.2	671	214	680	35.4	512							
SD		2.6	70	40	40	12.8	129							
K042-2	n=2	52.7	864	206	644	24.1	387	3.2	13.9	6.1	14.1	7.9	62	0.19
SD		6.8	75	27	67	2.7	40	1	1.65	3.4	12.91	0.6	59	0.12
K067-1	n= 2	64.3	629	274	748	29.5	425							
SD		0.6	10	2	49	2.0	20							
K049-1	n= 2	59.5	563	227	652	24.8	382	4.3	23.2	2.4	1	5.6	0.7	0.25
SD		2.4	8	4	23	0.8	15	0.4	1.5	0.0	1	0.4	0.4	0.01
FJ185-1	n= 5	40.5	770	176	577	22.6	349	7.5	22.7	18.1	37	7.0	149.0	0.34
SD		1.5	33	17	28	3.1	38	1.5	8.5	0.7	2	0.1	10.9	0.04
FJ181	n= 2	68.4	450	223	659	31.0	404							
SD		5.0	12	13	25	1.3	2							

Supplementary Table 9: Continued

Comments	# of analyses	Sc	Ti	V	Mn	Co	Ni	Cu	Zn	Ga	Sr	Y	Zr	Nb
<i>LA-ICP-MS (ppm)</i>														
<i>Lherzolite (olivine <Fo_{89.5})</i>														
FJ188-2	n= 6	34.1	1690	142	612	18.3	286	6.6	16.2	17.6	98	10.6	179.0	0.50
SD		1.3	307	6	23	0.5	11	0.3	0.5	1.2	2	0.7	12.5	0.03
K047-2	n= 4	57.5	2420	241	921	31.5	389							
SD		1.8	721	13	54	2.0	24							
K049-2	n= 3	80.2	7541	285	1006	26.1	191	2.4	14.8	7.3	64	19.4	28.9	0.43
SD		3.8	782	20	32	1.1	4	1.7	0.3	0.3	6	1.5	1.9	0.05
K045-1	n= 10	57.0	3080	255	1007	33.0	382	12.7	20.4	6.2	68	9.5	13.7	0.51
SD		1.7	433	8	96	1.5	30	29.8	1.4	0.7	7	1.1	3.0	0.08
FJ185-2	n= 6	42.2	1657	189	728	22.1	330	4.7	23.3	18.0	120	12.0	167.5	0.45
SD		1.2	146	17	42	2.0	22	0.3	9.7	1.7	11	1.4	12.1	0.02
FJ167-3	n= 2	4.5	77	16	52	1.6	24	0.1	0.7	0.2	9	0.7	3.3	0.04
SD		0.1	9	0	1	0.0	0	0.0	0.0	0.0	0	0.1	0.5	0.00
FJ190A-1	n= 7	64.8	1396	287	761	38.9	525							
SD		3.1	169	85	85	23.4	237							

Supplementary Table 9: Continued

Comments	# of analyses	Sc	Ti	V	Mn	Co	Ni	Cu	Zn	Ga	Sr	Y	Zr	Nb
<i>LA-ICP-MS (ppm)</i>														
<i>Dunite</i>														
K008	n= 2	53.5	1167	84	687	22.7	384	4.1	8.6	1.9	118	3.9	15.0	0.07
SD		3.4	202	10	26	2.6	59	0.1	0.6	0.4	3	0.3	3.1	0.02
K159	n= 2	55.6	687	195	815	26.6	423	1.9	17.4	2.5	50	7.0	10.8	0.21
SD		3.1	11	11	6	0.6	8	0.1	2.5	0.0	4	0.5	2.5	0.04
<i>Harzburgite</i>														
FJ186B	n= 1	56.0	503	126	628	22.8	360	7.6	11.5	1.3	16	1.6	2.2	0.07
FJ063	n= 3	71.2	883	138	721	29.1	508	3.8	12.9	1.6	53	6.8	9.6	0.03
SD		0.4	48	3	78	10.6	213	4.6	5.8	0.3	3	0.2	0.3	0.02
<i>Wehrlite</i>														
K048-1	n= 4	67.8	3798	264	920	32.3	326							
SD		1.3	293	1	27	0.3	14							
K014-1	n= 8	86.4	3634	250	839	31.2	293							
SD		2.2	362	15	21	1.0	7							
FJ194	n= 4	86.6	3393	239	928	29.8	279							
SD		3.0	148	7	72	1.3	11							
K047-1	n= 4	60.6	6082	285	1034	31.5	379	24.4	17.3	7.3	99	15.8	34.6	1.46
SD		2.5	1506	34	63	2.5	22	33.3	1.6	0.7	17	2.3	8.8	0.46
K046	n= 3	59.8	7204	301	742	27.3	417	20.7	16.7	9.8	70	18.0	47.4	7.50
SD		1.1	97	1	66	2.0	36	9.7	0.7	1.7	19	0.4	3.6	3.68
K048-2	n= 2	1026.0	8125	4639	41190	2166.5	25425							
SD		64.0	15	139	440	10.5	5							

Supplementary Table 10: Average REE concentrations of clinopyroxene

Comments	# of analyses	La	Ce	Pr	Nd	Sm	Eu	Gd	Tb	Dy	Ho	Er	Tm	Yb	Lu		
<i>LA-ICP-MS (ppm)</i>																	
<i>Lherzolite (olivine \geqFo_{89.5})</i>																	
FJ167-2		n= 2	0.153	0.268	0.027	0.092	0.029	0.012	0.053	0.012	0.095	0.022	0.068	0.010	0.065	0.009	
SD			0.076	0.103	0.008	0.019	0.002	0.001	0.001	0.000	0.002	0.001	0.003	0.000	0.004	0.000	
K015A-2		n= 9	1.261	0.989	0.042	0.152	0.192	0.095	0.570	0.153	1.275	0.332	1.019	0.151	0.964	0.139	
SD			1.341	1.143	0.045	0.043	0.010	0.005	0.030	0.006	0.049	0.014	0.034	0.005	0.027	0.007	
FJ205		n= 6	1.545	2.603	0.280	1.148	0.200	0.163	0.402	0.100	0.833	0.228	0.719	0.102	0.771	0.112	
SD			0.241	0.382	0.054	0.203	0.061	0.030	0.058	0.028	0.097	0.028	0.062	0.019	0.083	0.012	
FJ188-1		n= 5	6.762	19.440	2.736	12.040	2.588	0.961	2.342	0.354	2.230	0.466	1.334	0.187	1.250	0.177	
SD			0.349	1.407	0.347	2.103	0.715	0.224	0.752	0.116	0.653	0.112	0.347	0.044	0.259	0.034	
K011-1		n= 2	0.859	2.342	0.321	1.349	0.335	0.147	0.443	0.098	0.760	0.196	0.596	0.095	0.667	0.102	
SD			0.024	0.041	0.008	0.022	0.006	0.004	0.009	0.000	0.015	0.004	0.010	0.001	0.019	0.004	
K041-2		n= 5	3.089	7.024	0.827	2.646	0.350	0.131	0.452	0.107	0.873	0.220	0.721	0.113	0.774	0.117	
SD			0.142	0.315	0.036	0.083	0.012	0.006	0.021	0.004	0.023	0.006	0.025	0.005	0.035	0.003	
K042-2		n=2	0.642	1.107	0.106	0.532	0.267	0.141	0.685	0.150	1.280	0.294	0.920	0.137	0.954	0.122	
SD			0.578	1.004	0.094	0.408	0.058	0.030	0.005	0.008	0.080	0.009	0.068	0.011	0.054	0.005	
K067-1		n= 2	0.163	0.323	0.035	0.135	0.091	0.054	0.382	0.108	0.958	0.251	0.828	0.129	0.873	0.134	
SD			0.003	0.001	0.001	0.011	0.001	0.001	0.000	0.002	0.002	0.005	0.009	0.002	0.009	0.002	
K049-1		n= 2	0.972	1.082	0.058	0.107	0.062	0.036	0.287	0.083	0.769	0.206	0.677	0.103	0.701	0.098	
SD			0.507	0.754	0.046	0.080	0.002	0.003	0.024	0.008	0.047	0.010	0.040	0.009	0.050	0.007	
FJ185-1		n= 5	1.572	2.712	0.290	1.002	0.260	0.212	0.623	0.138	1.106	0.258	0.831	0.119	0.900	0.124	
SD			0.050	0.167	0.021	0.105	0.023	0.019	0.072	0.006	0.049	0.010	0.029	0.008	0.057	0.002	
FJ181		n= 2	1.091	1.488	0.112	0.278	0.071	0.040	0.210	0.063	0.629	0.176	0.600	0.101	0.735	0.112	
SD			0.018	0.166	0.023	0.070	0.008	0.002	0.003	0.002	0.019	0.009	0.036	0.007	0.026	0.003	

Supplementary Table 10: Continued

Comments	# of analyses	La	Ce	Pr	Nd	Sm	Eu	Gd	Tb	Dy	Ho	Er	Tm	Yb	Lu
<i>LA-ICP-MS (ppm)</i>															
<i>Lherzolite (olivine <Fo_{89.5})</i>															
FJ188-2	n= 6	3.945	10.487	1.572	7.280	1.873	0.734	1.822	0.306	1.885	0.405	1.152	0.162	1.085	0.164
SD		0.078	0.259	0.052	0.381	0.168	0.059	0.161	0.031	0.133	0.032	0.071	0.010	0.075	0.007
K047-2	n= 4	2.231	5.978	0.872	4.105	1.200	0.456	1.506	0.283	1.881	0.413	1.158	0.163	1.059	0.153
SD		1.029	2.749	0.394	1.745	0.414	0.137	0.370	0.057	0.338	0.066	0.162	0.023	0.145	0.018
K049-2	n= 3	2.712	7.994	1.534	9.073	3.248	1.146	3.791	0.620	3.831	0.755	2.003	0.256	1.623	0.217
SD		0.431	0.820	0.064	0.189	0.134	0.067	0.297	0.043	0.293	0.058	0.150	0.019	0.112	0.012
K045-1	n= 10	1.565	4.886	0.808	4.287	1.371	0.534	1.737	0.282	1.848	0.382	1.034	0.138	0.925	0.131
SD		0.258	1.029	0.168	0.928	0.299	0.073	0.239	0.040	0.219	0.051	0.152	0.016	0.115	0.025
FJ185-2	n= 6	6.032	17.333	2.550	11.750	2.682	0.963	2.408	0.374	2.278	0.450	1.283	0.184	1.252	0.176
SD		1.107	2.519	0.372	1.731	0.389	0.096	0.401	0.038	0.245	0.047	0.159	0.023	0.183	0.017
FJ167-3	n= 2	0.568	1.583	0.202	0.751	0.129	0.045	0.106	0.019	0.124	0.027	0.081	0.012	0.079	0.011
SD		0.001	0.024	0.002	0.002	0.001	0.001	0.005	0.001	0.008	0.002	0.006	0.001	0.006	0.001
FJ190A-1	n= 7	5.023	10.883	1.268	4.737	1.015	0.379	1.166	0.227	1.576	0.368	1.073	0.159	1.033	0.150
SD		1.018	2.746	0.351	1.354	0.248	0.087	0.192	0.029	0.157	0.030	0.085	0.014	0.100	0.014

Supplementary Table 10: Continued

Comments	# of analyses	La	Ce	Pr	Nd	Sm	Eu	Gd	Tb	Dy	Ho	Er	Tm	Yb	Lu
<i>LA-ICP-MS (ppm)</i>															
<i>Dunite</i>															
K008															
	n= 2	1.733	4.856	0.656	2.875	0.723	0.243	0.705	0.122	0.757	0.154	0.462	0.067	0.488	0.076
	SD	0.024	0.226	0.031	0.170	0.036	0.022	0.067	0.008	0.062	0.008	0.032	0.003	0.054	0.005
K159	n= 2	7.390	15.675	1.551	4.560	0.620	0.217	0.790	0.140	1.138	0.271	0.826	0.122	0.804	0.124
SD		0.550	1.985	0.286	1.050	0.171	0.056	0.100	0.023	0.084	0.018	0.041	0.008	0.056	0.003
<i>Harzburgite</i>															
FJ186B	n= 1	0.743	0.989	0.055	0.117	0.034	0.021	0.095	0.023	0.233	0.065	0.231	0.036	0.234	0.046
FJ063	n= 3	0.639	2.140	0.387	2.210	0.790	0.286	1.083	0.170	1.296	0.263	0.773	0.106	0.645	0.089
SD		0.062	0.201	0.034	0.184	0.073	0.021	0.101	0.015	0.041	0.017	0.012	0.003	0.071	0.005
<i>Wehrlite</i>															
K048-1	n= 4	1.945	6.184	1.037	5.368	1.741	0.641	2.059	0.349	2.147	0.442	1.169	0.160	0.978	0.139
SD		0.173	0.657	0.127	0.636	0.158	0.055	0.106	0.016	0.081	0.018	0.043	0.008	0.037	0.005
K014-1	n= 8	1.476	3.935	0.689	3.902	1.460	0.554	1.917	0.333	2.077	0.440	1.154	0.156	0.952	0.135
SD		1.268	1.990	0.178	0.583	0.115	0.045	0.169	0.029	0.179	0.042	0.105	0.016	0.091	0.011
FJ194	n= 4	4.960	12.071	1.669	7.254	2.041	0.722	2.260	0.391	2.413	0.504	1.354	0.194	1.258	0.185
SD		3.064	7.323	0.918	3.290	0.593	0.183	0.416	0.063	0.403	0.081	0.262	0.045	0.336	0.055
K047-1	n= 4	4.205	12.105	1.866	9.525	2.693	0.977	2.968	0.495	3.038	0.620	1.712	0.222	1.535	0.216
SD		0.647	2.212	0.399	2.258	0.661	0.218	0.666	0.084	0.511	0.112	0.181	0.022	0.179	0.021
K046	n= 3	5.803	17.240	2.604	12.870	3.700	1.469	3.990	0.603	3.813	0.739	1.977	0.251	1.520	0.201
SD		0.207	0.396	0.099	0.343	0.151	0.155	0.086	0.038	0.145	0.020	0.124	0.016	0.043	0.012
K048-2	n= 2	0.183	0.237	0.010	0.022	0.016	0.022	0.229	0.106	1.510	0.659	3.005	0.719	6.575	1.345
SD		0.069	0.071	0.000	0.022	0.017	0.002	0.042	0.009	0.080	0.021	0.145	0.061	0.475	0.035

Supplementary Table 11: Average trace element concentrations of spinel

Comments	# of analyses	Sc	Ti	V	Co	Ni	Cu	Zn	Ga
<i>LA-ICP-MS (ppm)</i>									
<i>Lherzolite (olivine $\geq Fo_{89.5}$)</i>									
K042-2	n=12	1.8	486	766	275	2948	8	1040	66.0
SD		2.3	103	25	10	94	9	37	2.5
K049-1	n= 11	6.7	578	785	296	2352	12	1592	84.3
SD		11.0	349	256	42	243	15	368	26.9
FJ167-3	n= 4	1.4	773	613	242	3011	17	1006	67.1
SD		0.6	285	17	6	147	13	14	3.4
FJ185-1	n= 7	1.0	485	764	277	2990	5	1006	60.7
SD		0.1	12	14	6	137	0	45	3.0
FJ188-1	n= 3	1.2	1037	595	300	3821	3	1301	113.6
SD		0.1	126	61	45	525	0	212	18.6
FJ205	n= 10	1.6	278	845	315	2292	6	1621	54.6
SD		1.4	15	21	9	187	6	62	1.1
<i>Lherzolite (olivine $< Fo_{89.5}$)</i>									
K045-1	n= 8	2.7	2542	874	251	2440	29	1204	102.6
SD		1.3	597	65	16	66	61	127	16.4
K050A-2	n= 2	11.0	2574	993	270	2477	12	1335	90.7
SD		9.0	1629	35	10	84	4	139	30.8
FJ167-3	n= 3	1.2	917	600	219	2479	8	1048	69.1
SD		0.4	91	32	5	33	5	29	0.7
FJ167-3	n= 4	0.9	888	636	258	3124	3	1175	81.1
SD		0.3	55	43	8	102	1	33	1.7
FJ188-2	n= 7	4.3	1677	676	256	2939	9	1108	83.6
SD		2.7	126	21	12	127	4	64	3.5
FJ185-2	n= 8	0.7	996	604	261	3134	2	1281	90.5
SD		0.2	228	60	2	87	0	94	2.8

Supplementary Table 11: Continued

Comments	# of analyses	Sc	Ti	V	Co	Ni	Cu	Zn	Ga
<i>LA-ICP-MS (ppm)</i>									
<i>Dunite</i>									
K159	n= 6	1.5	503	867	266	2914	9	1381	69.1
SD		0.7	64	60	18	164	5	69	5.2
FJ024	n= 4	2.4	713	1855	299	2070	4	1798	76.0
SD		0.3	168	95	16	117	2	262	5.0
<i>Harzburgite</i>									
FJ186B	n= 8	2.2	577	1168	335	1597	3	2111	52.2
SD		1.0	81	98	8	56	2	163	5.2
FJ063	n= 6	11.8	2311	1319	267	1397	51	1709	45.2
SD		5.2	201	62	15	172	89	182	3.1
<i>Wehrlite</i>									
K046	n= 10	2.3	5539	914	239	2665	2	1082	103.7
SD		0.3	304	30	13	105	1	98	4.8
K047-1	n= 9	1.7	4500	921	268	2504	3	1157	110.6
SD		0.4	1345	141	17	198	1	82	6.1

Supplementary Table 12: LA-ICP-MS first-row transition element concentrations in Koro xenolith olivines

Sample	Al	Ti	Ca	Ni	Sc	V	Cr	Co	Cu	Mn
<i>LA-ICP-MS (ppm)</i>										
<i>Lherzolite (olivine $\geq Fo_{89.5}$)</i>										
*K015A-2 (n=4)	47	16	344	2921	2.5	2.3	40	148	0.9	1073
SD	2	0	24.	7	0.0	0.0	2	0	0.1	2.996
*K041-2 (n=4)	66	12	361	2837	2.4	2.5	41	148	1.3	1010
SD	2	2	33	75	0.1	0.2	2	2		10
*K042-2 (n=4)	87	11	460	2807	2.7	3.2	60	146	1.4	1002
SD	1	0	40	119	0.1	0.1	0	3		3
*K049-1 (n=10)	42	5	277	2919	2.2	1.7	25	142	0.6	1002
SD	17	1	88	59	0.1	0.1	2	2	0.1	56
*FJ167-2 (n=2)	130	13	523	2991	2.8	3.1	83	146	1.2	1017
SD	18	0	61	61	0.2	0.0	2	5	0.3	5
*FJ185-1 (n=3)	96	15.9	483	2869	2.9	3.2	64	146	1.5	1023
SD	6	1.0	11	85	0.2	0.1	1	2	0.0	14
*FJ185-1 (n=4)	76	19.7	457	3028	2.8	3.0	66	148	2.0	1057
SD	1	0.6	8	13	0.0	0.0	0	1	0.1	0
*FJ188-1 (n=4)	96	22.9	467	2953	2.7	2.9	69	149	0.8	1159
SD	7	0.8	25	8	0.0	0.1	1	0	0.1	3
*FJ205 (n=3)	18	9.4	127	2980	1.9	1.3	12	144	0.0	1019
SD	1	0.3	20	10	0.0	0.0	0	1	0.0	4
K001	229	10	139	3071	1.9	2.7	136	153	2.2	1006
K002	38	30	347	2814	3.6	0.8	17	144	0.3	1036
K011-1	21	11	121	3086	2.0	1.3	15	154	0.4	1019
K012-1	45	13	240	3029	3.1	4.5	43	154	2.6	1047
K012-3	54	14	272	3145	2.3	2.5	38	156	1.6	1025
K015A-2	139	15	474	3030	2.7	3.7	89	154	1.3	1020
K022	30	8	158	2975	2.0	1.3	14	153	0.2	979
K025-1	19	8	91	2952	2.1	1.2	21	150	0.1	1012
K026	12	6	28	3046	1.6	0.6	11	152	0.3	998
K030	49	3	57	3080	1.8	2.2	21	153	0.9	986
K031	21	5	73	3126	2.1	1.0	20	155	0.1	991
K033-1	24	6	12	2938	1.5	0.7	6	153	0.3	1073
K039-1	27	17	197	2990	2.0	2.3	30	150	0.3	959

K039-2	70	5	372	3038	2.3	2.8	65	152	1.5	996
K040	64	9	359	2886	2.6	2.9	56	151	1.0	995
K041-1	76	12	305	3007	2.3	2.7	42	154	1.3	1006
K042-1	88	11	394	2991	2.6	3.0	59	151	1.4	998
K043	14	5	77	3073	1.9	1.1	11	152	0.4	993
K044-1	176	21	633	2974	2.9	4.3	165	152	0.6	985
K044-2	61	14	348	3038	2.7	3.8	80	152	0.4	1001
K048A-2	28	5	183	3089	2.1	1.6	27	154	0.5	991
K048-4	80	13	328	3044	2.4	2.9	45	152	1.5	1005
K050A-1	68	15	317	3045	2.5	2.6	42	152	1.6	1002

Supplementary Table 12: Continued

Sample	Al	Ti	Ca	Ni	Sc	V	Cr	Co	Cu	Mn
<i>LA-ICP-MS (ppm)</i>										
K051 (n=2)	56	21	319	3169	2.4	2.5	37	148	1.1	1051
SD	3	0	8	52	0.0	0.0	1	3	0.0	31
K052	98	13	460	3048	2.8	3.1	84	144	1.2	1039
K053-1 (n=2)	33	20	223	2959	1.8	5.9	21	134	1.4	910
SD	0	5	12	258	0.2	1.0	2	11	0.0	63
K055-1	19	9	171	3210	2.1	3.2	37	149	1.4	1071
K056	19	4	100	2152	1.3	0.9	10	102	0.3	708
K060-2	28	9	92	3150	2.1	1.5	19	156	0.6	1134
K064 (n=2)	109	6	705	3137	2.6	3.6	88	146	1.2	1030
SD	4	1	15	55	0.1	0.1	1	2	0.1	9
K066	40	11	74	3550	2.2	1.7	32	166	0.3	1157
K067	36	8	132	3240	2.6	1.8	19	155	0.4	1106
K070	38	18	245	3475	2.4	2.1	34	160	1.3	1133
K072	125	17	604	3066	2.9	3.8	95	148	1.2	1102
K074	117	10	634	3149	3.0	3.7	87	150	1.8	1065
K076	34	5	175	2783	1.8	1.6	20	131	0.8	910
K077	30	5	207	2793	1.8	1.3	19	130	0.8	898
K083	47	10	133	3400	2.2	2.2	31	158	2.3	1122
K085	50	12	300	3254	2.4	3.2	35	152	1.7	1083
K090	444	38	134	2286	2.7	1.2	66	117	0.8	947
K099	81	6	192	3094	1.9	1.6	32	144	0.7	993
K102	57	16	289	3104	2.1	2.2	35	149	0.8	1117
K103	24	11	70	3280	2.0	1.3	20	152	0.8	1054
K106	84	19	385	3136	2.5	3.0	55	150	1.3	1071
K107	95	12	199	3260	2.3	2.4	44	153	1.5	1074
K109-2	38	14	163	3560	2.6	2.1	49	166	0.8	1159
K110	23	6	90	3380	1.9	1.2	17	158	0.8	1106
K121	46	5	293	3462	2.3	2.2	37	161	1.1	1101
K122	42	6	383	3334	1.8	1.4	25	154	0.4	1090
K127	114	5	189	3410	2.3	1.2	21	164	0.7	1186
K131	39	5	332	3367	2.1	1.8	46	156	0.5	1066
K132	71	9	374	3304	2.3	2.4	48	154	0.6	1062

K137	43	9	290	3275	2.3	2.1	38	151	0.7	1076
K138	21	2	163	2416	1.4	1.1	14	112	0.4	795
K146	27	13	144	3060	2.0	1.4	17	144	0.4	1033
K147	56	7	349	3321	1.8	1.5	56	149	0.4	1005
K154	49	7	309	3281	2.3	2.1	41	151	0.4	1040
K163	59	10	356	3126	2.2	2.2	34	153	0.4	1263
K164	60	12	329	3111	2.3	2.2	31	155	0.4	1087
K166	52	9	324	3155	2.0	1.6	31	154	0.4	1105
K170	50	8	317	3185	2.3	2.3	31	153	0.4	1076
K175-1	53	9	323	3136	2.3	2.3	30	153	0.4	1108
K176	55	13	318	3039	2.2	2.3	26	150	0.4	1070
K176-2	91	9	458	3111	2.6	6.4	70	149	0.4	1050

Supplementary Table 12: Continued

Sample	Al	Ti	Ca	Ni	Sc	V	Cr	Co	Cu	Mn
<i>LA-ICP-MS (ppm)</i>										
K179	48	8	300	3097	2.1	2.1	29	151	0.4	1062
K180	69	7	412	3210	2.5	2.7	44	154	0.4	1075
K181-1	69	18	387	3092	2.5	2.7	56	146	0.4	1009
K182	30	6	201	3216	1.8	1.4	20	154	0.4	999
K183	133	16	610	3077	2.7	3.5	72	147	0.4	1090
K185	85	8	491	3185	2.4	2.9	60	148	0.4	1063
K187	55	8	347	3504	2.5	2.5	35	156	0.4	1083
K188	56	10	415	3380	2.6	2.3	46	149	0.4	1025
K196	37	10	182	3720	2.3	2.0	28	167	0.4	1166
K198	38	5	246	1943	1.5	1.5	28	87	0.4	623
K199	47	9	324	3453	2.4	2.2	33	155	0.4	1089
K202	37	9	261	3096	2.2	2.1	25	139	0.4	976
K205	43	13	266	3141	2.3	2.1	29	145	0.4	1028
FJ009	26	34	56	2780	2.2	1.6	10	151	0.4	1041
FJ013	20	9	66	3077	1.7	1.0	14	152	0.4	956
FJ017	183	18	512	2858	3.4	4.3	117	151	0.4	1032
FJ020	42	8	208	2957	2.3	1.7	30	150	0.4	996
FJ021	45	19	228	2957	2.1	2.1	27	152	0.4	1016
FJ031	121	12	521	3027	2.8	3.5	96	151	0.4	1083
FJ053-1	30	3	206	2965	1.7	1.4	28	151	0.2	948
FJ055-1	26	7	119	2989	1.9	1.3	15	149	0.2	982
FJ060	107	13	53	2998	1.9	1.7	8	151	1.9	1008
FJ066-2	29	4	111	3676	2.0	1.5	14	160	132.0	997
FJ067	36	11	67	2888	2.2	1.4	20	154	0.5	1071
FJ104	32	3	138	3063	1.8	1.0	11	152	0.5	985
FJ140	27	9	183	3072	2.2	1.6	21	151	0.2	1015
FJ143	98	10	113	3098	1.7	1.5	20	152	0.8	1028
FJ145	56	8	258	3026	2.4	1.9	38	157	0.9	1044
FJ154	102	8	93	3076	1.9	1.4	27	154	0.4	990
FJ155-1	61	4	69	3114	1.7	1.1	31	150	0.5	945
FJ166	51	6	256	3079	2.1	2.1	31	153	1.0	997
FJ171	57	11	284	3056	2.4	2.4	36	154	0.7	1008

FJ177	58	16	286	2938	2.2	2.3	34	151	1.1	1032
FJ180	19	8	140	3025	2.1	1.2	17	150	0.4	987
FJ181	33	6	176	2986	2.3	1.8	29	151	0.1	1010
FJ183	29	6	144	3131	1.7	1.3	26	153	0.2	1010
FJ184-1	102	16	442	2990	2.7	3.3	73	150	0.8	981
FJ198B-1	65	8	324	3113	2.4	2.5	53	153	0.5	1034
FJ199	89	17	386	3008	2.7	3.1	63	151	0.9	1003
FJ200	64	16	321	3071	2.4	2.5	45	153	0.6	984
FJ215	84	16	416	3069	2.8	2.8	74	152	1.0	996

Supplementary Table 12: Continued

Sample	Al	Ti	Ca	Ni	Sc	V	Cr	Co	Cu	Mn
<i>LA-ICP-MS (ppm)</i>										
<i>Lherzolite (olivine <Fo_{89.5})</i>										
*K045 (n=4)	194	47	816	2369	4.1	5.1	124	158	0.8	1302
SD	9	5	94	87	0.4	0.2	5	4	0.2	61
*K047-2 (n=4)	154	93	706	2502	3.4	5.0	120	156	0.8	1281
SD	18	6	14	25	0.1	0.1	17	1	0.4	9
*K050A-2 (n=4)	66	20	462	2976	2.6	2.3	63	145	0.8	1043
SD	1	1	28	17	0.0	0.0	3	0	0.1	3
*FJ167-3 (n=6)	109	18	493	2824	2.8	3.0	67	147	0.9	1065
SD	14	4	34	37	0.2	0.1	3	3	0.0	11
*FJ185-2 (n=2)	152	31	532	2745	2.9	2.7	53	144	0.6	1357
SD	30	3	23	10	0.0	0.1	1	1	0.1	58
FJ188-2 (n=5)	102	83	539	2932	2.4	3.4	63	147	1.4	1197
SD	4	4	15	6	0.0	0.0	4	0	0.1	2
K006	21	18	92	2765	1.6	1.2	10	159	1.9	1414
K015-1	133	23	496	2847	2.8	3.8	78	155	1.2	1224
K037-2	86	47	367	2735	2.0	2.5	44	153	0.4	1395
K038-1	77	24	399	2679	2.7	3.0	64	159	0.3	1292
K038-2	81	40	365	2883	2.5	3.0	67	148	0.3	1102
K039-4	423	57	1334	2266	4.8	9.6	230	169	1.5	1155
K060-1	117	32	645	2757	3.0	3.8	136	146	0.8	1207
K062 (n=2)	20	17	77	2559	1.8	1.2	17	151	0.7	1195
SD	0	1	1	61	0.0	0.0	1	4	0.1	45
K068 (n=2)	100	49	526	2535	2.6	3.9	67	151	1.5	1404
SD	3	0	2	4	0.1	0.1	1	0	0.2	15
K075-1	125	21	581	2821	2.6	3.6	66	147	1.8	1160
K081-1	117	16	583	2831	2.5	2.9	86	139	0.8	1245
K087	143	70	608	2100	3.1	4.5	52	162	1.3	1573
K094	381	44	540	2240	2.2	1.9	45	159	1.1	1561
K105	79	31	418	2992	2.7	2.4	66	150	1.4	1228
K108	124	46	584	2821	2.2	3.0	68	148	0.4	1320
K112	81	24	419	2927	2.8	3.4	63	146	1.3	1177
K165	61	5	329	3067	2.1	1.8	48	156	0.4	1285

K191	153	29	559	2440	2.3	3.0	55	128	1.1	1149
FJ032	118	46	495	3012	2.2	2.9	66	155	0.7	1060

Supplementary Table 12: Continued

Sample	Al	Ti	Ca	Ni	Sc	V	Cr	Co	Cu	Mn
<i>LA-ICP-MS (ppm)</i>										
<i>Lherzolite (olivine <Fo_{89.5})</i>										
FJ155-2	142	53	591	2503	3.1	4.2	72	163	1.1	1329
FJ178	108	14	417	2936	2.7	3.4	67	155	0.8	1134
FJ190A-1	98	20	387	2867	2.5	2.9	62	152	0.4	1118
<i>Harzburgite</i>										
K010	37	13	175	2986	2.0	2.7	25	158	0.6	1075
K025-2	28	11	48	2957	1.9	1.0	12	154	0.9	1050
K129	21	4	165	3160	2.2	1.4	29	148	0.3	1040
K152	44	8	257	3214	2.1	1.9	26	151	0.7	1069
K193	66	8	385	3290	1.9	2.1	49	147	0.6	1037
FJ063 (n=4)	34	21	183	2887	2.1	1.4	56	141	5.2	1050
SD	19	2	37	22	0.0	0.2	28	0	1.5	6
FJ186B (n=2)	18	8	165	2909	2.0	0.9	15	147	0.4	986
SD	0	0	33	151	0.2	0.0	1	3		1
<i>Dunite</i>										
K003	32	20	133	2668	1.6	1.3	12	155	1.7	1460
K008 (n=5)	25	18	102	2763	1.4	0.7	37	139	3.3	1113
SD	9	3	24	9	0.1	0.1	8	1	0.9	3
K012-2	33	29	145	2875	2.2	2.2	23	161	2.8	1205
K037-1	418	60	1685	2361	4.9	7.9	541	155	1.7	1086
K109-1	126	21	791	1710	2.8	2.5	46	121	0.6	1178
K119	51	20	375	3072	3.6	1.8	62	131	0.2	1043
K124	80	33	538	2630	2.1	2.3	47	139	0.3	1599
K159 (n=4)	56	13	416	2941	2.3	2.2	40	147	1.2	1262
SD	4	1	17	27	0.1	0.2	2	2	0.3	67
K186	71	5	389	3251	2.4	2.3	50	147	0.8	1060
FJ024 (n=2)	16	6	217	2720	2.4	0.9	10	128	0.5	881
SD	5	1	40	51	0.1	0.4	1	1	0.2	6
FJ106	58	19	356	2919	3.3	1.7	63	141	0.1	1062
FJ198A-1	32	26	30	2592	2.1	1.0	10	149	2.0	1241
<i>Wehrlite</i>										
K014	81	18	390	1942	2.0	1.3	22	165	0.9	1523

K046 (n=4)	265	88	967	2506	3.9	7.0	218	148	1203
SD	5	1	6	11	0.0	0.2	1	1	10
K047-1	172	91	547	2425	3.3	5.4	95	163	0.7
K171-1	166	43	561	1865	2.7	3.1	69	130	1.7
FJ194	97	52	386	1909	3.1	2.4	55	172	0.5
<i>Olivine in host basalt</i>									
FJ024_Ol-host-a	307	51		2453	3.8	6.0	346	135	3.1
FJ024_Ol-host-b	286	56		2530	3.7	5.7	371	130	2.5

* = Thin section

Supplementary Table 13: LA-ICP-MS REE concentrations in Koro xenolith olivines

Sample	La	Ce	Pr	Nd	Sm	Eu	Gd	Tb
<i>LA-ICP-MS (ppm)</i>								
<i>Lherzolite (olivine $\geq Fo_{89.5}$)</i>								
*K041-2 (n=4)	0.00013	0.00060	0.00020	0.00037	0.00018	0.00009	0.00043	0.00011
SD	0.00004	0.00069	0.00018	0.00032	0.00010	0.00003	0.00025	0.00003
*K042-2 (n=4)	0.00017	0.00061	0.00023	0.00056	0.00029	0.00013	0.00028	0.00014
SD	0.00014	0.00034	0.00011	0.00058	0.00016	0.00005	0.00012	0.00003
*K049-1 (n=10)	0.00174	0.00365	0.00061	0.00247	0.00085	0.00033	0.00096	0.00021
SD	0.00348	0.00689	0.00074	0.00345	0.00090	0.00033	0.00085	0.00026
*FJ167-2 (n=2)	0.00099	0.00321	0.00054	0.00224	0.00105	0.00055	0.00128	0.00037
SD	0.00081	0.00299	0.00044	0.00099	0.00052	0.00033	0.00045	0.00015
FJ185-1 (n=3)	0.0002	0.0009	0.0002	0.0013	0.0005	0.0002	0.0006	0.0002
SD	0.0001	0.0004	0.0001	0.0012	0.0004	0.0002	0.0007	0.0001
K001	0.00038	0.00056	0.00010	0.00211	0.00065	0.00004	0.00117	0.00023
K002	0.00053	0.00064	0.00011	0.00148	0.00048	0.00020	0.00065	0.00012
K011-1	0.00022	0.00022	0.00008	0.00061	0.00118	0.00018	0.00052	0.00012
K012-1	0.00035	0.00069	0.00013	0.00138	0.00077	0.00004	0.00075	0.00012
K012-3	0.00013	0.00019	0.00009	0.00140	0.00070	0.00026	0.00091	0.00012
K015A-2	0.00009	0.00014	0.00013	0.00157	0.00051	0.00013	0.00054	0.00016
K022	0.00057	0.00143	0.00031	0.00181	0.00075	0.00020	0.00091	0.00008
K025-1	0.00015	0.00019	0.00008	0.00159	0.00093	0.00019	0.00043	0.00006
K026	0.00040	0.00027	0.00016	0.00088	0.00034	0.00016	0.00045	0.00008
K030	0.00028	0.00044	0.00018	0.00143	0.00071	0.00027	0.00032	0.00018
K031	0.00003	0.00018	0.00014	0.00176	0.00062	0.00019	0.00042	0.00008
K033-1	0.00024	0.00045	0.00003	0.00133	0.00060	0.00018	0.00014	0.00013
K039-1	0.00048	0.00122	0.00012	0.00234	0.00148	0.00027	0.00136	0.00050
K039-2	0.00065	0.00108	0.00020	0.00120	0.00071	0.00026	0.00106	0.00029
K040	0.00081	0.00133	0.00027	0.00086	0.00104	0.00031	0.00091	0.00031
K041-1	0.00280	0.00214	0.00034	0.00161	0.00050	0.00030	0.00009	0.00013
K042-1	0.00020	0.00023	0.00014	0.00081	0.00051	0.00018	0.00091	0.00011
K043	0.00032	0.00059	0.00020	0.00224	0.00076	0.00013	0.00095	0.00010
K044-1	0.00010	0.00039	0.00014	0.00186	0.00078	0.00026	0.00119	0.00027

K044-2	0.00038	0.00048	0.00018	0.00120	0.00090	0.00018	0.00063	0.00017
K048A-2	0.00031	0.00039	0.00011	0.00146	0.00065	0.00017	0.00041	0.00005
K048-4	0.00039	0.00086	0.00013	0.00147	0.00072	0.00025	0.00057	0.00013
K050	0.00012	0.00011	0.00007	0.00140	0.00072	0.00014	0.00049	0.00013

Supplementary Table 13: LA-ICP-MS REE concentrations in Koro xenolith olivines

Sample	Dy	Ho	Er	Tm	Yb	Lu
<i>LA-ICP-MS (ppm)</i>						
<i>Lherzolite (olivine $\geq Fo_{89.5}$)</i>						
*K041-2 (n=4)	0.00103	0.00052	0.00310	0.00095	0.01076	0.00287
SD	0.00013	0.00006	0.00056	0.00014	0.00104	0.00022
*K042-2 (n=4)	0.00156	0.00074	0.00440	0.00127	0.01353	0.00357
SD	0.00023	0.00007	0.00041	0.00006	0.00046	0.00010
*K049-1 (n=10)	0.00108	0.00052	0.00244	0.00083	0.00962	0.00256
SD	0.00082	0.00027	0.00083	0.00030	0.00222	0.00054
*FJ167-2 (n=2)	0.00311	0.00124	0.00673	0.00180	0.01780	0.00475
SD	0.00117	0.00029	0.00078	0.00052	0.00410	0.00066
FJ185-1 (n=3)	0.0017	0.0009	0.0049	0.0014	0.0166	0.0039
SD	0.0005	0.0002	0.0007	0.0003	0.0024	0.0006
K001	0.00099	0.00034	0.00143	0.00051	0.00660	0.00206
K002	0.00122	0.00070	0.00463	0.00150	0.01950	0.00566
K011-1	0.00077	0.00042	0.00129	0.00047	0.00610	0.00205
K012-1	0.00156	0.00072	0.00329	0.00106	0.01030	0.00296
K012-3	0.00092	0.00056	0.00329	0.00096	0.01190	0.00329
K015A-2	0.00203	0.00107	0.00585	0.00133	0.01600	0.00464
K022	0.00080	0.00019	0.00175	0.00038	0.00577	0.00189
K025-1	0.00005	0.00020	0.00106	0.00031	0.00551	0.00171
K026	0.00026	0.00014	0.00036	0.00024	0.00262	0.00126
K030	0.00072	0.00042	0.00180	0.00049	0.00487	0.00112
K031	0.00056	0.00013	0.00121	0.00026	0.00400	0.00202
K033-1	0.00042	0.00014	0.00045	0.00012	0.00148	0.00068
K039-1	0.00331	0.00092	0.00392	0.00108	0.00830	0.00247
K039-2	0.00162	0.00070	0.00469	0.00110	0.01160	0.00343
K040	0.00244	0.00101	0.00529	0.00133	0.01620	0.00445
K041-1	0.00113	0.00050	0.00380	0.00088	0.01250	0.00323
K042-1	0.00230	0.00072	0.00424	0.00105	0.01390	0.00357
K043	0.00077	0.00016	0.00094	0.00042	0.00469	0.00148
K044-1	0.00375	0.00147	0.00663	0.00165	0.01510	0.00442
K044-2	0.00163	0.00063	0.00305	0.00102	0.01060	0.00289
K048A-2	0.00037	0.00027	0.00122	0.00067	0.00555	0.00213

K048-4	0.00205	0.00075	0.00411	0.00118	0.01370	0.00380
K050	0.00152	0.00063	0.00413	0.00128	0.01330	0.00391

Supplementary Table 13: Continued

Sample	La	Ce	Pr	Nd	Sm	Eu	Gd	Tb
<i>LA-ICP-MS (ppm)</i>								
K051 (n=2)	0.00079	0.00055	0.00014	0.00230		0.00024	0.00191	0.00059
SD	0.00025	0.00028	0.00011				0.00130	
K052	0.00004							0.00004
K053-1 (n=2)	0.00144	0.00202	0.00077	0.00295	0.00270	0.00117	0.00535	0.00073
SD	0.00050	0.00022	0.00040	0.00175		0.00084	0.00075	0.00002
K055-1	0.00041	0.00037	0.00002	0.00017	0.00011	0.00009	0.00089	0.00040
K056				0.00350				0.00002
K060-2	0.00013	0.00019	0.00004					
K064 (n=2)	0.00025	0.00042					0.00138	0.00021
SD		0.00030					0.00123	
K066	0.00004	0.00015						
K070	0.00011	0.00008	0.00004					
K072	0.00064	0.00052				0.00004	0.00103	0.00018
K074	0.00005	0.00012						0.00014
K076								
K077		0.00004						0.00007
K083	0.00078	0.00108	0.00021	0.00070				
K085		0.00030						0.00008
K090	0.00016	0.00017						
K099	0.00050	0.00034	0.00008	0.00017				
K102	0.00001	0.00010						0.00003
K103		0.00011						0.00005
K106	0.00040	0.00045	0.00003			0.00003	0.00046	0.00010
K107	0.00110	0.00071	0.00016	0.00120	0.00021	0.00006		0.00004
K109-2	0.00011	0.00028	0.00007	0.00180		0.00013		0.00002
K110	0.00046	0.00022		0.00070	0.00018	0.00011	0.00011	
K121	0.00095	0.00012		0.00070				0.00001
K122	0.00007	0.00012	0.00012		0.00011			0.00005
K127	0.00830	0.00405	0.00138	0.00710	0.00069	0.00066	0.00170	0.00014
K131	0.00011	0.00010		0.00019				
K132	0.00011	0.00012	0.00006	0.00070			0.00038	0.00015
K137	0.00400	0.00075	0.00109	0.00140	0.00026	0.00025	0.00150	0.00022
K138	0.00126	0.00007	0.00055	0.00160		0.00008	0.00025	0.00003

K146	0.00309	0.00009	0.00039	0.00143	0.00018		0.00001
K147	0.00105	0.00056	0.00003				
K154	0.00008	0.00045		0.00037			0.00009
K163	0.00000						
K164	0.00106	0.00062	0.00025	0.00042		0.00003	0.00003
K166	0.00011	0.00009				0.00015	
K170							
K175-1						0.00012	0.00014
K176	0.00002			0.00018		0.00042	
K176-2	0.15900	0.02600	0.03300	0.13600	0.02500	0.01000	0.03600
							0.00520

Supplementary Table 13: Continued

Sample	Dy	Ho	Er	Tm	Yb	Lu
<i>LA-ICP-MS (ppm)</i>						
K051 (n=2)	0.00191	0.00058	0.00289	0.00104	0.01040	0.00291
SD	0.00130	0.00005	0.00032	0.00025	0.00240	0.00037
K052	0.00128	0.00056	0.00312	0.00097	0.01520	0.00313
K053-1 (n=2)	0.01015	0.00222	0.00915	0.00196	0.01875	0.00279
SD	0.00075	0.00072	0.00205	0.00004	0.00035	0.00047
K055	0.00240	0.00083	0.00470	0.00083	0.01120	0.00212
K055-1	0.00410	0.00110	0.00360	0.00079	0.01140	0.00225
K056		0.00008	0.00039	0.00011	0.00400	0.00089
K060-2	0.00008	0.00004	0.00063	0.00020	0.00310	0.00139
K064 (n=2)	0.00192	0.00050	0.00320	0.00073	0.01010	0.00221
SD	0.00078	0.00015	0.00071	0.00003	0.00040	0.00001
K066	0.00028	0.00005	0.00069	0.00010	0.00260	0.00149
K070	0.00038	0.00035	0.00290	0.00067	0.01010	0.00291
K072	0.00167	0.00138	0.00700	0.00168	0.01980	0.00464
K074	0.00110	0.00061	0.00380	0.00088	0.01270	0.00364
K076	0.00059	0.00010	0.00119	0.00047	0.00590	0.00164
K077	0.00051	0.00014	0.00112	0.00035	0.00580	0.00108
K083	0.00038	0.00041	0.00082	0.00027	0.00500	0.00127
K085	0.00194	0.00053	0.00400	0.00092	0.01140	0.00194
K090	0.00006	0.00001	0.00054	0.00021	0.00770	0.00261
K093	0.00050	0.00022	0.00055	0.00023	0.00300	0.00120
K099	0.00059	0.00041	0.00176	0.00035	0.00450	0.00150
K102	0.00080	0.00023	0.00232	0.00063	0.00820	0.00194
K103	0.00005		0.00063	0.00023	0.00470	0.00097
K106	0.00170	0.00058	0.00283	0.00074	0.01200	0.00287
K107	0.00037	0.00039	0.00330	0.00110	0.00720	0.00265
K109-2	0.00015	0.00021	0.00126	0.00032	0.00480	0.00129
K110	0.00033	0.00013	0.00152	0.00052	0.00400	0.00157
K121	0.00048	0.00026	0.00254	0.00078	0.00810	0.00183
K122	0.00103	0.00056	0.00250	0.00078	0.00870	0.00234
K127	0.00111	0.00036	0.00253	0.00088	0.01490	0.00405
K131	0.00072	0.00045	0.00214	0.00077	0.01130	0.00209
K132	0.00076	0.00055	0.00328	0.00083	0.01290	0.00201

K137	0.00190	0.00043	0.00257	0.00045	0.00770	0.00205
K138	0.00074	0.00039	0.00156	0.00051	0.00600	0.00118
K146	0.00045	0.00035	0.00262	0.00063	0.00530	0.00185
K147	0.00053	0.00031	0.00153	0.00061	0.00760	0.00178
K154	0.00065	0.00021	0.00148	0.00065	0.00680	0.00193
K163	0.00089	0.00037	0.00315	0.00100	0.01030	0.00274
K164	0.00190	0.00051	0.00365	0.00093	0.01240	0.00236
K166	0.00219	0.00077	0.00262	0.00098	0.00980	0.00280
K170	0.00079	0.00044	0.00280	0.00088	0.00970	0.00217
K175-1	0.00007	0.00048	0.00350	0.00088	0.00990	0.00279
K176	0.00015	0.00035	0.00350	0.00058	0.01190	0.00278
K176-2	0.03300	0.00810	0.02220	0.00350	0.03500	0.00550

Supplementary Table 13: Continued

Sample	La	Ce	Pr	Nd	Sm	Eu	Gd	Tb
<i>LA-ICP-MS (ppm)</i>								
K179								
K180								
K181-1						0.00004	0.00028	0.00002
K182	0.00025	0.00024	0.00002					
K183	0.00490	0.00468	0.00069	0.00240		0.00033	0.00054	0.00008
K185	0.00101	0.00049	0.00024	0.00020				0.00014
K187	0.00030	0.00004	0.00015	0.00080				
K188	0.00007	0.00022						0.00011
K196			0.00002					
K198	0.00173	0.00070	0.00010	0.00085				0.00002
K199	0.00013							
K202	0.00005	0.00004						0.00002
K205								
FJ009	0.00029	0.00040	0.00013	0.00054	0.00062	0.00012	0.00041	0.00019
FJ013	0.00020	0.00044	0.00015	0.00036	0.00044	0.00017	0.00086	0.00010
FJ017	0.00018	0.00030	0.00013	0.00107	0.00073	0.00017	0.00193	0.00031
FJ020	0.00300	0.00077	0.00041	0.00330	0.00087	0.00031	0.00103	0.00016
FJ021	0.01860	0.00070	0.00439	0.02040	0.00421	0.00190	0.00640	0.00098
FJ031	0.00026	0.00043	0.00007	0.00072	0.00061	0.00015	0.00068	0.00021
FJ053-1	0.00015	0.00011	0.00008	0.00115	0.00066	0.00014	0.00044	0.00012
FJ055-1	0.00293	0.00501	0.00072	0.00420	0.00124	0.00027	0.00137	0.00027
FJ060	0.00082	0.00074	0.00008	0.00122	0.00069	0.00015	0.00070	0.00010
FJ066-2	0.00017	0.00017	0.00005	0.00051	0.00052	0.00013	0.00048	0.00016
FJ067	0.00093	0.00116	0.00014	0.00120	0.00075	0.00024	0.00100	0.00013
FJ104	0.00027	0.00035	0.00004	0.00030	0.00011	0.00020	0.00029	0.00009
FJ140	0.00253	0.00054	0.00038	0.00233	0.00094	0.00039	0.00103	0.00020
FJ143	0.00860	0.00619	0.00172	0.00560	0.00151	0.00029	0.00121	0.00029
FJ145	0.00030	0.00031	0.00014	0.00158	0.00073	0.00027	0.00050	0.00007
FJ154	0.00164	0.00017	0.00031	0.00240	0.00094	0.00019	0.00058	0.00008
FJ155-1	0.00266	0.00111	0.00060	0.00300	0.00126	0.00037	0.00071	0.00011
FJ166	0.00010	0.00005	0.00003	0.00029	0.00050	0.00010	0.00106	0.00014
FJ171	0.00012	0.00009	0.00007	0.00082	0.00074	0.00012	0.00039	0.00013
FJ177	0.00006	0.00006	0.00012	0.00169	0.00087	0.00023	0.00073	0.00018

FJ180	0.00012	0.00003	0.00010	0.00101	0.00059	0.00009	0.00046	0.00007
FJ181	0.00014	0.00013	0.00009	0.00062	0.00093	0.00013	0.00027	
FJ183	0.00024	0.00011	0.00012	0.00088	0.00079	0.00015	0.00039	0.00010
FJ184-1	0.00027	0.00032	0.00007	0.00142	0.00084	0.00014	0.00067	0.00012
FJ198B-1	0.00007	0.00015	0.00008	0.00105	0.00098	0.00022	0.00051	0.00016
FJ199	0.00013	0.00004	0.00005	0.00060	0.00069	0.00030	0.00108	0.00009
FJ200	0.00011	0.00009	0.00007	0.00120	0.00040	0.00021	0.00070	0.00016
FJ215	0.00025	0.00049	0.00017	0.00170	0.00036	0.00020	0.00074	0.00027

Supplementary Table 13: Continued

Sample	Dy	Ho	Er	Tm	Yb	Lu
<i>LA-ICP-MS (ppm)</i>						
K179	0.00081	0.00032	0.00370	0.00069	0.00860	0.00240
K180	0.00051	0.00051	0.00380	0.00105	0.01260	0.00277
K181-1	0.00152	0.00066	0.00360	0.00102	0.01270	0.00323
K182	0.00018	0.00013	0.00112	0.00014	0.00560	0.00155
K183	0.00250	0.00081	0.00530	0.00088	0.01600	0.00375
K185	0.00090	0.00079	0.00360	0.00114	0.01100	0.00307
K187	0.00075	0.00033	0.00256	0.00065	0.00930	0.00287
K188	0.00116	0.00050	0.00350	0.00070	0.01300	0.00290
K196	0.00119	0.00052	0.00360	0.00069	0.01030	0.00219
K198	0.00081	0.00027	0.00218	0.00046	0.00760	0.00208
K199	0.00007	0.00023	0.00215	0.00071	0.00870	0.00211
K202	0.00059	0.00024	0.00158	0.00056	0.00850	0.00246
K205	0.00046	0.00029	0.00245	0.00074	0.00970	0.00265
FJ009	0.00073	0.00033	0.00231	0.00072	0.00870	0.00283
FJ013	0.00065	0.00012	0.00066	0.00049	0.00508	0.00232
FJ017	0.00288	0.00133	0.00610	0.00192	0.01690	0.00493
FJ020	0.00093	0.00032	0.00188	0.00064	0.00760	0.00228
FJ021	0.00590	0.00145	0.00606	0.00106	0.01260	0.00297
FJ031	0.00164	0.00094	0.00411	0.00125	0.01320	0.00414
FJ053-1	0.00061	0.00041	0.00218	0.00067	0.00800	0.00290
FJ055-1	0.00192	0.00057	0.00270	0.00060	0.00750	0.00227
FJ060	0.00040	0.00026	0.00104	0.00031	0.00280	0.00092
FJ066-2	0.00055	0.00032	0.00234	0.00049	0.00630	0.00196
FJ067	0.00070	0.00032	0.00160	0.00042	0.00490	0.00183
FJ104	0.00086	0.00020	0.00235	0.00066	0.00560	0.00172
FJ140	0.00108	0.00046	0.00188	0.00090	0.00780	0.00201
FJ143	0.00241	0.00069	0.00255	0.00059	0.00580	0.00152
FJ145	0.00100	0.00041	0.00295	0.00073	0.01020	0.00266
FJ154	0.00060	0.00032	0.00156	0.00046	0.00557	0.00140
FJ155-1	0.00042	0.00029	0.00120	0.00036	0.00349	0.00090
FJ166	0.00151	0.00050	0.00268	0.00091	0.01100	0.00310
FJ171	0.00126	0.00051	0.00316	0.00096	0.01070	0.00288
FJ177	0.00105	0.00044	0.00356	0.00113	0.01110	0.00301

FJ180	0.00106	0.00026	0.00147	0.00057	0.00600	0.00223
FJ181	0.00052	0.00023	0.00166	0.00066	0.00610	0.00220
FJ183	0.00054	0.00022	0.00118	0.00047	0.00660	0.00225
FJ184-1	0.00251	0.00092	0.00511	0.00144	0.01700	0.00437
FJ198B-1	0.00122	0.00081	0.00402	0.00102	0.01220	0.00331
FJ199	0.00138	0.00090	0.00556	0.00149	0.01510	0.00373
FJ200	0.00118	0.00057	0.00419	0.00119	0.01360	0.00303
FJ215	0.00194	0.00086	0.00482	0.00121	0.01520	0.00400

Supplementary Table 13: Continued

Sample	La	Ce	Pr	Nd	Sm	Eu	Gd	Tb
<i>LA-ICP-MS (ppm)</i>								
<i>Lherzolite (olivine <Fo_{89.5})</i>								
*K045 (n=4)	0.00067	0.00228	0.00045	0.00323	0.00154	0.00075	0.00253	0.00067
SD	0.00052	0.00286	0.00028	0.00134	0.00058	0.00029	0.00122	0.00032
*FJ167-3 (n=6)	0.00103	0.00232	0.00036	0.00148	0.00070	0.00035	0.00099	0.00037
SD	0.00106	0.00186	0.00026	0.00161	0.00067	0.00033	0.00077	0.00024
FJ185-2 (n=3)	0.0005	0.0008	0.0003	0.0032	0.0016	0.0006	0.0026	0.0008
SD	0.0001			0.0002	0.0001	0.0002	0.0000	0.0002
K006	0.00027	0.00044	0.00023	0.00252	0.00128	0.00036	0.00091	0.00016
K015-1	0.00020	0.00026	0.00011	0.00192	0.00137	0.00034	0.00119	0.00029
K037-2	0.00050	0.00094	0.00023	0.00149	0.00098	0.00032	0.00107	0.00045
K038-1	0.00031	0.00057	0.00011	0.00215	0.00096	0.00035	0.00146	0.00033
K038-2	0.00039	0.00050	0.00015	0.00061	0.00027	0.00025	0.00084	0.00022
K039-4	0.00063	0.00115	0.00028	0.00265	0.00107	0.00062	0.00378	0.00102
K060-1	0.00016	0.00033		0.00170	0.00250	0.00070	0.00080	0.00047
K062 (n=2)	0.00031	0.00042	0.00005	0.00130				0.00012
SD	0.00019	0.00017						
K068 (n=2)	0.00011	0.00032	0.00023	0.00168	0.00170	0.00013	0.00124	0.00027
SD	0.00000	0.00014	0.00000	0.00143	0.00000	0.00000	0.00087	0.00016
K075-1	0.00047	0.00038	0.00015			0.00015	0.00049	0.00015
K081-1	0.00023	0.00055	0.00003	0.00088	0.00032	0.00017	0.00102	0.00020
K087	0.00006	0.00053				0.00025	0.00116	0.00036
K094	0.17600	0.16300	0.01140	0.03700	0.00350	0.00181	0.00200	0.00049
K105	0.00128	0.00213	0.00032	0.00190	0.00019	0.00006	0.00077	0.00025
K108	0.00056	0.00091	0.00015	0.00065	0.00070	0.00082	0.00280	0.00073
K112	0.00017	0.00041	0.00011			0.00012	0.00075	0.00010
K165	0.00103	0.00028	0.00031	0.00072	0.00027		0.00012	0.00009
K191	0.06000	0.07300	0.00880	0.03260	0.00570	0.00182	0.00590	0.00096
FJ032	0.00040	0.00047	0.00021	0.00183	0.00059	0.00048	0.00161	0.00063

Supplementary Table 13: Continued

Sample	Dy	Ho	Er	Tm	Yb	Lu
<i>LA-ICP-MS (ppm)</i>						
<i>Lherzolite (olivine <Fo_{89.5})</i>						
*K045 (n=4)	0.00586	0.00211	0.00861	0.00207	0.02135	0.00515
SD	0.00178	0.00047	0.00170	0.00050	0.00344	0.00082
*FJ167-3 (n=6)	0.00305	0.00126	0.00649	0.00182	0.02027	0.00528
SD	0.00125	0.00034	0.00132	0.00037	0.00349	0.00096
FJ185-2 (n=3)	0.0059	0.0022	0.0102	0.0026	0.0288	0.0070
SD	0.0001	0.0000	0.0004	0.0001	0.0015	0.0008
K006	0.00106	0.00020	0.00101	0.00040	0.00444	0.00144
K015-1	0.00345	0.00164	0.00793	0.00213	0.02050	0.00535
K037-2	0.00276	0.00131	0.00752	0.00171	0.01800	0.00524
K038-1	0.00313	0.00087	0.00489	0.00109	0.01290	0.00365
K038-2	0.00220	0.00098	0.00576	0.00134	0.01670	0.00431
K039-4	0.00730	0.00280	0.01200	0.00275	0.02130	0.00477
K060-1	0.00390	0.00200	0.00750	0.00174	0.02060	0.00360
K062 (n=2)	0.00049	0.00019	0.00186	0.00047	0.00355	0.00125
SD	0.00023	0.00001	0.00115	0.00006	0.00035	0.00013
K068 (n=2)	0.00370	0.00135	0.00655	0.00212	0.01945	0.00454
SD	0.00040	0.00008	0.00115	0.00057	0.00435	0.00067
K075-1	0.00241	0.00100	0.00650	0.00168	0.01690	0.00425
K081-1	0.00310	0.00148	0.00690	0.00167	0.01910	0.00418
K087	0.00430	0.00109	0.00690	0.00139	0.01830	0.00453
K094	0.00460	0.00143	0.00800	0.00157	0.02010	0.00487
K105	0.00249	0.00118	0.00590	0.00165	0.01890	0.00432
K108	0.00380	0.00198	0.00960	0.00170	0.02290	0.00454
K112	0.00183	0.00076	0.00480	0.00145	0.01870	0.00443
K165	0.00086	0.00015	0.00124	0.00027	0.00920	0.00203
K191	0.00650	0.00228	0.00760	0.00158	0.01590	0.00340
FJ032	0.00584	0.00205	0.01070	0.00244	0.02570	0.00540

Supplementary Table 13: Continued

Sample	La	Ce	Pr	Nd	Sm	Eu	Gd
<i>LA-ICP-MS (ppm)</i>							
<i>Lherzolite (olivine <Fo_{89.5})</i>							
FJ155-2	0.00286	0.00378	0.00091	0.00430	0.00185	0.00046	0.00129
FJ178	0.00061	0.00024	0.00012	0.00090	0.00036	0.00033	0.00082
FJ190A-1	0.00016	0.00025	0.00008	0.00128	0.00093	0.00024	0.00065
<i>Harzburgite</i>							
K010	0.00017	0.00035	0.00019	0.00083	0.00068	0.00026	0.00092
K025-2	0.00087	0.00116	0.00018	0.00185	0.00079	0.00011	0.00077
K129	0.00086	0.00008	0.00023	0.00100			0.00026
K152	0.00056	0.00018	0.00011		0.00018		
K193	0.00361	0.00023	0.00018	0.00050			0.00063
FJ186B (n=2)	0.00044	0.00044	0.00014	0.00036	0.00039	0.00013	0.00048
SD	0.00033	0.00004	0.00000	0.00014	0.00002	0.00005	0.00015
<i>Dunite</i>							
K003	0.00039	0.00061	0.00026	0.00209	0.00148	0.00051	0.00129
K008 (n=2)	0.00832	0.01161	0.00132	0.00680	0.00226	0.00131	0.00345
SD	0.00729	0.00990	0.00081	0.00410	0.00024	0.00016	0.00055
K012-2	0.00032	0.00052		0.00216	0.00106	0.00050	0.00288
K037-1	0.00016	0.00050	0.00020	0.00103	0.00152	0.00062	0.00293
K109-1	0.00632	0.01320	0.00182	0.00510	0.00137	0.00064	0.00154
K119	0.00095	0.00246	0.00024	0.00071	0.00047	0.00036	0.00104
K124	0.00220	0.00019	0.00027	0.00210			0.00122
K186	0.00109	0.00023		0.00043			0.00038
FJ024 (n=2)	0.00390	0.00250		0.01800			0.00800
SD	0.00010	0.00080		0.00000			0.00000
FJ106	0.00522	0.00589	0.00059	0.00239	0.00087	0.00026	0.00045
FJ198A-1	0.00248	0.00445	0.00098	0.00640	0.00172	0.00064	0.00262
<i>Wehrlite</i>							
K014	0.00013	0.00030	0.00010				0.00048
K046 (n=4)	0.00137	0.00122	0.00055	0.00244	0.00139	0.00070	0.00305
SD	0.00200	0.00063	0.00054	0.00213	0.00034	0.00026	0.00102
K047-1	0.00034			0.00134	0.00072	0.00052	0.00201
K171-1	0.01730	0.03640	0.00440	0.01970	0.00290	0.00188	0.00520

FJ194	0.00014	0.00041	0.00014	0.00143	0.00058	0.00024	0.00113
<i>Olivine in host basalt</i>							
FJ024_Ol-host-a		0.00050					
FJ024_Ol-host-b		0.00150	0.00110	0.00460			0.00450

* = *Thin section*

Supplementary Table 13: Continued

Sample	Tb	Dy	Ho	Er	Tm	Yb	Lu
<i>LA-ICP-MS (ppm)</i>							
<i>Lherzolite (olivine <Fo_{89.5})</i>							
FJ155-2	0.00070	0.00670	0.00195	0.00890	0.00258	0.02360	0.00582
FJ178	0.00020	0.00261	0.00078	0.00546	0.00150	0.01600	0.00447
FJ190A-1	0.00029	0.00286	0.00103	0.00460	0.00109	0.01570	0.00381
<i>Harzburgite</i>							
K010	0.00014	0.00099	0.00032	0.00120	0.00048	0.00538	0.00166
K025-2	0.00009	0.00050	0.00025	0.00080	0.00025	0.00392	0.00176
K129		0.00024	0.00010	0.00051	0.00039	0.00390	0.00174
K152	0.00005	0.00083	0.00049	0.00185	0.00068	0.00780	0.00236
K193	0.00004	0.00038	0.00015	0.00223	0.00080	0.00660	0.00179
FJ186B (n=2)	0.00013	0.00026	0.00020	0.00114	0.00043	0.00595	0.00179
SD	0.00002	0.00005	0.00007	0.00023	0.00001	0.00015	0.00009
<i>Dunite</i>							
K003	0.00040	0.00213	0.00059	0.00248	0.00053	0.00800	0.00218
K008 (n=2)	0.00045	0.00331	0.00074	0.00195	0.00040	0.00358	0.00124
SD	0.00009	0.00136	0.00022	0.00087	0.00022	0.00028	0.00018
K012-2	0.00049	0.00396	0.00112	0.00500	0.00122	0.01110	0.00313
K037-1	0.00091	0.00810	0.00273	0.01180	0.00257	0.02080	0.00542
K109-1	0.00046	0.00480	0.00163	0.00750	0.00203	0.01670	0.00389
K119	0.00019	0.00196	0.00092	0.00510	0.00195	0.01870	0.00438
K124	0.00048	0.00410	0.00182	0.00940	0.00249	0.03070	0.00622
K186	0.00009	0.00073	0.00053	0.00343	0.00083	0.01400	0.00285
FJ024 (n=2)			0.00114	0.00200	0.00067	0.01050	0.00280
SD			0.00066	0.00040	0.00021	0.00440	0.00060
FJ106	0.00023	0.00240	0.00112	0.00684	0.00185	0.02050	0.00602
FJ198A-1	0.00053	0.00419	0.00100	0.00356	0.00068	0.00970	0.00264
<i>Wehrlite</i>							
K014		0.00159	0.00039	0.00280	0.00093	0.01260	0.00344
K046 (n=4)	0.00096	0.00876	0.00298	0.01357	0.00304	0.02935	0.00632
SD	0.00015	0.00085	0.00012	0.00037	0.00009	0.00050	0.00014
K047-1	0.00052	0.00572	0.00222	0.00984	0.00212	0.02520	0.00607
K171-1	0.00092	0.00550	0.00157	0.00960	0.00164	0.01920	0.00403

FJ194	0.00034	0.00253	0.00095	0.00540	0.00160	0.01780	0.00503
<i>Olivine in host basalt</i>							
FJ024_Ol-host-a	0.00059	0.01120	0.00170	0.01080	0.00210	0.04300	0.00360
FJ024_Ol-host-b	0.00049	0.00580	0.00210	0.00740	0.00180	0.02000	0.00400

* = *Thin section*

Appendix 4. Chapter 3 supplementary tables

Supplementary Table 14: Olivine major element EPMA data

Location: Marum ophiolite

Sample:	MA4	087	*087	088	090	414	*414	423	*423	*423	*425	*425	*425	473	*473	*473	488
Rock type:	Hrz	Dun ± opx	Dun ± opx	Dun	Hrz	Dun ± cpx	Dun ± cpx	Hrz	Hrz	Hrz	Hrz	Hrz	Hrz	Hrz	Hrz	Hrz	Hrz
Analyses:	n=11	n=5		n=9	n=13	n=5		n=4	Core	Inc	Core	Inc (spl)	Rim	n=6	Core	Rim	n=6

EPMA (wt. %)

SiO ₂	41.36	41.03	41.49	41.01	40.94	41.51	40.94	40.71	41.22	41.63	41.16	41.7	41.12	40.92	40.98	41.31	41.00
FeO	7.04	6.21	6.18	5.32	8.01	8.96	8.74	7.84	7.71	6.41	7.51	6.2	7.52	7.92	7.68	7.24	7.54
NiO	0.40	0.39	0.34	0.42	0.37	0.26	0.21	0.41	0.41	-	-	-	-	0.41	0.43	-	0.41
MnO	0.10	0.35	<0.09	0.08	0.12	0.14	<0.09	0.11	<0.09	<0.09	<0.09	<0.09	<0.09	0.12	<0.09	<0.09	0.11
MgO	50.23	52.48	52.33	52.22	49.97	50.36	50.31	50.21	51.06	52.24	51.43	52.56	51.43	50.30	50.95	51.62	50.49
CaO	0.01	0.03	-	0.03	0.02	0.08	-	0.02	-	-	-	-	-	0.01	-	-	0.02
TOTAL	99.18	100.50	100.34	99.08	99.44	101.33	100.21	99.31	100.4	100.28	100.1	100.46	100.06	99.68	100.03	100.17	99.56
Mg#	92.7	93.8	93.8	94.6	91.8	90.9	91.1	92.0	92.2	93.6	92.4	93.8	92.4	91.9	92.2	92.7	92.3

Location: Marum ophiolite

Sample:	*488	*488	489	*489	*489	490	*490	*490	492	*492	*492
Rock type:	Hrz	Hrz	Hrz	Hrz	Hrz	Hrz	Hrz	Hrz	Hrz	Hrz	Hrz
Analyses:	Core	Rim	n=5	Core	Rim	n=6	Core	Rim	n=5	Core	Rim

EPMA (wt. %)

SiO ₂	41.18	41.5	40.76	41.6	41.47	41.02	41.15	40.92	40.55	41.05	41.24
FeO	7.48	7.08	8.00	7.78	7.56	7.65	7.49	7.18	7.77	7.66	7.46
NiO	0.37	-	0.41	0.37	-	0.40	-	-	0.40	0.40	-
MnO	<0.09	<0.09	0.12	<0.09	<0.09	0.12	<0.09	<0.09	0.10	<0.09	<0.09
MgO	51.34	51.59	50.17	50.96	51.51	51.35	51.27	51.2	51.02	50.99	51.06
CaO	-	-	0.02	-	-	0.02	-	-	0.01	-	-
TOTAL	100.37	99.82	99.49	100.27	100.52	100.56	99.91	99.3	99.86	100.1	99.76
Mg#	92.4	92.9	91.8	92.1	92.4	92.3	92.4	92.7	92.1	92.2	92.4

Location: Papuan ultramafic belt

Sample:	KD1	KD2	KD3	714	*714	*714	715	*715	*715	716	*716	*716	720	*720	*720	725	726
---------	-----	-----	-----	-----	------	------	-----	------	------	-----	------	------	-----	------	------	-----	-----

Rock type:	Hz	Dun	Dun	Hz	Hz	Hz	Hz	Hz	Hz	Hz	Hz	Hz	Hz	Hz	Hz	Hz	Hz
Analyses:n=12	n=12	n=13	n=11	n=11	Core	Rim	n=8	Core	Rim	n=11	Core	Rim	n=7	Core	Rim	n=12	n=14
<i>EPMA (wt. %)</i>																	
SiO ₂	41.13	41.33	41.27	41.03	41.3	41.55	40.85	41.58	41.57	40.81	41.57	41.49	41.04	41.13	41.57	41.38	40.66
Cr ₂ O ₃	0.41	-	-	-	-	-	-	-	-	-	-	-	-	-	-	-	-
FeO	7.49	6.72	8.45	7.59	7.73	6.19	7.20	7.16	5.87	7.18	6.63	5.99	7.08	7.02	5.54	7.00	7.73
NiO	0.41	0.42	0.34	0.44	0.27	0.21	0.42	0.19	0.21	0.41	0.22	0.2	0.40	0.26	0.26	0.41	0.42
MnO	0.11	0.10	0.14	0.11	<0.09	<0.09	0.11	<0.09	<0.09	0.10	<0.09	<0.09	0.10	<0.09	<0.09	0.09	0.11
MgO	49.72	50.41	49.36	51.53	50.78	52.19	51.56	51.57	52.27	51.83	51.94	52.31	51.93	51.12	52.22	51.50	51.01
CaO	-	0.01	0.02	0.01	-	-	0.01	-	-	0.01	-	-	0.01	-	-	0.01	0.01
TOTAL	99.37	99.01	99.60	100.71	100.08	100.13	100.15	100.5	100	100.36	100.36	99.99	100.57	99.53	99.59	100.3	99.93
Mg#	92.2	93.0	91.2	92.4	92.1	93.8	92.7	92.8	94.1	92.8	93.3	94.0	92.9	92.8	94.4	92.9	92.2

Major elements (wt.% oxide). Mg# = 100 x Mg/(Mg + Fe) molar. Al₂O₃, TiO₂, P₂O₅ <0.01 wt. %. Na₂O, Cr₂O₃ <0.02 wt.% except KD1 *
 Indicates data from Jaques (1980) and Jaques & Chappell (1980).

Supplementary Table 15: Orthopyroxene major element EPMA data in PNG tectonites

Location		Marum ophiolite																				
:																						
Sample:		MD4 423 *423 *423 †425 *425 *425 473 *473 *473 †087 *087 *087 090 488 *488 *488 489 *489 *489 490																				
Rock type:		Hz	Hz	Hz	Hz	Hz	Hz	Hz	Hz	Dun	Dun	Dun	Hz	Hz	Hz	Hz	Hz	Hz	Hz	Hz	Hz	
Analyse s:		n=14	n=6	Core	Rim	Core	Rim	n=5	Core	Rim	Core	Rim	n=10	n=7	Core	Rim	n=6	Core	Rim	n=7		
<i>EPMA (wt. %)</i>																						
SiO ₂	56.9 8	57.2 4	57.77 3	57.7 1	57.72	57.69	57.38	57.96	56.60	58.50	58.50	58.63	57.6 5	57.87 3	57.8 58.83	57.5 3	57.6 6	57.8 8	57.79			
TiO ₂	-	-	-	-	<0.0 1	-	0.01	-	-	<0.01	-	-	-	-	-	-	-	-	-	-		
Al ₂ O ₃	0.62	0.90	0.84	0.57	0.52	0.65	0.39	1.04	0.91	0.66	0.11	0.15	<0.09	0.81	0.92	0.58	0.11	0.84	0.64	0.21	0.76	
Cr ₂ O ₃	0.33	0.44	0.38	0.28	0.25	0.32	0.18	0.46	0.24	0.22	0.12	0.18	0.17	0.35	0.46	0.38	<0.07	0.41	0.35 7	<0.0 0.38		
FeO	4.78	5.16	5.1	5.22	4.95	4.98	4.91	5.28	5.21	5.32	6.21	3.91	3.94	5.34	4.92	4.9	4.99	5.18	4.94	5.07	4.95	
NiO	0.08	0.09	-	-	-	-	0.09	-	-	0.39	-	-	0.07	0.09	-	-	0.09	-	-	0.09		
MnO	0.12	0.13	<0.09 9	<0.09 9	<0.09	<0.09	0.14	<0.09	<0.09	0.08	<0.09	<0.09	0.14	0.12	<0.09 9	<0.09	0.13 9	<0.09 9	<0.09 0.13	<0.09 0.13	0.13	
MgO	36.0 5	34.9 5	35.62 7	35.5 7	35.8 7	35.7	36.03	34.83	35.63	35.16	52.46	36.86	36.75 7	34.6	35.05 9	35.9	36.65 5	34.7 6	35.4	36.3	35.92	
CaO	0.60	0.68	0.69	0.6	0.51	0.66	0.36	0.74	0.58	0.54	0.03	0.43	0.53	0.64	0.72	0.59	0.18	0.87	0.88	0.3	0.57	
TOTAL	99.5 8	99.6 0	100.4 7	99.9 0	99.8 2	100.0	99.56	99.96 3	100.5 1	98.50 3	100.3 1	100.0 3	100.0 2	92.0 5	100.1 4	99.9 6	100.7 1	99.8 3	99.9 6	99.7 0	100.6	
Mg#	93.1	92.4	92.6	92.4	92.8	92.7	92.9	92.2	92.4	92.2	93.8	94.4	94.3	92.0	92.7	92.9	92.9	92.3	92.8	92.7	92.8	
<i>Location</i>																						
Marum ophiolite																						
Papuan ultramafic belt																						
Sample:		*490 *490 492 *492 *492 KD1 714 715 716 720 725 726																				
Rock type:		Hz	Hz	Hz	Hz	Hz	Hz	Hz	Hz	Hz	Hz	Hz	Hz	Hz	Hz	Hz	Hz	Hz	Hz	Hz	Hz	
Analyse s:		Core	Rim	n=9	Core	Rim	n=6	n=6	n=6	n=8	n=18	n=14	n=2									
<i>EPMA (wt. %)</i>																						
SiO ₂	57.9 2	58.0 6	57.42 1	57.7 6	57.8	56.73	58.60	58.75	58.48	58.50	58.90	58.87										

Al ₂ O ₃	0.46	<0.0 9	0.70	0.37	0.29	0.77	0.24	0.12	0.11	0.11	0.11	0.17
Cr ₂ O ₃	0.3	<0.0 7	0.40	0.25	<0.0 7	0.37	0.23	0.14	0.14	0.14	0.12	0.17
FeO	4.78	5.06	5.04	4.92	5.17	4.97	4.93	4.57	4.62	4.60	4.52	4.95
NiO	-	-	0.09	-	-	0.08	0.09	0.09	0.08	0.08	0.09	0.09
MnO	<0.0 9	<0.0 9	0.12	<0.0 9	<0.0 9	0.12	0.12	0.12	0.12	0.11	0.11	0.11
MgO	36.0 1	36	35.56 2	35.5 6	35.93	36.67	36.91	36.94	36.96	36.71	36.59	
CaO	0.5	0.26	0.73	0.76	0.22	0.52	0.19	0.12	0.13	0.13	0.12	0.18
TOTAL	99.9 7	99.3 8	100.0 7	99.5 3	99.5 0	99.51 2	101.1 4	100.8 4	100.6 4	100.6 100.7	100.7 3	101.1
Mg#	93.1	92.7	92.6	92.8	92.5	92.8	93.0	93.5	93.4	93.5	93.5	93.0

Major elements (wt. % oxide). * indicates data from Jaques (1980) and Jaques & Chappell (1980). FeO* = Total iron. K₂O, P₂O₅ <0.01 wt. %. Na₂O <0.02 wt. %. †indicates data calibrated by EDS (Jaques, 1980). Mg# = 100 x Mg/(Mg + Fe) molar.

Supplementary Table 16: Clinopyroxene major element EPMA data in PNG tectonites

Location:	Marum ophiolite											
Sample:	MA4	090	*414	423	*425	473	488	*488	489	490	492	*492
Rock type:	Hrz	Hrz	Dun (inc in spl)	Hrz	Hrz	Hrz	Hrz	Hrz	Hrz	Hrz	Hrz	Hrz
Analyses:	n=4	n=6		n=4		n=3	n=1		n=6	n=3	n=6	
<i>EPMA (wt. %)</i>												
SiO ₂	55.00	54.50	53.62	54.15	54.62	54.37	54.66	55.17	54.20	54.70	54.18	54.33
TiO ₂	-	-	-	0.01	-	-	-	-	0.01	-	<0.01	-
Al ₂ O ₃	0.57	0.73	1.13	0.82	0.88	0.80	0.66	0.37	0.73	0.56	0.65	0.37
V ₂ O ₃	0.01	-	-	0.03	-	-	-	-	-	-	-	-
Cr ₂ O ₃	0.44	0.43	1.25	0.56	0.61	0.44	0.48	0.50	0.63	0.39	0.53	0.72
FeO	1.47	1.67	1.71	1.56	1.56	1.66	1.46	1.43	1.59	1.59	1.53	1.56
NiO	0.05	0.04	-	0.05	-	0.05	0.04	-	0.04	0.04	0.05	-
MnO	0.07	0.06	<0.09	0.06	<0.09	0.06	0.07	<0.09	0.06	0.07	0.06	<0.09
MgO	18.14	17.72	17.03	17.68	18.58	17.81	17.80	18.65	17.74	18.31	18.15	18.09
CaO	24.56	23.74	25.07	24.33	23.92	24.23	24.60	24.36	24.16	24.34	24.29	23.93
Na ₂ O	0.15	0.11	<0.17	0.15	<0.17	0.12	0.13	<0.17	0.21	0.16	0.15	<0.17
TOTAL	100.47	99.02	99.82	99.39	100.17	100.13	99.89	100.48	99.38	100.18	99.62	99.00
Ca/(Mg+Ca+Fe)	0.482	0.478	0.500	0.485	0.469	0.482	0.487	0.474	0.482	0.477	0.479	0.476
Mg#	95.7	95.0	94.7	95.3	95.5	95.0	95.6	95.9	95.2	95.4	95.5	95.4

Major elements (wt. % oxide). * indicates published data from Jaques (1980) and Jaques & Chappell (1980). FeO* = Total iron. K₂O, P₂O₅ < 0.01 wt. %. Mg# = 100 x Mg/(Mg + Fe) molar.

Supplementary Table 17: Spinel major element EPMA data in PNG tectonites

Location: Marum ophiolite															
Sample:	MA4	087	*087	*087	088	090	414	*414	423	*423	*423	†425	*425	*425	*425
Rock type:	Hrz	Dun	Dun	Dun	Dun	Hrz	Dun	Dun	Hrz	Hrz	Hrz	Hrz	Hrz	Hrz	Hrz
Analyses:	n=16	n=4	Core	Rim	n=11	n=6	n=4	Core	n=5	Core	Rim	Hrz	Core	Hrz	Rim
<i>EPMA (wt. %)</i>															
SiO ₂	0.00	<0.02	-	-	<0.02	<0.02	<0.02	-	<0.02	-	-	-	-	-	-
TiO ₂	0.01	0.03	<0.07	<0.07	0.02	<0.01	0.16	0.22	<0.01	<0.07	<0.07	-	<0.07	<0.07	<0.07
Al ₂ O ₃	12.21	6.13	6.88	6.7	3.70	14.02	14.37	14.07	13.70	14.16	14.98	14.36	14.36	16.03	
V ₂ O ₃	0.10	0.07	-	-	0.04	0.20	0.15	-	0.14	-	-	-	-	-	-
Cr ₂ O ₃	57.69	63.34	62.84	62.36	65.65	52.16	49.11	49.56	55.48	54.88	53.37	55.33	55.33	53.26	
FeO	17.82	18.94	19.91	20.1	17.37	20.59	25.76	25.78	18.90	19.63	20.57	18.88	19.13	19.08	
MnO	0.24	0.33	0.26	<0.09	0.33	0.32	0.37	0.53	0.29	<0.09	0.25	-	<0.09	<0.09	
NiO	-	0.03	-	-	0.04	0.03	0.06	-	0.07	-	-	-	-	-	-
ZnO	-	0.15	-	-	0.09	0.25	0.15	-	0.14	-	-	-	-	-	-
MgO	10.65	10.00	10.53	10.22	10.11	9.50	8.97	9.5	10.91	11.42	10.98	11.63	11.63	11.8	
CaO	-	<0.01	0.19	0.18	<0.01	<0.01	<0.01	0.11	<0.01	0.2	0.19	-	0.07	0.07	
TOTAL	98.77	99.02	100.61	99.56	97.35	97.08	99.10	99.77	99.62	100.29	100.34	100.20	100.45	100.26	
Fe ₂ O ₃	-	2.21	-	-	1.63	2.62	6.43	-	2.17	-	-	2.48	-	-	
FeO	-	16.96	-	-	15.90	18.23	19.97	-	16.94	-	-	16.65	-	-	
Cr#	0.76	0.87	0.86	0.86	0.92	0.71	0.70	0.70	0.73	0.72	0.71	0.72	0.72	0.69	
Mg#	51.6	48.5	48.5	47.5	50.9	45.1	38.3	39.6	50.7	50.9	48.8	52.3	52.0	52.4	
Location: Marum ophiolite															
Sample:	473	*473	*473	488	*488	*488	489	490	*490	*490	492	*492	*492	*492	*492
Rock type:	Hrz	Hrz	Hrz	Hrz	Hrz	Hrz	Hrz	Hrz	Hrz	Hrz	Hrz	Hrz	Hrz	Hrz	Hrz
Analyses:	n=4	Core	Rim	n=4	Core	Rim	n=4	n=6	Core	Rim	n=6	Core	Rim	Core	Rim
<i>EPMA (wt. %)</i>															
SiO ₂	<0.02	-	-	<0.02	-	-	<0.02	<0.02	-	-	<0.02	-	-	-	-
TiO ₂	<0.01	0.12	<0.07	<0.01	<0.07	<0.07	0.03	<0.01	<0.07	<0.07	<0.01	<0.07	<0.07	<0.07	<0.07
Al ₂ O ₃	14.79	15.19	15.95	14.13	14.22	15.67	12.92	12.43	11.82	12.62	11.65	10.76	10.83		
V ₂ O ₃	0.21	-	-	0.14	-	-	0.17	0.11	-	-	0.19	-	-	-	-
Cr ₂ O ₃	53.19	53.47	57.37	56.39	55.51	54.47	56.70	57.04	58.39	57.06	57.50	59.38	59		
FeO	19.86	20.28	20.53	16.93	18.16	18.67	18.38	18.96	18.24	19.76	18.53	19.28	19.6		

MnO	0.29	0.34	0.32	0.28	0.36	<0.09	0.31	0.32	0.27	<0.09	0.31	<0.09	<0.09
NiO	0.06	-	-	0.05	-	-	0.05	0.04	-	-	0.04	-	-
ZnO	0.17	-	-	0.14	-	-	0.18	0.21	-	-	0.16	-	-
MgO	10.50	11.49	11.29	11.30	11.08	10.89	10.38	10.21	11.06	10.6	10.26	10.73	10.28
CaO	<0.01	0.2	0.15	<0.01	0.1	0.07	<0.01	<0.01	0.07	0.09	<0.01	0.12	0.07
TOTAL	99.07	101.09	100.61	99.35	99.43	99.7	99.11	99.32	99.78	100.33	98.66	100.27	99.71
Fe ₂ O ₃	2.57	-	-	0.67	-	-	1.04	1.47	-	-	1.41	-	-
FeO	17.54	-	-	16.32	-	-	17.44	17.63	-	-	17.26	-	-
Cr#	0.71	0.70	0.71	0.73	0.72	0.70	0.75	0.75	0.77	0.75	0.77	0.79	0.79
Mg#	48.5	50.2	49.5	54.3	52.1	51.0	50.2	49.0	51.9	48.9	49.7	49.8	48.3

Location: Papuan ultramafic belt

Sample:	KD1	KD2	KD3	714	*714	*714	715	*715	*715	720	725	726	716	*716	*716
Rock type:	Hrz	Dun	Dun	Hrz	Hz	Hz	Hz	Hz	Hz	Hz	Hz	Hz	Hz	Hz	Hz
Analyses:n=6	n=17	n=14	n=7	Core	Rim	n=4	Core	Rim	n=7	n=10	n=2	n=7	Core	Rim	
<i>EPMA (wt. %)</i>															
SiO ₂	-	-	-	<0.02	-	-	<0.02	-	-	<0.02	0.02	0.02	<0.02	-	-
TiO ₂	-	0.06	0.21	<0.01	<0.07	<0.07	<0.01	<0.07	<0.07	<0.01	0.02	<0.01	<0.01	<0.07	<0.07
Al ₂ O ₃	12.39	12.62	14.74	4.91	5.47	5.07	2.73	2.6	2.76	2.60	2.66	3.88	2.65	2.6	2.61
V ₂ O ₃	0.19	0.19	0.22	0.16	-	-	0.19	-	-	0.19	0.17	0.18	0.19	-	-
Cr ₂ O ₃	55.58	56.61	50.78	66.78	66.08	66.75	68.10	68.7	68.23	68.80	67.84	66.99	68.78	68.06	68.52
FeO	21.51	18.69	23.22	18.67	17.85	19.12	19.04	19.5	20.1	19.17	19.25	19.13	19.80	19.06	19.7
MnO	0.29	0.25	0.31	0.33	0.56	0.33	0.34	0.57	0.53	0.36	0.37	0.36	0.38	0.43	0.41
NiO	0.04	0.04	0.06	0.03	-	-	0.03	-	-	0.03	0.04	0.02	0.03	-	-
ZnO	-	-	-	0.14	-	-	0.12	-	-	0.13	0.15	0.15	0.14	-	-
MgO	8.56	10.17	8.96	8.96	10.14	9.16	8.63	9.12	8.73	8.76	8.67	8.58	8.34	9.24	9.09
CaO	-	-	-	<0.01	<0.07	<0.07	<0.01	<0.07	<0.07	<0.01	<0.01	<0.01	<0.01	<0.07	<0.07
TOTAL	98.57	98.65	98.50	99.98	100.1	100.43	99.18	100.49	100.35	100.04	99.18	99.32	100.30	99.39	100.33
Fe ₂ O ₃	-	-	-	0.08	-	-	0.56	-	-	0.68	0.90	0.34	0.59	-	-
FeO	-	-	-	18.60	-	-	18.54	-	-	18.56	18.45	18.82	19.27	-	-
Cr#	0.75	0.75	0.70	0.90	0.89	0.90	0.94	0.95	0.94	0.95	0.95	0.92	0.95	0.95	0.95
Mg#	41.5	49.2	40.8	46.1	50.3	46.1	44.7	45.5	43.6	44.9	44.5	44.4	42.9	46.4	45.1

Major elements (wt. % oxide).* indicates published data from Jaques (1980) and Jaques & Chappell (1980). K₂O, P₂O₅ <0.01 wt. %. FeO* = Total iron. All Fe determined as FeO: Fe₂O₃ and FeO calculated from stoichiometry. †indicates data calibrated by EDS (Jaques, 1980). Low totals for samples 088 and 090 caused by micro-pitting on surface due to weathering. Cr# = Cr/(Cr+Al) molar. Mg# = 100 x Mg/(Mg + Fe) molar.

Supplementary Table 18: Olivine trace element abundances

Location	Sample	Rock type	Li	Na	Al	P	Ca	Sc	Ti	V	Cr	Co	Ni	Cu	Zn	Ga	Sr	Y	Zr	Nb	
<i>LA-ICP-MS (ppm)</i>																					
MO	087	Dun	-	-	-	-	243	2.1	1.1	0.2	23	129	2910	0.1	37	-	-	-	-	-	
	088	Dun	-	-	-	-	147	2.0	1.5	0.1	16	120	3217	-	31	-	-	-	-	-	
	414	Dun	-	-	-	-	662	4.4	3.1	0.1	9	144	1901	-	35	-	-	-	-	-	
	090	Hrz	-	-	4.8	24.2	122	1.9	0.8	0.5	13	134	2850	0.1	41	0.007	-	-	-	-	
	423	Hrz	-	-	-	-	114	2.5	0.5	0.3	12	136	3120	0.5	48	-	-	-	-	-	
	425	Hrz	-	-	-	-	123	2.4	0.4	0.2	21	132	3038	0.7	46	-	-	-	-	-	
	473	Hrz	-	-	4.7	23.6	106	1.6	0.8	0.4	13	132	3061	0.6	37	-	-	-	-	-	
	489	Hrz	-	-	4.5	24.0	140	2.7	2.1	0.6	16	134	3042	0.3	43	0.012	-	-	0.003	-	
	492	Hrz	-	-	3.3	23.6	121	2.2	0.9	0.6	13	132	3002	0.2	39	-	-	-	-	-	
PUB	714	Hrz	1.3	-	2.2	22.8	124	3.0	0.2	0.5	19	137	3127	0.2	44	0.01090.00250.00060.001	-	-	-	-	
	716	Hrz	1.5	-	1.3	24.2	66	2.7	0.4	0.4	17	133	3060	-	46	0.00890.00890.00060.00430.0016	-	-	-	-	
	720	Hrz	1.4	2.0	1.4	23.3	62	2.8	0.2	0.4	16	130	3114	0.0	44	-	0.0119-	-	-	-	-
	726	Hrz	1.3	-	2.1	23.9	117	2.7	0.1	0.9	47	133	3007	0.1	47	0.00890.0039-	-	-	-	-	-

Bold values analyzed using different conditions from Jaques (2018). All values in ppm.

Supplementary Table 19: Olivine REE abundances

Location	Sample	Rock type	La	Ce	Pr	Nd	Sm	Eu	Gd
<i>LA-ICP-MS (ppm)</i>									
MO	087	Dun	0.00001	0.00004	0.00002	Ce	0.00004	0.00001	0.00038
	088	Dun	0.00054	0.00061	0.00028	0.00004	0.00037	0.00015	-
	090	Hrz	0.00002	0.00001	0.00001	0.00061	0.00004	0.00001	0.00010
	414	Dun	0.00001	-	-	0.00001	0.00004	-	0.00017
	423	Hrz	0.00011	0.00021	0.00001	0.0001	0.00033	-	0.00020
	425	Hrz	-	-	0.00002	-	-	0.00005	0.00037
	473	Hrz	-	0.00003	0.00001	0.00005	0.00004	-	0.00009
PUB	714	Hrz	0.00030	0.00054	0.00006	0.00010	0.00024	0.00001	0.00026
	715	Hrz	0.00278	0.00659	0.00088	0.00094	0.00036	0.00015	0.00056
	716	Hrz	0.00005	0.00032	-	-	0.00025	0.00008	0.00047
	720	Hrz	0.00033	0.00054	0.00008	0.00014	0.00039	0.00003	0.00023
	726	Hrz	0.00008	0.00310	0.00005	-	0.00035	0.00002	0.00016

Supplementary Table 19: Continued

Location	Sample	Rock type	Tb	Dy	Ho	Er	Tm	Yb	Lu
<i>LA-ICP-MS (ppm)</i>									
MO	087	Dun	-	-	0.00003	0.00012	0.00018	0.00194	0.00040
	088	Dun	0.00003	0.00029	0.00009	0.00050	0.00023	0.00235	0.00051
	090	Hrz	-	-	-	-	0.00001	0.00019	0.00020
	414	Dun	-	-	0.00020	0.00013	0.00060	0.00850	0.00214
	423	Hrz	-	-	-	-	0.00001	0.00056	0.00013
	425	Hrz	0.00002	0.00012	-	-	0.00003	0.00050	0.00012
	473	Hrz	0.00001	-	-	0.00008	0.00005	0.00022	0.00019
	714	Hrz	0.00003	-	0.00001	0.00003	-	0.00015	0.00014
	715	Hrz	0.00009	0.00075	0.00020	0.0003	0.00007	0.00091	0.00019
	716	Hrz	-	-	0.00003	-	0.00001	0.00031	0.00012
PUB	720	Hrz	-	-	0.00340	0.00014	0.00003	0.00015	0.00006
	726	Hrz	-	0.00003	-	-	0.00001	0.00023	0.00008

Supplementary Table 20: Orthopyroxene trace element abundances

Location	Sample	Rock type	Li	Na	Al	P	Ca	Sc	Ti	V	Cr	Co	Ni	Cu	Zn	Ga
<i>LA-ICP-MS (ppm)</i>																
MO	489	Hrz	1.0	54	4642	26	6906	18	38	36	2901	54	702	0.4	36	0.9
	492	Hrz	0.7	39	3715	25	5734	14	8	41	2656	53	687	0.6	34	0.5
	473	Hrz	0.7	22	5654	26	5698	16	10	48	3248	53	670	0.6	33	0.6
	090	Hrz	0.6	24	4692	26	4967	17	10	42	2786	52	595	0.2	36	0.6
PUB	714	Hrz	0.9	11	1285	27	1445	10	6	12	1427	56	744	0.2	35	0.2
	716	Hrz	1.3	91	624	25	892	6	8	9	959	53	710		34	0.1
	720	Hrz	2.8	83	534	26	1013	4	8	8	840	53	705	0.3	40	0.1
	726	Hrz	0.6	9	1027	25	1250	8	3	12	1307	55	714	0.2	36	0.2
Location	Sample	Rock type	Sr	Y	Zr	La	Ce	Dy	Er	Yb	Lu					
<i>LA-ICP-MS (ppm)</i>																
MO	MA4	Hrz	0.10	0.10	-	-	-	-		0.0121	0.0250	0.0100				
	489	Hrz	0.06	0.10	0.08	-	-	-		0.0119	0.0144	0.0293	-			
	492	Hrz	0.02	0.02	0.01	-	-	-		0.0020	0.0030	0.0090	-			
	473	Hrz	0.01	0.02	0.01	-	-	-		0.0025	0.0041	0.0116	-			
PUB	090	Hrz	0.01	0.03	0.01	-	-	-		-	0.0035	0.0101	-			
	714	Hrz	-	-	-	-	-	0.0003	-	-	0.0016	-				
	716	Hrz	0.10	-	-	-	-	0.0009	0.0008	-	0.0020	-				
	720	Hrz	0.20	-	-	-	0.0015	0.0044	-	0.0016	-					
	726	Hrz	-	-	-	-	0.0005	0.0002	-	-	0.0017	-				

Appendix 5. Standards and LOD values

Supplementary Table 1: EPMA standard reference materials used at the University of Alberta

Standards for ol, opx, cpx, spl	Element/Line	Crystal	Standards for ol Aluminium method	Element/Line	Crystal
Cr ₂ O ₃ chromium oxide Alfa	Cr ka	PET	Cr ₂ O ₃ chromium oxide Alfa	Cr ka	PET
NaAlSi ₃ O ₈ albite VA 131705	Na ka	TAP	Fo90.5	Mg ka	TAP
KAlSi ₃ O ₈ sanidine Itrongay	K ka	PETH	CaMgSi ₂ O ₆ diopside Wakefield	Ca ka	PETH
Spessartine Little 3 CB1 only	Mn ka	LIFH	Fo90.5	Si ka	TAP
CaMgSi ₂ O ₆ diopside Wakefield	Ca ka	PETH	Fo90.5	Fe ka	LIFH
Enstatite Mg ₂ Si ₂ O ₆	Si ka	TAP	Frank Smith pyrope garnet	Al ka	TAP
Fe ₂ SiO ₄ fayalite Rockport	Fe ka	LIFH	Frank Smith pyrope garnet (Mn,Fe) ₃ Al ₂ Si ₃ O ₁₂ spessartine, Navegadora	Al ka	TAP
TiO ₂ Rutile MTI	Ti ka	PET	Mine	Mn ka	LIFH
Enstatite Mg ₂ Si ₂ O ₆	Mg ka	TAP	Ni nickel Alfa	Ni ka	LIFH
Frank Smith pyrope garnet	Al ka	TAP	Cobalt Co	Co ka	LIFH
Ni nickel Alfa	Ni ka	LIFH	Standards for pl and ilm	Element/Line	Crystal
Ca ₅ (PO ₄) ₃ F apatite, Wilberforce	P ka	PETH	FeTiO ₃ Ilmenite 96189	Ti ka	PET
V vanadium Alfa	V ka	PET	KAISi ₃ O ₈ sanidine Itrongay	K ka	PETH
Standards for sulfides	Element/Line	Crystal	FeTiO ₃ Ilmenite 96189	Fe ka	LIFH
Iron disulfide FeS ₂	S ka	PET	Plagioclase (labradorite) 115900	Al ka	TAP
Fe metal	Fe ka	LLIF	Plagioclase (labradorite) 115900	Ca ka	PETH
Iron disulfide FeS ₂	S ka	PET	K-253 NIST RM glass Ba Mn Zn Si Co Cu	Mn ka	LIFH
Ni nickel Alfa	Ni ka	LLIF			
Cobalt Co	Co ka	LLIF			
Copper Cu	Cu ka	LLIF			
Sphalerite ZnS	Zn ka	LLIF			

Supplementary Table 2: EPMA standard analyses done at the Australian National University

San Carlos olivine USNM 111312/444

(wt%)	This work N = 56	1 SD	Recommended Values ¹	% RD
SiO ₂	40.59	0.49	40.82	-0.6%
FeO	9.50	0.12	9.55	-0.5%
NiO	0.365	0.011	0.37	-1.4%
MnO	0.138	0.01	0.14	-1.4%
MgO	49.18	0.50	49.42	-0.5%
CaO	0.10	0.01		
Total	99.87		100.30	
100Mg/(Mg+Fe)	90.2		90.2	

SD = standard deviation. % RD = percentage deviation from recommended value. Standards used were as follows: Mg (periclase), Si (quartz), K (sanidine), Ca (CaAl₂O₄ synthetic, augite), Ti (TiO₂ synthetic), Cr (Cr₂O₃ synthetic, chromite), Mn (rhododonite), Fe (Fe metal, andradite) and Ni (Ni metal).

Supplementary Table 3: XRF bulk-rock major element analyses for MUH-1, OKUM-1, and BHVO-2 reference materials from supplementary material in Waterton *et al.* (2020)

Date	Sample	SiO ₂	TiO ₂	Al ₂ O ₃	Fe ₂ O ₃ (Total)	MnO	MgO	CaO	Na ₂ O	K ₂ O	P ₂ O ₅	Total	LOI	Sr	Zr	V	Ni	Cr	Co
2014_08	MUH-1-1	43.90	–	1.37	9.97	0.130	42.30	1.42	–	–	–	99.20	10.01	–	–	–	–	–	–
2014_08	MUH-1-2	43.76	–	1.36	10.05	0.130	42.42	1.42	–	–	–	99.23	9.92	–	–	–	–	–	–
2014_12	MUH-1-3	45.16	–	1.44	9.52	0.130	40.90	1.36	–	–	–	98.68	9.71	–	–	–	3045	127	–
2014_12	MUH-1-4	44.44	–	1.41	9.83	0.140	41.37	1.39	–	–	–	98.71	9.75	–	–	–	2932	121	–
2015_05	MUH-1-5	44.06	–	1.47	9.63	0.133	42.42	1.40	–	–	–	99.26	9.84	–	–	–	2896	97	–
2015_05	MUH-1-6	44.58	–	1.47	9.52	0.133	42.04	1.38	–	–	–	99.25	9.81	–	–	–	2915	110	–
2015_05	MUH-1-7	44.32	–	1.47	9.75	0.132	41.99	1.37	–	–	–	99.17	9.99	–	–	–	2879	112	–
2015_05	MUH-1-8	43.93	–	1.47	9.56	0.132	42.50	1.37	–	–	–	99.10	10.05	–	–	–	2971	112	–
2015_05	MUH-1-9	43.99	–	1.48	9.46	0.134	42.32	1.39	–	–	–	98.90	10.16	–	–	–	2933	115	–
2015_05	MUH-1-10	44.13	–	1.49	9.75	0.135	42.08	1.38	–	–	–	99.10	10.04	–	–	–	2930	113	–
2015_07	MUH-1-11	42.99	–	1.47	10.37	0.143	42.43	1.45	–	–	–	99.00	10.33	–	–	–	2943	100	–
2015_07	MUH-1-12	43.58	–	1.48	10.11	0.138	42.02	1.44	–	–	–	98.90	10.34	–	–	–	2981	112	–
2015_07	MUH-1-13	42.97	–	1.51	10.64	0.146	42.12	1.49	–	–	–	99.00	10.13	–	–	–	3004	109	–
2015_07	MUH-1-14	43.85	–	1.49	9.90	0.135	42.36	1.41	–	–	–	99.29	9.93	–	–	–	2958	115	–
2015_08	MUH-1-15	43.21	–	1.42	9.93	0.138	42.85	1.42	–	–	–	99.12	10.17	–	–	–	–	–	–
2016_03	MUH-1-16	43.92	–	1.53	9.81	0.129	42.44	1.36	–	–	–	99.36	9.84	–	–	–	2954	119	–
2016_03	MUH-1-17	44.20	–	1.49	9.91	0.127	42.16	1.34	–	–	–	99.39	9.87	–	–	–	2946	127	–
2016_03	MUH-1-18	43.98	–	1.48	9.85	0.127	42.26	1.34	–	–	–	99.19	9.79	–	–	–	2917	111	–
2016_03	MUH-1-19	43.81	–	1.52	10.04	0.128	41.97	1.40	–	–	–	99.05	9.87	–	–	–	2828	106	–
2016_03	MUH-1-20	44.10	–	1.49	9.67	0.127	42.12	1.35	–	–	–	99.02	9.80	–	–	–	2871	108	–
2017_05	MUH-1-21	43.72	–	1.45	9.74	0.130	42.10	1.37	–	–	–	98.70	10.21	–	–	–	2937	101	–
2017_05	MUH-1-22	43.70	–	1.47	10.03	0.132	41.87	1.39	–	–	–	98.65	10.23	–	–	–	2925	117	–
2017_05	MUH-1-23	43.77	–	1.45	9.81	0.131	42.27	1.38	–	–	–	99.01	10.15	–	–	–	2919	98	–
2017_05	MUH-1-24	43.83	–	1.47	9.72	0.130	41.93	1.39	–	–	–	98.66	10.17	–	–	–	2928	107	–
2017_05	MUH-1-25	43.68	–	1.49	9.89	0.132	42.07	1.39	–	–	–	98.84	10.14	–	–	–	2946	111	–
2017_07	MUH-1-26	43.87	–	1.49	10.04	0.130	42.08	1.40	–	–	–	99.18	10.34	–	–	–	–	–	–
2017_07	MUH-1-27	43.74	–	1.47	9.88	0.130	42.14	1.40	–	–	–	98.90	10.33	–	–	–	–	–	–
2017_12	MUH-1-28	43.75	–	1.53	9.98	0.135	41.96	1.47	–	–	–	99.00	9.93	–	–	–	2981	127	–
2017_12	MUH-1-29	43.50	–	1.47	9.90	0.134	41.83	1.39	–	–	–	98.35	9.93	–	–	–	3027	129	–
2017_12	MUH-1-30	43.46	–	1.50	9.82	0.134	41.91	1.39	–	–	–	98.36	9.79	–	–	–	2997	136	–
2017_12	MUH-1-31	43.67	–	1.49	9.72	0.135	42.07	1.39	–	–	–	98.63	9.92	–	–	–	2947	135	–

2017_12	MUH-1-32	43.87	-	1.50	9.80	0.137	42.20	1.41	-	-	-	99.07	9.92	-	-	-	-	2971	130
2018_03	MUH-1-33	43.95	-	1.52	10.03	0.150	41.97	1.42	-	-	-	99.18	10.07	-	-	-	-	-	-
	Average	43.86	-	1.47	9.87	0.134	42.11	1.40	-	-	-	98.98	10.01	-	-	-	-	2944	115
	SD	0.42	-	0.04	0.24	0.005	0.34	0.03	-	-	-	0.27	0.19	-	-	-	-	47	11

Supplementary Table 3: Continued

Date	Sample	SiO ₂	TiO ₂	Al ₂ O ₃	Fe ₂ O ₃ (Total)	MnO	MgO	CaO	Na ₂ O	K ₂ O	P ₂ O ₅	Total	LOI	Sr	Zr	V	Ni	Cr	Co
2015_05	OKUM-1	44.96	0.39	8.41	12.86	0.186	22.95	8.36	1.21	0.048	0.025	99.40	4.65	—	—	174	—	2340	86
2015_05	OKUM-2	45.79	0.38	8.29	12.52	0.185	22.53	8.27	1.22	0.047	0.025	99.26	4.40	—	—	165	—	2326	79
2015_05	OKUM-3	45.76	0.38	8.32	12.47	0.186	22.66	8.28	1.20	0.045	0.024	99.33	4.67	—	—	164	—	2335	94
2015_05	OKUM-4	46.23	0.38	8.21	12.66	0.182	22.27	8.19	1.17	0.047	0.024	99.36	5.61	—	—	171	—	2300	91
2015_05	OKUM-5	46.19	0.38	8.27	12.33	0.185	22.40	8.27	1.20	0.044	0.024	99.29	5.15	—	—	165	—	2351	76
2015_05	OKUM-6	45.96	0.38	8.32	12.53	0.185	22.35	8.30	1.22	0.047	0.025	99.32	4.60	—	—	171	—	2377	91
2015_05	OKUM-7	46.02	0.38	8.28	12.59	0.183	22.38	8.22	1.21	0.044	0.026	99.33	4.55	—	—	164	—	2319	79
2015_05	OKUM-8	46.14	0.38	8.35	12.46	0.185	22.39	8.31	1.21	0.047	0.024	99.50	4.49	—	—	169	—	2342	72
2015_05	OKUM-9	45.81	0.39	8.37	12.63	0.186	22.58	8.31	1.22	0.043	0.025	99.56	4.51	—	—	155	—	2367	70
2015_05	OKUM-10	45.92	0.39	8.30	12.61	0.185	22.45	8.26	1.20	0.046	0.023	99.38	4.51	—	—	169	—	2328	80
2015_05	OKUM-11	45.84	0.38	8.40	12.64	0.186	22.53	8.31	1.21	0.049	0.022	99.57	4.53	—	—	168	—	2337	87
2015_07	OKUM-12	45.88	0.39	8.42	12.79	0.186	22.40	8.28	1.11	0.025	0.025	99.51	4.72	—	—	165	—	2634	89
2018_04	OKUM-13	45.80	0.38	8.36	12.49	0.189	22.34	8.38	1.16	0.049	0.027	99.18	4.38	—	—	165	—	2575	84
2018_04	OKUM-14	46.14	0.37	8.46	12.45	0.188	22.46	8.43	1.16	0.049	0.027	99.73	4.67	—	—	155	—	2555	96
2018_04	OKUM-15	46.12	0.38	8.43	12.62	0.189	22.40	8.41	1.16	0.053	0.026	99.79	4.74	—	—	171	—	2550	88
2018_04	OKUM-16	46.06	0.37	8.32	12.61	0.188	22.40	8.41	1.18	0.050	0.026	99.61	4.79	—	—	161	—	2545	92
2018_04	OKUM-17	45.92	0.38	8.38	12.45	0.190	22.32	8.43	1.17	0.051	0.027	99.32	4.79	—	—	176	—	2533	91
2018_04	OKUM-18	46.18	0.38	8.40	12.27	0.188	22.48	8.40	1.17	0.053	0.026	99.55	4.72	—	—	171	—	2552	65
2018_04	OKUM-19	45.79	0.37	8.35	12.64	0.189	22.24	8.38	1.18	0.047	0.028	99.21	4.47	—	—	168	—	2527	86
2018_04	OKUM-20	45.87	0.37	8.43	12.58	0.188	22.37	8.36	1.17	0.046	0.028	99.41	4.46	—	—	168	—	2537	85
2018_04	OKUM-21	45.87	0.38	8.38	12.30	0.189	22.29	8.40	1.16	0.048	0.026	99.04	4.73	—	—	167	—	2522	87
2018_04	OKUM-22	46.17	0.37	8.40	12.50	0.188	22.43	8.42	1.18	0.053	0.027	99.74	4.78	—	—	169	—	2550	95
2018_04	OKUM-23	45.86	0.38	8.32	12.58	0.189	22.23	8.39	1.16	0.051	0.028	99.19	4.79	—	—	156	—	2543	69
2018_04	OKUM-24	45.95	0.38	8.39	12.47	0.188	22.37	8.39	1.15	0.051	0.026	99.37	4.77	—	—	176	—	2576	85
2018_04	OKUM-25	45.97	0.37	8.26	12.57	0.187	22.11	8.34	1.16	0.049	0.028	99.04	4.75	—	—	167	—	2533	81
2018_04	OKUM-26	46.15	0.38	8.45	12.41	0.188	22.45	8.38	1.18	0.042	0.027	99.66	4.41	—	—	161	—	2540	87
2018_04	OKUM-27	45.78	0.37	8.36	12.53	0.188	22.25	8.40	1.17	0.047	0.026	99.12	4.41	—	—	161	—	2545	66
2018_04	OKUM-28	46.00	0.38	8.47	12.63	0.187	22.41	8.40	1.16	0.050	0.027	99.71	4.72	—	—	165	—	2567	93
2018_04	OKUM-29	46.11	0.38	8.40	12.63	0.189	22.44	8.42	1.15	0.055	0.026	99.80	4.77	—	—	164	—	2566	100
2018_04	OKUM-30	46.16	0.38	8.45	12.56	0.188	22.37	8.42	1.16	0.047	0.027	99.76	4.75	—	—	170	—	2551	92
2018_04	OKUM-31	46.00	0.38	8.38	12.38	0.190	22.34	8.42	1.16	0.048	0.026	99.32	4.73	—	—	156	—	2538	94
2018_04	OKUM-32	46.05	0.38	8.46	12.56	0.190	22.37	8.43	1.18	0.050	0.027	99.70	4.69	—	—	175	—	2535	90

Average	45.95	0.38	8.37	12.54	0.187	22.41	8.36	1.18	0.048	0.026	99.44	4.68	—	—	166	—	2478	85
SD	0.23	0.01	0.07	0.13	0.002	0.15	0.07	0.03	0.005	0.001	0.22	0.24	—	—	6	—	105	9

Supplementary Table 3: Continued

Date	Sample	SiO ₂	TiO ₂	Al ₂ O ₃	Fe ₂ O ₃ (Total)	MnO	MgO	CaO	Na ₂ O	K ₂ O	P ₂ O ₅	Total	LOI	Sr	Zr	V	Ni	Cr	Co
2017_06	BHVO-2/1	49.94	2.72	13.63	12.43	0.165	7.30	11.47	2.20	0.505	0.265	100.6	2	—	—	—	—	—	—
2017_06	BHVO-2/2	50.02	2.73	13.66	12.45	0.165	7.29	11.48	2.19	0.507	0.267	100.7	6	—	—	—	—	—	—
2017_06	BHVO-2/3	49.97	2.73	13.66	12.41	0.165	7.29	11.49	2.20	0.507	0.267	100.6	8	—	—	—	—	—	—
2017_06	BHVO-2/4	49.94	2.72	13.65	12.42	0.165	7.29	11.49	2.20	0.505	0.266	100.6	5	—	—	—	—	—	—
2017_06	BHVO-2/5	49.83	2.72	13.61	12.40	0.165	7.29	11.47	2.20	0.504	0.267	100.4	6	—	—	—	—	—	—
2017_06	BHVO-2/6	49.95	2.73	13.62	12.43	0.165	7.31	11.51	2.19	0.504	0.266	100.6	7	—	—	—	—	—	—
2017_06	BHVO-2/7	50.00	2.73	13.65	12.42	0.164	7.30	11.49	2.19	0.505	0.266	100.7	2	—	—	—	—	—	—
2017_06	BHVO-2/8	49.92	2.73	13.62	12.42	0.166	7.29	11.49	2.20	0.507	0.268	100.6	1	—	—	—	—	—	—
2017_06	BHVO-2/9	49.97	2.73	13.64	12.43	0.165	7.29	11.49	2.19	0.508	0.268	100.6	8	—	—	—	—	—	—
2017_06	BHVO-2/10	49.95	2.72	13.66	12.43	0.165	7.29	11.48	2.20	0.507	0.266	100.6	6	—	—	—	—	—	—
2018_04	BHVO-2 A	49.43	2.69	13.35	12.47	0.173	7.25	11.41	2.21	0.484	0.278	99.75	-0.51	382	171	330	296	—	—
2018_04	BHVO-2 B	49.74	2.69	13.49	12.28	0.172	7.31	11.43	2.25	0.481	0.282	100.1	3	-0.48	398	172	327	293	—
2018_04	BHVO-2 C	49.53	2.69	13.44	12.41	0.173	7.25	11.42	2.21	0.481	0.280	99.88	-0.55	388	171	325	295	—	
2018_04	BHVO-2 D	49.64	2.69	13.47	12.18	0.173	7.27	11.42	2.25	0.481	0.281	99.86	-0.59	396	172	340	291	—	
2018_04	BHVO-2 E	49.49	2.70	13.42	12.25	0.173	7.24	11.48	2.24	0.482	0.283	99.76	-0.61	386	172	327	295	—	
2018_04	BHVO-2 F	49.44	2.69	13.47	12.42	0.172	7.29	11.40	2.24	0.483	0.280	99.89	-0.54	425	180	322	299	—	
2018_04	BHVO-2 G	49.44	2.69	13.38	12.27	0.172	7.27	11.39	2.23	0.479	0.283	99.60	-0.53	385	173	328	295	—	
2018_04	BHVO-2 H	49.41	2.69	13.37	12.31	0.173	7.23	11.43	2.22	0.484	0.284	99.60	-0.48	386	177	330	312	—	
2018_04	BHVO-2 I	49.67	2.69	13.43	12.27	0.173	7.28	11.42	2.22	0.482	0.283	99.92	-0.52	389	174	327	284	—	
2018_04	BHVO-2 J	49.27	2.68	13.33	12.08	0.173	7.20	11.38	2.20	0.477	0.281	99.07	-0.54	391	172	324	296	—	
2018_04	BHVO-2 K	49.44	2.69	13.43	12.36	0.171	7.25	11.40	2.24	0.481	0.280	99.74	-0.57	389	173	320	305	—	

2018_04	BHVO-2 L	49.51	2.69	13.40	12.10	0.173	7.24	11.44	2.23	0.479	0.283	99.55	-0.47	385	177	337	298	-
												100.1						-
2018_04	BHVO-2 M	49.72	2.70	13.50	12.32	0.172	7.32	11.44	2.25	0.482	0.279	8	-0.45	394	174	325	302	
2018_04	BHVO-2 N	49.48	2.69	13.47	12.32	0.172	7.26	11.46	2.23	0.484	0.277	99.84	-0.43	397	176	341	298	-
2018_04	BHVO-2 O	49.23	2.68	13.33	12.21	0.172	7.24	11.36	2.23	0.481	0.283	99.22	-0.38	400	174	324	290	-
2018_04	BHVO-2 P	49.59	2.69	13.51	12.04	0.174	7.29	11.45	2.23	0.482	0.285	99.74	-0.44	406	178	337	294	-
2018_04	BHVO-2 Q	49.29	2.69	13.39	12.39	0.171	7.24	11.42	2.21	0.482	0.281	99.56	-0.45	389	171	344	297	-
												100.2						-
2018_04	BHVO-2 R	49.71	2.69	13.45	12.51	0.172	7.26	11.41	2.24	0.483	0.274	0	-0.50	380	173	329	292	
2018_04	BHVO-2 S	49.17	2.69	13.41	12.48	0.172	7.21	11.39	2.22	0.481	0.278	99.50	-0.51	381	170	336	292	-
												100.1						-
2018_04	BHVO-2 T	49.66	2.69	13.46	12.42	0.172	7.28	11.42	2.23	0.483	0.282	0	-0.65	387	175	329	305	-
												100.0						-
Average		49.65	2.70	13.50	12.34	0.170	7.27	11.44	2.22	0.490	0.276	5	-0.51	392	174	330	296	
SD		0.26	0.02	0.11	0.12	0.004	0.03	0.04	0.02	0.012	0.007	0.49	0.07	10	3	7	6	-

Major element oxide data expressed as wt. %, trace element data as ppm.

Supplementary Table 4: Trace element solution ICP-MS standards vs. reference values

DATE:	Aug-19	Jun-20	Jun-20				
SAMPLE:	MUH-1	MUH-1	MUH-1	MUH-1			
LAB:	UofA	UofA	UofA				
INSTRUMENT	Element XR	Element XR	Element XR	Reference value	UofA	relative	
All data in PPM		Run1	Run2		Average	STD DEV %	Accuracy %
Rb85(LR)	0.271	0.239	0.253	0.270	0.254	6.360	5.891
Sr88(LR)	9.630	10.043	8.899	8.500	9.524	6.080	-12.046
Y89(LR)	1.053	0.970	0.960	0.970	0.994	5.122	-2.509
Nb93(LR)	0.057	0.056	0.048	0.062	0.054	9.668	13.683
Mo98(LR)	1.038	0.791	0.769		0.866	17.245	
Cs133(LR)	0.106	0.100	0.096	0.099	0.100	5.394	-1.485
Ba138(LR)	5.246	7.191	4.836	4.980	5.758	21.851	-15.617
La139(LR)	0.215	0.146	0.130	0.134	0.163	27.592	-21.983
Ce140(LR)	0.301	0.219	0.207	0.200	0.242	21.253	-21.194
Pr141(LR)	0.042	0.037	0.035	0.035	0.038	9.610	-8.177
Nd143(LR)	0.198	0.189	0.183	0.177	0.190	3.981	-7.399
Sm147(LR)	0.068	0.071	0.067	0.068	0.069	3.088	-1.254
Eu151(LR)	0.029	0.026	0.027	0.026	0.027	5.109	-3.777
Gd157(LR)	0.114	0.097	0.098	0.110	0.103	9.254	6.481
Tb159(LR)	0.023	0.022	0.020	0.021	0.022	6.654	-2.120
Dy163(LR)	0.169	0.161	0.154	0.153	0.162	4.595	-5.645
Ho165(LR)	0.038	0.037	0.036	0.036	0.037	2.431	-3.302
Er167(LR)	0.118	0.117	0.107	0.108	0.114	5.445	-5.216
Yb173(LR)	0.124	0.123	0.112	0.118	0.120	5.451	-1.280
Lu175(LR)	0.020	0.020	0.020	0.019	0.020	2.032	-5.670
Hf178(LR)	0.030	0.034	0.025	0.044	0.030	14.093	32.239
Ta181(LR)	0.003	0.003	0.003		0.003	9.069	
Pb208(LR)	0.399	0.369	0.355	0.420	0.375	5.996	10.773
Th232(LR)	0.014	0.018	0.014	0.018	0.015	13.362	15.129
U238(LR)	0.012	0.015	0.013	0.014	0.013	9.111	5.663

Supplementary Table 4: Continued

DATE:	Aug-19	Aug-19				
SAMPLE:	BHVO-2	BHVO-2	BHVO-2			
LAB:	UofA					
INSTRUMENT	Element XR	Element XR	Reference value	UofA Average	relative STD DEV %	Accuracy %
All data in PPM						
Rb85(LR)	11.320	9.854	9.261	10.587	1.037	-14.319
Sr88(LR)	500.162	435.759	394.100	467.961	45.540	-18.742
Y89(LR)	30.976	27.369	25.910	29.173	2.550	-12.593
Nb93(LR)	21.136	18.680	18.100	19.908	1.736	-9.989
Mo98(LR)	3.508	3.121	4.070	3.314	0.274	18.570
Cs133(LR)	0.110	0.100	0.100	0.105	0.007	-5.451
Ba138(LR)	146.424	134.977	130.900	140.700	8.094	-7.487
La139(LR)	16.778	15.524	15.200	16.151	0.886	-6.257
Ce140(LR)	41.069	38.103	37.530	39.586	2.097	-5.478
Pr141(LR)	5.787	5.348	5.339	5.567	0.311	-4.277
Nd143(LR)	26.967	24.956	24.270	25.962	1.422	-6.970
Sm147(LR)	6.562	6.099	6.023	6.331	0.328	-5.106
Eu151(LR)	2.328	2.066	2.043	2.197	0.185	-7.520
Gd157(LR)	7.177	6.466	6.207	6.821	0.503	-9.898
Tb159(LR)	1.085	0.977	0.939	1.031	0.076	-9.796
Dy163(LR)	5.992	5.505	5.280	5.748	0.344	-8.868
Ho165(LR)	1.112	1.017	0.989	1.064	0.067	-7.658
Er167(LR)	2.889	2.648	2.511	2.768	0.170	-10.241
Yb173(LR)	2.202	2.050	1.994	2.126	0.108	-6.611
Lu175(LR)	0.308	0.287	0.275	0.298	0.015	-8.057
Hf178(LR)	4.913	4.581	4.470	4.747	0.235	-6.200
Ta181(LR)	1.185	1.103	1.154	1.144	0.058	0.889
Pb208(LR)	1.709	1.585	1.653	1.647	0.088	0.361
Th232(LR)	1.252	1.193	1.224	1.222	0.042	0.128
U238(LR)	0.425	0.412	0.412	0.418	0.010	-1.558

Supplementary Table 4: Continued

DATE:	Aug-19	Aug-19					Aug-19	
SAMPLE:	BIR-1	BIR-1	BIR-1				OKUM724b	OKUM724b
LAB:	UofA						UofA	
INSTRUMENT	Element XR	Element XR	Reference value	UofA	relative STD DEV	Element XR	Reference value	
All data in PPM			MAX	Average	%	Accuracy %		
Rb85(LR)	0.246	0.235	0.210	0.241	0.008	-14.545	1.052	0.960
Sr88(LR)	138.763	131.248	108.600	135.006	5.313	-24.314	18.793	16.100
Y89(LR)	18.864	17.957	15.600	18.411	0.641	-18.017	10.520	9.080
Nb93(LR)	0.636	0.612	0.553	0.624	0.017	-12.848	0.403	0.370
Mo98(LR)	0.166	0.149	0.068	0.157	0.012	-131.482	0.450	
Cs133(LR)	0.005	0.006	0.006	0.005	0.000	15.108	0.198	0.184
Ba138(LR)	7.418	7.266	6.750	7.342	0.108	-8.772	6.412	6.200
La139(LR)	0.684	0.673	0.627	0.679	0.008	-8.258	0.432	0.412
Ce140(LR)	2.132	2.125	1.920	2.128	0.005	-10.855	1.358	1.270
Pr141(LR)	0.417	0.410	0.372	0.413	0.004	-11.059	0.252	0.235
Nd143(LR)	2.672	2.664	2.397	2.668	0.005	-11.310	1.588	1.494
Sm147(LR)	1.202	1.209	1.113	1.205	0.005	-8.310	0.738	0.715
Eu151(LR)	0.596	0.574	0.520	0.585	0.016	-12.506	0.328	0.300
Gd157(LR)	2.052	1.981	1.809	2.017	0.050	-11.478	1.242	1.170
Tb159(LR)	0.417	0.402	0.362	0.409	0.011	-13.009	0.251	0.229
Dy163(LR)	2.972	2.887	2.544	2.930	0.060	-15.158	1.738	1.610
Ho165(LR)	0.662	0.649	0.572	0.656	0.010	-14.648	0.384	0.355
Er167(LR)	1.995	1.936	1.680	1.966	0.042	-16.995	1.150	1.041
Yb173(LR)	1.853	1.816	1.631	1.834	0.026	-12.472	1.073	1.009
Lu175(LR)	0.285	0.280	0.248	0.282	0.004	-13.721	0.161	0.148
Hf178(LR)	0.667	0.665	0.582	0.666	0.001	-14.328	0.575	0.551
Ta181(LR)	0.040	0.040	0.041	0.040	0.000	3.086	0.023	0.026
Pb208(LR)	2.997	2.969	3.037	2.983	0.020	1.770	0.212	0.260
Th232(LR)	0.031	0.031	0.033	0.031	0.000	5.333	0.029	0.031
U238(LR)	0.011	0.011	0.011	0.011	0.000	-1.383	0.011	0.012

Supplementary Table 5. Limit of detection (LOD) values measured via LA-ICP-MS at the University of Alberta on ol, opx, cpx, and spl from Koro and PNG peridotites

Ol	La139	Ce140	Pr141	Nd146	Sm147	Eu153	Gd157							
Ave	0.00006	0.00007	0.00005	0.00036	0.00027	0.00007	0.00035							
SD	0.00005	0.00009	0.00004	0.00027	0.00019	0.00005	0.00019							
Min	0.000011	0.000005	0.000001	0.000075	0.000052	0.000003	0.000091							
Max	0.00058	0.00100	0.00027	0.00190	0.00160	0.00047	0.00120							
Ol	Tb159	Dy163	Ho165	Er166	Tm169	Yb172	Lu175							
Ave	0.00004	0.00026	0.00004	0.00010	0.00006	0.00020	0.00006							
SD	0.00003	0.00012	0.00006	0.00014	0.00007	0.00024	0.00015							
Min	0.000008	0.000038	0.000007	0.000027	0.000010	0.000031	0.000011							
Max	0.00018	0.00072	0.00046	0.00160	0.00064	0.00230	0.00200							
Ol	Al27	Ca44	Sc45	Ti49	V51	Cr52	Mn55	Co59	Ni60					
Ave	0.04	2.4	0.01	0.02	0.00	0.04	0.05	0.01	0.05					
SD	0.05	1.2	0.003	0.01	0.01	0.02	0.09	0.05	0.16					
Min	0.002	0.16	0.000 4	0.001	0.000 2	0.02	0.002	0.000 3	0.002					
Max	0.38	7.1	0.04	0.04	0.18	0.09	1.30	0.90	1.70					
Opx	Sc45	Ti49	V51	Co59	Ni60	Cu63	Zn66	Ga69	Y89	Zr90	Nb93			
Ave	0.1	0.6	0.04	0.1	0.7	0.6	0.4	0.1	0.01	0.01	0.01			
SD	0.1	0.7	0.1	0.1	0.9	1.0	0.4	0.1	0.01	0.01	0.01			
Min	0.001	0.003	0.000 3	0.001	0.002	0.01	0.01	0.002	0.000 4	0.001 1	0.000			
Max	1.0	3.6	0.3	0.4	5.1	5.9	2.3	0.4	0.1	0.1	0.04			
Opx	La139	Ce140	Pr141	Nd146	Sm147	Eu153	Gd157	Tb159	Dy163	Ho165	Tm169	Yb172	Lu175	
Ave	0.002	0.002	0.001	0.02	0.004	0.004	0.020	0.001	0.008	0.003	0.004	0.003	0.008	0.001
SD	0.003	0.003	0.004	0.1	0.005	0.01	0.04	0.002	0.02	0.007	0.008	0.007	0.02	0.001
Min	0.000	0.000	0.000	0.000	0.000	0.000	0.001	0.000	0.000	0.000	0.000	0.000	0.000	0.000
Max	0.01	0.03	0.02	4	3	02	1	1	1	1	1	2	1	
Max	0.02	0.01	0.03	0.3	0.02	0.1	0.2	0.01	0.2	0.03	0.04	0.04	0.1	0.006
Cpx	Sc45	Ti49	V51	Mn55	Co59	Ni60	Cu63	Zn66	Ga69	Sr88	Y89	Zr90	Nb93	
Ave	0.1	0.4	0.03	0.1	0.1	0.3	0.4	0.3	0.1	0.02	0.01	0.01	0.004	
SD	0.1	0.3	0.03	0.1	0.1	0.3	0.4	0.2	0.03	0.01	0.01	0.01	0.003	
Min	0.001	0.002	0.000 1	0.003	0.000 2	0.003	0.000 5	0.001	0.000	0.000	0.000	0.000	0.000	0.01

Max	0.2	1.0	0.1	0.9	0.3	1.5	1.4	0.7	0.1	0.04	0.03	0.04	0.01	
Cpx	La139	Ce140	Pr141	Nd146	Sm147	Eu153	Gd157	Tb159	Dy163	Ho165	Er166	Tm169	Yb172	Lu175
Ave	0.02	0.01	0.004	0.05	0.01	0.01	0.1	0.01	0.01	0.001	0.02	0.002	0.1	0.02
SD	0.1	0.05	0.03	0.3	0.01	0.01	0.3	0.1	0.02	0.003	0.1	0.01	0.4	0.1
Min	0.000	0.000	0.000	0.000	0.000	0.000	0.000	0.000	0.000	0.000	0.000	0.000	0.000	0.000
Max	0.004	0.003	0.003	0.02	0.02	0.01	0.04	0.01	0.02	0.004	0.02	0.004	0.02	0.01
Max	0.8	0.3	0.3	2.0	0.1	0.05	2.4	0.6	0.2	0.02	0.5	0.0	2.7	0.4
Spl	Sc45	Ti49	V51	Co59	Ni60	Cu63	Zn66							
Ave	0.3	1.9	0.2	0.3	1.3	0.9	1.2							
SD	0.1	0.8	0.3	0.3	0.7	1.0	0.7							
Min	0.05	0.3	0.02	0.02	0.2	0.1	0.3							
Max	0.8	5.2	2.0	3.4	6.7	4.9	5.5							

All reported LA-ICP-MS values in Appendix 2 & 3 are above detection. Values are in ppm.

Supplementary Table 6. Limit of detection (LOD) values measured via LA-ICP-MS at the Australian National University on olivine and orthopyroxene from PNG peridotites

ol	Li7	Na23	Al27	P31	Ca43	Sc45	Ti49	V51	Cr52	Mn55	Co59	Ni60	Cu63	Zn66
Ave	0.1	0.4	0.07	0.7	16.9	0.01	0.1	0.007	0.1	0.1	0.05	0.1	0.05	0.06
SD	0.04	0.3	0.05	0.2	3.2	0.004	0.05	0.002	0.1	0.04	0.2	0.2	0.1	0.03
Min	0.03	0.1	0.03	0.4	10.8	0.007	0.01	0.003	0.05	0.02	0.001	0.03	0.004	0.02
Max	0.2	2.4	0.3	1.0	28.0	0.03	0.3	0.01	0.9	0.2	1.0	0.9	0.7	0.2
ol	Ga71	Sr88	Y89	Zr90	Nb93	La139	Ce140	Nd14 6	Sm14 7	Gd157	Dy163	Er166	Yb172	
Ave	0.007	0.001	0.001	0.002	0.001	0.000 4	0.000 5	0.002	0.002	0.002	0.001	0.001	0.001	
SD	0.004	0.001	0.000 5	0.001	0.000 3	0.000 3	0.000 4	0.001	0.002	0.001	0.001	0.000 4	0.001	
Min	0.000 2	0.000 2	0.000 3	0.000 2	0.000 3	0.000 1	0.000 1	0.001	0.001	0.000 5	0.000 4	0.000 3	0.000 5	
Max	0.02	0.005	0.003	0.005	0.001	0.002	0.002	0.009	0.01	0.006	0.003	0.002	0.003	
opx	Li7	Na23	Al27	P31	Ca43	Sc45	Ti49	V51	Cr52	Mn55	Co59	Ni60	Cu63	Zn66
Ave	0.1	0.4	0.07	0.7	17.4	0.01	0.7	0.007	0.09	0.1	0.05	0.1	0.03	0.07
SD	0.02	0.2	0.03	0.1	4.5	0.006	4.9	0.002	0.03	0.04	0.1	0.03	0.03	0.09
Min	0.09	0.2	0.03	0.4	10.0	0.008	0.04	0.003	0.04	0.06	0.003	0.04	0.01	0.01
Max	0.2	1.3	0.2	1.1	31.7	0.04	41.1	0.01	0.2	0.2	0.5	0.2	0.2	0.5
opx	Ga71	Sr88	Y89	Zr90	Nb93	La139	Ce140	Nd14 6	Sm14 7	Gd157	Dy163	Er166	Yb172	
Ave	0.009	0.001	0.001	0.002	0.001	0.001	0.001	0.002	0.002	0.002	0.001	0.001	0.001	
SD	0.004	0.001	0.000 3	0.001	0.001	0.001	0.003	0.001	0.001	0.001	0.001	0.001	0.001	

			0.000		0.000	0.000	0.000			0.000	0.000	0.000
Min	0.003	0.001	4	0.001	4	1	1	0.001	0.001	0.001	4	3
Max	0.03	0.006	0.002	0.005	0.004	0.006	0.02	0.007	0.007	0.005	0.005	0.008

All reported LA-ICP-MS values in Appendix 2 & 3 are above detection. Values are in ppm.

Supplementary Table 7: LA-CP-MS standard values per analytical session

SC-GB Element:		Al27	Int2SE LOD	Ti47	Int2SE LOD	Ca43	Int2SE LOD	Ni60	Int2SE LOD	V51	Int2SE LOD
Reference:		88.0		3.5		528		2986		3.7	
n=3	Ave	94.1	0.6	0.04	3.8	0.2	0.22	559	14.3	4.33	3068
n=3	Ave	91.8	0.7	0.04	4.0	0.1	0.16	497	8.8	3.43	3068
n=3	Ave	91.8	0.7	0.04	4.0	0.1	0.16	497	8.8	3.43	3068
n=3	Ave	93.8	1.3	0.03	3.7	0.1	0.17	513	14.0	3.70	3089
n=3	Ave	91.8	0.7	0.04	4.0	0.1	0.16	497	8.8	3.43	3068
n=3	Ave	91.8	0.7	0.04	4.0	0.1	0.16	497	8.8	3.43	3068
	SD	1.11			0.11			24.82			8.73
SC-GB Element:		Cr53	Int2SE LOD	Co59	Int2SE LOD	Cu63	Int2SE LOD	Mn55	Int2SE LOD		
Reference:		166.0		139.0		1.0		1042.0			
n=3	Ave	158	0.6	0.073	150.4	0.5	0.004	1.0	0.0	0.005	1002.6
n=3	Ave	160	0.6	0.056	150.0	0.5	0.004	1.0	0.0	0.004	998.0
n=3	Ave	160	0.6	0.056	150.0	0.5	0.004	1.0	0.0	0.004	998.0
n=3	Ave	156	0.7	0.058	150.2	0.5	0.004	0.9	0.0	0.004	1001.1
n=3	Ave	160	0.6	0.056	150.0	0.5	0.004	1.0	0.0	0.004	998.0
n=3	Ave	160	0.6	0.056	150.0	0.5	0.004	1.0	0.0	0.004	998.0
	SD	1.98			0.16			0.03			2.03

Supplementary Table 7: Continued

SC-GB	Element:	La139	Int2SE	LOD	Ce140	Int2SE	LOD	Pr141	Int2SE	LOD
n=3	Ave	0.00028	0.00018	0.00012	0.00041	0.00014	0.00008	0.00007	0.00007	0.00012
n=3	Ave	0.00018	0.00008	0.00009	0.00041	0.00011	0.00008	0.00018	0.00007	0.00007
n=3	Ave	0.00018	0.00008	0.00009	0.00041	0.00011	0.00008	0.00018	0.00007	0.00007
n=3	Ave	0.00021	0.00008	0.00004	0.00033	0.00012	0.00005	0.00012	0.00006	0.00005
n=3	Ave	0.00018	0.00008	0.00009	0.00041	0.00011	0.00008	0.00018	0.00007	0.00007
n=3	Ave	0.00018	0.00008	0.00009	0.00041	0.00011	0.00008	0.00018	0.00007	0.00007
n=9	Ave	0.00034	0.00013	0.00004	0.00308	0.00167	0.00010	0.00053	0.00025	0.00011
n=3	Ave	0.00023	0.00008	0.00023	0.00121	0.00060	0.02251	0.00037	0.00014	0.00022
	SD		0.00006		0.00095			0.00015		
SC-GB	Element:	Nd146	Int2SE	LOD	Sm147	Int2SE	LOD			
n=3	Ave	0.00102	0.00066	0.00171	0.00089	0.00056	0.00092			
n=3	Ave	0.00189	0.00079	0.00041	0.00129	0.00049	0.00022			
n=3	Ave	0.00189	0.00079	0.00041	0.00129	0.00049	0.00022			
n=3	Ave	0.00134	0.00059	0.00032	0.00072	0.00035	0.00029			
n=3	Ave	0.00189	0.00079	0.00041	0.00129	0.00049	0.00022			
n=3	Ave	0.00189	0.00079	0.00041	0.00129	0.00049	0.00022			
n=9	Ave	0.00076	0.00036	0.00019	0.00058	0.00030	0.00045			
n=3	Ave	0.00045	0.00024	0.00032	0.00042	0.00024	0.00042			
	SD		0.00059		0.00037					
SC-GB	Element:	Eu153	Int2SE	LOD	Gd157	Int2SE	LOD	Tb159	Int2SE	LOD
n=3	Ave	0.00034	0.00016	0.00012	0.00137	0.00063	0.00066	0.00028	0.00012	0.00006
n=3	Ave	0.00029	0.00013	0.00010	0.00139	0.00059	0.00053	0.00033	0.00010	0.00003
n=3	Ave	0.00029	0.00013	0.00010	0.00139	0.00059	0.00053	0.00033	0.00010	0.00003
n=3	Ave	0.00031	0.00014	0.00008	0.00140	0.00054	0.00025	0.00031	0.00011	0.00003
n=3	Ave	0.00029	0.00013	0.00010	0.00139	0.00059	0.00053	0.00033	0.00010	0.00003
n=3	Ave	0.00029	0.00013	0.00010	0.00139	0.00059	0.00053	0.00033	0.00010	0.00003
n=9	Ave	0.00033	0.00016	0.00084	0.00090	0.00036	0.00029	0.00032	0.00010	0.00011
n=3	Ave	0.00028	0.00014	0.00033	0.00081	0.00032	0.00045	0.00032	0.00009	0.00007
	SD		0.00002		0.00025			0.00002		

Supplementary Table 7: Continued

SC-GB	Element:	Dy163	Int2SE	LOD	Ho165	Int2SE	LOD
n=3	Ave	0.00284	0.00073	0.00039	0.00123	0.00025	0.00006
n=3	Ave	0.00333	0.00073	0.00029	0.00106	0.00020	0.00005
n=3	Ave	0.00333	0.00073	0.00029	0.00106	0.00020	0.00005
n=3	Ave	0.00357	0.00077	0.00020	0.00110	0.00021	0.00002
n=3	Ave	0.00333	0.00073	0.00029	0.00106	0.00020	0.00005
n=3	Ave	0.00333	0.00073	0.00029	0.00106	0.00020	0.00005
n=9	Ave	0.00327	0.00053	0.00212	0.00108	0.00016	0.00021
n=3	Ave	0.00294	0.00053	0.00034	0.00103	0.00014	0.00007
	SD	0.00024			0.00006		
SC-GB	Element:	Er166	Int2SE	LOD	Tm169	Int2SE	LOD
n=3	Ave	0.00628	0.00099	0.00015	0.00150	0.00025	0.00007
n=3	Ave	0.00573	0.00076	0.00008	0.00137	0.00023	0.00006
n=3	Ave	0.00573	0.00076	0.00008	0.00137	0.00023	0.00006
n=3	Ave	0.00562	0.00081	0.00007	0.00138	0.00026	0.00004
n=3	Ave	0.00573	0.00076	0.00008	0.00137	0.00023	0.00006
n=3	Ave	0.00573	0.00076	0.00008	0.00137	0.00023	0.00006
n=9	Ave	0.00570	0.00063	0.00022	0.00144	0.00018	0.00006
n=3	Ave	0.00542	0.00063	0.00013	0.00140	0.00017	0.00007
	SD	0.00024			0.00005		
SC-GB	Element:	Yb172	Int2SE	LOD	Lu175	Int2SE	LOD
n=3	Ave	0.01477	0.00180	0.00020	0.00390	0.00046	0.0000
n=3	Ave	0.01463	0.00157	0.00013	0.00401	0.00041	0.00004
n=3	Ave	0.01463	0.00157	0.00013	0.00401	0.00041	0.00004
n=3	Ave	0.01357	0.00170	0.00021	0.00399	0.00040	0.00004
n=3	Ave	0.01463	0.00157	0.00013	0.00401	0.00041	0.00004
n=3	Ave	0.01463	0.00157	0.00013	0.00401	0.00041	0.00004
n=9	Ave	0.01485	0.00115	0.00015	0.00370	0.00032	0.00008
n=3	Ave	0.01527	0.00120	0.00023	0.00344	0.00029	0.00007
	SD	0.00048			0.00021		

Supplementary Table 7: Continued

NIST612 Element:		Sc45	Int2SE LOD		Ti49	Int2SE LOD		V51	Int2SE LOD		Co59	Int2SE LOD		Cu63	Int2SE LOD	
	Reference:	39.9			44.0			38.8			35.5			37.8		
Ave	n=5	39.9	0.4	0.02	44.0	0.6	0.05	38.9	1.6	0.01	35.7	1.3	0.003	37.9	1.5	0.008
Ave	n=5	39.9	0.7	0.05	43.9	0.7	0.12	38.8	0.5	0.01	35.5	0.4	0.013	37.8	0.4	0.041
Ave	n=5	39.9	0.3	0.01	44.0	0.6	0.02	39.1	1.8	0.00	35.6	1.5	0.003	38.2	1.8	0.007
Ave	n=4	39.9	0.7	0.09	43.5	1.9	0.61	38.9	0.6	0.04	35.5	0.6	0.087	37.8	1.0	0.845
Ave	n=4	39.9	0.7	0.09	44.0	1.8	0.67	38.8	0.5	0.04	35.5	0.6	0.093	37.8	0.8	0.150
Ave	n=3	39.9	0.7	0.09	44.0	1.8	0.82	38.8	0.5	0.05	35.5	0.5	0.084	37.8	0.9	1.233
Ave	n=4	39.9	0.7	0.08	44.2	2.3	0.52	38.8	0.5	0.05	35.5	0.6	0.072	37.8	0.9	1.068
Ave	n=3	39.9	0.6	0.09	44.0	1.6	0.92	38.8	0.4	0.06	35.5	0.4	0.127	37.8	0.7	0.233
Ave	n=4	39.9	0.6	0.15	44.1	1.4	0.59	38.8	0.4	0.04	35.5	0.5	0.097	37.8	0.6	0.165
Ave	n=4	39.9	0.7	0.09	44.2	1.7	0.98	38.8	0.5	0.06	35.5	0.5	0.147	37.9	0.8	1.003
Ave	n=4	39.9	0.6	0.12	44.0	1.4	0.82	38.8	0.4	0.04	35.5	0.4	0.096	37.8	0.6	0.190
Ave	n=4	39.9	0.7	0.07	44.1	1.8	0.59	38.8	0.5	0.04	35.5	0.5	0.078	37.9	0.8	1.195
	SD		0.02			0.18			0.08			0.06			0.11	
NIST612 Element:		Ga69	Int2SE LOD		Y89	Int2SE LOD		Zr90	Int2SE LOD		Nb93	Int2SE LOD				
	Reference:	36.9			38.3			37.9			38.9					
Ave	n=5	36.9	1.2	0.002	38.3	0.5	0.002	37.9	0.5	0.003	38.9	0.5	0.002			
Ave	n=5	36.9	0.4	0.007	38.3	0.7	0.002	37.9	0.7	0.006	38.9	0.4	0.002			
Ave	n=5	37.1	1.5	0.002	38.3	0.4	0.002	37.9	0.4	0.002	39.0	0.5	0.002			
Ave	n=4	36.9	0.7	0.043	38.3	0.7	0.008	37.9	0.7	0.012	38.9	0.5	0.005			
Ave	n=4	37.0	0.7	0.060	38.4	0.7	0.004	37.9	0.7	0.014	38.9	0.5	0.004			
Ave	n=3	36.9	0.8	0.043	38.3	0.7	0.007	37.9	0.8	0.014	38.9	0.5	0.004			
Ave	n=4	36.9	0.8	0.067	38.3	0.7	0.010	37.9	0.7	0.012	38.9	0.5	0.006			
Ave	n=3	36.9	0.8	0.090	38.3	0.6	0.006	37.9	0.6	0.011	38.9	0.5	0.005			
Ave	n=4	36.9	0.8	0.053	38.3	0.6	0.006	37.9	0.7	0.014	38.9	0.4	0.004			
Ave	n=4	36.9	0.7	0.059	38.4	0.6	0.017	38.0	0.7	0.015	38.9	0.4	0.006			
Ave	n=4	36.9	0.7	0.057	38.3	0.6	0.005	37.9	0.7	0.012	38.9	0.4	0.005			
Ave	n=4	36.9	0.7	0.053	38.3	0.7	0.019	37.9	0.7	0.014	38.9	0.5	0.004			
	SD		0.07			0.03			0.03			0.02				

Supplementary Table 7: Continued

NIST612	Element: Reference:	La139 36.0	Int2SE 0.4	LOD 38.4	Ce140 38.4	Int2SE 0.8	LOD 37.9	Pr141 37.9	Int2SE 0.4	LOD 35.5	Nd146 35.5	Int2SE 0.5	LOD 0.00166
Ave	n=5	36.0	0.4	0.00151	38.4	0.8	0.00115	37.9	0.4	0.00116	35.5	0.5	0.00166
Ave	n=5	36.0	0.4	0.00070	38.4	0.4	0.00094	37.9	0.3	0.00096	35.5	0.5	0.00360
Ave	n=5	36.0	0.4	0.00146	38.4	0.9	0.00137	37.9	0.5	0.00112	35.5	0.4	0.00108
Ave	n=7	36.0	0.5	0.00002	38.4	0.2	0.00002	37.9	0.4	0.00002	35.5	0.5	0.00013
Ave	n=5	36.0	0.3	0.00009	38.4	0.3	0.00009	37.9	0.3	0.00008	35.5	0.3	0.00051
Ave	n=6	36.0	0.2	0.00012	38.4	0.2	0.00010	37.9	0.2	0.00008	35.5	0.3	0.00039
Ave	n=6	36.0	0.2	0.00012	38.4	0.2	0.00010	37.9	0.2	0.00008	35.5	0.3	0.00039
Ave	n=6	36.0	0.3	0.00007	38.4	0.3	0.00011	37.9	0.2	0.00015	35.5	0.3	0.00074
Ave	n=7	36.0	0.5	0.00002	38.4	0.2	0.00002	37.9	0.4	0.00002	35.5	0.5	0.00013
Ave	n=6	36.0	0.2	0.00012	38.4	0.2	0.00010	37.9	0.2	0.00008	35.5	0.3	0.00039
Ave	n=6	36.0	0.2	0.00012	38.4	0.2	0.00010	37.9	0.2	0.00008	35.5	0.3	0.00039
Ave	n=5	36.0	0.2	0.00029	38.4	0.2	0.00039	37.9	0.3	0.00024	35.5	0.3	0.00340
Ave	n=2	36.0	0.4	0.00004	38.4	0.4	0.00003	37.9	0.4	0.00003	35.5	0.4	0.00025
Ave	n=9	35.9	0.4	0.00004	38.3	0.5	0.00004	37.8	0.5	0.00019	35.4	0.5	0.00025
Ave	n=3	36.0	0.3	0.00003	38.4	0.3	0.00008	37.9	0.3	0.00023	35.5	0.3	0.00023
Ave	n=4	36.0	0.1	0.00016	38.4	0.1	0.00020	37.9	0.1	0.00013	35.5	0.2	0.00097
Ave	n=4	36.9	1.3	0.00016	39.4	1.4	0.00020	38.9	1.4	0.00013	36.4	1.3	0.00101
Ave	n=5	36.0	0.1	0.00014	38.4	0.1	0.00015	37.9	0.2	0.00012	35.5	0.2	0.00180
Ave	n=5	36.1	0.8	0.00014	38.5	0.8	0.00015	38.0	0.8	0.00012	35.6	0.8	0.00180
	SD	0.21		0.23			0.23			0.20			
NIST612	Element: Reference:	Sm147 37.7	Int2SE 0.5	LOD 35.6	Eu153 35.6	Int2SE 0.4	LOD 37.3	Gd157 37.3	Int2SE 0.5	LOD 0.00182			
Ave	n=5	37.7	0.5	0.00186	35.6	0.4	0.00131	37.3	0.5	0.00182			
Ave	n=5	37.7	0.5	0.00308	35.6	0.3	0.00063	37.3	0.6	0.00465			
Ave	n=5	37.7	0.4	0.00249	35.6	0.4	0.00151	37.3	0.5	0.00260			
Ave	n=7	37.7	0.9	0.00011	35.6	0.5	0.00003	37.3	1.0	0.00016			
Ave	n=5	37.7	0.3	0.00058	35.6	0.4	0.00015	37.3	0.4	0.00077			
Ave	n=6	37.7	0.3	0.00033	35.6	0.3	0.00009	37.3	0.4	0.00051			
Ave	n=6	37.7	0.3	0.00033	35.6	0.3	0.00009	37.3	0.4	0.00051			
Ave	n=6	37.7	0.3	0.00025	35.6	0.2	0.00006	37.3	0.3	0.00043			
Ave	n=7	37.7	0.9	0.00011	35.6	0.5	0.00003	37.3	1.0	0.00016			
Ave	n=6	37.7	0.3	0.00033	35.6	0.3	0.00009	37.3	0.4	0.00051			

Ave	n=6	37.7	0.3	0.00033	35.6	0.3	0.00009	37.3	0.4	0.00051
Ave	n=5	37.7	0.3	0.00248	35.6	0.2	0.00068	37.3	0.3	0.00378
Ave	n=2	37.7	0.4	0.00029	35.6	0.4	0.00005	37.3	0.4	0.00040
Ave	n=9	37.7	0.5	0.00026	35.5	0.5	0.00007	37.2	0.5	0.00035
Ave	n=3	37.7	0.4	0.00026	35.6	0.3	0.00007	37.3	0.4	0.00023
Ave	n=4	37.7	0.2	0.00110	35.6	0.1	0.00039	37.3	0.2	0.00190
Ave	n=4	38.6	1.3	0.00108	36.5	1.3	0.00041	38.4	1.4	0.00197
Ave	n=5	37.7	0.2	0.00059	35.6	0.2	0.00036	37.3	0.2	0.00170
Ave	n=5	37.8	0.8	0.00058	35.7	0.8	0.00036	37.4	0.8	0.00172
	SD	0.20			0.21			0.25		

Supplementary Table 7: Continued

NIST612	Element: Reference:	Tb159 37.6	Int2SE 0.5	LOD 35.5	Dy163 35.5	Int2SE 0.5	LOD 38.3	Ho165 38.3	Int2SE 0.6	LOD 38.0	Er166 38.0	Int2SE 0.6	LOD 0.00155
Ave	n=5	37.6	0.5	0.00104	35.5	0.5	0.00169	38.3	0.6	0.00111	38.0	0.6	0.00155
Ave	n=5	37.6	0.6	0.00088	35.5	0.6	0.00105	38.2	0.6	0.00046	37.9	0.7	0.00071
Ave	n=5	37.6	0.5	0.00141	35.5	0.5	0.00144	38.3	0.5	0.00159	37.9	0.5	0.00135
Ave	n=7	37.6	0.9	0.00002	35.5	1.0	0.00011	38.3	1.0	0.00002	38.0	1.0	0.00003
Ave	n=5	37.6	0.4	0.00007	35.5	0.4	0.00024	38.3	0.4	0.00005	38.0	0.5	0.00011
Ave	n=6	37.6	0.4	0.00005	35.5	0.4	0.00030	38.3	0.4	0.00005	38.0	0.4	0.00012
Ave	n=6	37.6	0.4	0.00005	35.5	0.4	0.00030	38.3	0.4	0.00005	38.0	0.4	0.00012
Ave	n=6	37.6	0.4	0.00005	35.5	0.3	0.00031	38.3	0.4	0.00006	38.0	0.4	0.00009
Ave	n=7	37.6	0.9	0.00002	35.5	1.0	0.00011	38.3	1.0	0.00002	38.0	1.0	0.00003
Ave	n=6	37.6	0.4	0.00005	35.5	0.4	0.00030	38.3	0.4	0.00005	38.0	0.4	0.00012
Ave	n=6	37.6	0.4	0.00005	35.5	0.4	0.00030	38.3	0.4	0.00005	38.0	0.4	0.00012
Ave	n=5	37.6	0.3	0.00069	35.5	0.2	0.00216	38.3	0.3	0.00040	38.0	0.2	0.00150
Ave	n=2	37.6	0.4	0.00005	35.5	0.5	0.00026	38.3	0.5	0.00002	38.0	0.5	0.00011
Ave	n=9	37.5	0.5	0.00005	35.4	0.5	0.00036	38.2	0.6	0.00004	37.9	0.6	0.00011
Ave	n=3	37.6	0.3	0.00004	35.5	0.3	0.00033	38.3	0.4	0.00004	38.0	0.4	0.00012
Ave	n=4	37.6	0.1	0.00021	35.5	0.2	0.00101	38.3	0.1	0.00009	38.0	0.2	0.00033
Ave	n=4	38.6	1.4	0.00020	36.4	1.3	0.00100	39.3	1.4	0.00009	39.0	1.4	0.00032
Ave	n=5	37.6	0.1	0.00012	35.5	0.2	0.00070	38.3	0.1	0.00014	38.0	0.2	0.00080
Ave	n=5	37.6	0.8	0.00012	35.6	0.8	0.00070	38.4	0.8	0.00013	38.1	0.8	0.00079
	SD	0.23		0.21			0.23			0.23			
NIST612	Element: Reference:	Tm169 36.8	Int2SE 0.6	LOD 39.2	Yb172 39.2	Int2SE 0.6	LOD 37.0	Lu175 37.0	Int2SE 0.6	LOD 0.00133			
Ave	n=5	36.8	0.6	0.00135	39.2	0.6	0.00156	37.0	0.6	0.00133			
Ave	n=5	36.8	0.6	0.00056	39.2	0.6	0.00127	37.0	0.6	0.00058			
Ave	n=5	36.7	0.5	0.00130	39.1	0.5	0.00218	37.0	0.5	0.00136			
Ave	n=7	36.8	1.0	0.00002	39.2	1.0	0.00006	37.0	1.0	0.00001			
Ave	n=5	36.8	0.4	0.00006	39.2	0.4	0.00021	37.0	0.4	0.00006			
Ave	n=6	36.8	0.4	0.00006	39.2	0.4	0.00018	37.0	0.4	0.00005			
Ave	n=6	36.8	0.4	0.00006	39.2	0.4	0.00018	37.0	0.4	0.00005			
Ave	n=6	36.8	0.4	0.00006	39.1	0.4	0.00017	37.0	0.4	0.00005			
Ave	n=7	36.8	1.0	0.00002	39.2	1.0	0.00006	37.0	1.0	0.00001			
Ave	n=6	36.8	0.4	0.00006	39.2	0.4	0.00018	37.0	0.4	0.00005			

Ave	n=6	36.8	0.4	0.00006	39.2	0.4	0.00018	37.0	0.4	0.00005
Ave	n=5	36.8	0.2	0.00042	39.2	0.3	0.00182	37.0	0.2	0.00042
Ave	n=2	36.8	0.4	0.00004	39.2	0.5	0.00009	37.0	0.4	0.00002
Ave	n=9	36.7	0.6	0.00006	39.1	0.6	0.00018	36.9	0.6	0.00007
Ave	n=3	36.8	0.4	0.00005	39.2	0.4	0.00018	37.0	0.4	0.00003
Ave	n=4	36.8	0.1	0.00021	39.2	0.2	0.00078	37.0	0.1	0.00018
Ave	n=4	37.8	1.4	0.00022	40.2	1.4	0.00078	38.0	1.3	0.00017
Ave	n=5	36.8	0.1	0.00016	39.2	0.2	0.00057	37.0	0.1	0.00033
Ave	n=5	36.9	0.8	0.00016	39.3	0.9	0.00058	37.1	0.8	0.00032
	SD	0.22		0.23			0.22			

Supplementary Table 7: Continued

GSD_1GElement:		Ga69		Ti49		Ni60		Ni61		Zn66	
	Reference:	54.0	7.0	7433.6		58.0	4.0	58.0	4.0	54.0	2.0
Ave	n=4	53.8	1.0	0.14	7427.369.0	1.23	58.0	1.6	0.93	57.5	6.6
Ave	n=4	54.1	1.1	0.09	7446.571.3	1.53	58.2	1.9	1.12	58.0	8.5
Ave	n=4	54.0	1.1	0.10	7442.061.3	0.84	58.1	1.8	0.67	57.4	9.2
Ave	n=4	54.0	1.1	0.13	7429.558.0	1.19	58.0	1.7	1.13	58.0	6.1
Ave	n=4	54.0	0.9	0.12	7453.587.0	1.38	58.1	1.6	1.00	58.4	6.5
Ave	n=4	54.0	1.1	0.12	7450.365.3	1.38	58.1	1.6	1.00	58.4	6.5
Ave	n=4	54.0	0.8	0.10	7431.056.0	1.17	58.0	1.2	0.80	58.4	6.7
Ave	n=4	54.0	0.9	0.08	7433.863.0	1.13	58.0	1.3	0.68	58.1	5.6
Ave	n=2	54.0	0.8	0.02	7434.055.5	0.17	58.0	0.8	0.13	58.0	2.2
Ave	n=2	54.0	0.6	0.04	7434.059.0	4.95	58.0	0.8	0.26	58.0	3.5
Ave	n=4	54.0	1.1	0.17	7439.372.8	1.19	58.0	1.7	0.64	57.9	7.7
	SD	0.07			8.75		0.08		0.34		1.02
GSD_1GElement:		Co59		V51		Sc45		Cu63			
	Reference:	40.0	2.0	44.0	2.0	52.0	2.0	42.0	2.0		
Ave	n=4	40.0	0.6	0.107	44.0	0.6	0.079	52.0	0.9	0.250	42.0
Ave	n=4	40.0	0.9	0.153	44.0	0.8	0.078	52.1	0.9	0.205	42.3
Ave	n=4	40.0	0.7	0.118	44.0	0.7	0.061	52.0	0.7	0.140	42.2
Ave	n=4	40.0	0.7	0.255	44.0	0.6	0.091	51.9	0.6	0.143	42.0
Ave	n=4	40.0	0.6	0.170	43.9	0.7	0.082	52.0	0.6	0.205	42.2
Ave	n=4	40.0	0.7	0.170	43.9	0.5	0.082	52.0	0.6	0.205	42.2
Ave	n=4	40.0	0.6	0.131	44.0	0.5	0.092	52.0	0.6	0.228	42.0
Ave	n=4	40.0	0.6	0.120	44.0	0.5	0.070	52.0	0.5	0.170	41.9
Ave	n=2	40.0	0.5	0.009	44.0	0.5	0.018	52.0	0.3	0.027	42.0
Ave	n=2	40.0	0.5	0.024	44.0	0.4	0.140	52.0	0.5	0.100	42.0
Ave	n=4	40.0	0.7	0.158	44.0	0.7	0.079	52.0	0.7	0.175	43.8
	SD	0.02			0.06		0.03		0.52		

Supplementary Table 7: Continued

NIST614 Element: Reference:	Sc45 0.74	Int2SE	LOD	Ti47 3.61	Int2SE	LOD	V51 1.01	Int2SE	LOD	Mn55 1.42	Int2SE	LOD
n=3 Ave	0.84	0.02	0.00	3.49	0.06	0.05	0.97	0.01	0.001	1.44	0.01	0.008
n=3 Ave	0.90	0.02	0.01	3.65	0.20	0.29	0.98	0.01	0.004	1.32	0.04	0.051
n=3 Ave	0.90	0.02	0.01	3.54	0.15	0.22	1.01	0.01	0.003	1.49	0.03	0.038
n=3 Ave	0.90	0.02	0.01	3.54	0.15	0.22	1.01	0.01	0.003	1.49	0.03	0.038
n=3 Ave	0.92	0.02	0.01	3.79	0.13	0.20	1.01	0.02	0.003	1.49	0.03	0.036
n=3 Ave	0.84	0.02	0.00	3.49	0.06	0.05	0.97	0.01	0.001	1.44	0.01	0.008
n=3 Ave	0.90	0.02	0.01	3.54	0.15	0.22	1.01	0.01	0.003	1.49	0.03	0.038
n=3 Ave	0.90	0.02	0.01	3.54	0.15	0.22	1.01	0.01	0.003	1.49	0.03	0.038
n=4 Ave	0.90	0.01	0.01	3.88	0.15	0.21	1.02	0.02	0.004	1.70	0.04	0.057
n=6 Ave	0.89	0.02	0.01	3.86	0.18	0.26	1.00	0.02	0.005	1.67	0.05	0.065
	SD	0.03		0.15		0.02				0.11		
NIST614 Element: Reference:	Co59 0.79	Int2SE	LOD	Ni60 1.10	Int2SE	LOD	Cu63 1.37	Int2SE	LOD			
n=3 Ave	0.70	0.01	0.001	1.06	0.08	0.006	2.54	0.03	0.001			
n=3 Ave	0.72	0.01	0.005	0.94	0.04	0.049	2.31	0.03	0.006			
n=3 Ave	0.73	0.01	0.005	0.92	0.03	0.030	2.27	0.04	0.004			
n=3 Ave	0.73	0.01	0.005	0.92	0.03	0.030	2.27	0.04	0.004			
n=3 Ave	0.73	0.01	0.005	0.95	0.03	0.027	2.18	0.03	0.005			
n=3 Ave	0.70	0.01	0.001	1.06	0.08	0.006	2.54	0.03	0.001			
n=3 Ave	0.73	0.01	0.005	0.92	0.03	0.030	2.27	0.04	0.004			
n=3 Ave	0.73	0.01	0.005	0.92	0.03	0.030	2.27	0.04	0.004			
n=4 Ave	0.73	0.01	0.007	0.99	0.04	0.044	2.83	0.05	0.009			
n=6 Ave	0.72	0.01	0.007	0.97	0.04	0.044	2.65	0.05	0.010			
	SD	0.01		0.06		0.21						

Supplementary Table 7: Continued

NIST614	Element: Reference:	La139 0.72	Int2SE	LOD	Ce140 0.81	Int2SE	LOD	Pr141 0.77	Int2SE	LOD	Nd146 0.75	Int2SE	LOD
n=3	Ave	0.67	0.02	0.00003	0.74	0.01	0.00002	0.72600	0.01033	0.00002	0.770	0.021	0.00018
n=3	Ave	0.64	0.01	0.00040	0.70	0.01	0.00015	0.69760	0.00900	0.00012	0.713	0.024	0.00040
n=3	Ave	0.67	0.01	0.00011	0.73	0.01	0.00015	0.71987	0.00797	0.00007	0.734	0.027	0.00043
n=3	Ave	0.67	0.01	0.00011	0.73	0.01	0.00015	0.71987	0.00797	0.00007	0.734	0.027	0.00043
n=3	Ave	0.66	0.01	0.00007	0.72	0.01	0.00007	0.72033	0.00883	0.00006	0.746	0.024	0.00057
n=3	Ave	0.67	0.02	0.00003	0.74	0.01	0.00002	0.72600	0.01033	0.00002	0.770	0.021	0.00018
n=3	Ave	0.67	0.01	0.00011	0.73	0.01	0.00015	0.71987	0.00797	0.00007	0.734	0.027	0.00043
n=3	Ave	0.67	0.01	0.00011	0.73	0.01	0.00015	0.71987	0.00797	0.00007	0.734	0.027	0.00043
n=4	Ave	0.68	0.01	0.00083	0.75	0.01	0.00133	0.73860	0.00975	0.00146	0.722	0.030	0.00385
n=3	Ave	0.69	0.01	0.00009	0.76	0.01	0.00011	0.74277	0.00833	0.00008	0.696	0.021	0.00029
n=4	Ave	0.73	0.01	0.00023	0.79	0.01	0.00027	0.77703	0.00670	0.00016	0.740	0.026	0.00105
	SD	0.02			0.02			0.02			0.02		
NIST614	Element: Reference:	Sm147 0.75	Int2SE	LOD	Eu153 0.77	Int2SE	LOD	Gd157 0.76	Int2SE	LOD			
n=3	Ave	0.75133	0.02000	0.00035	0.76567	0.01567	0.00004	0.77767	0.02533	0.00019			
n=3	Ave	0.74733	0.01967	0.00079	0.75853	0.01123	0.00024	0.73033	0.01933	0.00089			
n=3	Ave	0.76567	0.02267	0.00048	0.79723	0.01223	0.00015	0.76567	0.02000	0.00064			
n=3	Ave	0.76567	0.02267	0.00048	0.79723	0.01223	0.00015	0.76567	0.02000	0.00064			
n=3	Ave	0.76500	0.01900	0.00037	0.79100	0.01200	0.00008	0.76433	0.02067	0.00054			
n=3	Ave	0.75133	0.02000	0.00035	0.76567	0.01567	0.00004	0.77767	0.02533	0.00019			
n=3	Ave	0.76567	0.02267	0.00048	0.79723	0.01223	0.00015	0.76567	0.02000	0.00064			
n=3	Ave	0.76567	0.02267	0.00048	0.79723	0.01223	0.00015	0.76567	0.02000	0.00064			
n=4	Ave	0.74300	0.02050	0.00273	0.74350	0.01300	0.00402	0.73525	0.02275	0.00627			
n=3	Ave	0.72600	0.02233	0.00066	0.73300	0.01467	0.00029	0.70733	0.02867	0.00105			
n=4	Ave	0.77200	0.02725	0.00109	0.77350	0.01500	0.00043	0.74975	0.02800	0.00227			
	SD	0.01			0.02			0.02					

Supplementary Table 7: Continued

NIST614	Element: Reference:	Tb159 0.74	Int2SE	LOD	Dy163 0.75	Int2SE	LOD
n=3	Ave	0.76200	0.02633	0.00001	0.76833	0.02900	0.00009
n=3	Ave	0.73857	0.00950	0.00010	0.72967	0.01567	0.00045
n=3	Ave	0.76793	0.01140	0.00006	0.78100	0.01700	0.00043
n=3	Ave	0.76793	0.01140	0.00006	0.78100	0.01700	0.00043
n=3	Ave	0.76500	0.01233	0.00005	0.76867	0.01533	0.00031
n=3	Ave	0.76200	0.02633	0.00001	0.76833	0.02900	0.00009
n=3	Ave	0.76793	0.01140	0.00006	0.78100	0.01700	0.00043
n=3	Ave	0.76793	0.01140	0.00006	0.78100	0.01700	0.00043
n=4	Ave	0.72155	0.01023	0.00545	0.73075	0.01975	0.00459
n=3	Ave	0.70033	0.02300	0.00007	0.68767	0.02600	0.00023
n=4	Ave	0.76795	0.01145	0.00015	0.73975	0.02050	0.00155
	SD	0.02321			0.03038		
NIST614	Element: Reference:	Ho165 0.75	Int2SE	LOD	Er166 0.77	Int2SE	LOD
n=3	Ave	0.77867	0.03000	0.00002	0.77400	0.03067	0.00004
n=3	Ave	0.75233	0.00970	0.00009	0.74533	0.01533	0.00025
n=3	Ave	0.79287	0.01053	0.00011	0.78167	0.01433	0.00012
n=3	Ave	0.79287	0.01053	0.00011	0.78167	0.01433	0.00012
n=3	Ave	0.79363	0.01270	0.00004	0.77200	0.01567	0.00005
n=3	Ave	0.77867	0.03000	0.00002	0.77400	0.03067	0.00004
n=3	Ave	0.79287	0.01053	0.00011	0.78167	0.01433	0.00012
n=3	Ave	0.79287	0.01053	0.00011	0.78167	0.01433	0.00012
n=4	Ave	0.71480	0.00928	0.00745	0.72800	0.01725	0.01123
n=3	Ave	0.69767	0.02733	0.00006	0.73700	0.02833	0.00020
n=4	Ave	0.77663	0.01170	0.00016	0.74650	0.01750	0.00029
	SD	0.03381			0.02047		

Supplementary Table 7: Continued

NIST614	Element:	Tm169	Int2SE	LOD	Yb172	Int2SE	LOD	Lu175	Int2SE	LOD
	Reference:	0.73			0.78			0.73		
n=3	Ave	0.75033	0.03033	0.00007	0.82033	0.03133	0.00005	0.77967	0.03133	0.00002
n=3	Ave	0.73667	0.00877	0.00011	0.73200	0.01867	0.00048	0.76217	0.01037	0.00009
n=3	Ave	0.77367	0.00947	0.00007	0.76267	0.01767	0.00017	0.80633	0.01167	0.00006
n=3	Ave	0.77367	0.00947	0.00007	0.76267	0.01767	0.00017	0.80633	0.01167	0.00006
n=3	Ave	0.77127	0.01297	0.00010	0.77233	0.01733	0.00026	0.80240	0.01420	0.00010
n=3	Ave	0.75033	0.03033	0.00007	0.82033	0.03133	0.00005	0.77967	0.03133	0.00002
n=3	Ave	0.77367	0.00947	0.00007	0.76267	0.01767	0.00017	0.80633	0.01167	0.00006
n=3	Ave	0.77367	0.00947	0.00007	0.76267	0.01767	0.00017	0.80633	0.01167	0.00006
n=4	Ave	0.67173	0.00955	0.01220	0.72800	0.02225	0.01443	0.67750	0.01075	0.01800
n=3	Ave	0.66433	0.02667	0.00009	0.70533	0.02600	0.00032	0.67533	0.02700	0.00008
n=4	Ave	0.73610	0.01030	0.00019	0.76575	0.02325	0.00067	0.74743	0.01000	0.00011
	SD	0.04003			0.03490			0.04957		

Supplementary Table 7: Continued

NIST616	Element: Reference:	Sc45 0.026	Int2SE	LOD	Ti47 2.650	Int2SE	LOD	V51 0.228	Int2SE	LOD	Mn55 0.609	Int2SE	LOD
n=3	Ave	0.114	0.006	0.00	2.125	0.048	0.04	0.175	0.003	0.00	0.540	0.008	0.007
n=3	Ave	0.105	0.006	0.01	2.263	0.137	0.22	0.181	0.006	0.00	0.618	0.024	0.035
n=3	Ave	0.097	0.005	0.01	2.193	0.101	0.15	0.182	0.004	0.00	0.566	0.017	0.027
n=3	Ave	0.097	0.005	0.01	2.193	0.101	0.15	0.182	0.004	0.00	0.566	0.017	0.027
n=3	Ave	0.103	0.004	0.00	2.317	0.113	0.15	0.181	0.004	0.00	0.490	0.023	0.028
n=3	Ave	0.114	0.006	0.00	2.125	0.048	0.04	0.175	0.003	0.00	0.540	0.008	0.007
n=3	Ave	0.097	0.005	0.01	2.193	0.101	0.15	0.182	0.004	0.00	0.566	0.017	0.027
n=3	Ave	0.097	0.005	0.01	2.193	0.101	0.15	0.182	0.004	0.00	0.566	0.017	0.027
n=6	Ave	0.200	0.009	0.01	3.057	0.150	0.23	0.221	0.009	0.00	0.967	0.041	0.059
n=4	Ave	0.098	0.007	0.01	2.890	0.153	0.21	0.217	0.008	0.00	0.918	0.040	0.058
n=6	Ave	0.102	0.008	0.01	2.952	0.157	0.24	0.221	0.008	0.01	0.859	0.040	0.060
n=4	Ave	0.163	0.012	0.01	2.180	0.148	0.08	0.225	0.012	0.01	0.622	0.021	0.020
n=3	Ave	0.226	0.020	0.02	3.017	0.230	0.09	0.314	0.020	0.01	0.871	0.048	0.023
n=4	Ave	0.136	0.013	0.02	2.240	0.153	0.08	0.220	0.011	0.00	0.633	0.020	0.016
n=4	Ave	0.140	0.015	0.02	2.288	0.180	0.08	0.223	0.015	0.00	0.647	0.032	0.015
	SD	0.041			0.357			0.036			0.156		
NIST616	Element: Reference:	Co59 0.051	Int2SE	LOD	Ni60 0.435	Int2SE	LOD	Cu63 0.700	Int2SE	LOD			
n=3	Ave	0.026	0.001	0.001	0.230	0.040	0.006	1.601	0.013	0.001			
n=3	Ave	0.025	0.003	0.004	0.173	0.024	0.036	1.421	0.019	0.005			
n=3	Ave	0.024	0.003	0.004	0.162	0.014	0.021	1.405	0.016	0.003			
n=3	Ave	0.024	0.003	0.004	0.162	0.014	0.021	1.405	0.016	0.003			
n=3	Ave	0.029	0.003	0.004	0.165	0.015	0.020	1.299	0.017	0.003			
n=3	Ave	0.026	0.001	0.001	0.230	0.040	0.006	1.601	0.013	0.001			
n=3	Ave	0.024	0.003	0.004	0.162	0.014	0.021	1.405	0.016	0.003			
n=3	Ave	0.024	0.003	0.004	0.162	0.014	0.021	1.405	0.016	0.003			
n=6	Ave	0.035	0.004	0.006	0.264	0.038	0.063	2.200	0.044	0.010			
n=4	Ave	0.035	0.005	0.007	0.240	0.023	0.038	2.193	0.045	0.009			
n=6	Ave	0.035	0.004	0.007	0.229	0.025	0.042	2.103	0.042	0.008			
n=4	Ave	0.037	0.011	0.022	0.167	0.032	0.051						
n=3	Ave	0.060	0.017	0.025	0.236	0.042	0.058						

n=4	Ave	0.032	0.011	0.047	0.197	0.038	0.048
n=4	Ave	0.033	0.011	0.047	0.206	0.046	0.047
	SD	0.009			0.036		0.350

Supplementary Table 7: Continued

NIST616	Element: Reference:	La139 0.02980	Int2SE	LOD	Ce140 0.02920	Int2SE	LOD
n=3	Ave	0.02314	0.00068	0.00002	0.02236	0.00075	0.00001
n=3	Ave	0.02146	0.00101	0.00011	0.02140	0.00112	0.00012
n=3	Ave	0.02248	0.00087	0.00007	0.02169	0.00096	0.00007
n=3	Ave	0.02248	0.00087	0.00007	0.02169	0.00096	0.00007
n=3	Ave	0.02223	0.00091	0.00005	0.02156	0.00095	0.00005
n=3	Ave	0.02314	0.00068	0.00002	0.02236	0.00075	0.00001
n=3	Ave	0.02248	0.00087	0.00007	0.02169	0.00096	0.00007
n=3	Ave	0.02248	0.00087	0.00007	0.02169	0.00096	0.00007
n=4	Ave	0.02955	0.00193	0.00024	0.03020	0.00205	0.00026
n=6	Ave	0.02708	0.00180	0.00012	0.02535	0.00173	0.00011
n=4	Ave	0.02658	0.00150	0.00060	0.02638	0.00153	0.00080
n=4	Ave	0.02955	0.00122	0.00014	0.02920	0.00125	0.00012
n=3	Ave	0.03997	0.00240	0.00016	0.04057	0.00250	0.00015
n=4	Ave	0.02988	0.00135	0.00014	0.02888	0.00150	0.00091
n=4	Ave	0.03035	0.00190	0.00014	0.02923	0.00188	0.00090
	SD	0.00504			0.00534		
NIST616	Element: Reference:	Pr141 0.01500	Int2SE	LOD	Nd146 0.02270	Int2SE	LOD
n=3	Ave	0.01230	0.00044	0.00001	0.01670	0.00153	0.00015
n=3	Ave	0.01211	0.00075	0.00010	0.01600	0.00290	0.00062
n=3	Ave	0.01179	0.00062	0.00006	0.01570	0.00240	0.00036
n=3	Ave	0.01179	0.00062	0.00006	0.01570	0.00240	0.00036
n=3	Ave	0.01144	0.00064	0.00003	0.01630	0.00260	0.00036
n=3	Ave	0.01230	0.00044	0.00001	0.01670	0.00153	0.00015
n=3	Ave	0.01179	0.00062	0.00006	0.01570	0.00240	0.00036
n=3	Ave	0.01179	0.00062	0.00006	0.01570	0.00240	0.00036
n=4	Ave	0.01665	0.00230	0.00123	0.01673	0.00275	0.00024
n=6	Ave	0.01365	0.00110	0.00018	0.01558	0.00425	0.00140
n=4	Ave	0.01429	0.00117	0.00059	0.01780	0.00430	0.00105
n=4	Ave	0.01539	0.00085	0.00010	0.01838	0.00398	0.00053

n=3	Ave	0.02117	0.00147	0.00011	0.02417	0.00540	0.00059
n=4	Ave	0.01521	0.00088	0.00016	0.01785	0.00385	0.00111
n=4	Ave	0.01543	0.00110	0.00015	0.01895	0.00445	0.00106
	SD	0.00266			0.00221		

Supplementary Table 7: Continued

NIST616	Element:	Sm147	Int2SE	LOD	Eu153	Int2SE	LOD	Gd157	Int2SE	LOD
	Reference:	0.01640			0.01460			0.01620		
n=3	Ave	0.01232	0.00101	0.00012	0.01268	0.00059	0.00003	0.01234	0.00103	0.00012
n=3	Ave	0.01247	0.00197	0.00059	0.01220	0.00107	0.00014	0.01223	0.00207	0.00075
n=3	Ave	0.01223	0.00173	0.00024	0.01253	0.00091	0.00009	0.01223	0.00160	0.00034
n=3	Ave	0.01223	0.00173	0.00024	0.01253	0.00091	0.00009	0.01223	0.00160	0.00034
n=3	Ave	0.01277	0.00177	0.00022	0.01285	0.00087	0.00005	0.01210	0.00173	0.00036
n=3	Ave	0.01232	0.00101	0.00012	0.01268	0.00059	0.00003	0.01234	0.00103	0.00012
n=3	Ave	0.01223	0.00173	0.00024	0.01253	0.00091	0.00009	0.01223	0.00160	0.00034
n=3	Ave	0.01223	0.00173	0.00024	0.01253	0.00091	0.00009	0.01223	0.00160	0.00034
n=4	Ave	0.01588	0.00298	0.00039	0.01673	0.00185	0.00017	0.01515	0.00248	0.00034
n=6	Ave	0.01378	0.00298	0.00067	0.01330	0.00162	0.00024	0.01467	0.00327	0.00098
n=4	Ave	0.01323	0.00255	0.00122	0.01370	0.00148	0.00080	0.01323	0.00265	0.00116
n=4	Ave	0.01358	0.00345	0.00093	0.01418	0.00205	0.00016	0.01385	0.00338	0.00155
n=3	Ave	0.01963	0.00480	0.00104	0.01983	0.00300	0.00018	0.01877	0.00470	0.00190
n=4	Ave	0.01318	0.00373	0.00062	0.01540	0.00203	0.00024	0.01423	0.00370	0.00135
n=4	Ave	0.01288	0.00370	0.00061	0.01550	0.00215	0.00023	0.01453	0.00385	0.00135
	SD	0.00197			0.00212			0.00182		

Supplementary Table 7: Continued

NIST616	Element: Reference:	Tb159 0.01450	Int2SE	LOD	Dy163 0.01730	Int2SE	LOD
n=3	Ave	0.01174	0.00053	0.00002	0.01269	0.00096	0.00007
n=3	Ave	0.01104	0.00074	0.00007	0.01257	0.00163	0.00033
n=3	Ave	0.01190	0.00064	0.00003	0.01323	0.00147	0.00019
n=3	Ave	0.01190	0.00064	0.00003	0.01323	0.00147	0.00019
n=3	Ave	0.01127	0.00072	0.00002	0.01327	0.00137	0.00021
n=3	Ave	0.01174	0.00053	0.00002	0.01269	0.00096	0.00007
n=3	Ave	0.01190	0.00064	0.00003	0.01323	0.00147	0.00019
n=3	Ave	0.01190	0.00064	0.00003	0.01323	0.00147	0.00019
n=4	Ave	0.01376	0.00120	0.00004	0.01528	0.00228	0.00016
n=6	Ave	0.01226	0.00108	0.00011	0.01223	0.00235	0.00064
n=4	Ave	0.01259	0.00117	0.00110	0.01390	0.00240	0.00079
n=4	Ave	0.01480	0.00143	0.00024	0.01345	0.00260	0.00088
n=3	Ave	0.02020	0.00230	0.00030	0.01963	0.00380	0.00079
n=4	Ave	0.01458	0.00160	0.00019	0.01425	0.00303	0.00067
n=4	Ave	0.01458	0.00170	0.00018	0.01450	0.00313	0.00066
	SD	0.00233			0.00179		
NIST616	Element: Reference:	Ho165 0.01690	Int2SE	LOD	Er166 0.01570	Int2SE	LOD
n=3	Ave	0.01185	0.00062	0.00001	0.01269	0.00091	0.00003
n=3	Ave	0.01185	0.00075	0.00006	0.01203	0.00121	0.00016
n=3	Ave	0.01190	0.00064	0.00007	0.01273	0.00117	0.00008
n=3	Ave	0.01190	0.00064	0.00007	0.01273	0.00117	0.00008
n=3	Ave	0.01211	0.00072	0.00017	0.01283	0.00106	0.00005
n=3	Ave	0.01185	0.00062	0.00001	0.01269	0.00091	0.00003
n=3	Ave	0.01190	0.00064	0.00007	0.01273	0.00117	0.00008
n=3	Ave	0.01190	0.00064	0.00007	0.01273	0.00117	0.00008
n=4	Ave	0.01366	0.00114	0.00004	0.01590	0.00160	0.00028
n=6	Ave	0.01231	0.00119	0.00012	0.01328	0.00192	0.00032
n=4	Ave	0.01300	0.00120	0.00155	0.01455	0.00225	0.00171
n=4	Ave	0.01395	0.00145	0.00010	0.01528	0.00238	0.00032
n=3	Ave	0.01917	0.00220	0.00012	0.02130	0.00347	0.00037
n=4	Ave	0.01418	0.00138	0.00015	0.01485	0.00263	0.00074

n=4	Ave	0.01448	0.00160	0.00015	0.01500	0.00273	0.00073
	SD	0.00195			0.00233		

Supplementary Table 7: Continued

NIST616	Element:	Tm169	Int2SE	LOD	Yb172	Int2SE	LOD	Lu175	Int2SE	LOD
	Reference:	0.01440		0.02880			0.01450			
n=3	Ave	0.01166	0.00057	0.00002	0.01382	0.00096	0.00006	0.01208	0.00062	0.00001
n=3	Ave	0.01125	0.00073	0.00004	0.01193	0.00170	0.00017	0.01145	0.00078	0.00008
n=3	Ave	0.01182	0.00074	0.00005	0.01263	0.00140	0.00008	0.01197	0.00068	0.00003
n=3	Ave	0.01182	0.00074	0.00005	0.01263	0.00140	0.00008	0.01197	0.00068	0.00003
n=3	Ave	0.01142	0.00063	0.00006	0.01277	0.00143	0.00010	0.01224	0.00070	0.00003
n=3	Ave	0.01166	0.00057	0.00002	0.01382	0.00096	0.00006	0.01208	0.00062	0.00001
n=3	Ave	0.01182	0.00074	0.00005	0.01263	0.00140	0.00008	0.01197	0.00068	0.00003
n=3	Ave	0.01182	0.00074	0.00005	0.01263	0.00140	0.00008	0.01197	0.00068	0.00003
n=4	Ave	0.01303	0.00119	0.00007	0.01553	0.00203	0.00019	0.01450	0.00144	0.00006
n=6	Ave	0.01193	0.00111	0.00011	0.01382	0.00273	0.00053	0.01189	0.00116	0.00019
n=4	Ave	0.01223	0.00113	0.00135	0.01305	0.00248	0.00175	0.01238	0.00125	0.00156
n=4	Ave	0.01315	0.00133	0.00018	0.01563	0.00305	0.00046	0.01285	0.00143	0.00013
n=3	Ave	0.01813	0.00193	0.00019	0.02333	0.00463	0.00055	0.01767	0.00200	0.00018
n=4	Ave	0.01363	0.00153	0.00031	0.01560	0.00328	0.00044	0.01280	0.00140	0.00010
n=4	Ave	0.01385	0.00165	0.00031	0.01603	0.00348	0.00042	0.01278	0.00148	0.00010
	SD	0.00173			0.00281			0.00154		

Supplementary Table 8: LA-ICP-MS analyses done at the Australian National University

	BCR-2G					San Carlos Olivine		
	N = 35	1 SD	Recommended Values ²	Stated Uncertainty	% RD	N = 35	1 SD	Range of reported values ^{3, 4, 5, 6}
<i>(ppm)</i>								
Li	8.84	0.36	9	1	-1.8%	1.99	0.09	1.08–1.9
Na	22953	274	23962	520	-4.2%	66	3.16	55–82
Al	71355	1028	70920	2100	0.6%	106	5.43	104–196
P	1199	57	1615	44	-25.8%	37	1.45	32–42
K	16211	609	14900	150	8.8%	< 1		
Ca	49103	894	50460	790	-2.7%	529	63	524 (400–665)
Sc	31.7	0.77	33	2	-3.9%	3.37	0.43	2.4–3.2
Ti	13629	330	14100	1000	-3.3%	28.4	0.75	9.7–25
V	414	4	425	18	-2.6%	3.20	0.06	2.7–4.5
Cr	15.1	0.27	17	2	-11.2%	111	1.6	95–146
Mn	1504	29	1550	70	-3.0%	1243	21	1015–1117
Co	37.5	0.33	38	2	-1.3%	152	1.6	138–186
Ni	12	0.28	13	12	-7.7%	2821	72	2803–2950
Cu	17.5	0.34	21	5	-16.7%	0.95	0.09	0.9–1.7
Zn	159	4	125	5	27.2%	93	2.2	54–58
Sr	319	5	342	4	-6.7%	0.006	0.008	<0.01
Y	30.1	0.77	35	3	-14.0%	0.050	0.002	0.059–0.115
Zr	162	3.9	184	15	-12.0%	0.057	0.004	<0.1(0.003–0.009)
Nb	11.7	0.13	12.5	1	-6.4%	0.0009	0.0005	<0.02 (0.0005)

1. Jarosewich *et al.* (1980)
2. GeoREM (2017)
3. Compilation of LA-ICP-Ms and ion probe values by De Hoog *et al.* (2010)
4. Ca value of 524 ppm by INAA (Köhler & Brey 1990)
5. Al, Ca, Cr, Mn, Co and Ni by high precision EPMA (Sobolev *et al.* 2007)
6. Ca, Co, Mn and Ni by high precision EPMA (Herzberg 2014)

SD = standard deviation. % RD = percentage deviation from recommended value.

References in Supplementary Table 8

- De Hoog JCM, Gall L, Cornell DH (2010) Trace-element geochemistry of mantle olivine and application to mantle petrogenesis and geothermobarometry. *Chem Geol* 270:196–215
- Herzberg C, Vidito C, Starkey NA (2016) Nickel–cobalt contents of olivine record origins of mantle peridotite and related rocks. *Am Mineral* 101:1952–1966
- Jarosewich E, Nelen JA, Norberg JA (1980) Reference samples for electron microprobe analysis. *Geostandard Newslett* 4: 43–47
- Jenner FE, O'Neill HStC (2012) Major and trace element analysis of basaltic glasses by laser-ablation ICP-MS. *Geochem Geophys Geosyst* 13: 1-17, Q03003, doi:10.1029/2011GC003890
- Jochum KP, Weis U, Stoll B, Kuzmin D, Yang Q, Raczek I, Jacob DE, Stracke A, Birbaum K, Frick DA, Günther D, Enzweiller J (2011) Determination of reference values for NIST SRM 610–617 glasses following ISO guidelines. *Geostand Geoanal Res* 35: 397–429
- Köhler T, Brey GP (1990) Ca-exchange between olivine and clinopyroxene as a geothermobarometer calibrated from 2 to 60 kbar in primitive natural lherzolites. *Geochim Cosmochim Ac* 54:2375–2388
- Paton C, Hellstrom J, Bence P, Woodhead J, Hergt J (2011) Iolite: Freeware for the visualization and processing of mass spectrometric data. *J Anal At Spectrom* 26:2508–2518

Sobolev AV, Hofmann AW, Kuzmin DV, Yaxley GM, Arndt NT, Chung SL, Danyushevsky LV, Elliott T, Frey FA, Garcia MO, Gurenko AA, Kamenetsky VS, Kerr AC, Krivolutskaya NA, Matvienkov VV, Nikogosian IK, Rocholl A, Sigurdsson IA, Sushchevskaya NM, Teklay M (2007) The amount of recycled crust in sources of mantle-derived melts. *Science* 316:412–417

Supplementary Table 9: PGE concentrations of standard reference materials and blank analyses

ID	Date	Sample wt (g)	Spike wt (g)	Spike type*	Os	Abs. 2sd	Ir	Abs. 2sd	Ru	Abs. 2sd
GP-13	Feb 2017	1.01053	0.03079	Peridotite P3	3.6128	0.0281	2.9844	0.0805	6.7451	0.1537
GP-13	Mar 2017	1.00304	0.02982	Peridotite P3	3.7363	0.0286	3.0825	0.0843	7.0506	0.1620
GP-13	Mar 2018	1.00300	0.04193	Peridotite P3	3.4718	0.0293	3.0673	0.0770	6.4246	0.1414
				Average	3.6070	0.0287	3.0448	0.0806	6.7401	0.1524
				SD	0.1323	0.0006	0.0528	0.0037	0.3130	0.0103
OKUM	Aug 2018	1.00549	0.08913	Picrite-2	1.0559	0.0230	0.9035	0.0199	4.9356	0.1066
OKUM	Aug 2018	1.00300	0.06188	Picrite-2	0.8169	0.0163	0.8633	0.0193	4.6667	0.1023
OKUM	Sept 2018	1.00227	0.08484	Picrite	0.7664	0.0083	0.8732	0.0192	4.1653	0.1306
OKUM	Sept 2018	1.01010	0.08475	Picrite	0.8381	0.0085	0.8213	0.0180	4.1151	0.1268
OKUM	Sept 2018	1.00126	0.06130	Picrite-2	0.8711	0.0164	0.8718	0.0198	4.3512	0.0978
OKUM	Nov 2018	1.00703	0.06287	Picrite-2	0.7778	0.0162	0.8851	0.0277	4.7767	0.1206
OKUM	Jan 2019	1.00589	0.08506	Picrite	0.8836	0.0088	0.8505	0.0222	4.1986	0.1205
OKUM	Jan 2019	1.00589	0.08269	Picrite	0.7395	0.0080	0.7546	0.0354	4.6809	0.1380
OKUM	Jan 2019	1.00673	0.08269	Picrite	0.7647	0.0082	0.8499	0.0215	4.9421	0.1496
OKUM	Jan 2019	1.00276	0.08493	Picrite	0.7639	0.0084	0.9041	0.0289	4.6809	0.1380
				Average	0.8278	0.0122	0.8577	0.0232	4.5513	0.1231
				SD	0.0939	0.0053	0.0442	0.0057	0.3165	0.0169
Blank	Jun 2016	0.08388	Blank-2	0.0002	0.0003	0.0006	0.0001	<LOD		
Blank	Jun 2016	0.08407	Blank-2	<LOD		0.0008	0.0001	<LOD		
Blank	Jan 2017	0.01079	Blank-2	0.0002	0.0001	0.0022	0.0004	<LOD		
Blank	July 2017	0.08373	Blank-2	0.0004	0.0005	<LOD		0.0168	0.0117	
Blank	Jan 2017	0.01059	Blank-2	0.0010	0.0001	0.0016	0.0002	<LOD		
				Average	0.0004	0.0002	0.0013	0.0002	0.0168	0.0117
				SD	0.0004	0.0002	0.0007	0.0002		

All PGEs in ppb. * = In house spikes.

Supplementary Table 9: Continued

ID	Date	Sample wt (g)	Spike wt (g)	Spike type*	Pt	Abs. 2sd	Pd	Abs. 2sd	Re	Abs. 2sd
GP-13	Feb 2017	1.01053	0.03079	Peridotite P3	6.9006	0.2093	6.8588	0.2490	0.3114	0.0080
GP-13	Mar 2017	1.00304	0.02982	Peridotite P3	6.9208	0.2103	5.7444	0.1940	0.3083	0.0095
GP-13	Mar 2018	1.00300	0.04193	Peridotite P3	6.1725	0.1631	5.6120	0.1643	0.2954	0.0076
				Average	6.6646	0.1942	6.0717	0.2024	0.3050	0.0084
				SD	0.4263	0.0269	0.6849	0.0430	0.0085	0.0010
OKUM	Aug 2018	1.00549	0.08913	Picrite-2	11.7437	0.2715	12.2353	0.2859	0.4986	0.0106
OKUM	Aug 2018	1.00300	0.06188	Picrite-2	11.4900	0.2744	11.3379	0.2708	0.4976	0.0108
OKUM	Sept 2018	1.00227	0.08484	Picrite	10.9883	0.2480	10.9265	0.2484	0.4815	0.0101
OKUM	Sept 2018	1.01010	0.08475	Picrite	10.7565	0.2414	10.8042	0.2459	0.4804	0.0101
OKUM	Sept 2018	1.00126	0.06130	Picrite-2	10.8286	0.2567	11.5032	0.2789	0.4758	0.0102
OKUM	Nov 2018	1.00703	0.06287	Picrite-2	11.5440	0.2786	11.7881	0.2815	0.5156	0.0116
OKUM	Jan 2019	1.00589	0.08506	Picrite	11.3391	0.2560	10.8569	0.2459	0.4752	0.0100
OKUM	Jan 2019	1.00589	0.08269	Picrite	11.2250	0.2525	11.0246	0.2502	0.4807	0.0101
OKUM	Jan 2019	1.00673	0.08269	Picrite	11.5066	0.2588	11.7508	0.2672	0.4888	0.0103
OKUM	Jan 2019	1.00276	0.08493	Picrite	11.9045	0.2679	11.7239	0.2660	0.5159	0.0108
				Average	11.3326	0.2606	11.3951	0.2641	0.4910	0.0105
				SD	0.3818	0.0121	0.4837	0.0155	0.0154	0.0005
Blank	Jun 2016	0.08388	Blank-2	0.0771	0.0025	<LOD		0.0002	0.00004	
Blank	Jun 2016	0.08407	Blank-2	0.0561	0.0021	<LOD		0.0001	0.00004	
Blank	Jan 2017	0.01079	Blank-2	0.0383	0.0312	<LOD		0.0109	0.0100	
Blank	July 2017	0.08373	Blank-2	0.0448	0.0027	0.1560	0.0190	0.0015	0.0001	
Blank	Jan 2017	0.01059	Blank-2	0.0100	0.0006	<LOD		0.0031	0.0031	
				Average	0.0453	0.0078	0.1560	0.0190	0.0032	0.0027
				SD	0.0246	0.0131			0.0045	0.0043

All PGEs in ppb. * = In house spikes.

Supplementary Table 9. Continued

ID	Date	Sample wt (g)	Spike wt (g)	Spike type*	$^{187}\text{Re}/^{188}\text{Os}$	Abs. 2σ	$^{187}\text{Os}/^{188}\text{Os}$	Abs. 2σ
GP-13	Feb 2017	1.01053	0.03079	Peridotite P3	0.4151	0.0112	0.1265	0.0002
GP-13	Mar 2017	1.00304	0.02982	Peridotite P3	0.3974	0.0127	0.1260	0.0002
GP-13	Mar 2018	1.00300	0.04193	Peridotite P3	0.4100	0.0111	0.1264	0.0003
				Average	0.4075	0.0117	0.1263	0.0002
				SD	0.0091	0.0009	0.0002	0.0001
OKUM	Aug 2018	1.00549	0.08913	Picrite-2	2.3124	0.0705	0.2651	0.0012
OKUM	Aug 2018	1.00300	0.06188	Picrite-2	2.9773	0.0878	0.2655	0.0012
OKUM	Sept 2018	1.00227	0.08484	Picrite	3.0813	0.0727	0.2679	0.0005
OKUM	Sept 2018	1.01010	0.08475	Picrite	2.8065	0.0654	0.2539	0.0004
OKUM	Sept 2018	1.00126	0.06130	Picrite-2	3.2480	0.0926	0.2493	0.0007
OKUM	Nov 2018	1.00703	0.06287	Picrite-2	3.2543	0.1000	0.2796	0.0006
OKUM	Jan 2019	1.00589	0.08506	Picrite	2.6308	0.0612	0.2447	0.0007
OKUM	Jan 2019	1.00589	0.08269	Picrite	3.1902	0.0757	0.2737	0.0005
OKUM	Jan 2019	1.00673	0.08269	Picrite	3.0826	0.0028	0.2704	0.0011
OKUM	Jan 2019	1.00276	0.08493	Picrite	3.3158	0.0787	0.2773	0.0009
				Average	2.9899	0.0707	0.2647	0.0008
				SD	0.3200	0.0268	0.0118	0.0003
Blank	Jun 2016		0.08388	Blank-2			0.2062	0.0096
Blank	Jun 2016		0.08407	Blank-2				
Blank	Jan 2017		0.01079	Blank-2			0.5366	0.0149
Blank	July 2017		0.08373	Blank-2			0.2605	0.0184
Blank	Jan 2017		0.01059	Blank-2				
				Average			0.3344	0.0143
				SD			0.1772	0.0045

All PGEs in ppb. * = In house spikes.

Appendix 6. Database references

Supplementary Table 1: References for $^{187}\text{Os}/^{188}\text{Os}$, Os, PGE, Al_2O_3 wt. % and spinel Cr# database

Tectonic setting	Reference
Abyssal peridotites	
	Alard, O., Luguet, A., Pearson, N. J., Griffin, W. L., Lorand, J. P., Gannoun, A., ... & O'Reilly, S. Y. (2005). In situ Os isotopes in abyssal peridotites bridge the isotopic gap between MORBs and their source mantle. <i>Nature</i> , 436(7053), 1005-1008.
	Day, J. M., Walker, R. J., & Warren, J. M. (2017). $^{186}\text{Os}-^{187}\text{Os}$ and highly siderophile element abundance systematics of the mantle revealed by abyssal peridotites and Os-rich alloys. <i>Geochimica et Cosmochimica Acta</i> , 200, 232-254.
	Harvey, J., Gannoun, A., Burton, K. W., Rogers, N. W., Alard, O., & Parkinson, I. J. (2006). Ancient melt extraction from the oceanic upper mantle revealed by Re-Os isotopes in abyssal peridotites from the Mid-Atlantic ridge. <i>Earth and Planetary Science Letters</i> , 244(3-4), 606-621.
	Lassiter, J. C., Byerly, B. L., Snow, J. E., & Hellebrand, E. (2014). Constraints from Os-isotope variations on the origin of Lena Trough abyssal peridotites and implications for the composition and evolution of the depleted upper mantle. <i>Earth and Planetary Science Letters</i> , 403, 178-187.
	Li, W., Liu, C., Tao, C., & Jin, Z. (2019). Osmium isotope compositions and highly siderophile element abundances in abyssal peridotites from the Southwest Indian Ridge: Implications for evolution of the oceanic upper mantle. <i>Lithos</i> , 346, 105167.
	Liu, C. Z., Snow, J. E., Brügmann, G., Hellebrand, E., & Hofmann, A. W. (2009). Non-chondritic HSE budget in Earth's upper mantle evidenced by abyssal peridotites from Gakkel ridge (Arctic Ocean). <i>Earth and Planetary Science Letters</i> , 283(1-4), 122-132.
	Luguet, A., Lorand, J. P., & Seyler, M. (2003). Sulfide petrology and highly siderophile element geochemistry of abyssal peridotites: A coupled study of samples from the Kane Fracture Zone (45°W 23°20'N, MARK area, Atlantic Ocean). <i>Geochimica et Cosmochimica Acta</i> , 67(8), 1553-1570.
	Marchesi, C., Garrido, C. J., Harvey, J., González-Jiménez, J. M., Hidas, K., Lorand, J. P., & Gerville, F. (2013). Platinum-group elements, S, Se and Cu in highly depleted abyssal peridotites from the Mid-Atlantic Ocean Ridge (ODP Hole 1274A): influence of hydrothermal and magmatic processes. <i>Contributions to Mineralogy and Petrology</i> , 166(5), 1521-1538.
	Rehkämper, M., Halliday, A. N., Alt, J., Fitton, J. G., Zipfel, J., & Takazawa, E. (1999). Non-chondritic platinum-group element ratios in oceanic mantle lithosphere: petrogenetic signature of melt percolation?. <i>Earth and Planetary Science Letters</i> , 172(1-2), 65-81.
	Sichel, S. E., Esperança, S., Motoki, A., Maia, M., Horan, M. F., Szatmari, P., ... & Mello, S. L. (2008). Geophysical and geochemical evidence for cold upper mantle beneath the Equatorial Atlantic Ocean. <i>Revista Brasileira de Geofísica</i> , 26(1), 69-86.

- Snow, J. E., & Reisberg, L. (1995). Os isotopic systematics of the MORB mantle: results from altered abyssal peridotites. *Earth and Planetary Science Letters*, 133(3-4), 411-421.
- Standish, J. J., Hart, S. R., Blusztajn, J., Dick, H. J. B., & Lee, K. L. (2002). Abyssal peridotite osmium isotopic compositions from cr-spinel. *Geochemistry, Geophysics, Geosystems*, 3(1), 1-24.
- Warren, J. M. (2016). Global variations in abyssal peridotite compositions. *Lithos*, 248, 193-219.

Arc peridotites

- Abe, N., Arai, S., & Yurimoto, H. (1998). Geochemical characteristics of the uppermost mantle beneath the Japan island arcs: implications for upper mantle evolution. *Physics of the Earth and Planetary Interiors*, 107(1-3), 233-248.
- Arai, S., Takada, S., Michibayashi, K., & Kida, M. (2004). Petrology of peridotite xenoliths from Iraya volcano, Philippines, and its implication for dynamic mantle-wedge processes. *Journal of Petrology*, 45(2), 369-389.
- Bénard, A., Le Losq, C., Nebel, O., & Arculus, R. J. (2018). Low-Ca boninite formation by second-stage melting of spinel harzburgite residues at mature subduction zones: new evidence from veined mantle xenoliths from the West Bismarck Arc. *Contributions to Mineralogy and Petrology*, 173(12), 105.
- Birner, S. K., Warren, J. M., Cottrell, E., Davis, F. A., Kelley, K. A., & Falloon, T. J. (2017). Forearc peridotites from Tonga record heterogeneous oxidation of the mantle following subduction initiation. *Journal of Petrology*, 58(9), 1755-1780.
- Brandon, A. D., & Draper, D. S. (1996). Constraints on the origin of the oxidation state of mantle overlying subduction zones: an example from Simcoe, Washington, USA. *Geochimica et Cosmochimica Acta*, 60(10), 1739-1749.
- Franz, L., Becker, K. P., Kramer, W., & Herzig, P. M. (2002). Metasomatic mantle xenoliths from the Bismarck microplate (Papua New Guinea)—thermal evolution, geochemistry and extent of slab-induced metasomatism. *Journal of Petrology*, 43(2), 315-343.
- Ishii, T., Robinson, P. T., Maekawa, H., & Fiske, R. (1992). Petrological studies of peridotites from diapiric serpentinite seamounts in the Izu-Ogasawara-Mariana forearc, Leg 125. In *Proceedings of the ocean drilling program, scientific results* (Vol. 125, No. 445-485). College Station: Ocean Drilling Program.
- Kepezhinskas, P., Defant, M. J., & Widom, E. (2002). Abundance and distribution of PGE and Au in the island-arc mantle: implications for sub-arc metasomatism. *Lithos*, 60(3-4), 113-128.
- Liu, J., Scott, J. M., Martin, C. E., & Pearson, D. G. (2015). The longevity of Archean mantle residues in the convecting upper mantle and their role in young continent formation. *Earth and Planetary Science Letters*, 424, 109-118.
- Maury, R. C., Defant, M. J., & Joron, J. L. (1992). Metasomatism of the sub-arc mantle inferred from trace elements in Philippine xenoliths. *Nature*, 360(6405), 661-663.
- McCoy-West, A. J., Bennett, V. C., Puchtel, I. S., & Walker, R. J. (2013). Extreme persistence of cratonic lithosphere in the southwest Pacific: Paleoproterozoic Os isotopic signatures in Zealandia. *Geology*, 41(2), 231-234.
- McInnes, B. I., McBride, J. S., Evans, N. J., Lambert, D. D., & Andrew, A. S. (1999). Osmium isotope constraints on ore metal recycling in subduction zones. *Science*, 286(5439), 512-516.
- Okamura, H., Arai, S., & Kim, Y. U. (2006). Petrology of forearc peridotite from the Hahajima Seamount, the Izu-Bonin arc, with special reference to chemical characteristics of chromian spinel. *Mineralogical Magazine*, 70(1), 15-26.

- Parkinson, I. J., & Arculus, R. J. (1999). The redox state of subduction zones: insights from arc-peridotites. *Chemical Geology*, 160(4), 409-423.
- Parkinson, I. J., & Pearce, J. A. (1998). Peridotites from the Izu–Bonin–Mariana forearc (ODP Leg 125): evidence for mantle melting and melt–mantle interaction in a supra-subduction zone setting. *Journal of Petrology*, 39(9), 1577-1618.
- Pearce, J. A., Barker, P. F., Edwards, S. J., Parkinson, I. J., & Leat, P. T. (2000). Geochemistry and tectonic significance of peridotites from the South Sandwich arc–basin system, South Atlantic. *Contributions to Mineralogy and Petrology*, 139(1), 36-53.
- Senda, R., Tanaka, T., & Suzuki, K. (2007). Os, Nd, and Sr isotopic and chemical compositions of ultramafic xenoliths from Kurose, SW Japan: Implications for contribution of slab-derived material to wedge mantle. *Lithos*, 95(3-4), 229-242.
- Widom, E., Kepezhinskas, P., & Defant, M. (2003). The nature of metasomatism in the sub-arc mantle wedge: evidence from Re–Os isotopes in Kamchatka peridotite xenoliths. *Chemical Geology*, 196(1-4), 283-306.

OIB-hosted peridotite xenoliths

- El-Rus, M. A., Neumann, E. R., & Peters, V. (2006). Serpentization and dehydration in the upper mantle beneath Fuerteventura (eastern Canary Islands): Evidence from mantle xenoliths. *Lithos*, 89(1-2), 24-46.
- Bizimis, M., Griselin, M., Lassiter, J. C., Salters, V. J., & Sen, G. (2007). Ancient recycled mantle lithosphere in the Hawaiian plume: osmium–hafnium isotopic evidence from peridotite mantle xenoliths. *Earth and Planetary Science Letters*, 257(1-2), 259-273.
- Bonadiman, C., Beccaluva, L., Coltorti, M., & Siena, F. (2005). Kimberlite-like metasomatism and ‘garnet signature’ in spinel-peridotite xenoliths from Sal, Cape Verde Archipelago: relics of a subcontinental mantle domain within the Atlantic oceanic lithosphere?. *Journal of Petrology*, 46(12), 2465-2493.
- Coltorti, M., Bonadiman, C., Hinton, R. W., Siena, F., & Upton, B. G. J. (1999). Carbonatite metasomatism of the oceanic upper mantle: evidence from clinopyroxenes and glasses in ultramafic xenoliths of Grande Comore, Indian Ocean. *Journal of Petrology*, 40(1), 133-165.
- Goto, A., & Yokoyama, K. (1988). Lherzolite inclusions in olivine nepheline tuff from Salt Lake Crater, Hawaii. *Lithos*, 21(1), 67-80.
- Hauri, E. H., & Hart, S. R. (1994). Constraints on melt migration from mantle plumes: a trace element study of peridotite xenoliths from Savai'i, Western Samoa. *Journal of Geophysical Research: Solid Earth*, 99(B12), 24301-24321.
- Jackson, E. D., & Wright, T. L. (1970). Xenoliths in the Honolulu volcanic series, Hawaii. *Journal of Petrology*, 11(2), 405-433.
- Jackson, M. G., Shirey, S. B., Hauri, E. H., Kurz, M. D., & Rizo, H. (2016). Peridotite xenoliths from the Polynesian Austral and Samoa hotspots: Implications for the destruction of ancient 187Os and 142Nd isotopic domains and the preservation of Hadean 129Xe in the modern convecting mantle. *Geochimica et Cosmochimica Acta*, 185, 21-43.
- Kuno, H. (1969). Mafic and ultramafic nodules in basaltic rocks of Hawaii. *Geological Society of America, Memoirs*, 115, 189-234.
- Lyons, J., Geist, D., Harpp, K., Diefenbach, B., Olin, P., & Vervoort, J. (2007). Crustal growth by magmatic overplating in the Galápagos. *Geology*, 35(6), 511-514.

- Neumann, E. R. (1991). Ultramafic and mafic xenoliths from Hierro, Canary Islands: evidence for melt infiltration in the upper mantle. *Contributions to Mineralogy and Petrology*, 106(2), 236-252.
- Neumann, E. R., Wulff-Pedersen, E., Johnsen, K., Andersen, T., & Krogh, E. (1995). Petrogenesis of spinel harzburgite and dunite suite xenoliths from Lanzarote, eastern Canary Islands: implications for the upper mantle. *Lithos*, 35(1-2), 83-107.
- Neumann, E. R., Wulff-Pedersen, E., Pearson, N. J., & Spencer, E. A. (2002). Mantle xenoliths from Tenerife (Canary Islands): evidence for reactions between mantle peridotites and silicic carbonatite melts inducing Ca metasomatism. *Journal of Petrology*, 43(5), 825-857.
- Ryabchikov, J. D., Ntaflos, T., Kurat, G., & Kogarko, L. N. (1995). Glass-bearing xenoliths from Cape Verde: evidence for a hot rising mantle jet. *Mineralogy and Petrology*, 55(4), 217-237.
- Schaefer, B. F., Turner, S., Parkinson, I., Rogers, N., & Hawkesworth, C. (2002). Evidence for recycled Archaean oceanic mantle lithosphere in the Azores plume. *Nature*, 420(6913), 304-307.
- Sen, G. (1988). Petrogenesis of spinel Iherzolite and pyroxenite suite xenoliths from the Koolau shield, Oahu, Hawaii: implications for petrology of the post-eruptive lithosphere beneath Oahu. *Contributions to Mineralogy and Petrology*, 100(1), 61-91.
- Siena, F., Beccaluva, L., Coltorti, M., Marchesi, S., & Morra, V. (1991). Ridge to hot-spot evolution of the Atlantic lithospheric mantle: evidence from Lanzarote peridotite xenoliths (Canary Islands). *Journal of Petrology*, (2), 271-290.
- Simon, N. S., Neumann, E. R., Bonadiman, C., Coltorti, M., Delpech, G., Grégoire, M., & Widom, E. (2008). Ultra-refractory domains in the oceanic mantle lithosphere sampled as mantle xenoliths at ocean islands. *Journal of Petrology*, 49(6), 1223-1251.
- Snortum, E., Day, J. M., & Jackson, M. G. (2019). Pacific lithosphere evolution inferred from Aitutaki mantle xenoliths. *Journal of Petrology*, 60(9), 1753-1772.
- Wulff-Pedersen, E., Neumann, E. R., & Jensen, B. Á. (1996). The upper mantle under La Palma, Canary Islands: formation of Si- K- Na-rich melt and its importance as a metasomatic agent. *Contributions to Mineralogy and Petrology*, 125(2-3), 113-139.
- Ophiolite peridotites**
- Aldanmaz, E. R. C. A. N., Meisel, T., Celik, O. F., & Henjes-Kunst, F. (2012). Osmium isotope systematics and highly siderophile element fractionation in spinel-peridotites from the Tethyan ophiolites in SW Turkey: implications for multi-stage evolution of oceanic upper mantle. *Chemical Geology*, 294, 152-164.
- Batanova, V. G., Brügmann, G. E., Bazylev, B. A., Sobolev, A. V., Kamenetsky, V. S., & Hofmann, A. W. (2008). Platinum-group element abundances and Os isotope composition of mantle peridotites from the Mamonia complex, Cyprus. *Chemical Geology*, 248(3-4), 195-212.
- Chen, C., Su, B. X., Xiao, Y., Uysal, İ., Lin, W., Chu, Y., ... & Sakyi, P. A. (2020). Highly siderophile elements and Os isotope constraints on the genesis of peridotites from the Kızıldağ ophiolite, southern Turkey. *Lithos*, 105583.
- Fischer-Gödde, M., Becker, H., & Wombacher, F. (2011). Rhodium, gold and other highly siderophile elements in orogenic peridotites and peridotite xenoliths. *Chemical Geology*, 280(3-4), 365-383.

- Gong, X. H., Shi, R. D., Griffin, W. L., Huang, Q. S., Xiong, Q., Chen, S. S., ... & O'Reilly, S. Y. (2016). Recycling of ancient subduction-modified mantle domains in the Purang ophiolite (southwestern Tibet). *Lithos*, 262, 11-26.
- Hanghøj, K., Kelemen, P. B., Hassler, D., & Godard, M. (2010). Composition and genesis of depleted mantle peridotites from the Wadi Tayin Massif, Oman Ophiolite; major and trace element geochemistry, and Os isotope and PGE systematics. *Journal of Petrology*, 51(1-2), 201-227.
- Huang, W., Van Hinsbergen, D. J., Maffione, M., Orme, D. A., Dupont-Nivet, G., Guilmette, C., ... & Kapp, P. (2015). Lower Cretaceous Xigaze ophiolites formed in the Gangdese forearc: Evidence from paleomagnetism, sediment provenance, and stratigraphy. *Earth and Planetary Science Letters*, 415, 142-153.
- O'Driscoll, B., Day, J. M., Walker, R. J., Daly, J. S., McDonough, W. F., & Piccoli, P. M. (2012). Chemical heterogeneity in the upper mantle recorded by peridotites and chromitites from the Shetland Ophiolite Complex, Scotland. *Earth and Planetary Science Letters*, 333, 226-237.
- Schulte, R. F., Schilling, M., Anma, R., Farquhar, J., Horan, M. F., Komiya, T., ... & Walker, R. J. (2009). Chemical and chronologic complexity in the convecting upper mantle: Evidence from the Taitao ophiolite, southern Chile. *Geochimica et Cosmochimica Acta*, 73(19), 5793-5819.
- Secchiari, A., Gleissner, P., Li, C., Goncharov, A., Milke, R., Becker, H., ... & Montanini, A. (2020). Highly siderophile and chalcophile element behaviour in abyssal-type and supra-subduction zone mantle: New insights from the New Caledonia ophiolite. *Lithos*, 354, 105338.
- Secchiari, A., Montanini, A., Bosch, D., Macera, P., & Cluzel, D. (2016). Melt extraction and enrichment processes in the New Caledonia Iherzolites: Evidence from geochemical and Sr–Nd isotope data. *Lithos*, 260, 28-43.
- Snortum, E., & Day, J. M. (2020). Forearc origin for Coast Range Ophiolites inferred from osmium isotopes and highly siderophile elements. *Chemical Geology*, 550, 119723.
- Snow, J. E., Schmidt, G., & Rampone, E. (2000). Os isotopes and highly siderophile elements (HSE) in the Ligurian ophiolites, Italy. *Earth and Planetary Science Letters*, 175(1-2), 119-132.
- van Acken, D., Becker, H., & Walker, R. J. (2008). Refertilization of Jurassic oceanic peridotites from the Tethys Ocean—implications for the Re–Os systematics of the upper mantle. *Earth and Planetary Science Letters*, 268(1-2), 171-181.
- Xu, Y., & Liu, C. Z. (2019). Subduction-Induced Fractionated Highly Siderophile Element Patterns in Forearc Mantle. *Minerals*, 9(6), 339.
- Xu, Y., Liu, J., Xiong, Q., Su, B. X., Scott, J. M., Xu, B., ... & Pearson, D. G. (2020). The complex life cycle of oceanic lithosphere: A study of Yarlung-Zangbo ophiolitic peridotites, Tibet. *Geochimica et Cosmochimica Acta*, 277, 175-191.